

**Experimental and Computational Investigation of Electrohydrodynamically –  
Enhanced Nucleate Boiling**

by

Samuel Charles Neu

A Thesis

Submitted to the Faculty

of the

WORCESTER POLYTECHNIC INSTITUTE

in partial fulfillment of the requirements for the

Degree of Doctor of Philosophy

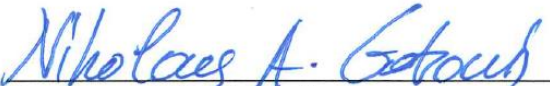
in

Aerospace Engineering

November 2016

APPROVED:

  
\_\_\_\_\_  
Professor John J. Blandino

  
\_\_\_\_\_  
Professor Nikolaos A. Gatsonis

  
\_\_\_\_\_  
Professor Jamal Yagoobi

  
\_\_\_\_\_  
Professor Mark W. Richman

  
\_\_\_\_\_  
Professor Michael A. Demetriou



## Acknowledgement

There are so many people I would like to thank who have been instrumental in helping me write this. First, I am grateful to WPI for supporting me as a TA since I started, and for providing me with laboratory space, equipment, and access to a great network of people. I would like to thank my committee, Professors Gatsonis, Demetriou, Richman, and Yagoobi for their time, and of course my advisor, Professor Blandino, for all of his help and guidance these past few years. I would like to thank all of my office mates over the years, for their help whenever I asked for it. I would also like to thank the ME office staff, as well as Randy, for assisting me whenever I had questions. Finally, I would like to thank my wife Alison, without whose support this would be impossible.

# Table of Contents

<b>Acknowledgement .....</b>	<b>iii</b>
<b>Table of Contents .....</b>	<b>iv</b>
<b>List of Tables .....</b>	<b>viii</b>
<b>List of Figures.....</b>	<b>ix</b>
<b>List of Symbols .....</b>	<b>xvi</b>
<b>Abstract.....</b>	<b>xix</b>
<b>1. Introduction.....</b>	<b>1</b>
<b>1.1. Thermal Control Overview.....</b>	<b>1</b>
<b>1.2. Objectives of This Research.....</b>	<b>4</b>
<b>1.3. Organization of the Thesis .....</b>	<b>6</b>
<b>2. Background .....</b>	<b>7</b>
<b>2.1. Physics of Nucleating Bubbles .....</b>	<b>7</b>
<b>2.2. Electrohydrodynamics .....</b>	<b>10</b>
<b>2.3. Present Work .....</b>	<b>12</b>
<b>3. Numerical modeling.....</b>	<b>16</b>
<b>3.1. Objectives .....</b>	<b>22</b>
<b>3.2. Model Description .....</b>	<b>22</b>
<b>3.3. Methodology.....</b>	<b>28</b>
<b>3.4. Model Geometry .....</b>	<b>29</b>
<b>3.4.1. AC/DC module, Electrostatics Interface.....</b>	<b>30</b>

3.4.2.	Multiphase Flow Module, Laminar Two-Phase Flow (Phase Field) Interface.....	32
3.4.3.	Heat Transfer Module, Heat Transfer in Fluids Interface.....	40
<b>3.5.</b>	<b>Reference Case Description .....</b>	<b>47</b>
<b>3.6.</b>	<b>Results.....</b>	<b>49</b>
3.6.1.	The Impact of EHD on Detachment Frequency.....	50
3.6.2.	The Impact of an Artificial Nucleation Site and EHD on Bubble Coalescence and Shape 57	
3.6.3.	EHD-influenced Detachment Behavior in Different Channel Heights.....	63
3.6.4.	The Influence of an Artificial Nucleation Site and EHD on Neck Behavior.....	64
<b>3.7.</b>	<b>Conclusion.....</b>	<b>67</b>
<b>4.</b>	<b>Experimental Investigation of EHD Effects on Nucleate Boiling.....</b>	<b>73</b>
<b>4.1.</b>	<b>Objectives .....</b>	<b>73</b>
<b>4.2.</b>	<b>Experimental Setup .....</b>	<b>75</b>
4.2.1.	Introduction.....	75
4.2.2.	Apparatus Design.....	77
4.2.3.	Copper Preparation: Polishing and Fabrication of Artificial Nucleation Site.....	81
4.2.4.	Channel Assembly .....	90
4.2.5.	Fluid Delivery and Support Structure .....	94
4.2.6.	Heating and Biasing System .....	100
4.2.7.	Power Supply and DAQ System.....	103
4.2.8.	Imaging System .....	113
<b>4.3.</b>	<b>Methodology.....</b>	<b>115</b>
4.3.1.	Image Analysis .....	122
4.3.2.	Uncertainty Analysis.....	128
4.3.3.	Statistical Analysis.....	129

<b>4.4.</b>	<b>Results.....</b>	<b>132</b>
4.4.1.	What is the Effect of EHD on Nucleation Site Density? .....	134
4.4.2.	How can EHD Influence the Position in the Channel of Bubbles that Have Separated? .....	142
4.4.3.	Does the Polarity of the Electrodes Affect the Behavior of Nucleating Bubbles? .....	147
4.4.4.	How can EHD Influence Nucleating Bubble Shape and Evolution Prior to Separation? 150	
4.4.5.	Does the Bubble Departure Frequency Increase Under EHD Forces? .....	153
<b>4.5.</b>	<b>Discussions.....</b>	<b>156</b>
4.5.1.	Results Discussions.....	156
4.5.2.	Secondary Effects .....	159
4.5.3.	Experimental Explanation via Further Modeling Work .....	164
<b>5.</b>	<b>Conclusions &amp; Future Work.....</b>	<b>174</b>
5.1.	Lessons Learned.....	176
5.2.	Future Work .....	178
<b>6.</b>	<b>Works Cited.....</b>	<b>179</b>
<b>7.</b>	<b>Bibliography .....</b>	<b>185</b>
	<b>Buoyancy-Driven Bubble Pumps .....</b>	<b>185</b>
	<b>DEP-Driven Bubble Pump.....</b>	<b>185</b>
	<b>Bubble Tracking .....</b>	<b>187</b>
	<b>DEP Electrode Geometry.....</b>	<b>187</b>
	<b>Dynamics of Bubble Formation and Separation without DEP.....</b>	<b>187</b>
	<b>Dynamics of Bubble Formation and Separation with DEP .....</b>	<b>188</b>
	<b>DEP Enhanced Nucleate Boiling .....</b>	<b>189</b>
	<b>Electrohydrodynamics/DEP .....</b>	<b>191</b>
	<b>HFE-7100 Nucleate Boiling.....</b>	<b>191</b>

<b>DEP In Microgravity .....</b>	<b>191</b>
<b>Introductory Concepts .....</b>	<b>192</b>
<b>Two Phase Modeling and Flow.....</b>	<b>192</b>
<b>Minichannels .....</b>	<b>193</b>
<b>Embedded Systems .....</b>	<b>194</b>
<b>8. Appendices.....</b>	<b>195</b>
<b>8.1. Appendix A: System Design Background &amp; Trial Details.....</b>	<b>195</b>
8.1.1. Isolation Amplifier Design Background .....	195
8.1.2. Table of Trials.....	200
8.1.3. LabVIEW VI.....	205
8.1.4. Selected Trial Test Conditions.....	206
<b>8.2. Appendix B: Debugging and Setup Validation.....</b>	<b>211</b>
<b>8.3. Appendix C: MATLAB Scripts Used in Analysis.....</b>	<b>213</b>
8.3.1. BubbleCounter.m.....	213
8.3.2. BubbleCounter_wPosition.m .....	215
8.3.3. BubbleWidth.m.....	218
8.3.4. Frequency.....	221

*Certain materials are included under the fair use exemption of the U.S. Copyright Law and have been prepared according to the fair use*

## List of Tables

Table 1: Assumed Parameters for Baseline Case. ....	48
Table 2: Unique test numbers (corresponding to a “Trial”) utilized in statistical analysis. ....	133
Table 3: Reference conditions. ....	134
Table 4: Nucleation site density statistics for three different trials. ....	138
Table 5: Statistical results for EHD enhanced nucleation density increase (1000V vs. 0V) for Trial#60. ....	140
Table 6: Statistical results for EHD enhanced nucleation density increase (2000V vs. 0V) for Trial#61. ....	141
Table 7: Statistical results for EHD enhanced nucleation density increase (4000V vs. 0V) for Trial#62. ....	141
Table 8: Statistical results for EHD enhanced nucleation density increase (4000V vs. 0V) for Trial#69. ....	142
Table 9: Statistical Analysis for Bubble Height Comparison (Trial#59). ....	153
Table 10: Statistical Analysis for Bubble Width Comparison (Trial#59). ....	153
Table 11: Statistical data for bubble departure frequency, Trial#59. Uncertainty of 3 $\mu$ Hz due to time error. ....	156
Table 12: Isolation Amplifier Properties used in Calculation [82]. ....	195



## List of Figures

Figure 1: Example of a typical boiling curve, with the critical point denoted by a star. ....	7
Figure 2: Force balance on nucleating bubble on heated surface. ....	10
Figure 3: Hypothetical heat generating chip. ....	19
Figure 4: Change in contact angle along edge of an orifice (adapted from Figure 5.3 in Ref. [31]) depending on interface location (red or green lines) The phases are labeled for the $\theta_1$ angle.....	20
Figure 5: Illustration of the phase field variable through a vapor packet in a liquid medium.....	24
Figure 6: Relevant model features. ....	29
Figure 7: Description of Geometry, with variables representing important geometric features. .	47
Figure 8: Nucleation site inside the entire fluid domain.....	48
Figure 9: Visualization and Plotting of Bubble Detachment. ....	51
Figure 10 Sensitivity of bubble evolution to nucleation site cone angle. a (top, Case 2_3_50) 50° cone, b (bottom, Case 2_3_0) 0° cone. Each line style within a stated potential represents a distinct vapor region. ....	52
Figure 11: Zero degree (0°) (baseline) cone angle.....	53
Figure 12: Comparison of bubble neck behavior with 2kV of potential, comparing 0° (left, Case 2_3_0) and 50° (right, Case 2_3_50) cone angles at 19 ms. ....	54
Figure 13: Visualization of Detachment Event for 2kV, 50° Cone case (Case 2_3_50). ....	56
Figure 14: Maximum radius determination within MATLAB image processing. ....	57
Figure 15: Comparison of bubble growth radii for 50° cone (a (top), height variation with constant 2kV potential (Case 2_3_50 and Case 2_2.5_50), b (bottom) potential variation constant 3mm height, (Case 2_3_50 and Case 0_3_50)). ....	59

Figure 16: Maximum radius comparison for 0° cone angle, 3mm height (Case 2_3_0 and Case 0_3_0).	60
Figure 17: Series of screenshots from a solution (2kV, Height 3mm, Case 2_3_0)) showcasing bubble interaction with top electrode (phase field variable plotted, vapor phase corresponding to a value of “1”, liquid phase to a value of “0”).	61
Figure 18: Several snapshots during the 2kV, 50° cone angle simulation demonstrating multiple detachment and coalescence events (Case 2_3_0).	62
Figure 19: Several snapshots during the 2kV, 0° cone angle simulation demonstrating no detachment and coalescence events (Case 2_3_0).	63
Figure 20: Comparison of bubble growth vs. Channel Height (Case 2_2.5_50 and 2_3_50).	64
Figure 21: Comparison of bubble neck behaviors at t=19ms (a (top) Case 0_3_50, b (bottom) Case 2_3_50).	66
Figure 22: Description of Liquid Microlayer [56] ©UCLA 2002	70
Figure 23: High-level diagram of experimental setup.	77
Figure 24: (a) top, isometric view (b) bottom, exploded isometric view (one bottom mounting plate shown for clarity), copper electrode is 3”x1”x3/16” (for scale).	79
Figure 25: Copper surface with no finishing.	81
Figure 26: Mechanical Indentation Device	84
Figure 27: Depression created by designed indentation pin.	84
Figure 28: Center punch (units in inches), with front, top, side and isometric views.	86
Figure 29: Indentation created by custom center punch piece.	86
Figure 30: Indentation created by metal ferrule, 0.58mm diameter wire shown for scale on the electrode used in the experiment.	88

Figure 31: Metal ferrule used to create indentation in copper. ....	88
Figure 32: Diagram of heater setup, cross section of the fluid channel. Shown is the copper reducing cylinder, allowing for a 1/4" heater to make good contact with the 3/16" thick bottom electrode. ....	89
Figure 33: Using the center punch to create nucleation sites in a bench vise. Nucleation sites are numbered sequentially (from channel inlet, left in this image). ....	90
Figure 34: Copper electrodes with glass walls. ....	91
Figure 35: Channel construction with alignment fixture, one glass slide and bottom electrode shown. ....	92
Figure 36: Vaseline assisted mold removal. ....	93
Figure 37: Construction of the test channel. Forms are shown clamped together while potting compound sets. ....	94
Figure 38: Back of fluid pump syringe, after exhausting all fluid. ....	95
Figure 39: Outlet temperature and Reynolds number (in inlet tube) vs. volumetric flow rate in tube, for a 1ft long tube with a tube ID of 0.0065in. Assumed 20 °C inlet fluid passing through a copper tube immersed in 60°C water. ....	96
Figure 40: Sudden area expansion, leading to turbulent flow within a fluid channel. Left, an isometric view of the fluid inlet tube and flow direction into the channel. Right, a diagram of a sudden expansion as it would look in the channel. ....	98
Figure 41: Unheated entry length construction. ....	99
Figure 42: Copper reducing cylinder. ....	102
Figure 43: Thermocouple setup on reducing cylinder. ....	103

Figure 44: AMC1100 Isolation Device construction, showing the high potential input, Isolation amplifier, and low potential output. ....	106
Figure 45: AMC1100 Isolation Device construction, including two separate batteries (for high- and low- potential chip sides). ....	107
Figure 46: AMC1100 Isolation Device (box) shown in a protective Plexiglas container, alongside other components shown in Fig. 44 expected to float at high potential. ....	108
Figure 47: Data isolation system diagram. ....	108
Figure 48: Liquid Electrical Tape spread over possible corona discharge prone locations (wire ends, sharp points, etc.). Not shown is the underside of the PCB, which is also protected with liquid electrical tape. ....	110
Figure 49: Thermocouple amplifier calibration curve. ....	111
Figure 50: Channel Mounting Apparatus. ....	112
Figure 51: Thermocouple Placement. ....	112
Figure 52: Final Lab Setup (1: Image capture computer 2: data collection computer 3: fume hood and test setup 4: high-speed camera 5: high voltage power supply. ....	114
Figure 53: Channel section of apparatus showing metal support standoffs embedded in potting compound (protruding from bottom of each post). ....	117
Figure 54: Fluid Connections between syringe pump and fluid preheater. ....	117
Figure 55: Effect of refraction through fluid on focusing point in channel. ....	119
Figure 56: LabVIEW virtual instrument (VI). ....	120
Figure 57: LabVIEW timer logic used to control voltage ramping. ....	121
Figure 58: Testing hierarchy used to identify specific tests. ....	122

Figure 59: Data collected during a typical trial. Wall temperature of the bottom electrode(top), channel bias potential (middle), current (lower).....	123
Figure 60: Selecting nucleating bubbles within a custom MATLAB GUI. Green marks denote selected bubbles. ....	125
Figure 61: Example of statistical nucleation site density.....	126
Figure 62: Diagram of nucleating bubble, detaching upward as to pass through the control volume (dotted line) boundary.....	126
Figure 63: Trial#35 Test Conditions.....	135
Figure 64: Trial#35, t=3.4ms, no EHD.....	136
Figure 65: Trial#35, t=100ms, EHD.....	136
Figure 66: Comparison of nucleation site density between 1000V and 0V (Trial#60).....	139
Figure 67: Comparison of nucleation site density between 2000V and 0V (Trial#61).....	139
Figure 68: Comparison of Nucleation site density between 4000V and 0V (Trial#62).....	140
Figure 69: Comparison of nucleation site density between 1000V and 0V (Trial#60).....	142
Figure 70: Trial#59, F#1753, EHD off.....	143
Figure 71: Trial#59, F#4716, EHD Enabled (4kV).....	143
Figure 72: Trial#35, F#4194-4240.....	145
Figure 73: Comparison of large vapor packets between three potentials (from left to right: 1 kV, 2 kV, 4 kV) (from left to right, Trial#57, Trial#58, Trial#59).....	145
Figure 74: Bubble height in channel as a function of potential. N (number of snapshots) =24 for 1kV, 26 for 2kV, and 20 for 4kV. Error bars represent the standard deviation of the set of measurements.....	146
Figure 75: Reversed polarity setup. The red wire is the high potential, black is ground. ....	147

Figure 76: Ttrial#37, example of data acquired during a trial. ....	148
Figure 77: Trial#37 Chaotic Boiling during a rapid potential increase with reversed polarity. ..	149
Figure 78: Trial#38, low potential bubble "hovering" between two electrodes. ....	150
Figure 79: Comparison of bubble shapes without (left) and with (right) EHD (4kV). Bubble outlines are shown in red for clarity (Trial#35). ....	151
Figure 80: Distribution of bubble heights while nucleating, comparing EHD (4kV) and no EHD, for Trial#59. ....	152
Figure 81: Distribution of Bubble widths while nucleating, comparing EHD (4kV) and no EHD, for Trial#59. ....	152
Figure 82: Image intensity (corresponding to the passage of a bubble) of a bubble from a single site vs. real-time elapsed during Trial#59, EHD off. ....	154
Figure 83: Image intensity (corresponding to the passage of a bubble) of a bubble from a single site vs. real-time elapsed during Trial#59, EHD on. ....	154
Figure 84: Histogram of detachment frequency during Trial#59, comparing 4kV and 0kV .....	156
Figure 85: Isometric Channel View. ....	165
Figure 86: COMSOL model used to investigate electric field non-uniformity in the X-Y plane (dimensions in meters). Copper seen in yellow, quartz glass seen in light blue, and dark blue represents the fluid domain. ....	167
Figure 87: Example needle geometry. ....	168
Figure 88: Example of a calculation of electric field strength from a ground plane to the tip of a needle (located 5mm higher), comparing a COMSOL solution vs. an analytical solution. ....	168
Figure 89: Visualization of mesh resolution in the domain, showing increased density in the regions of interest. ....	169

Figure 90: Potential in the channel, scale in Volts.....	170
Figure 91: Force felt on a particle under EHD (3kV). Electrodes and glass sides are labeled, with the fluid domain comprising the rest of the solution domain. ....	172
Figure 92: Force on a particle (1kV).....	173
Figure 93: Comparison of finished copper. ....	176
Figure 94: Voltage Divider Resistances ©C.R. Nave [99]. ....	196
Figure 95: Schematic of Isolation Amplifier Circuit. ....	199
Figure 96: Test Conditions for Trial#35. ....	206
Figure 97: Test Conditions for Trial#57. ....	207
Figure 98: Test Conditions for Trial#58. ....	207
Figure 99: Test Conditions for Trial#59. ....	208
Figure 100: Test Conditions for Trial#60. ....	208
Figure 101: Test Conditions for Trial#61. ....	209
Figure 102: Test Conditions for Trial#62. ....	209
Figure 103: Test Conditions for Trial#63. ....	210
Figure 104: Test Conditions for Trial#69. ....	210
Figure 105: Verification of isolation amplifier effectiveness. ....	212

## List of Symbols

$B$	Magnetic field, Gauss
$c_i$	Confidence Interval
$C_p$	Specific Heat, J/g/K
$D$	Electric Displacement Field, C/m <sup>2</sup>
$E$	Electric Field, V/m
$e_i$	Unit vector
$F$	Force, N
$F_{ext}$	Other external forces in continuity equation, N
$F_g$	Force of gravity in continuity equation, N
$F_{st}$	Force of surface tension in continuity equation, N
$F_v$	Volumetric Force, N/m <sup>3</sup>
$g_{const}$	Gravitational constant, m/s <sup>2</sup>
$G$	Chemical Potential, Pa
$h_i$	Total height of the channel, m
$H_{vl}$	Enthalpy of vaporization, J/mol
$I$	Identity Matrix
$k_{l,v}$	Thermal conductivity, of liquid and vapor phases, W/m/K
$\dot{m}$	Mass flow rate, kg/s/m <sup>2</sup>
$M_w$	Molecular weight of vapor, g/mol
$n$	Unit normal
$p$	Pressure term in Navier-stokes equation, Pa



$p_o$	Atmospheric Pressure, Pa
$q$	Heat Flux, W
$\ddot{q}$	Heat flux, W/m <sup>2</sup>
$Q$	Heat added, W
$r$	Radius in polar coordinates, mm
$S_{ij}$	Placeholder tensor field
$T$	Temperature, K
$\mathbf{u}$	Velocity term in Navier stokes equation, m/s
$u_{int}$	Interface Velocity m/s
$v$	Particle Velocity, m/s
$V$	Electric Potential, V
$y$	Height of the channel at a given mesh element, m

### Greek Symbols

$\epsilon$	Combined relative permittivity
$\epsilon_o$	Permittivity of free space
$\epsilon_r$	Relative permittivity
$\tau^E$	Maxwell stress tensor, N/m <sup>2</sup>
$\rho_f$	Free charge density units, C/m <sup>3</sup>
$\rho_v$	Density of vapor, kg/m <sup>3</sup>
$\rho_{v,e}$	Electric Charge density in a volume C/m <sup>2</sup>
$\sigma$	Surface tension coefficient, N/m

$\delta$	Interface approximation function, 1/m,
$\delta_{ij}$	Kronecker delta function
$\phi$	Phase field variable
$\gamma$	Mobility
$\lambda$	Mixing energy density
$\chi$	Mobility tuning parameter
$\psi$	Placeholder variable
$\rho_l$	Density of liquid, kg/m <sup>3</sup>
$\tau$	Stress tensor, N/m <sup>2</sup>
$\mu$	Statistical Mean

#### Other Symbols

$\forall f_v$	Volume Fraction of Vapor Phase
$\forall f_l$	Volume Fraction of Liquid Phase

## Abstract

The importance of two-phase heat transfer for thermal management of aerospace avionic systems has become increasingly important as these systems have become miniaturized. Embedded active cooling systems are used to remove heat from processors and other electronic components and transferring this heat to radiators or other heat exchangers. As the characteristic dimension of flow channels for two-phase flow becomes comparable to bubble size, the mini-channels ( $< 3$  mm) used to direct the cooling fluid can complicate nucleate boiling heat transfer. Bubbles can encounter other heated walls, rapidly expanding and greatly reducing heat transfer as well as causing pressure oscillations and flow instabilities. The use of electrohydrodynamic (EHD) effects, through the introduction of non-uniform electric fields, can help mitigate this problem by altering the behavior of nucleating bubbles.

A combined experimental and computational study was undertaken using HFE-7100, an engineered fluid used in heat transfer applications, to investigate the potential for enhancement of nucleate boiling using EHD effects induced by applying a non-uniform electric field. In the experimental study, a minichannel was constructed consisting of an upper and lower copper electrode and glass side walls to allow visualization. The channel height and width were 3mm and 4.76 mm respectively, representative of the minichannel regime. The upper electrode was grounded while the lower electrode was heated and biased to high voltage. Optical imaging combined with post-processing and statistical analysis was used to quantify the effect of EHD on the bubble behavior. Bubbles were found to form preferentially on nucleation sites resulting from imperfections in the heated copper surface over artificially created nucleation sites. When a high voltage is applied across the electrodes, the electric field enhancement along the rim of the nucleation site is believed to influence the force balance on the forming bubble and thereby

influence the bubble departure size and frequency. EHD forces also act on the bubble surface as a result of the variation in permittivity between the liquid and vapor phases, altering its shape as has been previously reported in the literature. Test results are presented that demonstrate that the application of EHD increases the nucleation site density on the heated surface and increase the bubble departure frequency from individual sites. In addition, test results are presented to show that EHD forces alter the shape of bubbles during growth and the vertical position of the detached bubbles as they are carried along in the cross flow.

To better understand the underlying phenomena affecting the bubble shape and departure frequency, a numerical simulation of the bubble growth and departure was performed using COMSOL multiphysics software customized to incorporate a user-defined body force based on the Maxwell Stress Tensor. Tracking of the bubble surface, including coalescence and breakup was incorporated using the phase field variable method in which the Navier-Stokes and heat transfer equations are solved for each phase of the fluid. Results from the simulations confirmed the sensitivity of the bubble elongation and neck formation to the nucleation site geometry, specifically the angle along the rim where field enhancement occurs. The enhanced constriction of the bubble neck resulted in early detachment of bubbles when compared to simulations in which EHD was not applied. This finding provides some insight into the higher bubble departure frequency and nucleation site density observed in the experiment. The results from the combined experimental and numerical study suggest that EHD enhancement may provide a mechanism for extending the use of nucleate heat transfer to minichannels, thereby enabling additional options for cooling in compact, embedded systems.

# 1. Introduction

## 1.1. Thermal Control Overview

Energy usage is a rapidly growing aspect of modern life, yet due to current global phenomena such as pollution, resource scarcity, and climate change, there has been considerable scrutiny in how we generate and use energy, and how to dispose of waste by-products. In the United States, at the turn of the 20<sup>th</sup> century, 9.4 quadrillion BTUs were consumed in the form of coal, wood, natural gas, and petroleum. As of 2009, this increased by nearly an order of magnitude to 91.5 quadrillion BTUs of consumption [1]. In 2007, approximately 58% of this energy consumption was wasted in the form of waste heat (i.e. losses to system inefficiencies) [2]. In particular, energy generation results in a considerable waste heat problem, with up to 70% of the energy used to generate electricity being wasted as waste heat.

One particular, modern example of this phenomena is in the operation of data centers. Data centers are rapidly becoming an essential part of consumer and commercial spaces, with the rise of cloud computing, storage, and an increased use of connected services. In a whitepaper by Emerson Network Technologies [3], it is estimated that up to 37% of energy use in a data center is used for cooling the equipment inside. Specifically, the heat generated by data center components has risen considerably not just because of the increased demand, but also because of the increased speed of today's processors. This is explained partially by Moore's Law, which quantifies the observation that due to technological innovation, the number of transistors able to fit in a given space on an integrated circuit (IC) approximately doubles every two years [4]. As far back as 1965, Gordon Moore postulated that heat dissipation would become a problem with the continued development of integrated circuits. However, somewhat incorrectly, he assumed that

due to increasingly shrinking transistors, the same power input would be used to achieve a higher speed compared with a system with reduced dimensions. In the 1960's it may have not been possible to envision that power dissipation would dramatically increase over time. Azar [5] notes that while this increase in power dissipation appears counterintuitive to the original prediction of Moore, the rapid increase in processing speed and the performance-driven requirement to increase the number of elements on a silicon wafer pushes IC designs towards more powerful designs, rather than efficient. Azar further notes that due to this increase in performance, it can be extremely challenging to meet the thermal management needs of these devices on an increasingly shrinking scale.

The thermal management of computing components is not only important from a waste energy management standpoint, but also from a safety and performance standpoint. Increased power dissipation in these components leads to higher operating temperatures. Even within the specifications of a given component, continually high operating temperatures (near the upper part of a specified temperature range) may lead to a degradation in performance, relative to lower temperature operation [6]. Higher temperatures can also increase the rate of component failure, leading to increases in the Mean Time To Failure (MTTF) of components [7]. Should operating temperatures be high enough in a liquid cooled system, component failure can arise from thermal crises such as chip dryout (in which the cooling fluid is evaporated too quickly to cool a surface) and runaway temperature, where an expected cooling medium is unable to keep a component cool, and temperatures continue to rise far past safe operating conditions.

All categories of electronics (aerospace, commercial, consumer) have seen a drive towards smaller, more efficient systems. This increasing portability of computer systems makes thermal management even more important, as cooling technologies must evolve to ensure that systems can

get smaller while performance increases. Historically, large heat sinks and fans (with a characteristic size several orders of magnitude larger than the processors they were cooling) were used in desktop computer systems to maintain adequate ventilation. Kakaç discusses the evolution of these cooling systems over time [8]. For most electronic systems, this ranged from careful design (by placing power-generating components away from hot spots) to heat sinks, fans, with the most demanding applications requiring fluid cooling. This can range from single-phase pumped fluid loops to immersed components in non-conductive fluid. The rise of smartphones, embedded systems (systems that exist within a larger mechanical system and perform a specific function), and laptops means that using large heat sinks and fans may soon no longer be adequate or possible due to the compact design of these components. Additionally, the electrical power available for large, active cooling devices is limited in cases where the device itself has limited battery capacity [6]. Not only do the small, constrained spaces of these devices prevent the use of these large cooling systems, but an increase in the relative power dissipation of these systems has driven the adoption of new technologies. The power density of these components eventually became high enough that larger and more efficient heat sinks, followed by mounted fans, and eventually pumped fluid loops were needed. Looking forward, the expected continued decrease of component size, as well as an increase in relative performance and computing power, will necessitate more advanced means of cooling than the current state-of-the-art.

While data centers are one example of cost-sensitive and widespread equipment, component size is typically not a concern in data centers that can take up entire warehouses. Systems such as those used in embedded aerospace applications lead to high heat flux situations on a small scale, and without adequate cooling, component power can be limited. Engines, embedded computers and other systems, especially in space, require significant heat rejection to operate efficiently and

safely. Nucleate boiling is often recognized as being an extremely efficient form of heat transfer. Heat transfer systems that utilize nucleate boiling can achieve higher heat fluxes at lower wall (i.e. component) temperatures, which could lead to the more efficient management of small systems. However, nucleate boiling can be difficult to implement in these systems, due to their small size. While the physics and behavior of nucleate boiling is well understood on a macro scale, smaller scale systems can lead to different physical effects, making nucleate boiling an attractive, albeit unpredictable heat transfer option.

## 1.2. Objectives of This Research

The goal of this study was to explore how nucleate boiling heat transfer can be utilized on very small scales, as well as possible means of control or enhancement. Kandlikar [9] notes that several passive methods exist for the enhancement of nucleate boiling, including increasing nucleation site densities and utilizing structured, designed surfaces. These methods are well-known, but are not flexible in meeting demands that may change. Contrary to the passive methods noted by Kandlikar, active methods of nucleate boiling enhancement allow for customization of heat transfer performance, and can be scalable to different sizes. These methods include vibration, centrifugal forces, and electrohydrodynamic forces (EHD). While these methods require an external power source, EHD is attractive in that it requires no additional moving parts (to avoid the inherent unreliability of mechanical moving parts). EHD has a legacy of being utilized in a variety of systems, being explored as a pumping mechanism, as a means of increasing pool boiling heat transferred, and as a means of enabling nucleate boiling in microgravity [10] [11] [12]. The objectives of this study were to create a model that to explore whether nucleation site geometry could influence bubble growth and detachment with EHD, and with suitable design of the nucleation site, the application of a divergent electric field can influence the frequency of bubble



detachment in an embedded-scale size system. The second main objective was to create a physical experiment that could reliability demonstrate and measure the impact that EHD has on bubble growth and detachment, and do so in a device that would more closely approximate a real-world EHD-enhanced nucleate boiling solution. We also aim to quantify the importance of the nucleation site height and geometry relative to the overall channel height with respect to increasing the detachment frequency, and the feasibility of using an artificial nucleation site to generate and impact (with EHD) in an approximate real-world device.

The modeling efforts were used to guide the experimental work, which explored the impact of a cross flow on EHD-enhanced nucleate boiling, what this boiling looked like in the presence of many densely packed nucleation sites, and to determine some challenges and lessons learned if this were to be applied to a real-world system. This work characterized nucleate boiling under the influence of non-uniform electric fields in minichannels, and the results used to provide recommendations for the development of a future system. Performance results, as well as lessons learned, are provided so that future work may further develop a EHD-enhanced nucleate boiling system.

### 1.3. Organization of the Thesis

This thesis is organized in the following manner. First, in Chapter 2, a background discussion of the problem, as well as an extensive literature review of the relevant topics will be presented. Next, in Chapter 3, a numerical model will be described and results from simulations presented. Chapter 4 will present the experiment designed to investigate the EHD-enhanced nucleate boiling and associated results. Finally, in Chapter 5, conclusions and recommendations for future work will be presented

## 2. Background

Understanding the nature of EHD-enhanced nucleate boiling requires a background of fluid mechanics and heat transfer (in the form of the physics of nucleating bubbles), as well as an understanding of electrohydrodynamics, the interaction between electric fields and a fluid. A thorough understanding of these phenomena is necessary in order to develop a computational model of an EHD enhanced nucleate boiling system, as well as to develop an effective experiment.

### 2.1. Physics of Nucleating Bubbles

In the pursuit of more efficient boiling, many designs for heat transfer devices often turn to the phenomena of nucleate boiling. It is recognized that in a system, nucleate boiling can increase the performance of a heat transfer device [13] due to the energy required to change the phase of a fluid. Boiling involves the formation of vapor bubbles on a heated surface, via phase change from the liquid medium. For this study, both pool boiling and flow boiling in minichannels are

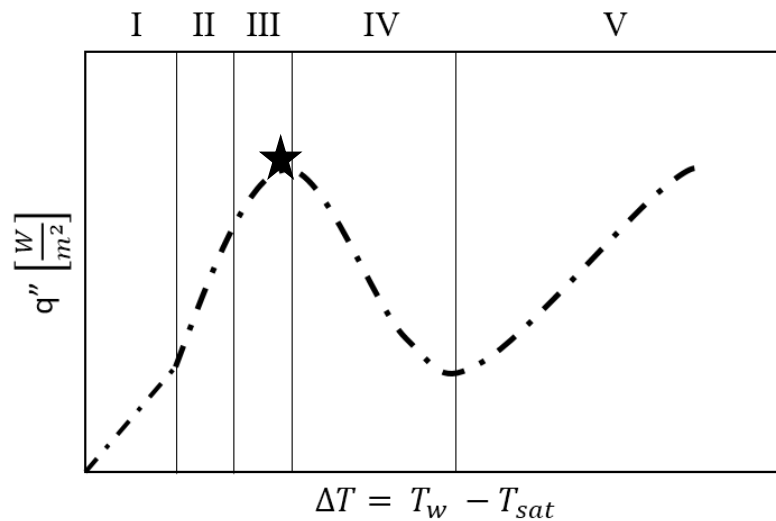


Figure 1: Example of a typical boiling curve, with the critical point denoted by a star.

examined, where the former relates to boiling occurring in a quiescent fluid medium, and flow boiling pertains to boiling occurring in enclosed channels with a bulk fluid flow. Nucleate boiling

can be described by identifying different regions with different properties, governed by the wall superheat (the temperature of the heated surface relative to the saturation temperature of a surrounding fluid) and the heat flux from that surface. These boiling regions are described in a notional nucleate boiling curve in Figure 1, which shows a typical pool boiling curve for the purpose of illustration (the curve is similar for flow boiling).

Initially, in the absence of any nucleation, free convection is the dominant form of heat transfer from the superheated wall to a fluid (Region I). In this region, buoyancy governs the circulation of warmer fluid away from the heated surface. Free convection involves no phase change and requires gravity to drive buoyant forces. As wall superheat,  $\Delta T$ , increases, the onset of nucleate boiling will occur with the presence of isolated bubbles (Region II). These will begin to form within cavities, which may be pits or scratches on the surface or artificially fabricated to enhance nucleation. Further increases in  $\Delta T$  lead to bubble coalescence in the form of columns and jets (Region III). Between Region III and IV is the critical heat flux point (marked by a star in Figure 1). After the critical heat flux point, film boiling starts to occur (Region IV and V), characterized by a thin layer of vapor film on the heated surface, sharply decreasing the heat transfer enhancement from by nucleating bubbles in a liquid. Film boiling can lead to chip dryout and a rapid decrease in the heat flux from the surface of the chip.

In the situation described above [Figure 1], the process of critical heat flux and the departure from nucleate boiling can occur very rapidly. Any increases in excess wall temperature past the critical point are marked by a transition to film boiling. The lack of distinct bubble departing from the surface would lead to a decrease in heat flux, exacerbating the further increase in wall temperature. This apparent feedback loop would lead to a rapid onset of this critical heat flux, as well as a potential “thermal emergency” in which the capability for a nucleate boiling device to

remote heat from a chip is diminished to the point where the chip overheats to a damaging temperature.

Specifically, in the case of minichannel boiling, work by Kandlikar [13] suggests that bubbles may encounter other heated walls and expand at lower wall superheats than would normally be required for the onset of the critical heat flux. Should this occur, the departure of nucleate boiling would occur even more rapidly due to the constrained channels, and the ability for slugs blocking the flow to expand very quickly. Additionally, minichannel nucleate boiling is characterized by flow oscillations, which jeopardizes any cross flow that would carry bubbles out of a constrained channel, further exacerbating the onset of critical heat flux.

The extension of nucleate boiling into minichannels is the primary goal of this work. The optimal design condition for a heat transfer device is one which operates at a point on the curve with a  $\Delta T$  just below that corresponding to the critical heat flux point. In order to influence the characteristics of nucleate boiling in minichannels, this study aims to explore modifying the behavior of nucleating bubbles in order to influence the overall boiling conditions. Varying the geometry of the surface in which nucleating bubbles will form is one way of accomplishing this. Nucleate boiling most predictably occurs on a cavity or imperfection on a surface. Bubbles tend to form on these imperfections, which contain trapped gas or vapor that serve as bubble nuclei. While these cavities can be present on any surface, controlling their geometry can offer additional means of controlling heat flux. Controlling the departure time, diameter, and growth rate of a nucleating bubble may have effects such as preventing coalescence. Preventing horizontal coalescence may provide a means of delaying the onset of downstream bubble coalescence and film boiling, and may allow for more densely backed nucleation sites. The existence of more cavities with trapped gas can lower the excess wall temperature required for nucleation.

Eastman [14] describes the force balance on a nucleating bubble, helping to clarify what causes detachment. Several forces act on a growing bubble, where there is an equilibrium condition (with respect to attachment). As soon as this equilibrium condition is no longer satisfied, the bubble detaches.

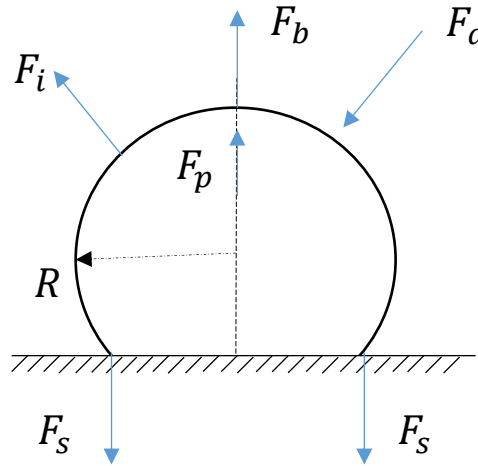


Figure 2: Force balance on nucleating bubble on heated surface.

This force balance is illustrated in Figure 2. In this figure,  $F_i$  represents inertial forces on the bubble,  $F_b$  the buoyant forces,  $F_d$  the drag force from the surrounding fluid,  $F_p$  the internal pressure forces, and  $F_s$  represents the surface tension forces acting to keep the bubble attached to the bottom, heated surface. Should any of the forces acting upwards (buoyancy), or normal to the surface (pressure) exceed the forces that hold the bubble to a surface (drag, surface tension), the bubble will detach

## 2.2. Electrohydrodynamics

Electrohydrodynamics (EHD) is the study of the interaction between fluids and electric fields [15]. Electrokinetic phenomena comprised the earliest discoveries of the field of Electrohydrodynamics, starting in the 18<sup>th</sup> century [16]. These early experiments included the development of the first electric battery, the voltaic pile. Later developments included

advancements made by Reuss (discussed in [16]), in which the phenomenon of electro-osmosis was observed before any theoretical descriptions had been made, or the underlying phenomena understood. These early experiments were described as being simple to carry out, leading to a large increase in further electrokinetic experimentation by other scientists, acting to further the understanding of such phenomena.

More recently, the application of EHD to the enhancement of heat transfer has seen increased interest. EHD enhancement methods can be non-invasive to the fluid domain. Most of these studies focus on the application of EHD to dielectric refrigerants. Jones [12] notes that as early as 1975, the underlying physics associated with the enhancement of fluid-liquid heat transfer due to non-uniform electric fields had been known for years.

Additionally, the use of electrostatic forces to manipulate fluids was explored in space, in order to manage propellants in microgravity. Jones [17], in a technical report written for NASA Marshall Space Flight Center, explores the application of electrohydrodynamics in reduced and microgravity situations, including the separation of components in heterogeneous fluids, liquid containment and transfer, fiber drawing, enhancing crystal growth, and mixing otherwise immiscible fluids [12].

Jones notes that one of the most prominent applications of EHD in a microgravity situation are for liquid orientation within a device. EHD forces can be used to provide a body force that can approximate a terrestrial gravitational field. This line of research has been explored additionally by Snyder [18]. In that study, it is noted that two-phase boiling heat transfer can be much more efficient than single phase systems, especially in weight and size constrained spacecraft thermal management systems. Without terrestrial gravity (and buoyant forces), however, there are no means for bubbles to be removed from a heated surface, leading to runaway heat transfer and

thermal crisis. Snyder uses EHD to simulate this buoyant force, enabling nucleate boiling where otherwise impossible. Particularly for spacecraft, EHD is of particular interest as there are no moving parts, and can lead to robust, fault-tolerant designs.

A subset of the described EHD forces are dielectrophoretic forces. The dielectrophoretic (DEP) force is defined as the “translational motion of neutral matter caused by the polarization effects in a non-uniform electric field.” [19] While this phenomenon is mentioned in prior studies, the first serious attempt at naming, characterizing, and studying the specific behavior of neutral matter when subjected to non-uniform electric fields can be attributed to Pohl [20] in the 1950’s. Pohl notes that DEP does not depend on ionized or charged particles, but rather arises due to the redistribution of charges within particles themselves. He also notes that these particles tend to move toward regions of higher field intensity, except in cases where the particle has more polarizability than the medium (where particles move away from regions of higher field intensity)

### 2.3. Present Work

Several studies will be examined in this section that have explored the potential benefits that nucleate boiling can have in the enhancement of heat transfer. Zuber [21], in a 1959 thesis, noted that developments in nuclear systems and rockets necessitated the need for very high heat transfer rates in constrained spaces. He notes that using forced convection (single-phase) would require exceedingly high fluid velocities, and therefore high pressure drops. This would increase the need for complicated pumping equipment and operational complexity. As a solution to this, he proposes that nucleate boiling can help achieve these same heat transfer rates with much lower fluid velocity.

While nuclear reactors and rockets still exist as potential application, considerably smaller systems such as electronics necessitate a similar need for high heat transfer performance, but in much smaller spaces. Misale [22] also notes that confined pool boiling has become a topic of



increasing importance, due to the prevalence of high-performance, compact heat exchanging devices. El-Genk [23] specifically notes the increases in CPU performance as it relates to transistor density, also increasing heat dissipation. Specific to CPUs, not only is temperature control vital to operating efficiently, but excess temperatures could destroy a CPU through several means, specifically melting solder joints or outgassing. El-Genk notes that these thermally-related failures can occur with alarming frequency if CPU temperatures exceed a given recommended value by just a few degrees centigrade. While many CPUs can achieve the desired level of cooling using passive or air-cooling (such as those found inside cellphones or desktop computers) embedded aerospace systems may need something more advanced. El-Genk specifically identifies dielectric liquids such as FC-72 as a potentially effective heat transfer fluid, specifically because the fluid must be in contact with the CPUs themselves and the boards they are mounted on. In conducting fluids, careful care must be taken to ensure that shorts are not caused between components.

Misale [22] also discusses fluids utilized in these confined pool boiling studies. Specifically, that study discusses the benefits of HFE-7100, another dielectric and liquid, as a fluid choice. Advantages mentioned are low saturation temperatures, chemical compatibility with other materials, and low toxicity. 3M [24], the provider of HFE-7100, also notes it's high boiling point, low surface tension, stability in both the thermal and chemical sense makes it useful in many aspects of industry. Other studies [23] have used fluids such as FC-72, but Misale notes a shift towards HFE-7100. Described as a hydroflouroether fluid, it is preferable due to its superior environmental characteristics. The EPA characterizes HFE-7100 as having little to no contribution to ozone formation in the atmosphere.

Some other current work relating to enhancing nucleate boiling heat transfer using EHD and DEP was undertaken by Patel [25]. In that study, it was noted that boiling processes do not function

in microgravity and cannot be used in a heat transfer device. Overcoming this limitation is possible by using electric forces, particularly DEP. Patel notes that bubbles in a highly non-uniform field can be polarized, causing a surface charge redistribution on the surface of the bubble. Patel expanded on this by utilizing a so-called DEP electrode installed above a heater. The electrode consisted of a stainless steel plate with 17 grooves, each 510 $\mu$ m wide. This was designed to increase the non-uniformity of an applied electric field so that bubbles could escape from the surface of the heater underneath. Using this design, a combination of EHD conduction pumping and DEP forces led to an increase of up to 1217% in the heat flux from the surface.

This study aims to expand on the DEP enhancement of nucleate boiling by utilizing electrodes that do not require a separate apparatus from the heated surface. The intent in the present study is to trigger the departure of smaller bubbles at a higher departure frequency, so as to prevent blocking of the channel. This is a different goal than to drive the bubbles once separated. The detached bubbles are assumed to be carried away in the cross flow.

One example of current work in this area is in work by Sunder and Tomar [29]. Sunder and Tomar discuss the possibility of using submerged needles to influence premature detachment in bubbles. In that study, bubbles were injected into a fluid domain. That study establishes a precedence for using embedded, integrated structures to influence detachment, but does not discuss this detachment in the presence of boiling, or in a minichannel. Further work is necessary to expand this work to discuss the feasibility of heat transfer devices utilizing their technique. Additionally, work by Son and Dhir [53] investigated methods of simulating boiling computationally (on the order of a single bubble) without the implementation of EHD.

Using many of the principles described in those studies, this study aims to expand on the DEP enhancement of nucleate boiling by utilizing electrodes that do not require a separate apparatus

from the heated surface. By doing this, it may approximate a real-world device more accurately in that there may not be space for separate structures in a channel.

The current work presents a case for exploring how nucleate boiling can be used to enhance heat transfer. Specifically, the usefulness of dielectric fluids presents a convenient tie-in with the use of EHD effects to enhance heat transfer. As outlined in Section 2.2, EHD is promising for a number of reasons, but there is little existing work on how EHD can be used to enhance heat transfer in small, confined spaces such as minichannels. In this study, a numerical modeling chapter is presented to explore some ways in which EHD effects can be exploited to enhance nucleate boiling heat transfer. Additionally, experiments were carried out that attempt to approximate a real-world EHD-enhanced nucleate boiling device, in order to characterize how EHD can be used to influence nucleate boiling heat transfer. Ultimately, this study should add to the long lineage of successful and promising studies about how EHD can be used to enhance heat transfer in a wide array of applications.

The primary contributions of this study were to:

- Investigate how EHD can influence nucleating and detached bubbles in a heated minichannel
- Develop an integrated model incorporating electrostatics, heat transfer, and fluid dynamics to model nucleate boiling in a minichannel with EHD

### 3. Numerical modeling

Today's rapid miniaturization of electronics and systems (as used on micro and nano-scale satellites) does not come with a proportional decrease in the amount of waste heat generated. In applications where size and cost are at a premium, it is necessary to ensure that thermal management is accomplished as inexpensively and compactly as possible [26]. Processors embedded in aerospace systems can lead to high heat flux conditions over a small scale, and without adequate cooling, component power can be limited. Embedded computers and other subsystems, especially in space, require significant heat rejection to operate efficiently and safely. Nucleate boiling is one of the most efficient means of heat transfer, but its implementation can be inefficient or impractical with hardware on the mini- or micro-scale. Restricted channels can lead to rapid bubble growth and flow oscillations, leading to a thermal runaway effect, where expanding vapor removes the cooling capacity of fluid and nucleating bubbles.

Kandlikar [27] discusses the issue of large pressure drops and unpredictable heat transfer performance related to flow boiling in small scale (mini- and micro- channel) heat transfer devices. Minichannels are defined in the literature as having hydraulic diameters from 200 $\mu\text{m}$  to 3mm, while microchannels have hydraulic diameters on the order of 10 $\mu\text{m}$  to 200 $\mu\text{m}$ . In minichannels, three flow patterns are encountered during flow boiling: isolated bubbles, confined bubbles, and annular flow, which can lead to undesirable operating conditions such as large, transient, pressure drops. The large pressure drops found in these channels are due to expanding bubbles pushing the interface downstream and upstream of the heated area.

Brutin et al. [28] performed an experimental study of convective boiling in minichannels using channels with a hydraulic diameter of 889 $\mu\text{m}$ , and a working fluid of n-pentane. In one test, bubbles are created through normal nucleate boiling and then begin to coalesce into slugs. This

generates an over-pressure (i.e. a sudden rise in pressure upstream) that reduces the flow rate in the system. Bubbles continue to grow until the channel is blocked. After this occurs, the large slugs force the direction of the flow back towards the channel entrance, leading to an entirely vapor-filled channel. The authors note a surface temperature rise due to the lack of fluid and heat-removing nucleating bubbles. This operating condition persists for a period of time after which the entire channel has built up enough upstream pressure to expel the vapor slug. After this, the channel re-fills with liquid, and the process is repeated.

Unstable heat transfer, as noted by Brutin, would not be suitable for sensitive aerospace applications. Flow oscillations can lead to unpredictable heat transfer performance due to periodic surface temperature rises, and chip dryout can cause a runaway effect that damages equipment. Any invasive means of controlling and influencing this phenomenon could lead to additional complexity in the form of moving parts or impurities in added components. Invasive methods could include internal structures to modify flow behavior, vibrating the entire structure, or including complex pumps or other moving parts. Lubricants used in these moving parts could seep into the channel and add impurities. One possible method of non-invasive control is through externally-applied, non-invasive, EHD forces. Many studies have used EHD as a means of controlling, enhancing, or enabling nucleate boiling. Jones utilized electric fields to enhance single-phase convection (inadvertently triggering nucleate boiling at lower wall superheats) [9]. Additionally, Snyder et al. explored the use of an EHD phenomenon known as dielectrophoresis (DEP) as a means of enabling nucleate boiling in microgravity [18]. Other studies discuss isolated, injected bubbles being influenced by uniform DC fields [29], or large-scale EHD-enhanced pool boiling [19], but to the best of the author's knowledge, there are no studies that computationally investigated EHD-enhanced nucleate boiling in the presence of a geometrically influenced, altered

nucleation site boiling in non-uniform electric fields in the minichannel regime. The studies cited here did not allow for methods to investigate the runaway heat transfer from chip dryout, the relationship between channel height and electrode geometry in the presence of other nucleating bubbles and low channel heights, or implement computational models that can explore the effect of changes to nucleation site geometry. This modeling study will present a method for modeling the growth and premature detachment of nucleating bubbles in the presence of an externally applied electric field. In addition, based on these results, the potential feasibility of using EHD forces to improve nucleate boiling in minichannels will be discussed in the presence of a small, constrained channel and artificial nucleation sites.

A model that couples the physics of heat transfer, nucleate boiling (two-phase flow), and electrohydrodynamics was necessary to study the growth and detachment of bubbles in the minichannel regime. First, understanding how nucleate boiling can improve heat transfer is necessary. This behavior can be generalized in the nucleate boiling curve (Figure 1), introduced and described in Section 2.1. The superheat,  $\Delta T$ , plotted on the x-axis, represents the excess wall temperature (the difference between wall temperature and saturation temperature of a fluid). As this increases, the heat flux from the surface to the fluid varies considerably based on the boiling regime characteristic of a particular range of excess wall temperature ( $T_w - T_{sat}$ ). These regimes are identified in Figure 1.

The modeling work in this study approximated boiling on a hypothetical, heated “chip”, or processor, which may have a heat sink or other interface between it and a fluid regime. A representation of this chip design is shown in Figure 3.

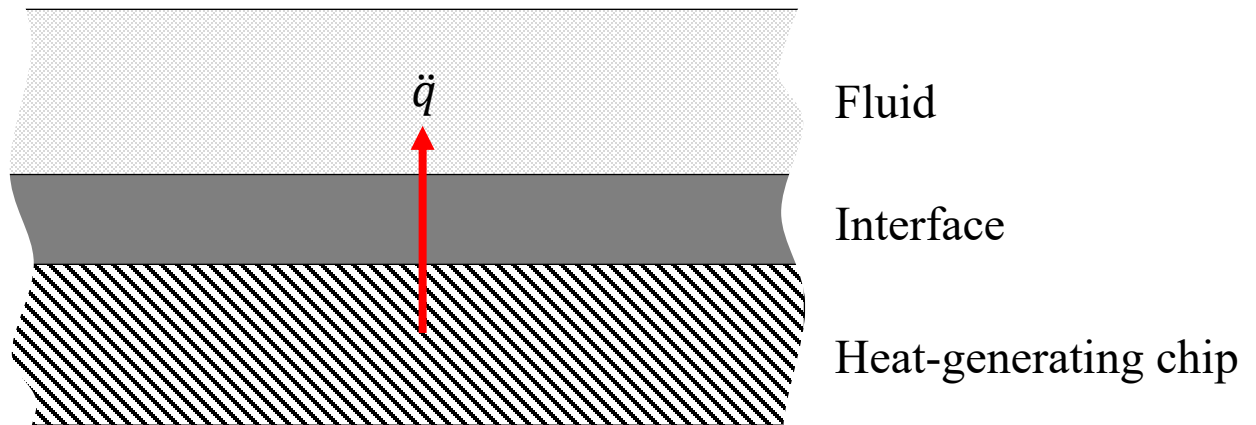


Figure 3: Hypothetical heat generating chip.

Heat transferred from a heat generating chip to a fluid can also be approximated by the curve in Figure 1. In the absence of any nucleation, free convection is the dominant form of heat transfer (Region I), in which buoyancy governs the circulation of warmer fluid away from the chip-fluid interface. As wall superheats increase, the onset of nucleate boiling will occur with the presence of isolated bubbles (Region II) filling the Fluid region. Further increases in  $\Delta T$  lead to bubble coalescence in the form of columns and jets (Region III). Between Region III and IV is the critical heat flux point (indicated by a dot). After the critical heat flux point, film boiling starts to occur (Region IV and V), leading to chip dryout and a rapid decrease in the heat flux on the surface of the chip

The optimal design condition for convective heat transfer from a device is an operating point located on the boiling curve with a superheat value just below that corresponding to the critical heat flux point. In order to influence the characteristics of nucleate boiling in minichannels, this study explored modifying the behavior of nucleating bubbles in order to influence the overall boiling conditions. Varying the geometry of the surface in which nucleating bubbles will form is

one way of accomplishing this. Nucleate boiling most predictably occurs on a cavity or imperfection on a surface. Bubbles tend to form on these imperfections, which contain trapped gas or vapor that serve as bubble nuclei. While these cavities can be present on any surface, controlling their geometry can offer additional means of controlling nucleation, and therefore heat flux. Controlling the time between bubble departures, bubble diameter, and growth rate of a nucleating bubble may have effects such as preventing coalescence. Preventing horizontal coalescence may provide a means of delaying the onset of downstream bubble coalescence and film boiling, and may allow for more densely packed nucleation sites. Here, horizontal coalescence is defined as

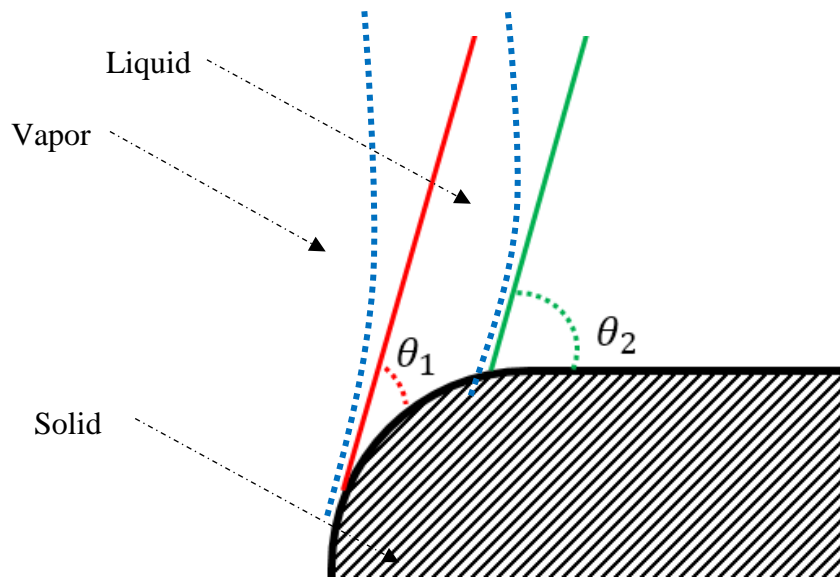


Figure 4: Change in contact angle along edge of an orifice (adapted from Figure 5.3 in Ref. [31]) depending on interface location (red or green lines) The phases are labeled for the  $\theta_1$  angle.

what happens when a bubble coalesces with a bubble from an adjacent site while still nucleating, as opposed to downstream coalescence which occurs when an upstream detached bubble coalesces with a downstream nucleating bubble. The existence of more cavities with trapped gas can lower the excess wall temperature required for nucleation.

A bubble attached to a solid surface creates a boundary between three phases. The boundary between these three phases defines a local angle, which is determined by a condition of



mechanical equilibrium. This equilibrium will, in general, depend on the properties of the phases in a complex way. In the context of a numerical model, it is necessary to define this interaction in terms of the contact angle behavior. However, the complex interaction at the three-phase contact line can make modeling the growth of a bubble from a nucleation site difficult [31]. Cattide et al. studied the sensitivity of bubble detachment from orifice diameters on the order of the bubble detachment size. In that work, the bubble interface was found to bind to an orifice rim during its growth prior to the time of detachment, and the interface shape at the three phase contact line can be determined based on that orifice size and not the contact angle. This relationship is illustrated in Figure 4, in which contact angles can be different depending on where in an orifice they attach to, while maintaining the same neck diameter. Alternatively, bubble detachment from a comparatively small cavity is defined only by the three phase contact angle between the surface, liquid, and vapor, and will also govern bubble base diameter during growth. This bubble base diameter can be difficult to determine without a robust model for the three-phase contact line in addition to a bubble growth model. This study investigates bubbles that grow and detach from orifices which have a diameter within an order of magnitude of the predicted departure diameters, due to the difficulty in determining contact angles for smaller nucleation sites.

Another means of delaying the onset of film boiling is to prevent large bubble slugs from forming downstream in a small channel. Higher heat fluxes increase the rate of bubble generation, leading to larger bubble diameters [32]. While maintaining smaller bubble departure diameters during boiling may lead to a lower heat flux in a channel, the presence of smaller detached bubbles may delay downstream coalescence under the influence of a cross flow, which in turn could delay the onset of transition or film boiling. Studies by Siedel [33] and Cattide [31] utilize porous upper electrodes to generate electric fields, allowing detached bubbles to pass through, away from the

heated surface. Kandlikar [34] notes that one of the fundamental issues related to nucleate boiling in minichannels is the possibility that growing or detached bubbles can encounter other heated walls, resulting in rapid expansion. This provides the motivation for studying the detachment of bubbles from a surface under the influence of EHD forces. The effect of a solid upper electrode on the growth of a bubble under EHD forces will be investigated. The geometry and evolution of the interface of a nucleating bubble in a small channel is integral to this analysis.

### 3.1. Objectives

Specifically, the goals of the numerical portion of the study aim to accomplish the following:

- Provide a means of studying bubble detachment on the mini-scale, coupled with electrodynamics and heat transfer physics
- Investigate nucleation site geometry as a means of controlling the growth and detachment of bubbles in a mini-channel
- Assess the feasibility of using EHD forces to control nucleate boiling characteristics in a representative minichannel
- Develop a model to capture the evolution of the interface of a growing bubble, and the coalescence and detachment between multiple bubbles

### 3.2. Model Description

Two-phase flows can be modeled with averaging techniques, looking at average void fractions within a volume [36]. However, in order to study the effect of EHD on a nucleating bubble and its interaction with a structure, a more comprehensive approach must be taken that can capture the deformation of the bubble interface.

There are several methods available to modeling multiphase flow. Recognizing that interface tracking is necessary in properly modeling two phase flow, Chung [37] recognizes that volume tracking methods, front tracking, level set, phase field can be all used for this, as well as other methods like particle-based formulations, moving meshes, and boundary integrals. One of the more common methods is volume tracking, or Volume of Fluid (VOF) methods that conserve a volume fraction function in a domain. This method solves the Navier Stokes equations and is capable of modeling compressible or incompressible flows. As described by Chung, the VOF formulation involves either re-meshing a grid as the fluid displaces or to constantly redefine element properties based on volume fraction.

Compared to the phase field method chosen here, the VOF method has some key differences and capabilities. In a study comparing multiphase flow methods by Anderson et al. [38], it is noted that VOF methods are similar to diffuse interface methods (like phase field) in that complex boundary shapes and topological changes can be described more readily than moving-mesh methods. However, it is noted that VOF methods must supplement the equations of motion with boundary conditions at the “free surface”, or the free boundary that exists between the immiscible fluids being modeled. While Anderson notes that applying these boundary conditions is applicable to a wide variety of applications, there are situations where the VOF method is not appropriate. Modeling bubble coalescence requires a different type of model.

Level set methods paired with the Navier-Stokes equations offer this ability. The Level Set Method (LSM) was developed by Osher et al. in 1988 as a means of numerically defining phase fronts propagating with a curvature dependent speed [39]. The phase field approach is similar to level set, with additional transport equations defining the motion of the interface being the primary difference between the two [40]. A phase field or level set variable ( $\phi$ ) can define one of two

phases with a gradual discontinuity in a solver (Figure 5). Unlike the LSM, the phase field approach eliminates the need for a moving mesh while capturing accurate interface dynamics, as well as providing the ability to model external body forces. This approach allows for the coupling of heat transfer physics, contact angle determination, and electrohydrodynamics on a nucleating bubble.

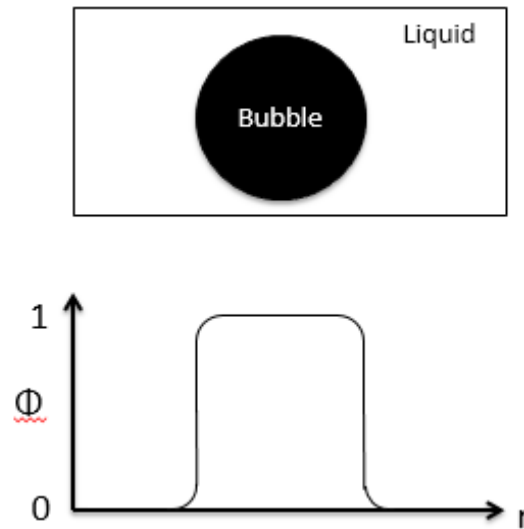


Figure 5: Illustration of the phase field variable through a vapor packet in a liquid medium.

Many methods exist for modeling two-phase flow in the presence of an electric field, but any method chosen must be able to capture complex interface dynamics. Methods based on the work done by Pohl [19], in which EHD forces are calculated on bodies assumed to be dielectric particles within a medium (See derivation and explanation provided in Pohl) would not be appropriate for capturing the deformation of bubble interfaces. Cattide et al. and Melcher [41] found that a Maxwell-stress tensor derived body force is the most useful in modeling nucleate boiling in the presence of an electric field. The Maxwell Stress Tensor (MST) is a tensor describing the stresses induced by electromagnetic fields interacting with a body with a given permittivity. In the discussion that follows, one derivation of the MST is described that starts with the Lorentz

Force Equation (LFE) (Equation 1). The LFE describes the interaction between a charged particle and electric and magnetic fields.

$$\mathbf{F} = q[\mathbf{E} + \mathbf{v} \times \mathbf{B}] \quad (1)$$

Where  $\mathbf{F}$  is a force,  $\mathbf{E}$  is an external electric field,  $\mathbf{B}$  is an external magnetic field, and  $\mathbf{v}$  is the instantaneous particle velocity. Any study exploring the effects of an electric field on a deforming medium must account for an extended interface. One such approach provided by Jackson [42] sums the momenta of every particle in some volume to determine the collective force (per unit volume) on a group of particles. Equation 2, worked out by Jackson, is an expression that can be used to calculate the force per unit volume at a single point in some medium with permittivity  $\epsilon$  due to the presence of either a non-uniform electric field or a uniform electric field and a non-uniform permittivity. This derivation starts with a sum of all momenta of every particle in a volume. Using Gauss's law and Ampere's law, that expression can be re-written in terms of the electric displacement field, introducing relative permittivity to the equation [36]. A complete derivation of (2) is provided in Jackson [42] following from Eq. 1, the LFE.

$$\mathbf{F}_v = \epsilon\epsilon_o \left[ \mathbf{E}(\nabla \cdot \mathbf{E}) + (\mathbf{E} \cdot \nabla)\mathbf{E} - \frac{1}{2}\nabla(\epsilon\epsilon_o E^2) \right] \quad (2)$$

Equation 2 defines the force per unit volume due to an electric field, but its implementation cannot account for local forces deforming certain parts of that volume (i.e. a bubble interface). The derivation described requires assuming a bulk volume, with no way to describe the magnitude of the force at discrete locations on a surface. Instead, a stress tensor can be more useful for the determination of boundary deformation. Equation 2 can be written in a different form to express the relationship fields that cause the forces, stresses that act on an area, and volumetric forces.

Equation 3 is the common form of the MST,  $\tau^E$ . The derivation of the MST from the LFE (Eq. 1), and how it relates to the force per unit volume (Eq. 2), is presented in Jackson [42]

$$\tau^E = \epsilon\epsilon_o \left( \mathbf{E}\mathbf{E} - \frac{1}{2}E^2\mathbf{I} \right) \quad (3)$$

The MST, written in terms of the electric field and relative permittivities, is used to express the electric field-induced stress on a surface in terms of a tensor, which can be incorporated into a numerical solution more readily than a volumetric force could be. The volumetric force can be recovered by calculating the divergence of the MST, and is shown in Eq. 4.

$$\mathbf{F}_v = \nabla \cdot \tau^E \quad (4)$$

Taking the divergence of the MST (Eq. 4) yields the same volumetric force equation as the one derived directly from the Lorentz Force equation (Eq. 1). Another formulation to calculate the force on a dielectric body in a field is the Korteweg-Helmholtz force density, described by Stratton [43] and Melcher [41]. This form (Eq. 5) of electric force equation is based on a principle of energy conservation (described in Melcher [41].) and are described as being broadly applicable to many problems.

$$\mathbf{F}_v = \rho_f \mathbf{E} - \frac{1}{2}E^2 \nabla \epsilon + \frac{1}{2} \nabla \left[ E^2 \rho \frac{\delta \epsilon}{\delta \rho} \right] \quad (5)$$

The first term represents the force acting on free charge (density) in an electric field, which is known as the Coulomb Force. The second represents the dielectrophoretic force. The dielectrophoretic force is the force exerted on a dielectric body in a non-uniform electric field. The third term represents the electrostriction force, and only arises in fluids with gradients in the permittivity. It is the electrostriction force that is responsible for the deformation of a dielectric material. Typically, a material will elongate in the direction of an electric field. This expression would be of great use in studying how a bubble deforms under an electric field, but the exact nature

of this deformation would be difficult to determine during a simulation of nucleation. As a bubble grows, its changing interface location influences the electric field (as the bubble has a different permittivity than the medium). Cattide et al.[31] note that form of Equation 5 is of little use in the presence of an interface between two phases because it cannot capture the interface behavior under EHD forces, meaning that a description of the body force based on the MST (stress tensors) is necessary, as opposed to one acting on an entire volume. Also shown in Melcher [41] is a derivation of the MST from Eq. 5, demonstrating the link between multiple electric field force formulations (such as ones derived from the LFE). Of particular relevance to this study is the effect that the bubble interface itself can have on the applied electric field, an effect not captured in Equation 5 in its current form. The transition in permittivity between the vapor and liquid phases can influence the electric field, leading to a force despite the absence of a non-uniform electric field. To investigate the influence that external (nucleation site and channel) geometry can have on an electric field, while in the presence of the distorting effect of the bubble's own interface, one must be able to include the effect of a changing and dynamic interface by utilizing a solution that is based on the MST.

These geometrically-enhanced electric field non-uniformities can help increase the magnitude of the EHD force on a liquid-vapor interface. The manner in which the MST is derived from the LFE is provided in Jackson [42], and forms the basis of the equations used in study. Since the force depends on the gradient of the relative permittivity (last term in Equation 5), the force is only imparted to the liquid-vapor interface. In two-phase flow, this force arises naturally from the difference in permittivity between a vapor phase and a liquid phase. Non-uniformities in the externally applied field can increase the magnitude of this force at specific points on the interface. The MST-derived volumetric force has been shown to increase greatly in magnitude in the

presence of external electric field non-uniformities [29]. In Section 3.4, the development and results of a model to capture the effects of an electric field on a nucleating bubble is presented. This model consists of the form the EHD volumetric force equation given by Eq. 5, applied at the interface of two fluids with differing permittivities. The MST is implemented alongside the phase field variable to model a stress on the fluid interface.

### 3.3. Methodology

Practical implementation of this model required striking a balance between the inclusion of the required physics and computational speed. The simplest approach that would still capture the behavior under study was to use a planar, 2-dimensional (2-D) model that couples the three physics modes of heat transfer, two-phase flow, and electrohydrodynamics. However, a planar 2-D model has shortcomings in that it cannot accurately model realistic surface tension forces due to the unphysical nature of infinitely long cylindrical bubbles. In addition, the boundary conditions for the planar 2-D phase field method cannot accurately capture the surface tension at the liquid-vapor-solid interface. For this reason, an axisymmetric 2-D model was chosen to allow a more realistic representation of the surface tension forces. However, this approach precludes the inclusion of drag forces from a cross flow, as well as studying the interactions between multiple bubbles in a long channel. The inclusion of such phenomena would require the development of a 3-dimensional (3-D) model, and while too computationally expensive for the present work, could be considered in follow-on work.

The model simulations were intended to study the detachment of bubbles from artificial nucleation sites in order to explore the sensitivity of bubble size and detachment frequency to applied potential, channel and nucleation site geometry. The key independent variables are the applied potential and the geometric parameters of the artificial nucleation site as shown in Figure



6. The primary variables in the geometry of the nucleation site are the radius of the fillet, the height of the indented cone, and the angle the cone makes with the bottom electrode.

COMSOL Multiphysics [35] was used for this study. COMSOL allows for the coupling of multiple physics environments, as well as the ability to parametrically define geometry. Additionally, COMSOL allows for the modification of any of the governing equations in order to encompass the desired physical phenomena. Three physics modules were utilized: Two-phase flow (phase field), Heat Transfer in Fluids, and Electrostatics. The boundary conditions and governing equations in each physics module are detailed in Sections 3.4.1-3.4.3.

### 3.4. Model Geometry

The relevant geometric features and boundary conditions of the simulation domain are presented in Figure 6. Each electrode is defined as constant potential boundary conditions in the electrostatics module, and also as a wetted wall in the Two-phase flow module. Pressure boundary conditions are also prescribed at the electrode surfaces, as well as the initial vapor interface between the fluid domain and the vapor domain. The heated electrode is represented in the heat transfer module as a constant heat flux.

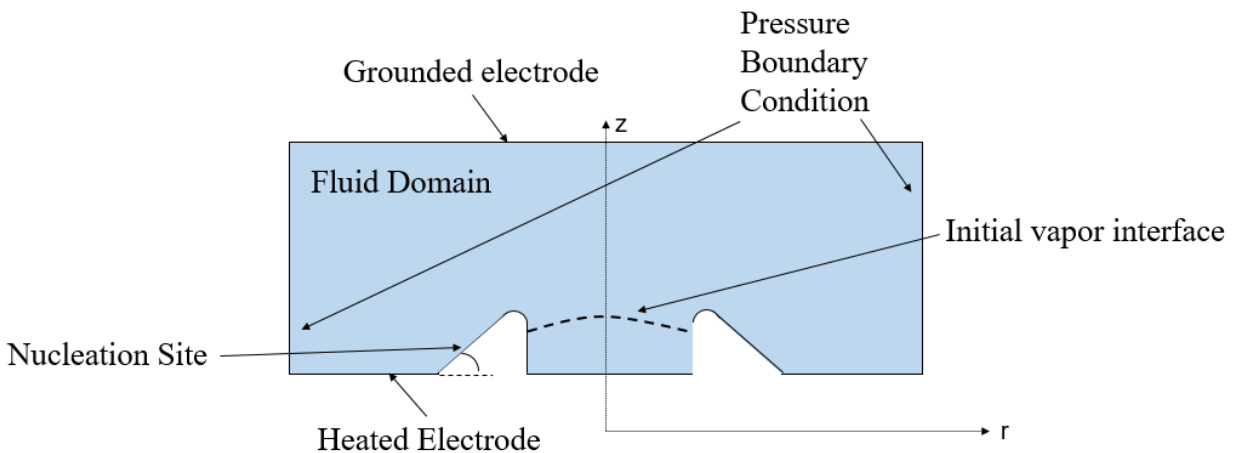


Figure 6: Relevant model features.

### 3.4.1. AC/DC module, Electrostatics Interface

The *AC/DC* module within COMSOL contains a specific interface for electrostatics problems, featuring domain and boundary condition selections related to electrostatics. This module solves Maxwell's equations over a domain to find the electric potential. For the assumed, axisymmetric 2-D solution, the COMSOL solver assumes spatial dependence in the r- and z-directions only, and no change in the azimuthal or  $\phi$ -direction. The electric field is defined in terms of the gradient of the potential  $V$ .

$$\mathbf{E} = -\nabla V \quad (6)$$

Also, the electric displacement field defines the relationship between the electric field and the relative permittivity, as shown in Eq. 7

$$\mathbf{D} = \epsilon_o \epsilon_r \mathbf{E} \quad (7)$$

Where  $\epsilon_r$  is the relative permittivity of a domain or material, and  $\epsilon_o$  is the relative permittivity of vacuum. In this model, the permittivity is assumed to be isotropic. The electric field is found from Gauss' Law (Eq. 8) in a domain with a permittivity  $\epsilon_o \epsilon_r$

$$-\nabla \cdot (\epsilon_o \epsilon_r \mathbf{E}) = \rho_{v,e} \quad (8)$$

where  $\rho_v$  is the charge density in a volume (zero in this model as the fluid is assumed to contain no free charges). In order to account for the change in permittivity between the vapor and liquid phases, two different relative permittivities must be defined,  $\epsilon_l$  and  $\epsilon_v$ , representing the permittivity of the liquid and permittivity of the vapor. Most gases can be approximated with a relative permittivity of constant 1, which is the same as a vacuum [45]. Typically, COMSOL applies permittivities to pre-defined material domains, however this approach doesn't allow for

application of the phase field method and EHD effects within an electrostatics domain. The material properties at a given location are defined fully in the laminar two-phase flow (phase field) interface, with fluid properties attributed to the labels of “Fluid 1” and “Fluid 2” applied to each fluid phase. However, these material properties are not global (within the COMSOL environment) and so are not applied in the Electrostatics Interface. Certain properties (such as temperature, density, etc.) can be used as inputs in one module after being solved for in another, but topological changes (such as bubble shape) do not update within the Electrostatics Interface. In order to incorporate the permittivity change into the governing equations found in the Electrostatics Interface, the permittivity can be related to the volume fraction (which does update within the Electrostatics Interface after being solved in the two-phase flow solver), and defined globally as:

$$\forall f_v (\epsilon_v) + \forall f_l (\epsilon_l) = \epsilon_r \quad (9)$$

Where  $\epsilon_r$  is the permittivity applied to the entire domain, and  $\forall f_v$  and  $\forall f_l$  are the volume fractions of the vapor phase and liquid phase respectively. The boundary condition on the lower electrode (Figure 6) prescribes the condition  $V = V_o$ , where  $V_o$  is a constant DC potential. The upper electrode represents the grounded plate, where  $V = 0$ . The side walls of the domain are set to a zero charge boundary condition, in which  $\mathbf{n} \cdot \mathbf{D} = 0$ . Physically, this last boundary condition implies that the electric field is perpendicular to a boundary, so that the effects of the interior boundaries do not reach as far as the external boundary, or that as the solution moves further away from the region of interest, there is no more change in the electric field.

### 3.4.2. Multiphase Flow Module, Laminar Two-Phase Flow (Phase Field)

#### Interface

The phase field method allows for interface tracking and basic fluid-fluid-solid interaction. The *Laminar Two-Phase Flow (Phase Field)* interface solves the incompressible Navier-Stokes equations in a domain, tracking the position and velocity of an interface between two fluid phases [40]. For convenience, from here on the laminar two-phase flow (phase field) interface will be referred to as the “LTPFPF interface.” The justification for using the incompressible form is based on work from Smolianski [46], which validated their assumption for several reasons, most notably the low Mach numbers in the domain (less than 0.3). The LTPFPF method serves to track the interface between two homogenous fluids, while solving the mass transport equations between phases.

In the liquid phase, the terms of the incompressible Navier-Stokes equations, shown in Equation 10, are solved. In the vapor phase, the incompressible Navier-Stokes equations were solved alongside the continuity equation, Equation 11 (as opposed to the more correct compressible equations), to reduce the computational complexity of solving compressible equations. The assumption of incompressibility is justified due to the small time scale over which the simulation takes place, and the small changes in pressure and temperature inside the fluid (which would affect density). The continuity equation, Equation 11, is also solved for the conservation of mass in both phases (modified for transport, shown later in the section)

$$\rho \frac{\partial \mathbf{u}}{\partial t} + \rho(\mathbf{u} \cdot \nabla)\mathbf{u} = \nabla \cdot [-p\mathbf{I} + \mu(\nabla\mathbf{u} + \nabla\mathbf{u}^T)] + \mathbf{F}_g + \mathbf{F}_{st} + \mathbf{F}_{ext} + \mathbf{F} \quad (10)$$

$$\nabla \cdot \mathbf{u} = 0 \quad (11)$$

In Eq. 10, the terms on the left represent inertial forces. On the right, the first term represents viscous forces. The remaining terms represent all relevant external body forces. Gravity, surface tension force, any other external contribution, and a user-defined volumetric force are all defined. The COMSOL CFD User's manual [47] defines these terms. The surface tension force  $\mathbf{F}_{st}$  is defined as:

$$\mathbf{F}_{st} = \nabla \cdot \left( \sigma (\mathbf{I} - (\mathbf{nn}^T)) \delta \right) \quad (12)$$

Where the  $\delta$  interface function (distinct from the Kronecker Delta Function  $\delta_{ij}$ ) applies the force only to the interface:

$$\delta = 6 |\nabla \phi| |\phi(1 - \phi)| \quad (13)$$

The MST-derived force (Eq. 2) is incorporated as the user-defined volumetric force to impose a force per unit volume on the transition zone between the liquid and vapor. Solving the Navier-Stokes equations alone are not enough to define a moving interface. The phase field method implemented by COMSOL tracks an interface by solving two more transport equations, one equation for the phase field variable, and one for a mixing energy density. These equations (Eq. 14 and Eq. 15) are based on work done by Cahn and Hilliard [48].

$$\frac{d\phi}{dt} + \mathbf{u} \cdot \nabla \phi = \nabla \cdot \frac{\gamma \lambda}{\epsilon^2} \nabla \psi \quad (14)$$

$$\psi = -\nabla \cdot \epsilon^2 \nabla \phi + (\phi^2 - 1)\phi + \left( \frac{\epsilon^2}{\lambda} \right) \frac{\partial f_{ext}}{\partial \phi} \quad (15)$$

Where  $\lambda$  is the mixing energy density and  $\epsilon$  is a capillary width term (both terms defined below) [49]. The variable  $\psi$  is a placeholder variable that links Eqs. 14 and 15, as they are derived from one equation originally. These two equations come from the Cahn-Hilliard Equation (Eq. 16):

$$\frac{d\phi}{dt} + \mathbf{u} \cdot \nabla\phi = \nabla \cdot \gamma \nabla G \quad (16)$$

Where  $G$  is a chemical potential (molar energy, not a pressure) measured in Pascals

$$G = \lambda \left[ -\nabla^2 \phi + \frac{\phi(\phi^2 - 1)}{\epsilon^2} \right] \quad (17)$$

Equation 17 is broken up into Eqs. 14 and 15 so it can be solved by the COMSOL phase field interface. The inclusion of the mixing energy density is another primary differentiator between the level-set method and the similar phase field method, in that its inclusion helps avoid an arbitrary liquid-vapor interface smoothing function, in which the interface is defined manually. As described by Yue [49], the mixing energy is a parameter that captures the fact that the interface's structure is determined by forces on the molecular level. Relating back to the "capillary width" described earlier, an  $\epsilon$  value approaching zero would mean that the smoothing governed by the mixing energy would approach the limit of a sharp interface. The capillary width and mixing energy density are related to the surface tension as shown in Equation 18, also derived by Yue:

$$\sigma = \frac{2\sqrt{2} \lambda}{3 \epsilon} \quad (18)$$

Additionally,  $\gamma$  is a parameter defined in Yue as the mobility. In COMSOL, this is related to  $\epsilon$  through the equation  $\gamma = \chi \epsilon^2$  where  $\chi$  is the mobility tuning parameter (set to 1 by default, controllable in the COMSOL interface). The mobility parameters help determine the time scale of the solution [47]. Set too low, and the interface will be driven further way from (phase) equilibrium, where if set too high, the interface will be forced to its equilibrium state. Equilibrium

is defined as a state where the interface has zero chemical potential. This relates to mass flux, in that Yue assumes that the mass flux is governed by the gradient of the chemical potential. This parameter helps govern the time scale of the diffusion.

The manner in which the interface is actually tracked is discussed in a paper by Yue [49]. One key to tracking an interface in a diffuse-interface model (such as the phase field) is through the incorporation of a mixing energy. This mixing energy is used to capture the interactions between molecules due to intermolecular forces between separate materials of a different composition (such as two phases). In the Cahn – Hilliard equations, the mixing energy is a function of the phase field,  $\phi$ . It is stated that since the mixing energy helps define the interaction between molecules of the phases, surface tension can also be incorporated. The location at which this phase field variable is zero denotes the “center” of an interface with a user-prescribed thickness. Modifying this value of thickness did not influence the solution. The velocity of this interface, and therefore the location, is tracked using the Cahn-Hilliard equation. This can be changed based on the motion of one phase (such as the vapor expansion when boiling) or bulk flow.

The interface is tracked using the two phase field equations described earlier in the section (Equations 14 and 15). These equations help define the advection of the interface (governed by variable  $\phi$ ) which moves throughout the domain. As the interface moves, the values on either side quickly transition to a constant value (representing liquid or vapor), and properties are defined by what the value of the phase field variable is. During boiling, if the volume of the vapor expands on one side of the interface, it helps move the interface velocity, accelerating it away from the growing vapor region and simulating bubble growth. This occurs in conjunction with surface tension, EHD forces, and normal stresses to track the shape and location of the interface.

The phase field method is important for the present work due to the necessity of capturing the coalescence of bubbles. Jamet [50] discusses the limitations of discontinuous interface modeling. While assuming the thickness of the interface is much smaller than the scale size of the phenomena being studied in the problem, it gives rise to invalid assumptions. One such assumption pertaining to the choice of the LTPFF model has to do with bubble coalescence. Defined as a situation where two bubbles merge to form a single bubble, coalescence is impossible to model in a discontinuous system. Jamet notes that in this case, the phase field model is singular and not well defined

The mechanism of bubble coalescence with this model is described in Yue [49]. Yue describes past studies that had to account for the recombination of interfaces by artificially removing the film separating two coalescing bubbles. This can influence the dynamics and behavior of the new body, depending on how and when the artificial separation occurs. Yue notes that the breakup and re-coalescence of bubbles arises naturally from the Cahn-Hilliard equations used by COMSOL's implementation of the LTPFF interface. Additionally, Yue further notes that the physical reality of bubble recombination is influenced by the Van der Waals' forces between molecules at the interfaces. The Cahn-Hilliard equations represent the physical reality of bubble interaction in their representation of the fluid interface, effectively modeling the true physics of the breakup and recombination process.

The boundary condition for the channel wall (Indicated in Figure 6, as the "Heated Electrode") in COMSOL is set to be a "wetted wall" boundary condition, in which the interface between the three phases is allowed to move along the wall (simulating bubble growth) and the contact angle must be prescribed. The boundary condition at the sides of the channel (with no cross flow) can be prescribed as hydrostatic (gage) pressures:



$$-g_{const}\rho_l(y - h_i) = p_0 \quad (19)$$

Where the  $y$  dimension represents the height of the channel at a given mesh element,  $h_i$  represents the total height of the channel, and gravity, represented by the gravitational constant  $g_{const}$ , acts in the negative  $z$ -direction. The model can also prescribe a constant pressure in the entire domain, or along the outlet sides of the channel as a function of the channel height. Pressure must vary as a function of channel height in order to account for the hydrostatic pressure difference. Prescribing a constant pressure along the outlet (assuming it is between the two electrodes) would be unphysical as it would not take any hydrostatic pressure into account. Equation 15 captures the maximum gage pressure desired in the channel when the vertical distance equals zero (i.e. at the bottom of the channel). At the top of the channel, the gage pressure corresponds to zero.

The notation “Fluid 1” and “Fluid 2” are used to identify the phase of the domain in COMSOL in the LTPFPF interface. In this model, the volume fraction of Fluid 2 (liquid) is defined in terms of the phase field variable using Equation 16 (where the subscript “1” denotes the liquid phase),

$$\forall_{f_l} = \min\left(\max\left(\frac{[1 + \phi]}{2}\right), 0, 1\right) \quad (20)$$

which bounds the volume fraction to between 0 and 1. Correspondingly, density and dynamic viscosity can be found in the domain with the relation (with  $X$  representing either property and the subscript identifying the property at a given phase)

$$X = X_l + (X_f - X_l)\forall_f \quad (21)$$

This expression defines a fluid property within regions of pure liquid and vapor, as well as the transitional interface. The two-phase flow interface allows for the inclusion of a volumetric force

in the Navier-Stokes equations. As described earlier, the externally-applied volumetric force for this work is found from the divergence of the MST. Studies have different approaches for incorporating the MST into the solver, with some [11] requiring manual definition of derivatives, unit normal, and interface thicknesses, where more “custom” solutions [29] require manual definition of derivatives and unit normals. COMSOL is able to differentiate the electric field components directly, allowing for a more direct solution of the volumetric force equation utilizing the MST (Eq. 4).

In order to implement the volumetric electric force into COMSOL, the  $F_r$  and  $F_z$  components of the force must be written in terms of the gradients of the electric field. COMSOL has the ability to differentiate the electric field with respect to the spatial coordinates throughout the domain. This allows the MST to be expressed as a 3x3 tensor (for the 2-D problem), from which with the divergence of the MST, which defies the volumetric force, can be applied to the problem-appropriate z- and r- components. The divergence of a tensor field  $\mathbf{S}$  in cylindrical polar coordinates is provided in [51]:

$$\begin{aligned} \nabla \cdot \mathbf{S} = & \frac{\partial S_{rr}}{\partial r} \mathbf{e}_r + \frac{\partial S_{r\theta}}{\partial r} \mathbf{e}_\theta + \frac{\partial S_{rz}}{\partial r} \mathbf{e}_z + \frac{1}{r} \left[ \frac{\partial S_{\theta r}}{\partial \theta} + (S_{rr} - S_{\theta\theta}) \right] \mathbf{e}_r + \dots \quad (22) \\ & \frac{1}{r} \left[ \frac{\partial S_{\theta\theta}}{\partial \theta} + (S_{r\theta} - S_{\theta r}) \right] \mathbf{e}_\theta + \frac{1}{r} \left[ \frac{\partial S_{\theta z}}{\partial \theta} + S_{rz} \right] \mathbf{e}_z + \dots \\ & \frac{\partial S_{zr}}{\partial z} \mathbf{e}_r + \frac{\partial S_{z\theta}}{\partial z} \mathbf{e}_\theta + \frac{\partial S_{zz}}{\partial z} \mathbf{e}_z \end{aligned}$$

Assuming radial symmetry, partial derivatives in the  $\theta$  direction vanish.

$$\begin{aligned} \nabla \cdot \mathbf{S} = & \frac{\partial S_{rr}}{\partial r} \mathbf{e}_r + \frac{\partial S_{rz}}{\partial r} \mathbf{e}_z + \frac{S_{rr} - S_{\theta\theta}}{r} \mathbf{e}_r + \frac{S_{r\theta} - S_{\theta r}}{r} \mathbf{e}_\theta + \frac{S_{rz}}{r} \mathbf{e}_z + \frac{\partial S_{zr}}{\partial z} \mathbf{e}_r \quad (23) \\ & + \frac{\partial S_{zz}}{\partial z} \mathbf{e}_z \end{aligned}$$

The components of a stress tensor can be written out in polar coordinates as

$$\tau = \begin{matrix} \tau_{rr} & \tau_{r\theta} & \tau_{rz} \\ \tau_{\theta r} & \tau_{\theta\theta} & \tau_{\theta z} \\ \tau_{zr} & \tau_{z\theta} & \tau_{zz} \end{matrix} \quad (24)$$

The tensor above can be simplified by neglecting terms with an azimuthal dependence. The terms that remain after simplification allow for the  $F_r$  and  $F_z$  components of the EHD force to be determined and applied to the entire domain (using Eq. 3, the MST and Eq. 4, its divergence). Since the force depends on the divergence of the electric field as well as the permittivity, only the region in which the permittivity changes (the phase field transition region) is affected by the EHD force. This is consistent with results from Sunder and Tomar [29], where the volumetric force is only applied to the transition region of the domain. Using indicial notation, the MST (Eq. 2) can be expressed as the following (where the  $E^2$  term is an implicit dot product):

$$\tau^E = \epsilon\epsilon_o \left( E_i E_j - \frac{1}{2} \delta_{ij} E^2 \right) \quad (25)$$

The full 3D tensor is given in Equation 22. For this particular problem, any  $E_\theta$  components vanish due to the lack of any azimuthal electric field components. Additionally, the Kronecker delta function vanishes if  $i \neq j$ , but remains for  $\tau_{\theta\theta}$ . In the case of  $\tau_{\theta\theta}$ , the first term in Equation 25 vanishes, but the second term remains. [52]

$$\tau^E = \begin{bmatrix} \epsilon\epsilon_o \left( E_r^2 - \frac{1}{2} (E_r^2 + E_z^2) \right) & 0 & \epsilon\epsilon_o (E_r E_z) \\ 0 & \epsilon\epsilon_o \left( -\frac{1}{2} (E_r^2 + E_z^2) \right) & 0 \\ \epsilon\epsilon_o (E_z E_r) & 0 & \epsilon\epsilon_o \left( E_z^2 - \frac{1}{2} (E_r^2 + E_z^2) \right) \end{bmatrix} \quad (26)$$

As shown in Eq. 4, the divergence of this Maxwell Stress Tensor is the volumetric EHD force. Applying the divergence of a tensor field as given by Eq. 23 to the MST given by Eq. 25, the force vector can be found:

$$\mathbf{F} = \nabla \cdot \boldsymbol{\tau}^E = \left[ \frac{\partial \tau_{rr}^E}{\partial r} + \frac{\tau_{rr}^E - \tau_{\theta\theta}^E}{r} + \frac{\partial \tau_{zr}^E}{\partial z} \right] \mathbf{e}_r + \left[ \frac{\tau_{rz}^E}{r} + \frac{\partial \tau_{rz}^E}{\partial r} + \frac{\partial \tau_{zz}^E}{\partial z} \right] \mathbf{e}_z \quad (27)$$

Implementation of this equation in COMSOL can result in singularities near  $r = 0$ . In order to avoid this non-physical behavior, the components of the force can be set to zero for values of  $r$  smaller than a specified limit, using the following statement.

$$\text{Force, } r - \text{component (units of m): } \text{if}(\text{abs}(r > t_f, F_r, 0)$$

$$\text{Force, } z - \text{component: } \text{if}(\text{abs}(r > t_f, F_z, 0)$$

Where  $t_f = 1e - 7$ . As defined by Eq. 27, this externally-applied, volumetric force is applied to the entire domain although it will only act upon regions with a sharp change in permittivity (defining the fluid interface). In addition to this volumetric force, there is a gravity force defined in the negative  $z$ -direction through the entire domain.

### 3.4.3. Heat Transfer Module, Heat Transfer in Fluids Interface

In COMSOL, the *Heat Transfer in Fluids* interface of the *Heat Transfer* module models heat transfer in fluids, including convection, conduction, and radiation. Neglecting radiative heat transfer for this case, the energy equation for the domain is given by:

$$\rho C_p \frac{\partial T}{\partial t} + \rho C_p \mathbf{u} \cdot \nabla T = \nabla \cdot (k \nabla T) + Q \quad (28)$$

where  $Q$  represents any additional heat gain or loss of the system. The bottom electrode is given a prescribed, constant heat flux  $q'' = q_0$ , and the domain is initially at saturation temperature to achieve boiling at the start of a simulation. This model utilized a constant heat flux boundary condition at the bottom as opposed to a constant temperature boundary condition. Using a constant heat flux at the bottom boundary better approximates the heat gain from a chip. A constant heat flux boundary condition in the model sets up future work to add in conjugate heat transfer from a solid surface to the liquid. In this future work, a heat generating component (i.e. electronic chip) would be assumed to dissipate a constant amount of heat. Realistically, an interface would exist between the chip itself and the fluid. In that case, with a constant heat flux boundary condition, the temperature of that interface could be more accurately determined. While out the scope of this model, the change of that interface would be more useful in studying the operation of a heat transfer device, due to the expected reduction in surface temperature due to an increase in heat flux with the application of EHD.

At the sides of the channel, the thermal boundary condition set to an “Outflow” condition. This will allow only convective heat transfer to occur at the boundary. At the upper electrode, there is no conduction or convection allowed (adiabatic). This assumes that the bulk of the heat transfer will happen through the channel sides, and that convective effects through the top electrode are negligible.

Ensuring that bubbles coalesce properly, as well as not developing discontinuous interfaces is a challenge that must be addressed. Jamet [50] mentions this challenge as it pertains to modeling of nucleate boiling. The modeling of bubble coalescence using the LTPFPF interface is addressed in Section 3.4.2, but another challenge arises in dealing with the critical location within the transition zone of the bubble. This location is where the temperature properties of both phases are

equal, and phase change is assumed to occur. In a bubble, the vapor temperature is both lower than, and higher than the critical point at the interface, with the interface representing the transition between the two phases. Jamet notes that discontinuous models cannot handle the modeling of the critical point accurately. Following Son and Dhir [53] the governing equations can be written assuming laminar flow, and the liquid-vapor interface can be maintained at a saturation temperature better approximate where the critical location is, and to ensure phase change occurs there.

According to Kandlikar [9], an increase in heat flux or superheat leads to a larger number of active nucleation sites as well as a higher frequency of bubble detachment from those sites. Son and Dhir [53], noted that the rate of vaporization (the mass flux from the liquid surface) must be calculated to use in the heat transfer equation. From their study, the rate of vaporization is described by:

$$\dot{m} = \frac{1}{H_{lv}} \mathbf{n} \cdot (k_l \nabla T_l - k_v \nabla T_v) \quad (29)$$

Where  $k_l$  and  $k_v$  represent the thermal conductivity of the liquid and vapor, respectively,  $T_l$  and  $T_v$  represent the temperature of the liquid and vapor, respectively, and  $\mathbf{n}$  is the unit normal. However, it is noted that the temperature gradient at the interface will be small, and may make estimating mass flux in this manner difficult. Son and Dhir [53] discuss the representation of the mass flux vector at the interface, using conservation equations.

$$\dot{\mathbf{m}} = \rho(\mathbf{u}_{int} - \mathbf{u}) = \frac{k \nabla T}{h_{fg}} \quad (30)$$

Where  $h_{fg}$  is the latent heat of vaporization,  $\mathbf{u}_{int}$  is the interface velocity vector, and  $\mathbf{u}$  is the surrounding velocity vector. To simplify the model, the mass flux can be approximated. Following

from the work of Son and Dhir, a COMSOL-developed model [54] describing boiling problems proposed the following estimation. In that example, mass flux can be approximated as follows

$$\dot{m} = C \rho_L \frac{T - T_{sat}}{T_{sat}} \quad (31)$$

Eq. 31 is an approximation based used to estimate the mass flux from one phase to another (described as being similar to setting a heat transfer coefficient on a boundary). The parameter  $C$  is a constant, set to a value large enough to keep the temperature at the liquid-vapor interface at the saturation temperature, but not too large in order to introduce numerical solution instabilities.  $C$ , combined with the temperature ratio term, serve as a tunable parameter that can approximate the interface velocity in a basic manner. If the surrounding liquid temperature corresponds to saturation, there will be no mass flux. While it is difficult to model the exact rate of phase change with this approximation, it allows for the relative behaviors (between simulations with different potentials or channel heights) to be modeled to ensure a valid comparison of bubble growth or contraction. The parameter  $C$  was chosen to be large enough to ensure solution completion (leading to numerical instabilities otherwise), and remained constant between every simulation (0.04 m/s).

Bubble expansion occurs due to the volume of the vapor expanding as liquid undergoes phase change through the bubble interface. In the model, this is achieved by modifying the mass conservation equation across the interface. As described above, the continuity equation accounts for the phase change from liquid to vapor, and the equation parameter  $C$  is chosen to ensure that the interface remains fixed at the saturation temperature. Although the boundary fluid is at the saturation temperature, the vapor in the bubble, or the liquid outside the bubble, will have a temperature variation solved for by COMSOL. Within the COMSOL software, the temperature solved in the Heat Transfer in Fluids interface is used to change the density of the fluid (which changes with temperature and phase). As the fluid expands, the bubble is seen to “grow”.

Without modification, the form of the heat transfer equation included in COMSOL (Eq. 28) does not include an energy gain or loss term resulting from phase change between a liquid and vapor phase, as it is typically employed to govern single phase heat transfer. The energy exchanged as a result of the mass flux (Eq. 30) undergoing a phase change is incorporated into the energy equation (Eq. 28) as Equation 32:

$$Q = \frac{\dot{m}\delta\Delta H_{vl}}{M_w} \quad (32)$$

Where the delta function  $\delta$  given by Equation 13 ensures that the heat gain or loss from phase change is only applied to the interface [47]. This ensures that any mass flux only occurs along the transition region defined by the delta function, i.e. the liquid-vapor interface.  $H_{vl}$  is the molar enthalpy of vaporization (J/mol), and  $M_w$  is the molecular weight of the vapor.

Additionally, the continuity equation was modified to include the mass flux (at the interface). The velocity of the interface is calculated with Equation 33, based on reference [56], where the right hand side is a simplification of the average density, mass flow rate through the interface, and the delta function:

$$\nabla \cdot \mathbf{u}_{int} = \dot{m}\delta \left( \frac{1}{\rho_v} - \frac{1}{\rho_L} \right) \quad (33)$$

Where  $\dot{m}$  is the rate of vaporization given in  $\frac{kg}{s \cdot m^2}$ ,  $\delta$  is the interface approximation given in  $\frac{1}{m}$ , and  $\rho_v, \rho_L$  are the vapor and liquid densities, respectively, in  $\frac{kg}{m^3}$ . This equation follows from the mass conservation equation derived by Son and Dhir [56] to account for volume expansion due to phase change, which was derived from an energy balance at the interface and mass continuity

$$\nabla \cdot \mathbf{u} = \frac{\dot{m}}{\rho^2} \cdot \nabla \rho \quad (34)$$



Together, Equations 30 through 34 define the interface of liquid and vapor to be held at the saturation temperature, and will also account for the phase change from liquid to vapor in both the continuity equation and energy equation. These equations are incorporated into the model as a “weak contribution.” As described in Ref. [47] weak contribution is an additional contribution to an equation, using the “weak formulation,” which is a means of altering the solution criteria of an equation in COMSOL. In a problem where the solution to an equation may be discontinuous near a boundary (such as in this case, along the interface), the weak formulation transforms a differential equation into an integral equation to approximate a solution as opposed to requiring an exact solution. Here, it is used in this manner to modify the continuity equation at the fluid interface described by the delta function  $\delta$ . Anywhere else in the solution, the right hand side of the continuity equation (Eq. 34) is still equal to zero. At the interface between the liquid and the vapor, however, the mass flux of vaporizing fluid can now be used to describe the velocity of the interface.

The three physics environments form the bulk of the model description. In COMSOL, the geometry was defined parametrically to facilitate making changes to the geometry. To reduce simulation time, the solution is calculated only in the fluid domain (i.e. the electric fields in the solid electrodes is not evaluated), assuming a lumped, 2-D heating domain (with no thermal conductivity or temperature gradient inside). The addition of any extra solid heating element is beyond the scope of this study. To reduce the complexity of the model, the heat transfer through a solid phase was not solved. In a higher fidelity model (in the context of a real device), the heat generating chip and the fluid channel would be modeled and heat transfer through each solid material would be analyzed, and the associated temperature drops found. By neglecting this, the model in this study effectively assumes there are no losses in the heat transfer path from a uniform, heat generating chip and the fluid. Future models could incorporate this, allowing for a more

accurate determination of chip temperatures. This would also require a discussion on conduction losses to other attached structures, radiative losses to the surroundings, and convective losses (in the case of a terrestrial heat transfer device). It is important to note some of the limitations of this approach. In a 2002 paper, Kandlikar [34] notes that there was little distinction between types of small diameter channel boiling related to mini- and micro-channels. As per Kandlikar's definition, a conventional channel has hydraulic diameters above 3mm, minichannels consist of hydraulic diameters of 200um to 3mm, and microchannels from 10 to 200um. In particular, his study on boiling microchannels finds that surface tension effects can become increasingly more significant, with small liquid slugs forming uniformly spaced apart in the channel, and very small (10-20um) diameter bubbles can form. The surface tension effects on walls cannot be captured by this type of model due to the lack of a contact angle submodel. Additionally, boiling these channels can be accompanied by severe pressure fluctuations due to vapor expansion in constrained spaces. In this model, the lack of outside influences changes what would be realistic.

Solutions were run for 100ms, with time steps of 1ms. This time step was varied in order to ensure that the solution did not change as a function of the time step, and was chosen to balance solution accuracy and speed. In COMSOL, the mesh is controlled by the solver itself, using finer mesh elements near sharper geometric features and the initial interface.

### 3.5. Reference Case Description

A baseline case was defined to use as a basis for comparison of the simulation results in this

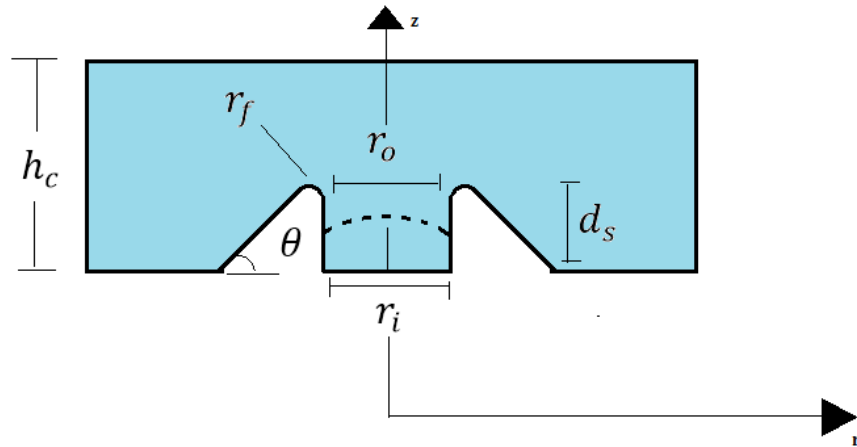


Figure 7: Description of Geometry, with variables representing important geometric features.

study. The working fluid was chosen to be HFE-7100, a refrigerant hydrofluorocarbon. A numerical study by Kunkelmann and Stephan [58] found bubble growth times on the order of 16ms with departure diameters of 2.3mm for HFE-7100 bubbles. This was within 20% of experimental results observed in prior studies as noted in that paper. The Kunkelmann and Stephan study used a method similar to the one outlined above, with a level-set type interface tracking coupled with an evaporation source term. Integral to any model of nucleate boiling is the definition of the contact angle between the liquid, the solid (structure), and the vapor. That study also found (experimentally) a contact angle of 40 degrees for the liquid-solid-vapor interface, measured counter-clockwise from the solid to the vapor interface of a nucleation bubble for an HFE-7100 bubble on a copper surface. HFE-7100 was chosen due to its effectiveness as a heat transfer fluid, as well as its dielectric properties. Additionally, HFE-7100 has a low toxicity and a low boiling point (61 °C). The liquid region in the simulation is assumed to be at a pressure of 500mbar to more closely match the study performed by Kunkelmann (as it most closely approximated the setup used in this study) on HFE-7100 boiling [58] The reference geometry (Figure 7) uses the

Kunkelmann and Stephan study as a baseline assuming the values given in in Table 1. For reference, Figure 8, shows the same pit, inside the full simulation domain, in order to show the relationship of the pit size to the height and width of the channel.

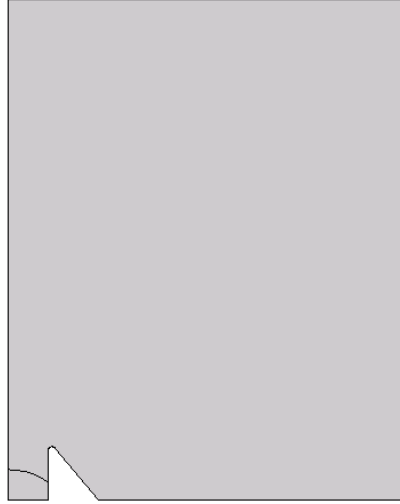


Figure 8: Nucleation site inside the entire fluid domain.

Table 1: Assumed Parameters for Baseline Case.

$h_c$	$r_f$	$r_o$	$r_i$	$d_s$	$\theta$	$V_o$
3 mm	0.02 mm	0.2 mm	0.2 mm	0.3 mm	$0^\circ$	0 kV

Where  $r_i$  and  $r_o$  define the inner and outer radii of the nucleation site,  $d_s$  describes the height of the nucleation site above the channel base,  $r_f$  describes the radius of the fillet,  $\theta$  describes the angle of the conical rim forming the nucleation site, and  $h_c$  describes the height of the channel. Note that for the baseline case the cavity will correspond to a cylindrical pit below the surface of the heated channel. Additionally, the time step was chosen to be 1ms, with simulations run for a duration of 100ms. A case naming convention for the simulations will be adopted to more readily

identify which parameters were assumed in a given simulation. Cases will be identified in the following manner:

$$V_o[\text{kV}]_h_c[\text{mm}]_\theta[\text{degrees}]$$

where the variables will be replaced with numeric values, using the units shown above in brackets.

This baseline geometry was chosen in order to maximize the magnitude of the force on the neck of the bubble. Sharper geometric features give rise to higher gradients in the electric field, leading to forces of a higher magnitude than that made by relatively shallow features. Past studies ([29] [61] [11]) have found that features with sizes on the order of the bubble diameter lead to EHD forces that can impact the entire bubble. However, in this study, in order to minimize the impact that the structure would have on the fluid flow (which is not modeled), smaller geometric features were chosen; the height of the nucleation site is an order of magnitude less than the height of the channel. Despite the rapid fall off of in the EHD force with distance from edges or corners of electrodes, it was anticipated that the neck of the forming bubble, which will be located along the conical rim in Figure 8, would be the most effective location to impart the EHD force. The results from the simulation are analyzed to investigate the effect of geometry and applied EHD forces on bubble detachment frequency and size at detachment.

### 3.6. Results

The COMSOL model allows for ease in the variation of the applied potential for different cases as well as easily varied geometric parameters, including the angle that the cavity makes to the bottom electrode. The output of the solution file is saved as a GIF format, where a separate MATLAB script is used for post processing. The solution is deterministic, i.e. it only depends on the input parameters and does not have a random element. The MATLAB script utilizes the image analysis toolbox in order to analyze the area, centroid, number of objects, and evolution of each frame of

the solution (prescribed to match a time step), and results can be plotted accordingly. The following results are organized as follows. First, the bubble detachment frequency, as it is influenced by EHD, is explored. Next, the influence of EHD and an artificial nucleation site on bubble coalescence is explored, followed by detachment in more constrained channels of differing heights. Finally, the neck behavior of the detaching bubbles under the influence of EHD forces is explored.

### 3.6.1. The Impact of EHD on Detachment Frequency

In order to interpret and quantitatively present the bubble evolution, detachment, and coalescence in each trial, a graphical method of depicting bubble evolution was devised. Figure 9 shows a representative visualization of the bubble growth and detachment process, along with a graphical representation of total vapor volume in the domain. The bottom panel shows the vapor volume in the domain over a continuous range of time. The numbered regions, along with the vertical lines, are extended volumes of vapor represented by the upper panel, where a visualization is given of the vapor in the channel.

Region I denotes the growth of a vapor packet inside the cavity. As this packet expands (representing the growth of a bubble), the volume of vapor is shown to grow as well. Regions II and III denote a condition in which a vapor packet detaches from the nucleation site, becoming a distinct bubble. Region III (solid line) represents the vapor left in the cavity, while Region II (dotted line) represents the volume in a bubble that detaches and impinges on the top wall. Region

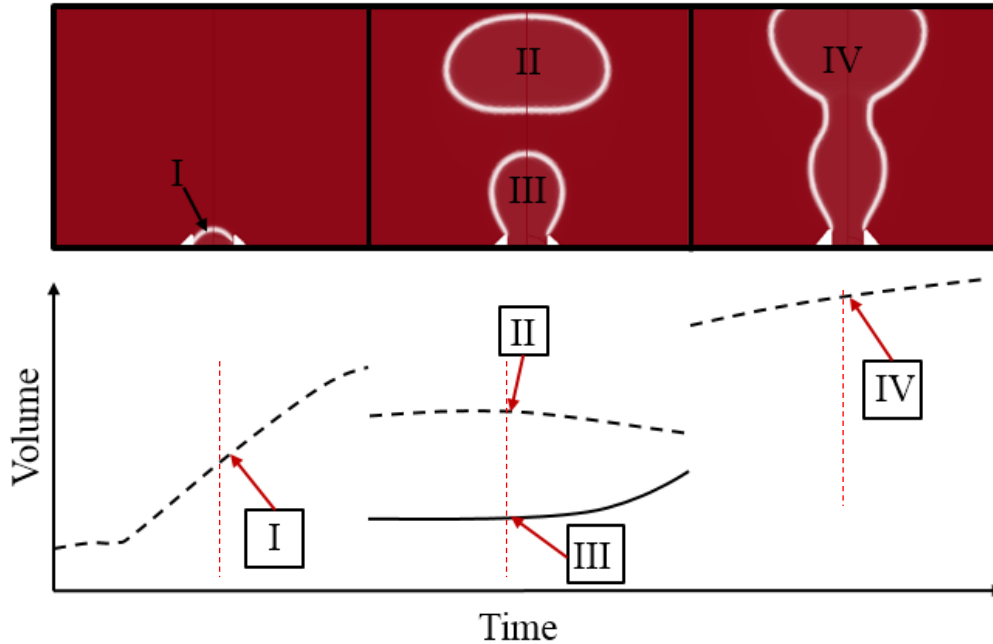


Figure 9: Visualization and Plotting of Bubble Detachment.

III vapor will continue to grow due to the heat flux being applied, while Region II will remain nearly constant due to its being adjacent to a location adjacent to a surface with no inward heat flux. Further along in the solution process, Region IV represents a situation where the two vapor packets coalesce, and continue to grow outward as one continuous unit. During this time, these packets and bubbles can exhibit oscillations in their radius and shape, as the inertial effects of coalescence take hold.

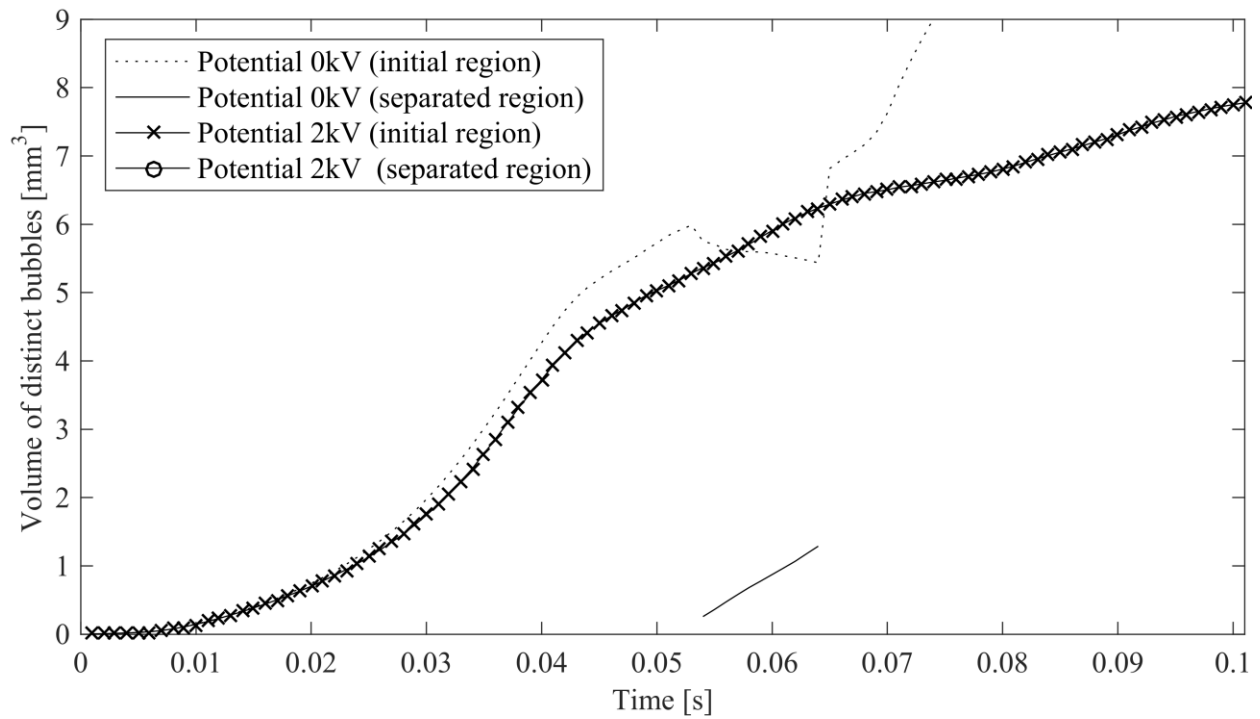
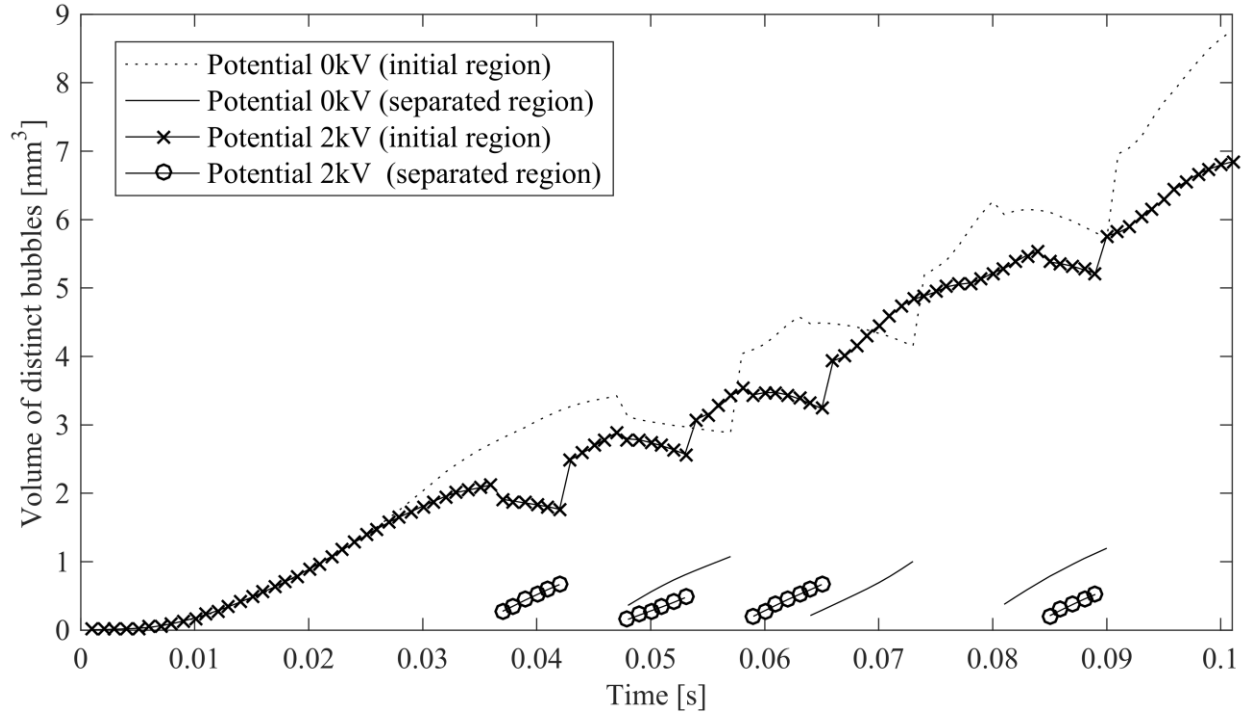


Figure 10 Sensitivity of bubble evolution to nucleation site cone angle. a (top, Case 2\_3\_50) 50° cone, b (bottom, Case 2\_3\_0) 0° cone. Each line style within a stated potential represents a distinct vapor region.



In this section, it was found that the application of EHD, in conjunction with an artificial nucleation site, served to increase the rate at which bubbles detached. Plots (as described above) are provided to back this up with data from several models, with different potentials and cone angles. Additionally, screenshots of model results are provided to show what the bubbles look like as they nucleate.

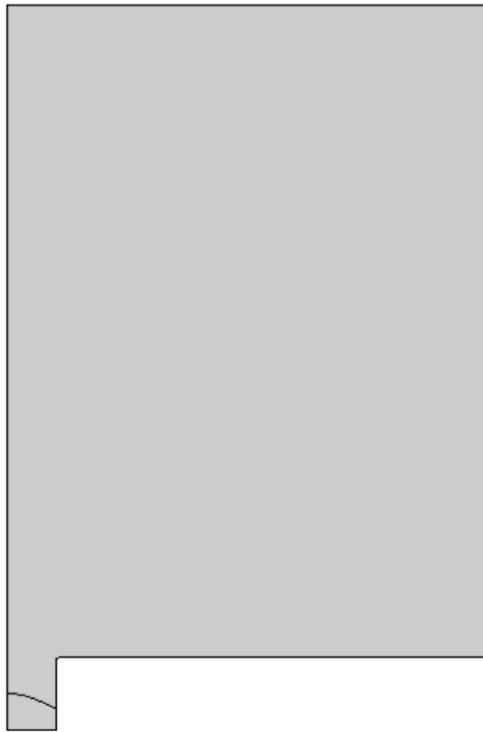


Figure 11: Zero degree ( $0^\circ$ ) (baseline) cone angle

Data from solutions of the baseline case are shown in Figure 10. There are two lines per each constant potential, representing a distinct vapor region. In Figure 10a, for example, at approximately 36 ms there is a detachment event, with the circle-marker line representing a vapor region resembling Region III in Figure 9. The original line shows a large drop in volume to represent the detached vapor, which resembles Region II. With  $\theta = 0^\circ$  (geometry shown in Figure 11) the effect of EHD on the growth rate and detachment frequency is minimized. In these plots,

detachment is defined as the point in which a “tracked” vapor packet (i.e. one continuous line on the graph) exhibits a discontinuity, i.e. loses large portion of its volume in a discontinuous manner. For example, in Figure 10a, a detachment event occurs at 34ms, where the line with the  $x$  symbols has a sharp drop in volume. For this case, corresponding to 2 kV of applied potential (2\_3\_50), the line with the  $o$  symbols represents a second vapor packet growing in tandem with the original vapor packet. Without the application of EHD, bubbles are seen to detach every 18ms in Figure 10a. With the application of EHD, bubble detachment is seen every 9ms. Based on these findings, EHD appears to increase the departure frequency of the bubble in the presence of a cone, but for the baseline case there appears to be no effect, and possibly a negative correlation (i.e. the EHD serves to decrease the detachment frequency).

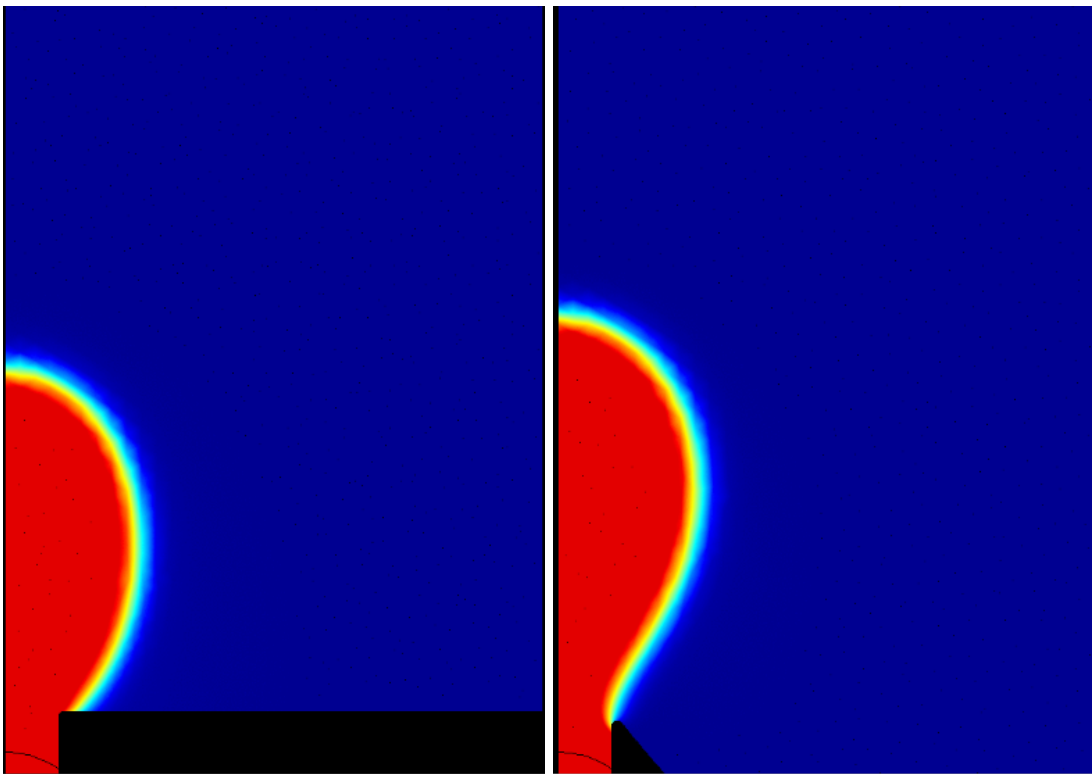


Figure 12: Comparison of bubble neck behavior with 2kV of potential, comparing  $0^\circ$  (left, Case 2\_3\_0) and  $50^\circ$  (right, Case 2\_3\_50) cone angles at 19 ms.

Additionally, the effect of the “orifice bounding,” in which the edge of the bubble is attached the rim surface of the nucleation site, was found to have a large effect on the neck (i.e.

minimum) diameter of a detaching bubble by plotting bubble growth on a flat channel surface (Figure 10b). This radius data, combined with images of the nucleating bubbles, allows for a visualization of bubble behavior during growth, and now it may influence volume.

Without an orifice with a cone angle, the bubble tends to form a larger neck (i.e. larger diameter attached region to the heated surface). In Figure 10b, the volume of the nucleating bubble is less than that of the zero-degree cone angle case (2\_3\_0), at nearly all stages of growth.

In Figure 10b, the bubble volume as a function of time for the two potential (0kV and 2kV) cases are nearly identical during the growth of the bubble up to 30ms. As suggested in Section 2, bubble volumes are expected to remain similar during growth both with and without the application of EHD. However, with the application of an external electric field, bubble growth begins to slow, as evidenced by a lessening of the slope in Figure 10a, and a detachment is seen nearly 10ms before the (0\_3\_50) case (of 0 kV). Additionally, detached bubbles have a much smaller maximum volume under the influence of an external electric field than those that are attached, as evident by inspection of the volume at the point of detachment in Figure 10. However, bubble elongation when under the effect of EHD can prevent detachment in a small channel. While the baseline geometry case (Figure 8 and Table 1) can sustain detachment events (in spite of an increasing vapor volume in the channel), the cases with an externally applied electric field exhibit a cessation of detachment events after 65ms, with the exception of one small event around 90ms.

A representative screenshot from the model output is shown in Figure 13. On the left, bubble growth just before a period of detachment is shown (34ms). On the right, bubble detachment is shown at the next point in time (35ms). Here, the interface is shown to represent a gradual detachment, with evidence of a brief, but noticeable area where the interface is halfway between liquid and vapor.

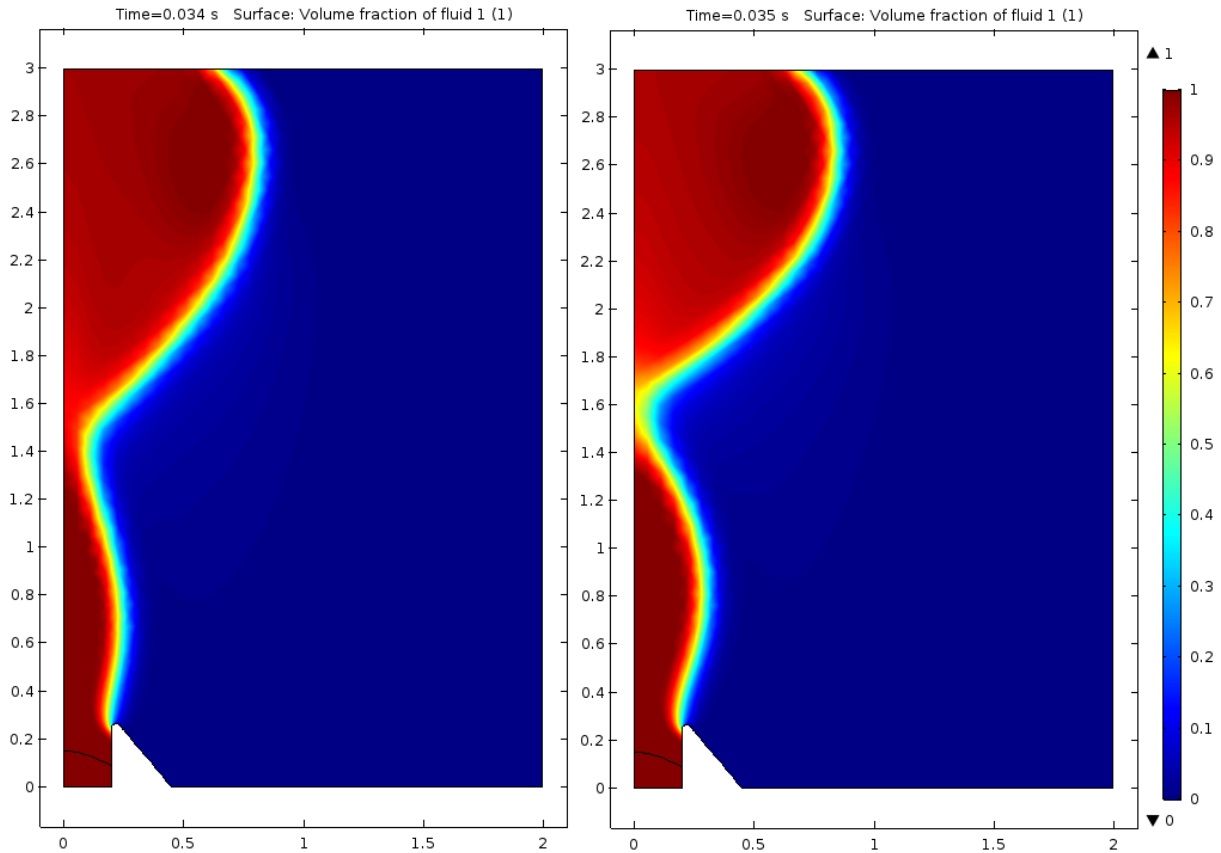


Figure 13: Visualization of Detachment Event for 2kV, 50° Cone case (Case 2\_3\_50).

The relative change in volume vs. time can help characterize detachment events, and also reveals the onset of separation, i.e. the point in time at which the equilibrium condition between buoyancy and surface tension breaks down, leading to a detachment event. This is discussed in Section 2.1. The rate of change of bubble volume vs. time always change directly before a detachment event (with the growth rate slowing prior to the detachment). Using MATLAB as a post-processing tool allows for more exact determination of bubble detachment and relative sizes than a visual inspection would, and expands the post processing capabilities of a COMSOL model far beyond what is normally possible. However, a plot of vapor volume alone does not fully define the nature of a detaching bubble.

### 3.6.2. The Impact of an Artificial Nucleation Site and EHD on Bubble Coalescence and Shape

Identifying changes in detachment frequency alone does not quantify all of the influence that EHD has on a nucleating bubble. As outlined in Section 3.2, an MST-based approach to calculating forces on a bubble under EHD is necessary as the bubble will deform, changing the shape of the

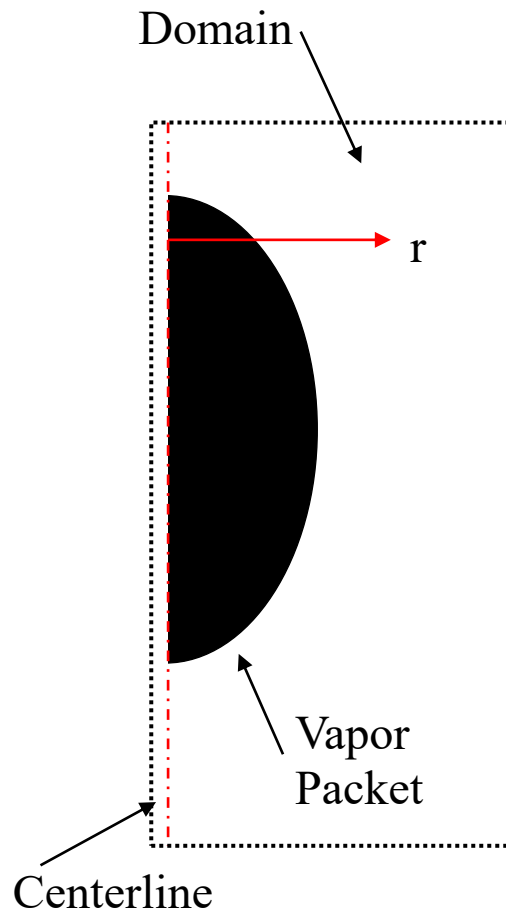


Figure 14: Maximum radius determination within MATLAB image processing.

electric field. Additionally, as two bubbles coalesce, the field is further impacted near the point of coalescence. To account for this, the MATLAB script used to calculate bubble volumes was modified to scan each frame of the solution, and to detect the maximum radius or height of a growing vapor packet in the domain vs. time. In these plots, the simulation video exports of

detaching bubbles are discretized into binary images, where the vapor region is defined as a “1”, and the liquid region a “zero.” This is accomplished via the MATLAB image processing toolbox. These binary images can be analyzed one row of pixels at a time, in order to determine at what maximum distance the vapor region extends out into the width of the channel. Figure 14 shows a diagram of what this process looks like, where the vapor packet is represented by a collection of pixels with one binary “on” (or 1) value. As the MATLAB scrip sweeps out along the radius from the centerline at every height, the width of the last vapor pixel is stored. This process repeats for every frame within a simulation video. These values are then analyzed to determine how wide the bubble was at any given point in time, and what the maximum width was at every point.

Kanlidkar [34] notes that bubble coalescence can lead to annular slug flow, leading to instabilities in heat transfer performance. As was seen in a comparison of bubble volumes, the introduction of an artificial nucleation site influences the shape of a detaching bubble. Additionally, an artificial nucleation site in conjunction with EHD serves to impact bubble behaviors further. The importance of this to heat transfer enhancement is evident if nucleation is assumed to occur at several sites in close proximity on a heated surface. Growing bubbles, which can have a rapidly expanding diameter could influence other adjacent growing bubbles and cause early (before detachment) coalescence events. EHD can help control this effect by influencing not only detachment frequency, but by controlling the shape during bubble growth. The bubble width data during nucleation is stored and plotted vs time, shown in Figure 15. These plots show the maximum radius (as defined by Figure 14) of all vapor in the domain over time, with each line representing a single solution (as defined by potential or channel height).

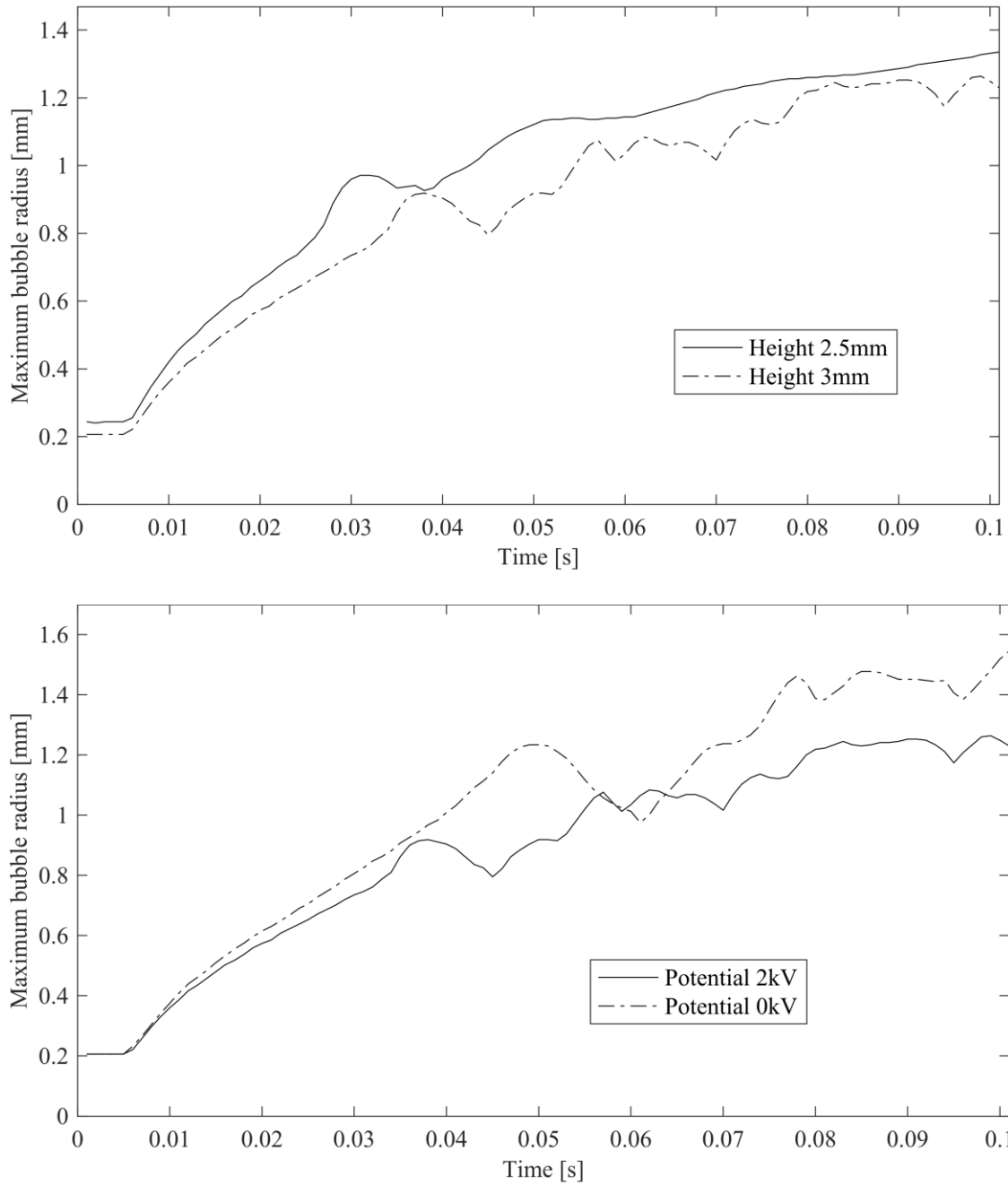


Figure 15: Comparison of bubble growth radii for 50° cone (a (top), height variation with constant 2kV potential (Case 2\_3\_50 and Case 2\_2.5\_50), b (bottom) potential variation constant 3mm height, (Case 2\_3\_50 and Case 0\_3\_50)).

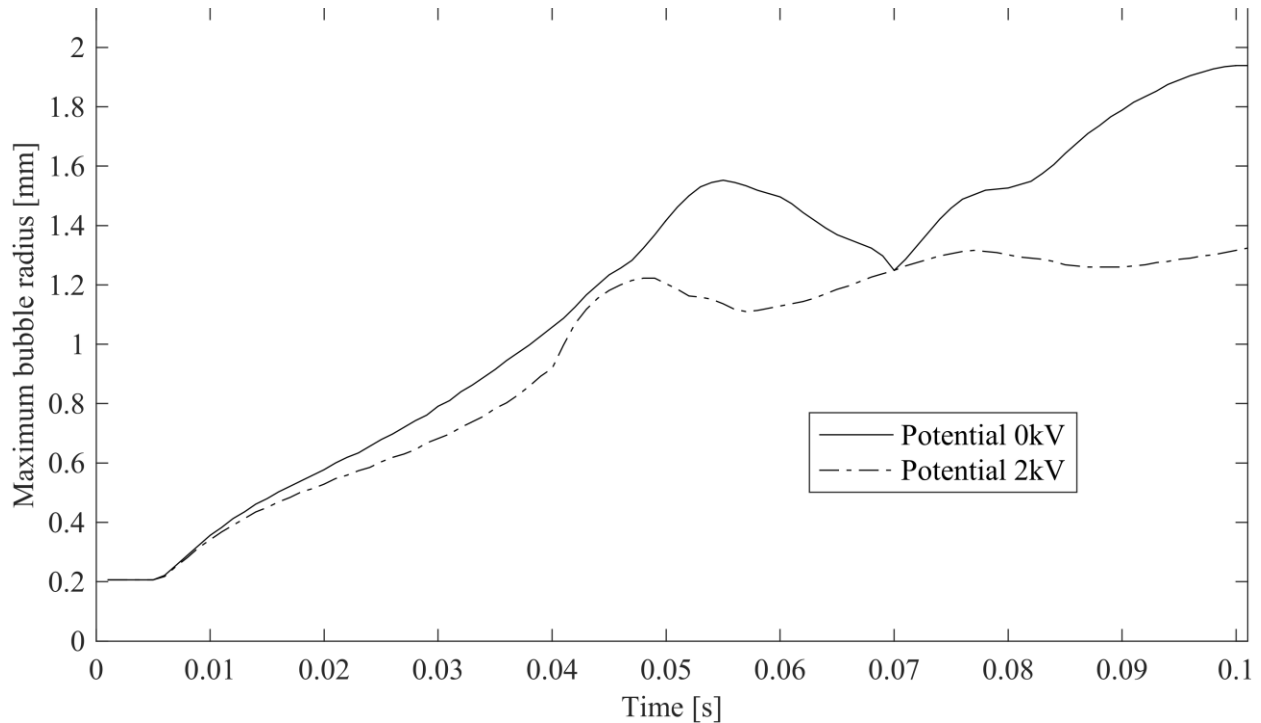


Figure 16: Maximum radius comparison for  $0^\circ$  cone angle, 3mm height (Case 2\_3\_0 and Case 0\_3\_0).

Figure 16 shows the comparison of maximum bubble radii during the growth and detachment process. For the case with a  $0^\circ$  cone angle (i.e. a perfectly cylindrical cavity) bubble radii are relatively constant (with and without EHD) until 10ms into the solution, where impact with the upper electrode causes compression and expansion of the vapor. This behavior is shown in Figure 17. In the case of a  $50^\circ$  cone angle, bubble radii remain similar (between 0kV and 2kV) from inception to nearly 30ms into the solution. Additionally, with a cone present, the variation of bubble radii over time is influenced by detachment events more so than with a  $0^\circ$  cone angle. With a  $0^\circ$  cone angle (Figure 16), bubble radii remain more stable over time (less oscillations), while a  $50^\circ$  cone angle means that detached bubble exhibit rapid changes in radii due to multiple detachment and coalescence events.



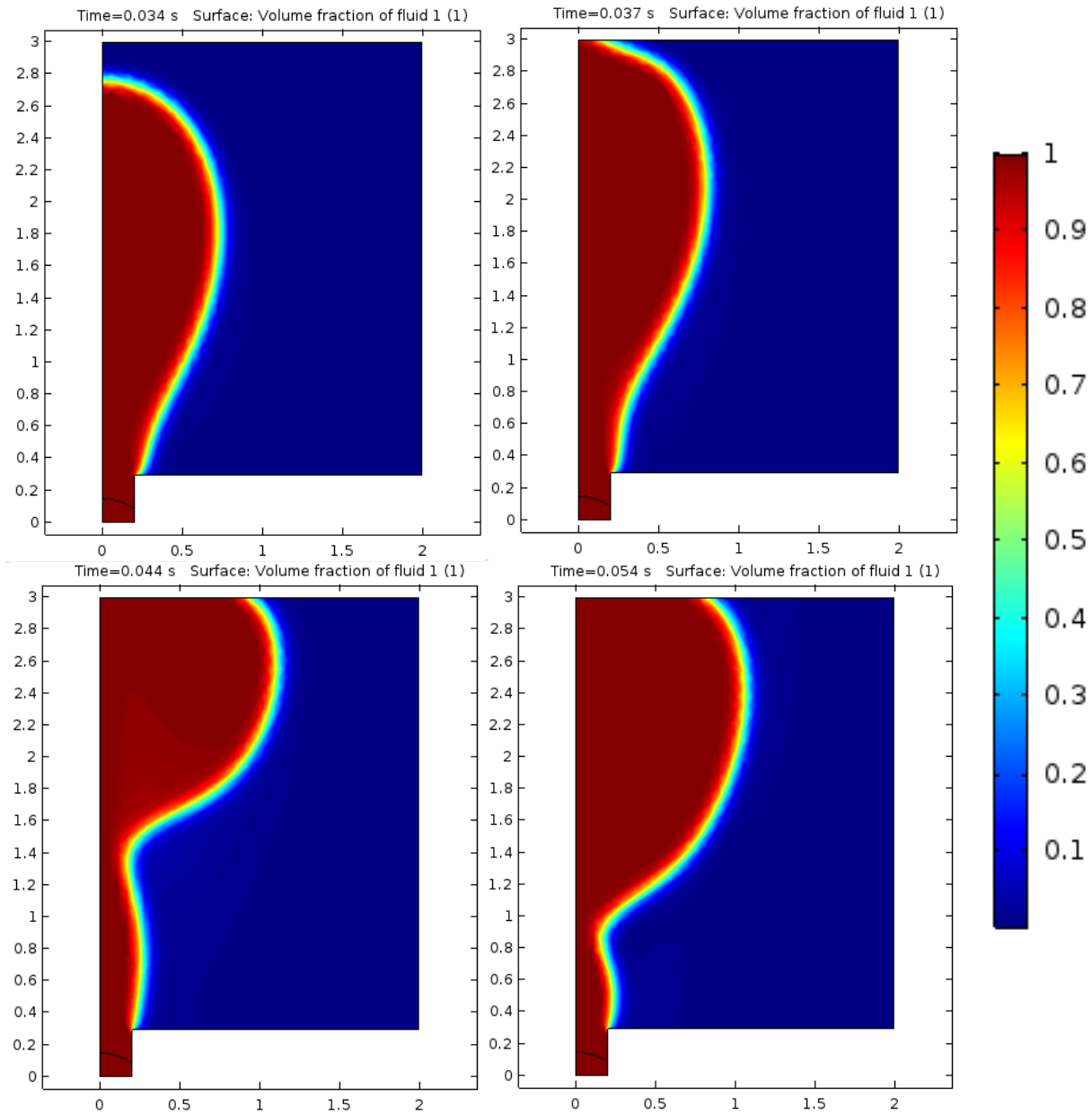


Figure 17: Series of screenshots from a solution (2kV, Height 3mm, Case 2\_3\_0)) showcasing bubble interaction with top electrode (phase field variable plotted, vapor phase corresponding to a value of “1”, liquid phase to a value of “0”).

This behavior is evident when comparing the multiple snapshots in time of the 50° test (Figure 18) and 0° test (Figure 19). After these detachment events, the maximum vapor region radius tends to reach a near constant value. However, with a non-zero cone angle, the maximum radius is much

smaller than the case without the artificial nucleation site. In both cases, the presence of EHD minimizes the maximum radius that a bubble achieves during the solution.

These images, combined with the quantifiable data, show how a bubble can grow, detach, and coalesce with EHD. This model allows for a study of how multiple bubbles present in a small space can be impacted by EHD, and how it changes the maximum vapor radius as they grow. Without coalescence, bubble shapes are also shown to be influenced by EHD.

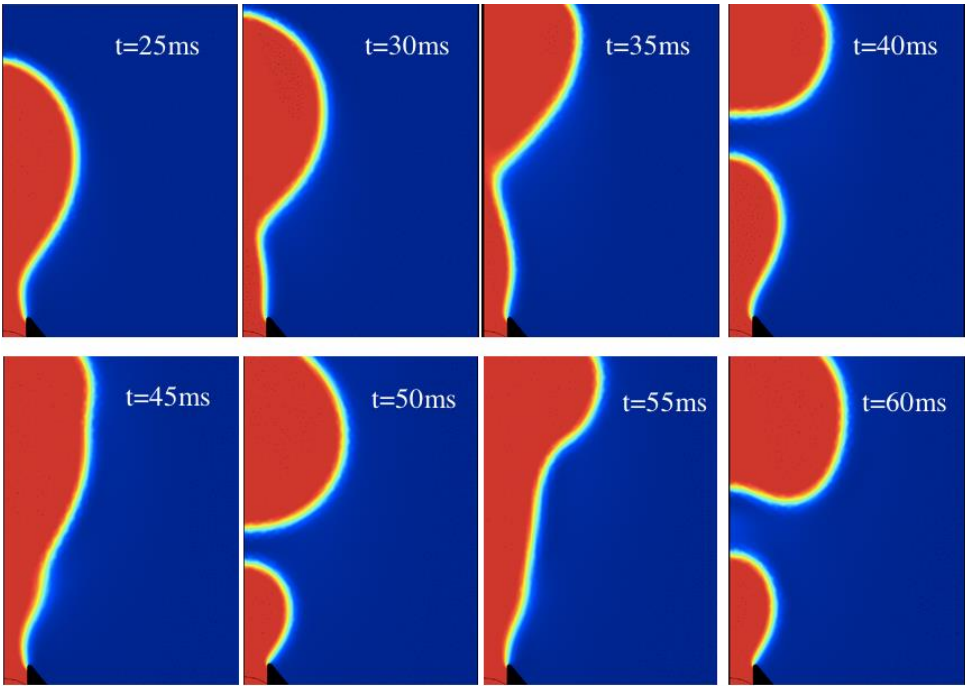


Figure 18: Several snapshots during the 2kV, 50° cone angle simulation demonstrating multiple detachment and coalescence events (Case 2\_3\_0).

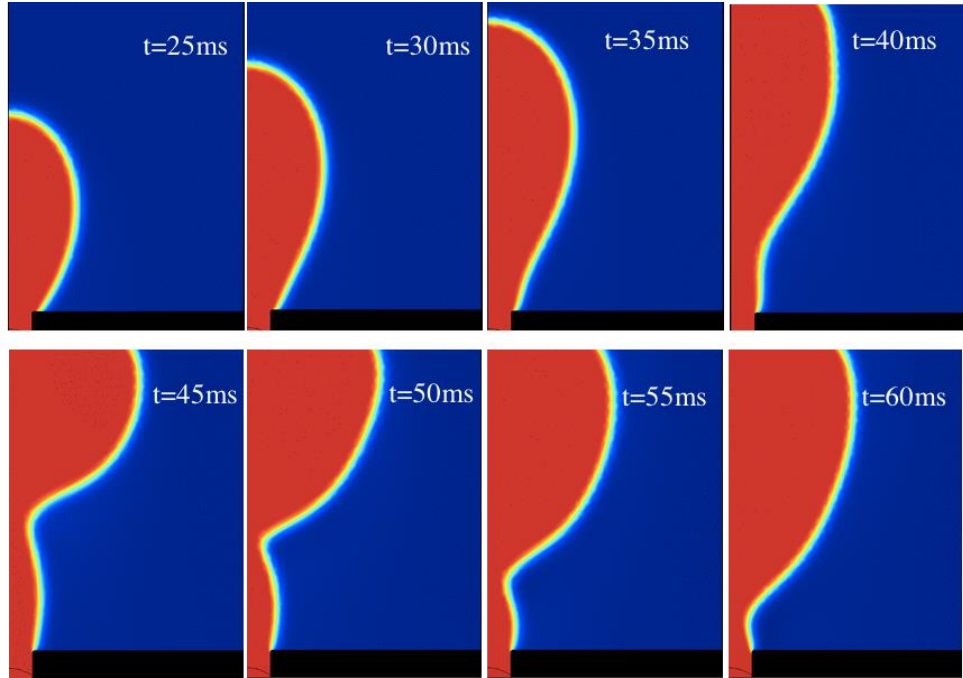


Figure 19: Several snapshots during the 2kV,  $0^\circ$  cone angle simulation demonstrating no detachment and coalescence events (Case 2\_3\_0).

### 3.6.3. EHD-influenced Detachment Behavior in Different Channel Heights

For a channel height of 3mm, the upper end of the minichannel regime, bubble detachment occurs frequently with the application of EHD. As the channel height is reduced, bubble detachment is less frequent, as evidenced by the stability of the radius over time (Figure 15b). At the onset of the simulation, both the 3mm and 2.5mm cases exhibit the same growth profile, which is to be expected. However, as the nucleating bubble makes contact with the upper surface of the channel, the behavior begins to diverge. In the plot of volume vs. time (Figure 20), a lower channel height yields no distinct nucleation events. Interestingly, the rate of bubble growth in Case 2\_2.5\_50 (2.5mm channel height) is slower than that of the 3mm channel height (Case 2\_3\_50). This may be due to the fact that when bubbles detach, it is easier for the next bubble to continue nucleating. When comparing the maximum radius of each, the case corresponding to the lower channel height (Case 2\_2.5\_50) exhibits some oscillatory patterns, as the bubble makes contact

with the upper electrode. However, the lack of additional nucleating bubbles coalescing with other bubbles already in contact with the top electrode means that the value of the maximum radius remains more stable.

The influence of channel height on bubble detachment is clear. With EHD, a bubble in a larger

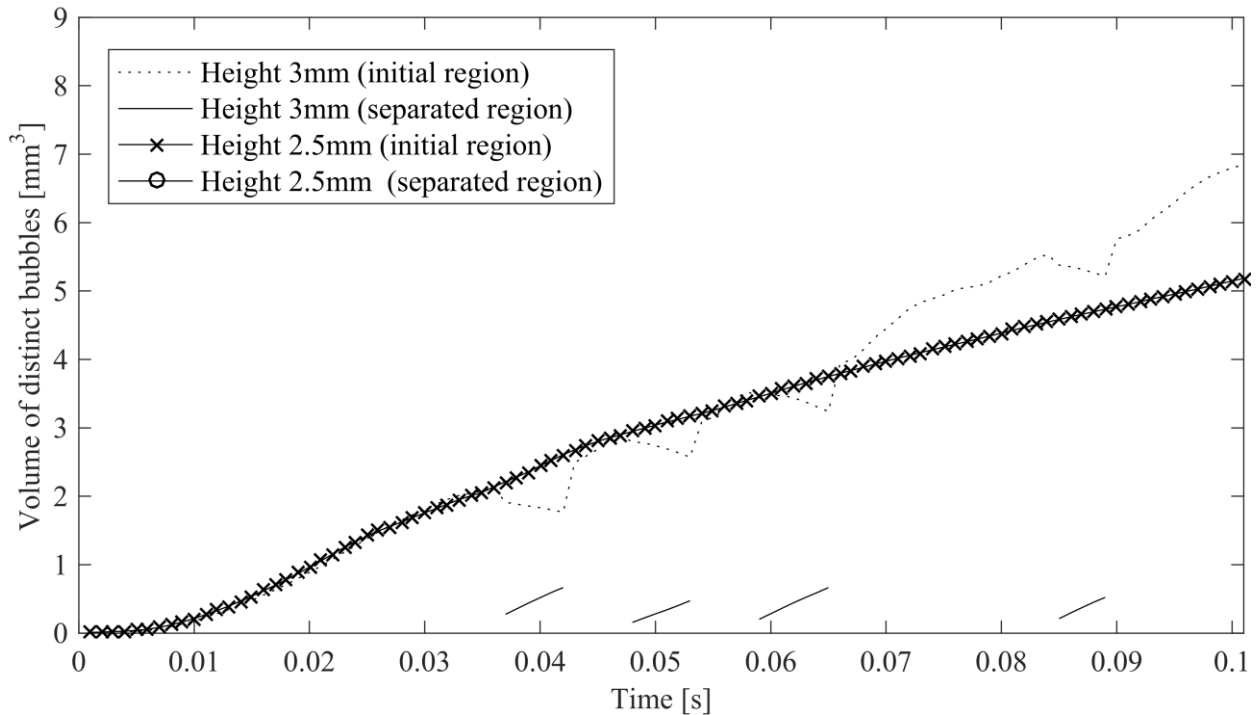


Figure 20: Comparison of bubble growth vs. Channel Height (Case 2\_2.5\_50 and 2\_3\_50).

channel has more room to grow and detach. In a smaller channel, bubbles impact the top wall earlier than in a smaller channel, and while the total vapor amount in the channel is conserved for a time, detachment does not occur as the bubble does not have sufficient space to form a neck.

### 3.6.4. The Influence of an Artificial Nucleation Site and EHD on Neck Behavior

The application of an electric potential results in a non-uniform electric field due to the cone, which accentuates non-uniformities in the electric field close to the neck of a detaching bubble. Figure 21 shows a detaching bubble subject to a 2kV electric field versus one with no applied

electric field 19 ms after simulation start. The neck in the presence of an electric field is shown to be pushed further into the nucleation site, and is thinner than a neck without an electric field. This matches the claims made by Sunder [29] in which a non-uniform field applied near the neck of the bubble can have the effect of pushing the interface down in the nucleation site, while applying additional force to the neck itself. It was found that the detachment of a nucleating bubble is a function of its neck size, and the model results suggest the effect that forcing the neck inwards has the effect of facilitating early detachment. Siedel [33] notes that a pressure gradient tends to force liquid inwards towards the neck, influencing detachment.

With the application of EHD, this process can be accelerated as the neck already exhibits a concave shape. In the above Sections, any influence of EHD on the shape or detachment frequency of the bubble can be attributed to the neck behavior. Narrower necks lead to earlier detachment, and in the case where a neck is not allowed to narrow (Section 3.6.3), bubble detachment does not occur.

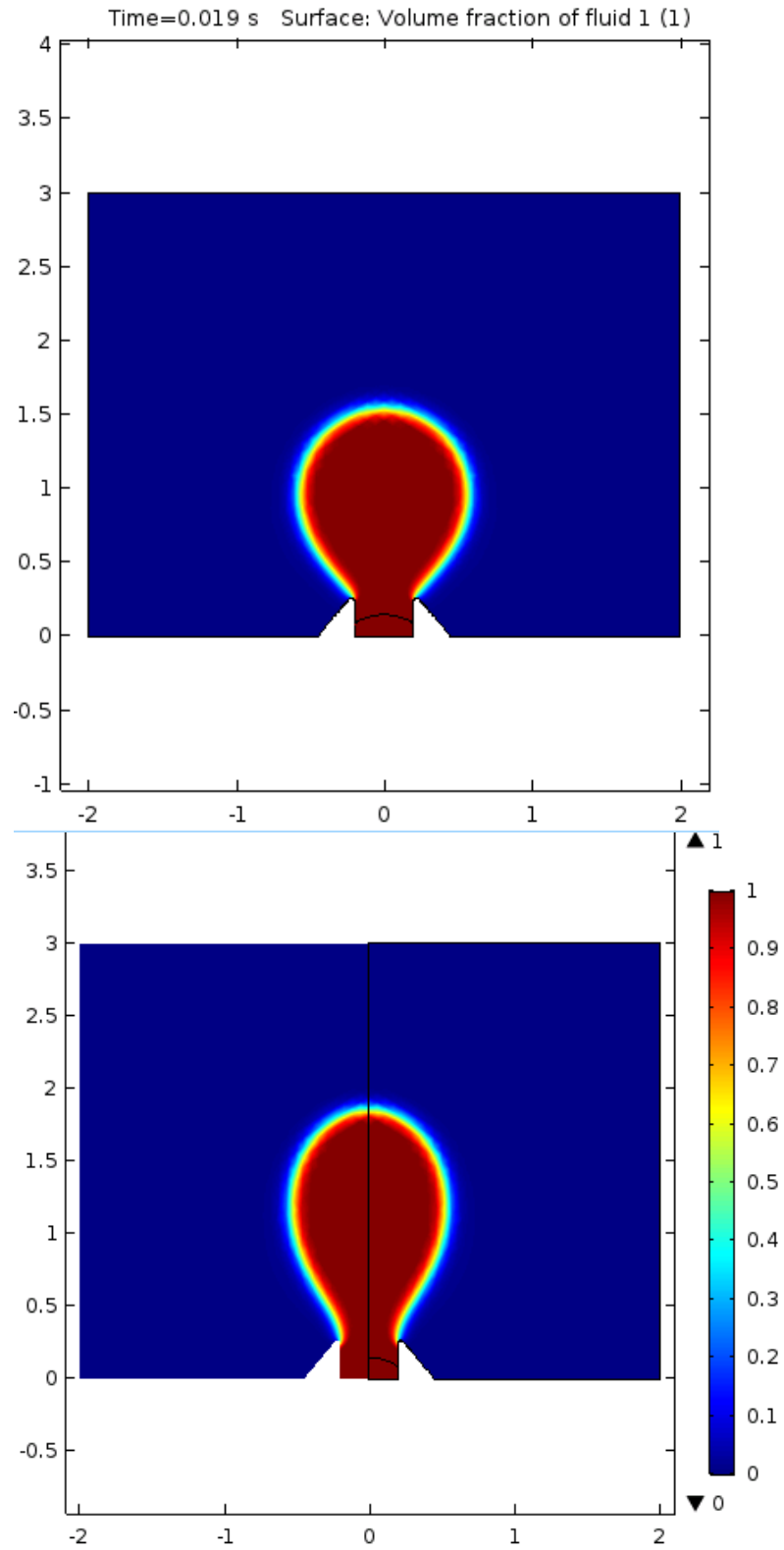


Figure 21: Comparison of bubble neck behaviors at  $t=19\text{ms}$  (a (top) Case 0\_3\_50, b (bottom) Case 2\_3\_50).

### 3.7. Conclusion

With an applied electric field and artificial nucleation site, the bubble volume at detachment is less than it would be for the baseline case. Typically, this would be expected to decrease the magnitude of the heat flux (should the departure frequency remain the same), which depends on bubble departure diameter. However, in a minichannel, these smaller bubbles could lead to a delay in the onset of bubble coalescence and large slugs forming. The presence of larger detached bubbles could negatively influence heat transfer, in the case of large slug coalescence and impingement on other heated walls. Should a cross flow exist, the smaller bubbles as a result of EHD and an artificial nucleation site may be more easily carried away, and be more manageable in a small channel. Additionally, the frequency of bubble detachment is increased both with an artificial nucleation site, and with the application of EHD.

One goal of these simulations was to determine how early bubble separation could occur under the influence of EHD forces, with multiple bubbles nucleating and detaching in a constrained channel. A secondary effect of attempting to accelerate nucleating bubbles away from a surface is the elongation of detaching bubbles. While they may impinge on an upper surface more frequently, narrower bubbles can delay coalescence for a series of densely packed artificial nucleation sites, during initial bubble formation and nucleation. Depending on the application, these consequences may be negative, or positive. In the case of densely packed nucleation sites, elongation could prevent horizontal coalescence, delaying the formation of a vapor layer on the electrode. However, in more constrained channels, elongated bubbles may impinge on the upper surface faster than regularly nucleating bubbles. In the case of minichannels with upper, heated walls, these elongated bubbles may expand faster as they come into contact with an upper wall, leading to a thermal crisis.

The presence of an artificial nucleation site heavily influences the evolution of a detaching bubble. The nucleation can influence detachment by governing how the bottom of the bubble neck attaches to the bottom surface. The application of an external electric field alone has little effect in the detachment of a bubble (in the conditions of this model), but if coupled with a specially designed artificial nucleation site, detachment shape and frequency can be significantly influenced.

The model was able to successfully capture coalescence and breakup. As previously stated, a continuous model was chosen in order to capture bubble coalescence. The phase field method has the advantage of enabling this while avoiding some of the shortcomings of other computational methods. In a moving-mesh method, the significant morphological changes brought about by breakup and coalescence would require a re-mesh at every step, leading to a high computational expense.

Dupuy et al. [55] mention that in Cahn-Hilliard models (such as COMSOL's implementation of the phase field tracking) when two interfaces being to approach, there first exists a "draining" of the fluid between the interfaces. Next, the interfaces rupture and reconnect due to a numerical singularity, and then continue to expand as required by solution of the Navier Stokes Equations for each phase.

In practice, this was observed. As bubbles approached each other, the interfaces would begin to combine. Due to the use of a diffuse interface, eventually two distinct mid-points ( $\phi = 0$ ) would combine to form one, which would be pushed apart by surface tension forces (which tends to keep bubbles spherical). Additionally, breakup occurred similarly. As a bubble grew and a neck formed, the side components of the neck would touch, forming one interface, immediately followed by breakup.



Future work would require this model be extended to a physical experiment, where additional challenges would have to be considered. Fabricating the proposed geometry could prove to be difficult, while applying an electric field across a channel should be easy. It is unknown if a bubble would be able to reliably nucleate and grow on an artificial nucleation site. While the modeling can establish a baseline for how a bubble might grow on a nucleation site, it would be difficult to determine the feasibility of this without performing further experiments.

One goal of the simulations was to lay the groundwork for a reliable, computational method of predicting bubble detachment. The strategy outlined here allows for a coupling of the three underlying physical phenomena. Based on this, several areas of future work can be identified that would increase model fidelity, and more closely approximate physical reality. While a 2-D axisymmetric model is simple, compared to a 3-D simulation, it cannot capture effects such as multiple nucleation sites or cross flow. Future studies will expand on this work in order to create a robust 3-D model. The inclusion of cross flow will allow for a more detailed study of bubble coalescence in the presence of multiple nucleation sites, as well as bubble coalescence downstream of any nucleation sites. Finally, the inclusion of a more robust contact angle model (for the three phase point) would be necessary for a more realistic approximation of forces.

One limitation of the model is that some of the more sophisticated aspects of bubble heat transfer are not incorporated. Cooper and Lloyd [57] discuss the existence of a “microlayer” in a 1969 study. During bubble growth, heat can be removed from the heated surface due to a thin liquid microlayer evaporating beneath the surface of the bubble.

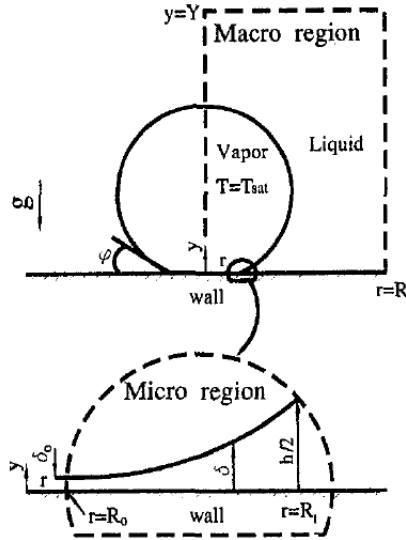


Figure 22: Description of Liquid Microlayer [56] ©UCLA 2002

This is described in Equation 35

$$\delta = 0.8\sqrt{\nu_l t} \quad (35)$$

Where the thickness  $\delta$  of the microlayer at a given location is a function of the liquid viscosity  $\nu_l$  and the time  $t$  it took the bubble to grow to a given size.

By neglecting the microlayer, the cooling effect associated with evaporation of the fluid in this microlayer beneath the bubble is not incorporated in the model. Hänisch and Walker [58]. note that the microlayer is best represented at a scale two orders of magnitude less than the macro-boiling region, making implementation of this layer into CFD interface tacking methods difficult. Additionally, this formulation is still difficult even in the presence of a triple line submodel (between liquid vapor and solid phase). Due to the lack of a contact angle submodel, incorporating the microlayer submodel would be even more difficult. Functionally, this means that in a real-world situation, bubble departure would be retarded as the extra cooling inhibits growth [59]. As a result, in this model, bubble departure frequencies may be overestimated both with and without EHD.

The model created in this study is built on, and derived techniques from, other studies on similar phenomena. These other studies, such as that by Sunder [29], use injected vapor into a fluid domain to model bubble detachment (with no boiling model incorporated). This work shows that using COMSOL, these three (electrostatics, heat transfer, fluid dynamics) physics formulations can be combined, leading to a model that has the potential of more accurately capturing the relevant physics. Additionally, other studies, such as that by Jamet [50] and Son and Dhir [53], use a similar formulation (phase field) to model boiling in a domain, but without EHD effects. Results from these studies helped guide the integrated model used in this study.

Other studies incorporated additional improvements that were not included here. Addition of a microlayer and a more robust contact angle submodel, as well as a 3D formulation would result in a higher fidelity model of bubble growth. The inclusion of a heat transfer submodel could allow for more accurate temperature determination of a heated chip, and allow for temperatures to be determined on the chip if the geometry is changed.

To the best of the author's knowledge, a model that combines the three physics modes (electrostatics, heat transfer, and fluid dynamics) in one model has not been attempted in this manner. It ties in with the other attempts described above, but takes many of those models an additional step by incorporating the combination of multiple physics submodels. The use of COMSOL multiphysics can add significant value to future modeling efforts. COMSOL allows for governing equations to be modified for more advanced efforts, while remaining accessible to many users. In addition, COMSOL models could be more readily extended to three dimensions, requiring less effort than custom models. In even more forward looking efforts, COMSOL could be used to model an entire integrated system in 3D (at significant computational expense).

Additionally, experimental work should be carried out to study the effects of multiple nucleation sites, possible fluid impurities, and cross flow in a well-defined channel. In the chapter below, the experimental work is described that aims to expand on some of the modeling work in this chapter.

## 4. Experimental Investigation of EHD Effects on Nucleate Boiling

Results from the numerical study presented in Chapter 3 suggest that the application of non-uniform electric fields to bubbles in the minichannel regime can influence nucleate boiling characteristics. Nucleate boiling is one of the most efficient means of heat transfer, but its implementation can be inefficient or dangerous to hardware on the mini- or micro-scale (see Chapter 2). Boiling in dimensionally restricted channels can lead to rapid bubble growth and flow oscillations, resulting in a thermal runaway effect, where large regions of expanding vapor remove the cooling capacity of fluid and nucleating bubbles. Without the cooling capacity of the fluid for which these systems are designed, high temperatures can lead to degraded performance or permanent damage. With this in mind, a greater understanding of nucleate boiling in the minichannel regime is required.

The experimental component of this study was designed to explore the growth and detachment of nucleating bubbles in the presence of an externally applied electric field, a promising means of influencing, or even controlling, two-phase flows. Specifically, the feasibility of using EHD forces to enhance and control nucleate boiling in minichannels will be investigated in the presence of a cross flow, artificial nucleation sites, and electric field non-uniformities. The experiments were designed to reveal the challenges of EHD-enhanced nucleate boiling in a minichannel in order to better understand potential implementation of the technique.

### 4.1. Objectives

Many other studies of nucleate boiling are concerned with overall heat transfer coefficients between the heating element and the bulk fluid [22]. In this study, the modification of heat transfer coefficients was of secondary importance compared to investigating the behavior of the growth and detachment of a nucleating bubble. At the minichannel scale, the heat transfer performance

can depend heavily on the behavior of the detaching bubbles, as the system can often be at the tipping point of runaway heat transfer [34]. As part of this study of the growth and detachment behavior of nucleating bubbles under the influence of an electric field, unique nucleation site geometries and test conditions (applied potentials) are explored to understand the effect they have on flow or pool boiling in confined channels, with respect to the overall boiling conditions in an entire channel.

In addition to studying bubble growth on a single, artificial nucleation site, studying the entire surface upon which bubbles freely nucleate can help researchers better understand how an applied electric field can influence the performance of the device at the macro scale, i.e. over a larger heated region containing hundreds of nucleation sites. Results from the modeling study presented in Chapter 3 suggest that these local non-uniformities can increase the frequency of detaching bubbles while minimizing their volume *at the respective, single nucleation site* [29]. However, the effect of these local non-uniformities on the overall boiling behavior from many sites, over the surface of an entire heated channel, is unknown. To better understand this overall behavior, the channel used in this work was designed to approximate a real-world device. Many other studies that examine the effect of an applied electric field on boiling do so with structures embedded in an apparatus designed for pool boiling [10] without a cross flow, or with bubbles of gas (not vapor), injected into the system [29]. In order to better approximate a real-world device, the apparatus in this work used a common conducting surface (the channel “bottom”) as the biased electrode and the heated surface containing the nucleation sites. This led to some practical challenges in the application of a high potential while connected to a heater. Additionally, a cross-flow was required in order to reproduce the drift of individual bubbles and larger vapor packets in a channel. Finally,

this work eliminated the need to externally inject bubbles of gas into the channel by using nucleation on a heated surface to create bubbles of vapor as would occur in an actual application.

The physical size of the channel used in these experiments corresponded to what is referred to as the miniscale in the literature [34], occupying the region between the conventional and micro-scale fluid flow regimes in channels. This scale regime is of particular interest, as there are several detrimental effects that can result from nucleate boiling that are not seen at the macro-scale. The minichannel regime is defined by the smallest (assuming non-circular) channel dimension [34], as opposed to the hydraulic diameter of the channel. For example, if a rectangular channel has a width within the minichannel regime but a longer length, it would be considered a minichannel. The study of boiling in the micro- or nano-scale, is much more difficult to image and was beyond the scope of this study.

The objectives of the experimental investigation of EHD effects on nucleate boiling were specifically to: 1) investigate the feasibility of using artificial nucleation sites to initiate and control nucleate bubble growth in an EHD-enhanced minichannel heat transfer device (with cross flow), 2) investigate the effect of EHD on nucleation site density, nucleating bubble shape, and bubble departure frequency 3) investigate the behavior of detached bubbles in a channel with EHD

## 4.2. Experimental Setup

### 4.2.1. Introduction

The test apparatus used for this work needed to be capable of superheating a working fluid to produce nucleation while supporting two electrodes to create the electric field. In addition, a pump was required to induce cross flow, an optical system to visualize bubble growth, a reliable data acquisition system to monitor and record voltages and temperature, and a flow channel to allow visualization while at the same time minimizing the possibility of leaks and contamination. This

section describes the design and construction of this apparatus, as well as some of the lessons learned during its construction.

Prior to apparatus design, the constraints of the system had to be defined. Foremost, the working fluid needed to be dielectric, with a high permittivity and optical clarity. Optical clarity was a necessity due to the imaging requirements of the study. Based on the physics discussed in Chapter 3, a relatively large difference in permittivity between the liquid and vapor medium increases the magnitude of the force on a bubble under the influence of EHD forces. In this study, the fluid used to satisfy the above criteria was HFE-7100 (discussed at length in Section 2.3).

The design of the experimental apparatus follows the fluid choice; as material choice is limited by compatibility with HFE-7100. In addition to the characteristics listed above, HFE-7100 is relatively safe to handle and compatible with many common materials, so the apparatus does not require extensive safety features specifically related to the fluid used [24]. Additionally, the low boiling point (61°C) of HFE-7100 helped drive the material choices for construction.

In addition, the apparatus had to be designed to allow conditioning of the fluid prior to testing. Typically, this could mean filtration, degassing, and preheating. Similar to previous work [63], the HFE-7100 was not degassed prior to testing. In some studies, degassing a fluid prior to use would ensure no other vapor is introduced into the system. Because the fluid was not pumped in a loop, degassing was deemed unnecessary. In addition, the need for filtration was eliminated by operating the channel in an open-cycle mode in which only fresh fluid is used and then discarded. To ensure that most, if not all, the length of the channel could be used for nucleate boiling, the apparatus was designed to preheat the fluid before entry in the fluid channel.



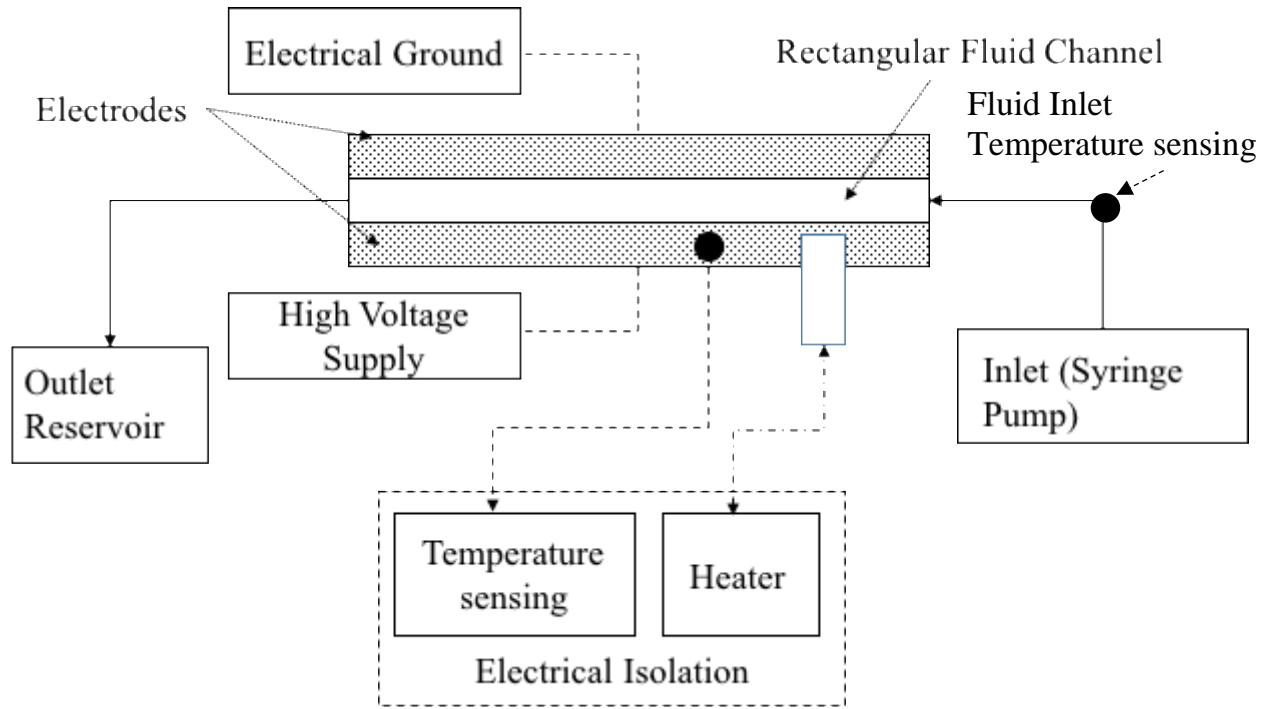


Figure 23: High-level diagram of experimental setup.

#### 4.2.2. Apparatus Design

Given the outline of the experimental apparatus described above, a device was designed that features transparent fluid channel side walls with the top and bottom walls acting as electrodes. The device also included an inlet, and outlet, temperature sensing of the fluid and heated channel, and electrical isolation for components floated at a high potential. A basic diagram of this test apparatus is shown in Figure 23. This diagram indicates the key electrical, fluidic, and instrumentation interfaces used. A SolidWorks model (side, isometric, and exploded view) of the actual channel and support is shown in 24a and 24b. The experimental apparatus was designed to be relatively low-cost and quick to fabricate so that multiple test articles with different size channel and nucleation site geometries could be evaluated should the need arise. The entire channel assembly is made up of five basic components: mold fixtures, unheated entry length channel, copper electrodes, glass viewing windows, and mounting plates. The unheated entry length channel is upstream, where the fluid enters the channel assembly. There, it can develop into a fully

developed flow before entering the visualization region. The mold fixtures hold in a potting compound that was used to keep the channel rigid. The fluid enters the channel comprised of a top and bottom copper electrode, and viewing glass on either side. Downstream, the fluid leaves the channel from the outlet into a reservoir. Initial versions of the design called for a custom-milled aluminum enclosure, but the complexities involved in its construction as well as the inflexibility in its design led to the creation of the present configuration. A design based on the use of 3D printed support molds was adopted in order to allow for ease in fabrication of channels with differing height.

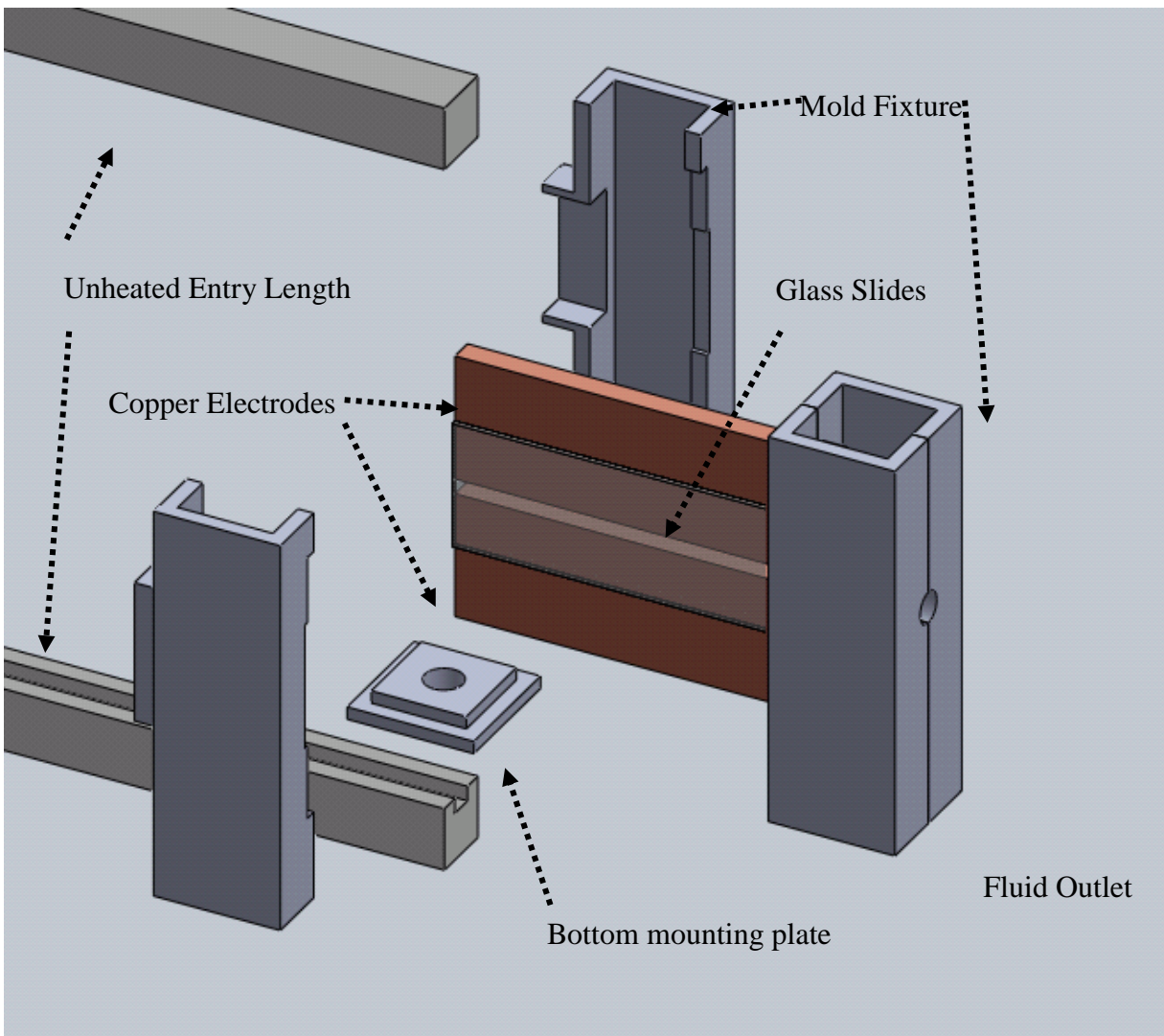
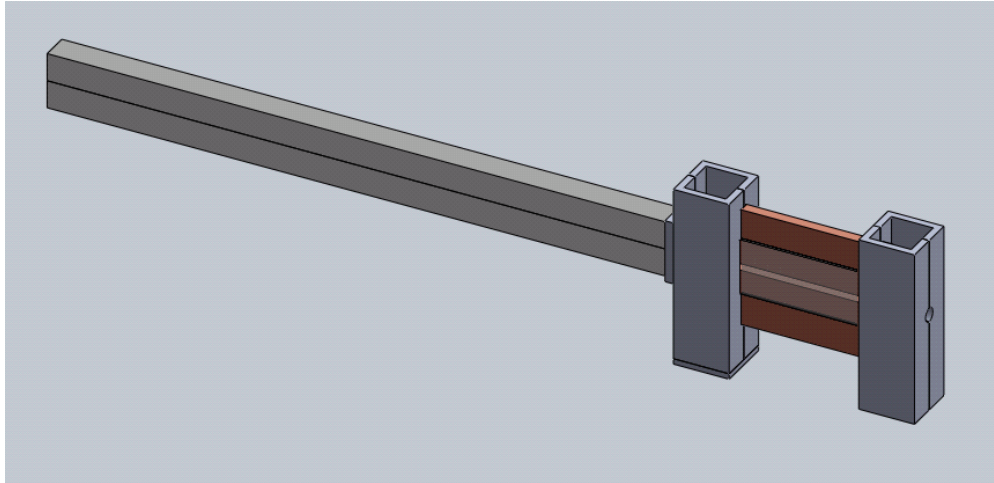


Figure 24: (a) top, isometric view (b) bottom, exploded isometric view (one bottom mounting plate shown for clarity), copper electrode is 3"x1"x3/16" (for scale).

Fabricating the apparatus first required a selection of height for the channel (the width is fixed), and the number and geometry of any artificial nucleation sites to be formed into the channel bottom. As confirmed through modeling, a convex, hollow cone-shaped cavity could provide local non-uniformities around the cavity to impart an electrohydrodynamic force on a nucleating bubble. Several studies find this as well: Siedel [33] mentions boiling of n-pentane with a few K superheat, at a site 500 $\mu\text{m}$  in diameter and 180 $\mu\text{m}$  deep. Bonjour [64] also uses indentation with a cone-point, generating a 200 $\mu\text{m}$  diameter and 280 $\mu\text{m}$  deep hole. Bonjour et al. notes that while natural nucleation sites are on the order of 10's of  $\mu\text{m}$ , experimental work on artificial sites typically use diameters from 400 to 1300 $\mu\text{m}$ . In that study, Bonjour et al. powers the heater for over a half an hour prior to testing to “activate” the sites, at which time the applied heat flux is decreased, leading to stable boiling from one site. Based on this past literature, a copper electrode with a nucleation site on the order of 500 $\mu\text{m}$  was desired. The preparation of this copper is described below.

#### 4.2.3. Copper Preparation: Polishing and Fabrication of Artificial Nucleation Site

As shown in Figure 23 and Figure 24, the top and bottom surfaces of the channel are electrically conducting and made from copper. The copper used was bar stock of high purity copper obtained from McMaster Carr (Multipurpose 110 Copper, 1" x 3/16" x 12"), cut down to size. Since the copper stock was already correct in two dimensions (1" and 3/16"), cutting would not risk altering or damaging the already flat surface. The copper surface is prepared so that the surface finish is as uniform as possible in order to allow reliable comparison of boiling characteristics at different locations. Each piece of copper is sanded identically, with sandpaper grits of increasing fineness. Five successive sanding steps were applied, with compressed air being used to clean the surface between each step to remove debris, so as to not damage the surface in successively higher-grit sanding operations with larger particles left from the previous sanding operation. Initially, a polishing compound (Never-Dull Magic Wadding Polish) was used on all sides of the copper to

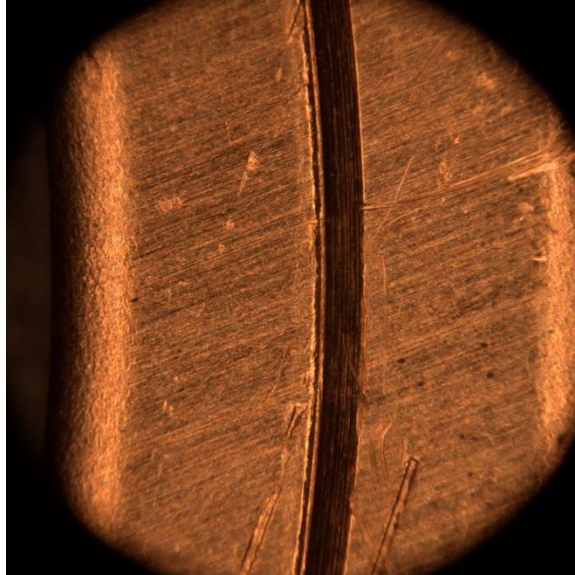


Figure 25: Copper surface with no finishing.

finish the surface. However, examination under a microscope showed that the polishing material was more abrasive than the finest grit sandpaper, leading to isolated scratches and other undesirable features on the surface. The procedure was therefore modified so that the polishing

compound was used only on the wide sides of the copper (i.e. the parts of the copper not in contact with the fluid), to provide a clean surface on which to adhere the glass sides. It was not deemed necessary to sand the sides, as the silicone adhesive would be enough to fill in gaps. Additionally, if the sides were sanded, it could compromise the fit within the mold. Once the copper surface has been sanded to the finest grit, it is ultrasonically cleaned to remove any other impurities. An example of a copper surface without finishing is shown in Figure 25. While this piece was not used as the electrode, it serves as a useful comparison point for how a surface can change after being treated. The curved vertical line is a feature of the copper sample (originally used as a vacuum seal). It is approximately 300 $\mu$ m wide (for scale).

A cone shaped cavity was produced by mechanical indentation, using a spring-loaded center punch, such as a Starrett Spring-Impact Center Marking Punch, model 18C. The spring action of the punch was found to deform the copper excessively, creating cavities that were on the order of 1-2mm wide. In order to create cavities on the order of micrometers (a size which was confirmed to work in the model) the center punches were instead used by manually pressing the tip lightly into the copper. The size of the artificial site was chosen to satisfy the criteria that a bubble bound to the orifice. In the model, this was accomplished simply by creating a site on the order of expected detachment diameters found in literature. In the experimental study, the order of the cavity size was initially determined by reviewing what size nucleation site would allow for bubble inception based on the literature. Griffith and Wallis [28] developed an expression for an “inception superheat”, in which bubbles can form on a surface

$$\Delta T = \frac{4\sigma T_{sat}}{\rho_v h_{lg} D_c} \quad (36)$$

Where  $D_c$  is the cavity mouth diameter. Larger cavity diameters lead to inceptions at lower wall superheats. Using the properties of HFE-7100 in Eq. 36 (assuming a 4°C superheat), and using the HFE-7100 value of 125,000 J/kg for  $h_{lg}$ , bubbles can form on a cavity mouth diameter of 5 $\mu$ m. From the literature, the average departure diameter for a representative study using HFE-7100 from a copper surface was 550 $\mu$ m. Due to the desire to have a bubble bind to an orifice that is on the order of the detachment diameter, a cavity only 5 $\mu$ m in diameter would not be adequate. In order for the site geometry to influence the neck behavior, bubbles should be encouraged to nucleate from and attach to larger sites. It was observed in the model that cavities of diameters significantly less than that of the bubble detachment diameter would cause bubbles to no longer bind to the outer lip, and continue growing on the flat surface. To account for this, the artificial nucleation site was designed to be conical due to the indentation from a center hole punch. Ideally, the center of the cone would consist of a cavity on the order of the calculated diameter, bubbles would grow, and bound to the large part of the cavity (on the order of the detachment diameter). Initially, results were promising. During initial trials with quiescent fluid, bubbles were able to form inside a larger cavity, expanding rapidly and bounding to the orifice (a method discussed by

Gerlach [65]). This much larger nucleation site was ineffective with a cross flow, however, and



Figure 26: Mechanical Indentation Device

bubbles did not reliably nucleate within the site. This may have been due to the cooling effects of a modest cross flow, especially in the presence of the raised portion of the nucleation site, acting as miniature fins.



Figure 27: Depression created by designed indentation pin.

An image of the site, taken with a Meiji UNIMAC Macrozoom lens on a Panasonic Lumix GF3 camera was then used with *ImageJ* image processing software [66] to inspect and determine the final diameter of the cavity.



Initial attempts at creating an artificial nucleation site involved modifying the end of a center-hole punch to mechanically indent nucleation sites with a desired profile in the copper surface. The idea behind this approach was that the contour desired for the nucleation site could be formed by indenting the copper surface with the “negative” of the contour, machined into a custom made punch with an indentation surface made from a harder metal. This indentation formed a “mesa” shape in the copper, into which the nucleation site would be punched. The indenter was fabricated by replacing the metal tip of a commercially available punch with a custom tip. The tip was formed by turning down a small section of a steel rod on a lathe and drilling a small hole in in the center using a #73 (0.61mm diameter) drill bit. This custom tip was then installed in the punch as shown in the process of forming a particular nucleation site geometry in the copper surface using an indenter is somewhat crude and at best forms only an approximation of the desired shape. Figure 28 shows several views of the indenter tip, along with the critical radii and depth. Figure 29 shows a photograph of the resulting nucleation site on a copper sample. The large indentation in the center was made using the custom punch, compared to indentations made from an unmodified center hole punch.

Ultimately, this nucleation site was unsuitable. While it was desired to later drill out the nucleation site in the middle, the depth of the “trough” around the raised portion was not large enough. It was desired to have a deeper channel around the site itself, in order to enhance the EHD effects observed in the results presented in Chapter 3. Due to this, the approach needed to be modified to first create a deeper channel. A second approach was devised consisted of using metal ferrules (VICI Valco), which could be pressed into the copper surface to make an indentation with approximately the correct cavity profile.

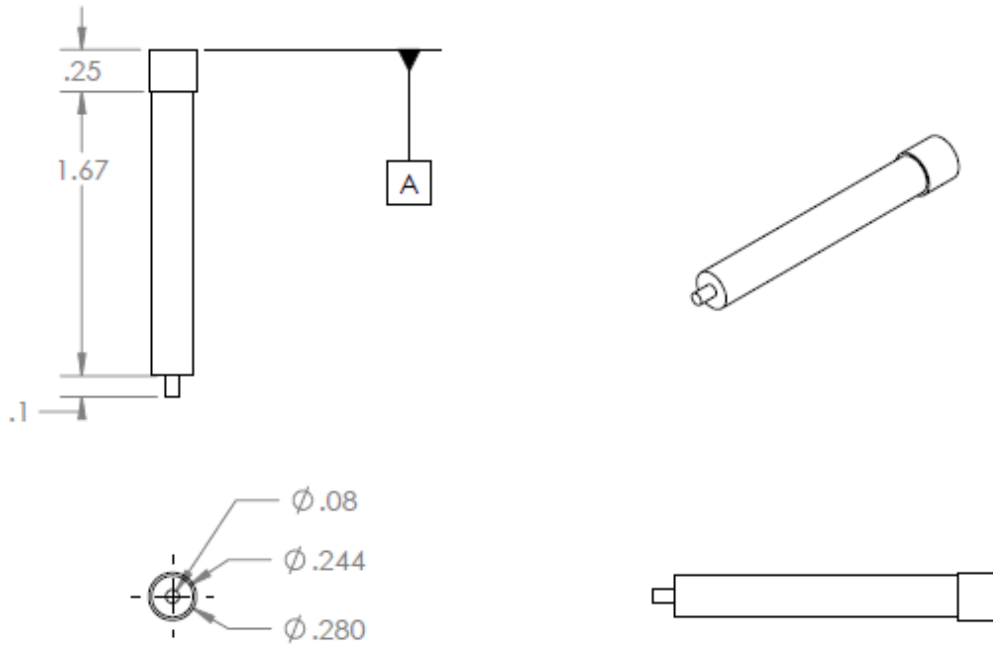


Figure 28: Center punch (units in inches), with front, top, side and isometric views.



Figure 29: Indentation created by custom center punch piece.

These ferrules are originally used for compression seals in tubing. The ferrules used were  $1/32$ " inner diameter at the tip, which led to holes being pressed in the copper. In metric units, the entire site was  $1.52\text{mm}$  in diameter, where the center plateau was  $0.76\text{mm}$  in diameter. The depth

of the “trough” between the two was 0.35mm. This depth was set by using the Starrett center hole punch set to its lowest pressure setting. As shown in Figure 6 from Chapter 3, the desired nucleation site consists of a center hole, where the bubble nucleates, surrounded by a ridge, which serves the purpose of intensifying the electric field and hence the EHD effect on the bubble surface. The hole in the center was created by pressing the punch-pin extremely lightly, i.e. by resting the pin on the surface and pushing down but not allowing the punch-pin to spring punch. This created holes with a diameter of 0.37mm. Depth was difficult to determine, but is observed to be less than the depth of the trough at 0.35mm. The custom punch-pin tip was a good exercise in nucleation site fabrication, the metal ferrules used offered a much tougher pressing medium (i.e. one that would not deform after several pressings), and offered a much smaller difference between inner and outer radii, leading to a narrower and deeper channel around the site itself. Typically, ferrules were observed to last approximately 10 pressings before deforming enough to require a new ferrule.

In addition to the nucleation site, the copper needs more preparation before the channel can be assembled. As seen in Figure 23, a heater and temperature sensing capability are required. Figure 32 is a diagram of the setup, showing a cross section of how the heater interfaces with the copper electrode. To better ensure thermal contact between the heater cartridge and the copper electrode, the heater was recessed deep inside the copper. A hole was drilled into the bottom electrode to allow for a device to act as an embedded interface between the cartridge heater and the copper electrode (approximately 1” deep). The thermocouple should be embedded inside the

bottom copper electrode as well, so a small (~1mm) diameter hole is drilled close to the hole for the heater, approximately 1/4" deep inside the copper electrode.

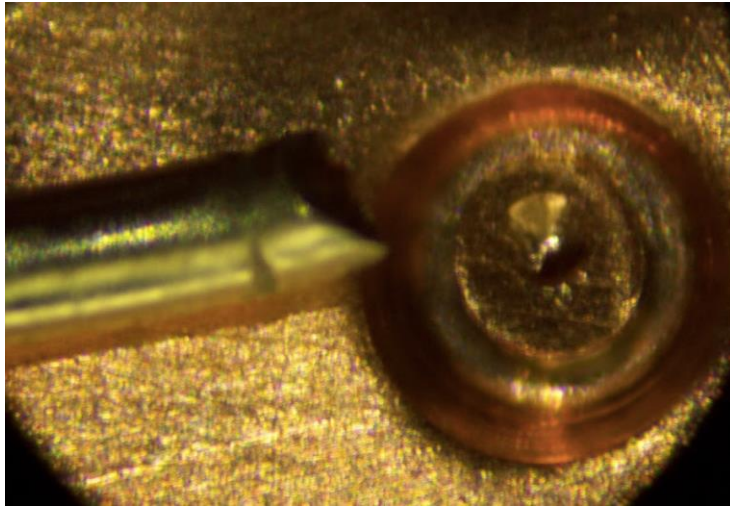


Figure 30: Indentation created by metal ferrule, 0.58mm diameter wire shown for scale on the electrode used in the experiment.



Figure 31: Metal ferrule used to create indentation in copper.

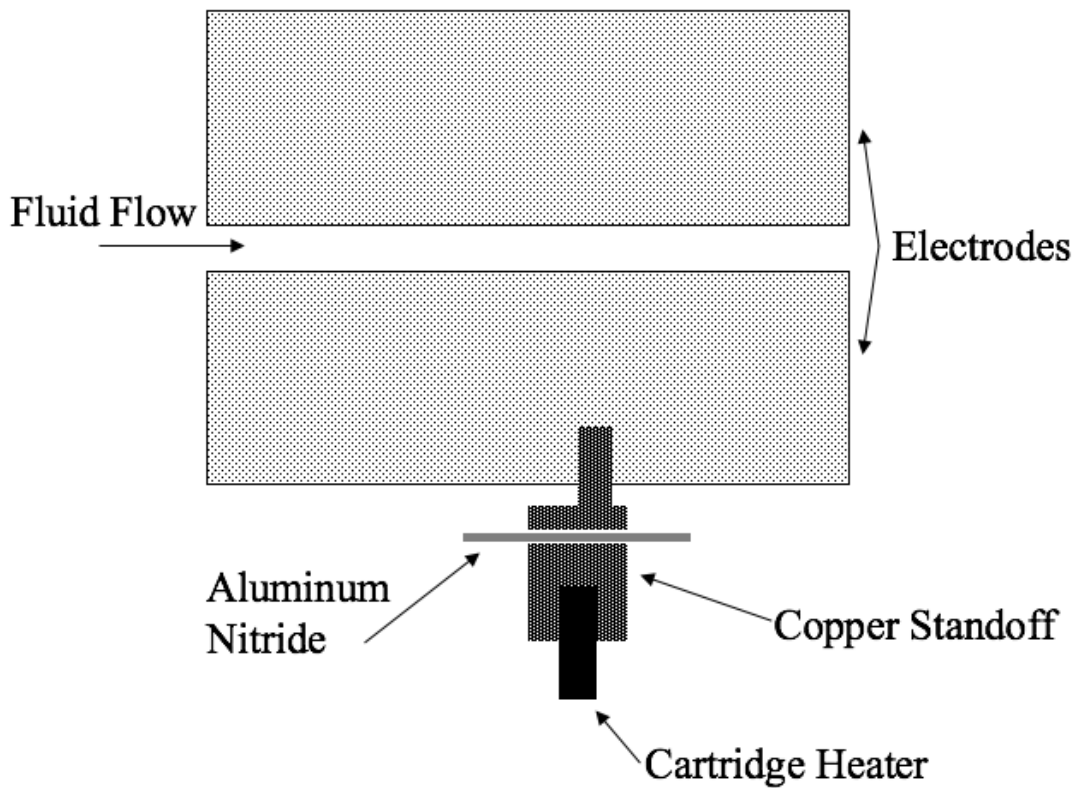


Figure 32: Diagram of heater setup, cross section of the fluid channel. Shown is the copper reducing cylinder, allowing for a 1/4" heater to make good contact with the 3/16" thick bottom electrode.

Once the copper channel was polished, the nucleation sites could be formed in the copper as described above. The copper channel electrodes were inserted into a standard bench vise, with padding placed on either side to protect the surface finish. Once firmly in place, a ruler was used to measure and mark out where the nucleation sites would be located. Nucleation sites start approximately 15mm from the inlet, with marks spaced approximately 10mm equidistant from each other. The manual hand-method of placing the nucleation sites resulted in a slight inaccuracy in placement (Figure 33), however the spacing between these sites was not considered critical.



Figure 33: Using the center punch to create nucleation sites in a bench vise. Nucleation sites are numbered sequentially (from channel inlet, left in this image).

#### 4.2.4. Channel Assembly

Assembly of the test channel involves numerous steps, and requires careful preparation to ensure consistent and leak-free construction. As shown in Figure 34, the channel is formed by two pieces of copper bar stock, forming the top and bottom conducting surfaces, and two glass slides serving as viewing ports for the high speed camera video.



Figure 34: Copper electrodes with glass walls.

Construction of this channel assembly requires care in order to ensure that the adhesive material does not impinge in the viewing area. The glass slides must be bonded correctly to the copper, or else fluid leaks through. Cyanoacrylate (CA) Glue was originally considered as a means of bonding the glass to the copper due to its strength and short cure time. However, upon curing, the CA glue resulted clouding of the glass, spoiling the ability to visualize bubbles. As a result, Dow Corning 700 (DC 700) Silicone Sealant [67] was used as the primary adhesive, with small amounts of CA glue used as far away from the viewing area as possible for structural strength, preserving visual acuity. While the DC 700 did not have enough rigidity on its own to maintain channel structural integrity while being assembled, its more viscous nature prevented seepage into the channel, and no clouding was observed. A fixture, shown in Figure 26, was built to aid in the assembly of the channel electrodes and side windows. Assembly consisted of placing a glass slide, which would become one of the side windows, inside the fixture, between two rigidly mounted glass slides used as alignment aids. The remaining parts of the assembly fixture were made from styrene. The bottom copper electrode is placed snugly into the alignment slides, with a thin line of DC 700

along the glass slide creating a seal. Small amounts of CA glue behind this seal hold it together. Once cured, the assembly is flipped and the process repeated for the top electrode.

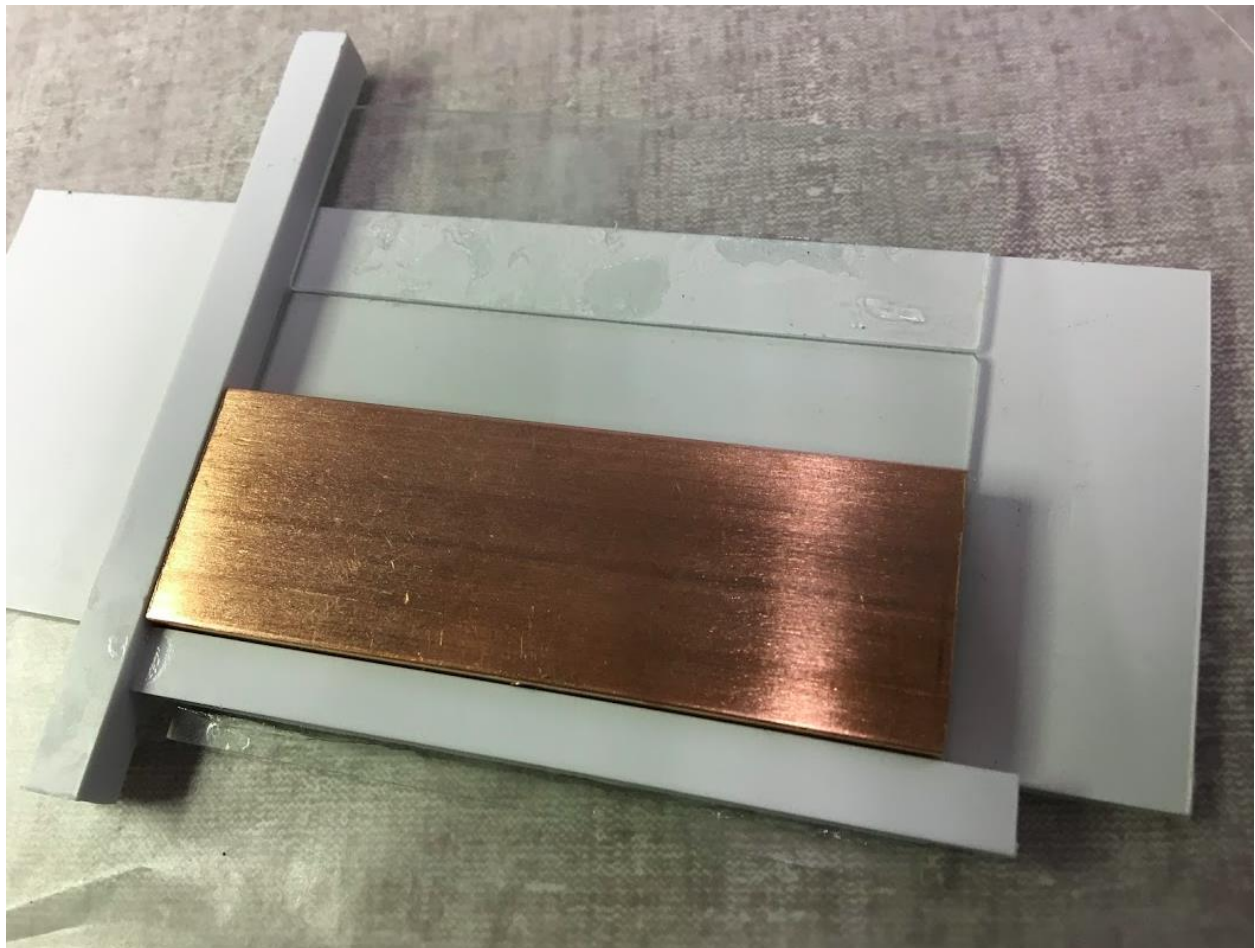


Figure 35: Channel construction with alignment fixture, one glass slide and bottom electrode shown.

Once assembled, these four pieces (comprising the channel itself) are held together and supported by insulating posts on either end made from a dielectric potting compound. These posts also provide support for the tubing used for the flow delivery to and removal from the channel, as well as supports for mounting the channel to a supporting structure. The potting compound is 832HT High Temperature Epoxy Encapsulating and Potting Compound (MG Chemicals) [68]. To form the supporting posts, the potting compound is poured into molds made from ABS<sup>plus</sup>, printed on a Statusys Dimension 1200ES Rapid Prototyping Machine [69]. Of great importance was the



ability to reuse the 3D printed molds, to facilitate a quick experimental turnaround when making new channels. Originally, it was desired to find a lubricant that would allow for the potting compound to separate easily from the mold. Graphite powder and WD-40 were attempted, with little success. Eventually, it was found that a layer of Vaseline petroleum jelly could be used effectively to facilitate separation of the printed molds from the potting compound once cured. The Vaseline was applied liberally to the inside of each mold prior to pouring the potting compound. After curing, the Vaseline enabled the mold fixture to be easily removed. Earlier attempts at removing the mold without this lubricant were unsuccessful, resulting in incomplete mold removal or damage to the structure.

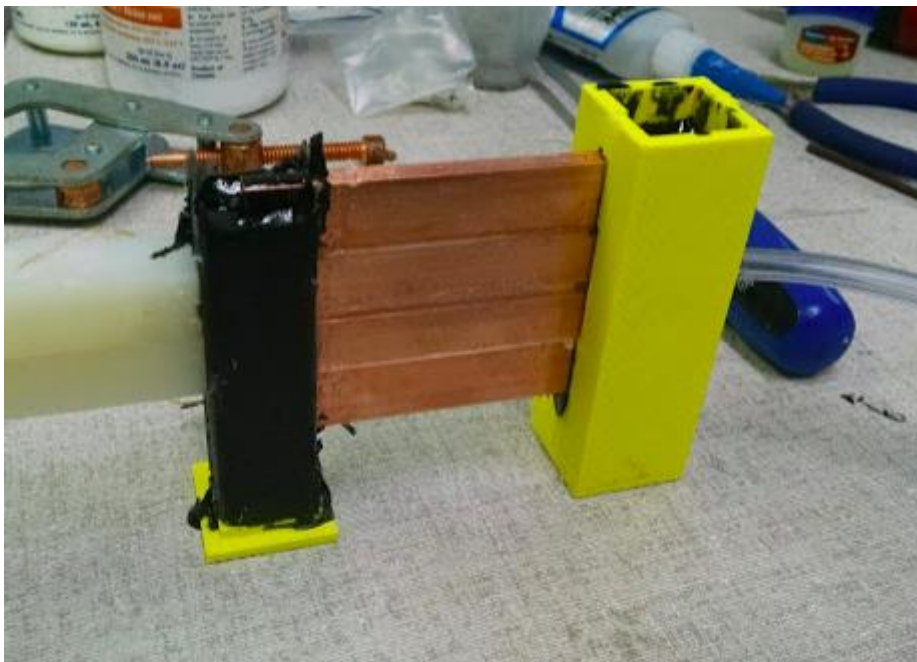


Figure 36: Vaseline assisted mold removal.

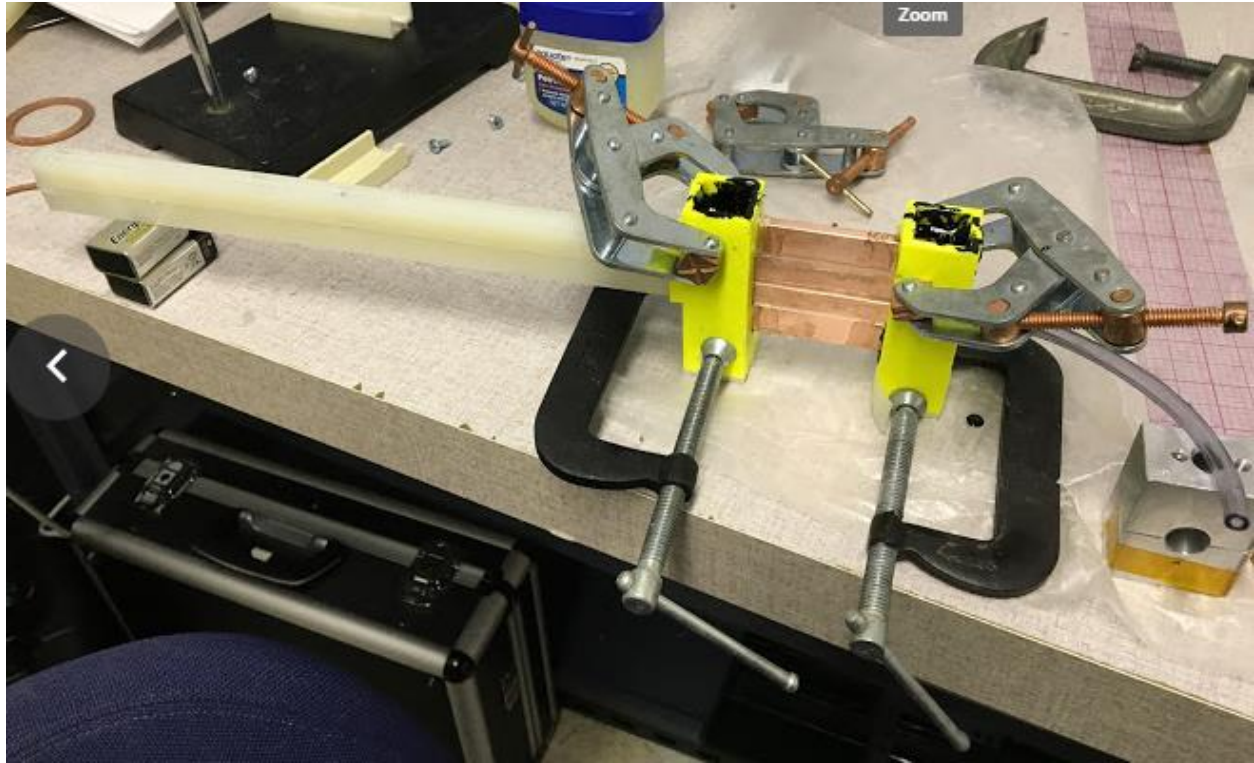


Figure 37: Construction of the test channel. Forms are shown clamped together while potting compound sets.

A completed channel is shown finishing the curing process in Figure 37. The vise grips hold the sides of the mold together, creating a seal so the highly viscous potting compound can't seep out the sides before curing. Discussed in later sections are the Unheated Entry Length shown (white structure to the left of the channel), as well as tubing used for the fluid outlet. These are positioned using slots in the mold, designed so that repeatability in the channel assembly can be maintained.

#### 4.2.5. Fluid Delivery and Support Structure

With channel construction complete, the rest of the apparatus was assembled, starting with the fluid delivery system. A syringe pump was used to generate the fluid cross flow in the channel [71]. For a given channel geometry and desired volumetric flow rate, controlled by the syringe pump settings, the velocity can be estimated in the channel. For this work, a New Era Pump

Systems NE-300 syringe pump [72] was used with a flow rate range of  $0.73 \cdot 10^{-3}$  L/hr – 1500 mL/hr. The syringe pump is shown in Figure 38.



Figure 38: Back of fluid pump syringe, after exhausting all fluid.

All tests used a volumetric flow rate of 4 ml/min resulting in a velocity in the range of 4.75 mm/s inside the channel (assuming a 3mm tall and 4.76mm wide rectangular channel). The volumetric flow rate was set in the syringe pump, while the mean velocity in the channel was determined by dividing the volumetric flow rate by the channel cross sectional area. The average velocity in the channel is necessary in order to ensure that the fluid flow in the channel is laminar, in order to provide more consistent test conditions.

As a part of this setup, it was determined that a preheater was necessary in order to control the temperature of the fluid, as well as an unheated entry length to settle the fluid after an abrupt area increase. Before the experiments commenced, it was postulated that the fluid may not heat up quickly enough from ambient temperature to saturation temperature in the channel itself. To

account for this possibility, a preheater was designed and described. Additionally, an unheated entry length is necessary to maintain the temperature of the fluid while it fully develops.

It was determined that depending on the selection of flow rate, the outlet temperature of the fluid would change as it passed through a preheater. A plot was generated (Figure 39) that compared the outlet fluid temperature with the Reynolds number, in order to ensure the fluid remained at an acceptable temperature while keeping the Reynolds number below the transition range (in a tube) of 2000, helping guide the selection of volumetric flow rate.

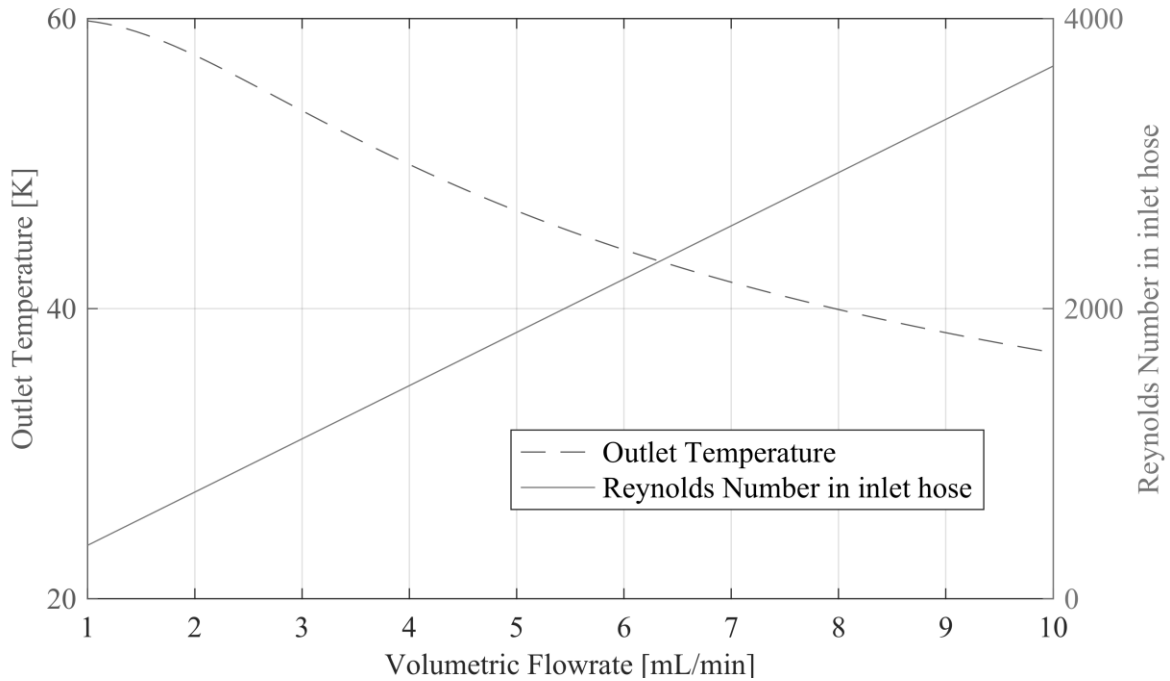


Figure 39: Outlet temperature and Reynolds number (in inlet tube) vs. volumetric flow rate in tube, for a 1ft long tube with a tube ID of 0.0065in. Assumed 20 °C inlet fluid passing through a copper tube immersed in 60°C water.

To generate these plots, the problem was set up as a heat transfer problem between a quiescent fluid bath surrounding a pipe containing a fluid with a prescribed mass flow rate (using techniques in [2]).

Several other studies utilize a fluid loop, in which fluid downstream of a heater is expelled into a reservoir, in which it is cooled, re-heated, and supplied again through an inlet [73][32][74]. In order to reduce complexity, and because only a relatively small quantity of HFE-7100 is used in each test, the flow system in these tests was operated in an open-loop configuration, with outlet fluid being collected, after which it could be discarded. A similar approach has been used in other EHD tests [75].

Because of the low (room) temperature of the fluid supply, and the need to avoid variations in the supply fluid temperature resulting from variation in the ambient temperature, it was necessary to incorporate a means of controlling the temperature of the fluid entering the channel. Depending on the inlet temperature of the fluid, it would take some time before the fluid reached a high enough superheat to initiate nucleate boiling while travelling along the heated length. The fluid inlet system was designed to allow the fluid to be heated to the saturation temperature prior to entry into the channel. To accomplish this, a fluid preheater was installed in order to raise the temperature of the fluid. The preheater consisted of a copper coil inserted in a beaker, a hot plate connected to an on-off PID controller, an Omega CN242-DC1-R2 [76]. This controller was used to set a water bath to a prescribed temperature. The controller allows the user to enter a temperature set point, and the controller displays the reading from a thermocouple being used to measure the controlled temperature. The PID controller automatically adjusts the power provided to the heater in order to keep the control thermocouple as close to the set temperature as possible. A 0.065” inner diameter copper tube is coiled through the water bath, which is placed directly downstream of the syringe pump. A thermocouple placed approximately 300 mm upstream of the channel inlet measures the fluid temperature entering the test section (i.e. the initial superheat). This system was designed to provide flexibility in performing experiments, and to ensure that bubbles were

generated in a consistent manner. Through preliminary testing, a preheat of 30°C was found to be adequate to allow boiling to begin as soon as the flow entered the heated channel. As will be discussed in Section 4.4, during testing it was observed that no preheat was necessary for the specific set of conditions used in these tests. With the fluid supplied at ambient temperature (22 °C), the applied heat flux and channel length were adequate for stable nucleate boiling to occur in the center of the channel (longitudinally).

In order to achieve consistent channel inlet conditions, a laminar flow with a well-developed velocity profile was desired. However, the design of the feed system led to a discontinuity in area between the supply tube and the square channel. Pak [77] discusses the case in which a small inlet expands suddenly into a larger channel, and how the length of the inlet must be carefully considered to allow for adequate flow development.

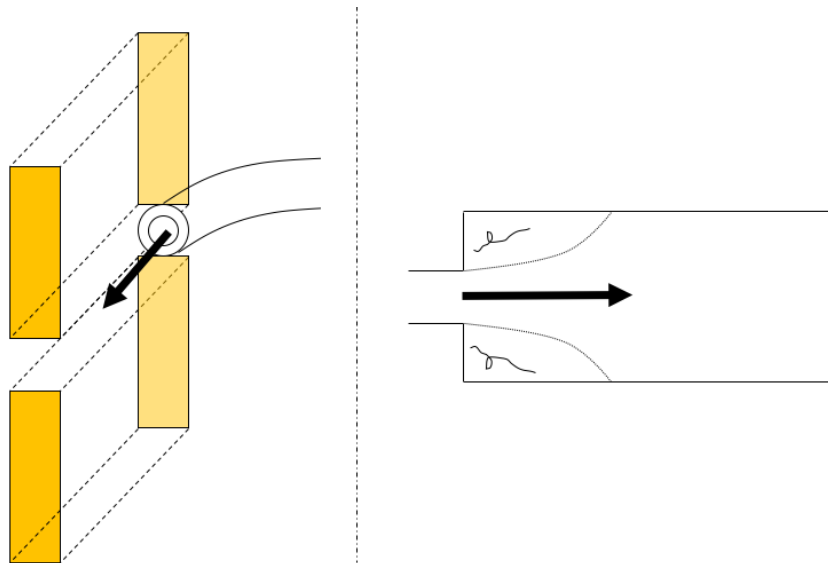


Figure 40: Sudden area expansion, leading to turbulent flow within a fluid channel. Left, an isometric view of the fluid inlet tube and flow direction into the channel. Right, a diagram of a sudden expansion as it would look in the channel.

Figure 40 illustrates how this could occur in the channel setup. Schetz [78] discusses sudden expansions, and experimental correlations developed from his experiments suggest a channel

length of greater than 7 step sizes downstream of the area change is necessary to justify neglecting the turbulent effects of a sudden expansion. Based on this previous work and the guidelines provided, a settling channel, or “entry length” was designed to insure laminar flow entering heated channel used for testing. The unheated entry length (UEL) was constructed with the same channel dimensions as the heated portion, which could be changed based on the dimensions of the channel being used. The UEL is a rectangular channel, long enough to allow the flow to develop a uniform, laminar velocity profile after passing through an upstream, abrupt expansion. The sudden expansion occurs due to the area discontinuity where the circular copper tubing connects to the rectangular channel. The UEL was also designed to insure a relatively low Reynolds number flow (on the order of 100-200 to achieve average flow velocities on the order of 1cm/s through the test section).

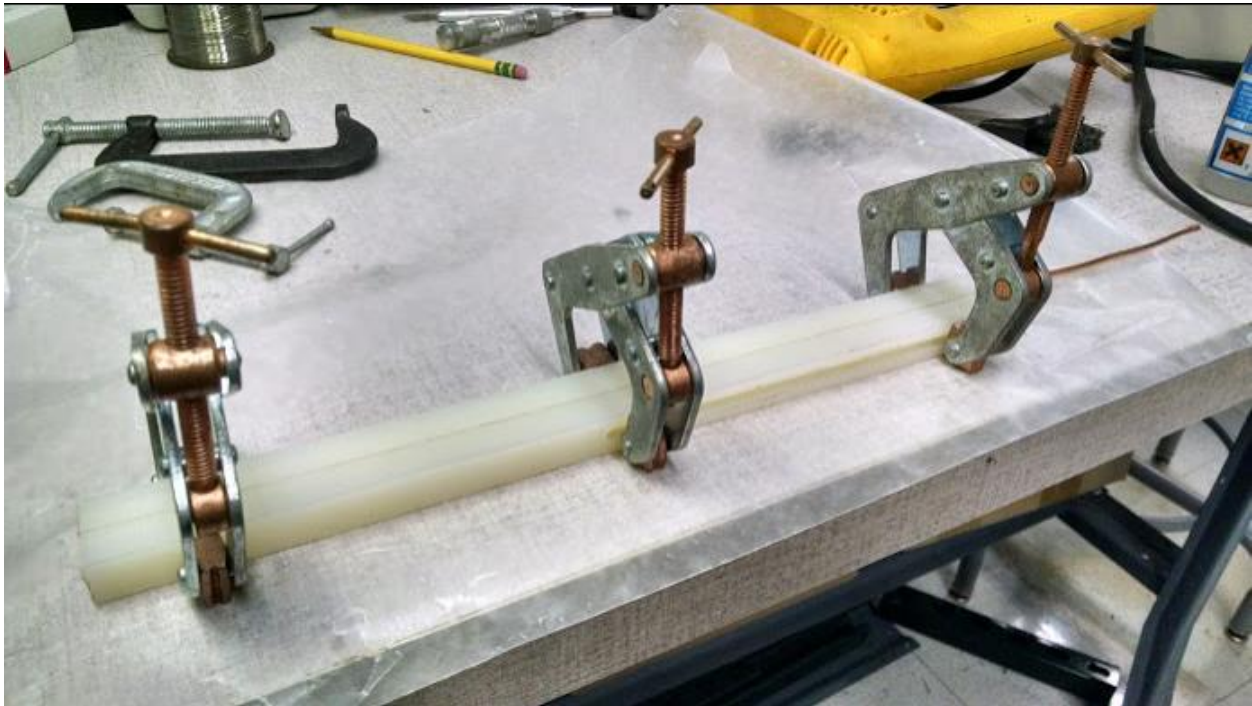


Figure 41: Unheated entry length construction.

This entry length was constructed by first milling a rectangular channel of the same dimensions as the heated portion into one  $\frac{1}{2}$ " by  $\frac{1}{2}$ " by 1ft piece of nylon stock (a material identified to be

compatible with HFE-7100 as well as having low thermal conductivity). Next, an identical, non-milled piece of nylon is attached to the milled piece (Figure 41). This is lined up with the heated channel, and secured with friction and stands (to counteract gravity pulling on the assembly during potting compound curing). Lastly, the potting compound cures to hold the entry length channel in place.

#### 4.2.6. Heating and Biasing System

This experimental apparatus required electrical biasing of the heated surface, as opposed to having a separate structure floated at a high potential, such as a wire or mesh embedded in the fluid. This required special care in the integration of the heater. Because of the high voltage (2 - 3 kV) applied to the heated electrode, the surrounding support structure, the cartridge heater, which is controlled by a VARIAC Type 3PN1010 transformer, as well as the thermocouple in the heated channel and its associated electronics, had to be isolated from the high voltage. For most of the components, this was accomplished by using electrically insulating materials. The potting compound is electrically insulating, meaning that the high potential is constrained to the bottom electrode. However, most electrically insulating materials would also retard heat transfer. Since the channel bottom (electrode) required heating to initiate nucleation, any connected heater would be ineffective in raising the temperature of the boiling surface enough to start the boiling process had it been isolated with an electrically insulating material. To resolve this, a thin sheet of aluminum nitride was used to electrically insulate the heating surface from the high potential while all allowing satisfactory heat conduction (Figure 43). Aluminum nitride features a dielectric strength of 17kV/mm [70], meaning that with expected potentials at a maximum of 3kV, a sheet of aluminum nitride approximately 170 $\mu$ m would be enough to insulate the connected electronic components. An aluminum nitride sheet of 380 $\mu$ m was used for this isolation. In addition to its



electrically insulating properties, aluminum nitride has good thermal conductivity, between 140-180 W/mK [70], on the order of standard aluminum alloy, a material known for good heat transfer characteristics. An 80 W cartridge heater, (1" long, ¼" Diameter, McMaster Carr) was used to provide heat to the bottom surface of the channel. Based on a heater input from an 80W heater at a VARIAC setting of 56%, the total flux from the heater is estimated to be 44.8 watts. Radiative losses are deemed to be negligible, and convective losses occur from the exposed parts of the copper. This includes the exposed part of the rectangular electrode (with a total area of approximately 23.4 cm<sup>2</sup>), and the area of the cylinder itself (estimated to be 10.1 cm<sup>2</sup>). Using a simplified convection equation, relating convection coefficient  $h$ , total surface area  $A$ , and temperature difference between a surface and quiescent air  $\Delta T$ , the total heat lost to convection is estimated from Equation 37.

$$\dot{Q} = hA(\Delta T) \quad (37)$$

Assuming a free convection coefficient of 10 W/m<sup>2</sup> K [2], and a temperature difference of 80 °C (if ambient temperature is 20 °C, and the temperature directly outside of the heater is 110°C) heat lost to convection is assumed to be 2.72 watts. This means that a total flux of approximately 116 kW/m<sup>2</sup> is transferred into the fluid. This is assumed to be uniform due to the high thermal conductivity of copper.

As shown in Figure 43, the cartridge heater connects to the heater surface via a reducing cylinder, with one end small enough to be inserted into a blind hole in the bottom of the heated channel electrode, and another wide enough to accommodate the heating element, which is inserted into another blind hole machined in the bottom of the reducing cylinder.

To incorporate the aluminum nitride electrical isolator, the copper reducing cylinder was cut horizontally, and the sheet of aluminum nitride was placed between the two halves. To ensure

good thermal contact between each half, a thermal paste (GE Electronics Thermal Grease [79]) was applied to each side of the aluminum nitride to facilitate heat transfer.



Figure 42: Copper reducing cylinder.

With a fluid flow rate of 4 ml/min, a cartridge heater temperature of 140°C corresponded to heated channel surface temperature of approximately 70°C, a data point used to assist in determining which cartridge heater temperature set points led to lower (i.e. closer to saturation temperature) wall temperatures. The cartridge heater temperature feedback is determined by the thermocouple placed directly above the copper enclosure, before the aluminum nitride sheet (Figure 43). The heater power is adjusted with a VARIAC, and set up with a temperature controller that can use a relay to switch the heater on and off to maintain a set point temperature. It was found that better control response was obtained with a VARIAC setting of 56% (with 120VAC in), which helped to avoid large temperature swings. To ensure good thermal contact, the thermocouple bead is

embedded in the layer of thermal paste, pressed firmly between the aluminum nitride sheet and the reducing cylinder.

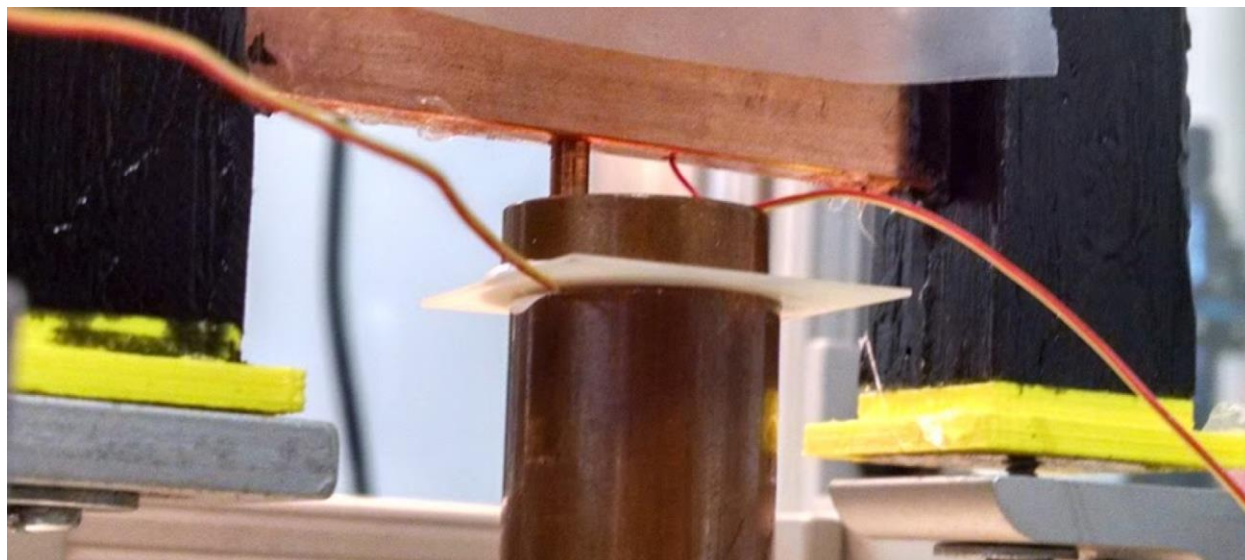


Figure 43: Thermocouple setup on reducing cylinder.

#### 4.2.7. Power Supply and DAQ System

Results from the modeling efforts presented in Chapter 3 suggest that potentials on the order of 3kV would be enough to deform the bubbles to a detectable extent. High potentials must be generated in a way that is safe, measurable, and repeatable. It was determined that a manually controlled power supply would preclude rapid set-point changes in potential while simultaneously monitoring other test conditions. In addition, a manually-controlled power supply would make it difficult to control the transient ramping characteristics (e.g. rise-rate) of applied potentials. It is also more difficult to accurately record the real-time voltage being applied to the device during a ramping event if the control was achieved through manual adjustment.

To meet these requirements, a computer-controlled power supply with a custom made user interface was utilized. This custom power supply unit, assembled from a previous project, consists of a rack-mounted case, utilizing a Spellman CZE30PN2000 power supply capable of generating

30kV at 300 $\mu$ A. This unit was attractive due to its remote programming and monitoring capability for voltage and current. The power supply is connected to a NI USDB-6008 DAQ controller to allow control via LabVIEW. Controls are integrated into a master LabVIEW monitor, giving the user the ability to control and monitor the potentials being applied the electrode. Past experience with high voltage, microfluidic systems suggested that arcing of the electrodes in the presence of very high voltage can be a problem. As a safety precaution, the LabVIEW control can limit the voltage applied to the system to an arbitrary value lower than the 30kV maximum. The power supply output was verified with a high voltage probe and a Fluke multimeter.

The dotted box in Figure 23 denotes the components that will also be at a high potential alongside the electrode. Due to the need for physical instrumentation links, the test setup required additional components to be electrically floated to high potential. To address this, an isolation amplifier is placed between the electrode and those components. The AMC1100 isolation transformer, as well as the TAC-80K thermocouple amplifier both are floated at high potential during testing. These components have a maximum potential limit, which will depend either on their technical specifications, or the initiation of a corona discharge somewhere in the circuitry (usually at sharp points). Given that the LabVIEW software (as described above) can provide an arbitrary safety limit, the limit must be chosen to prevent formation of a corona discharge, or one from exceeding the maximum allowable voltage differential for the isolation amplifier. A limit of 4kV was imposed on the system, due to the limits of the isolation amplifier (which has a transient maximum of just above 4kV), and the observation of damaging discharge occurring at above 4kV.

A data acquisition (DAQ) system was used to monitor and collect data. The inclusion of a DAQ card for was required in order to allow for a rapid, automatic measurement of temperature and voltage data. In many applications, isolated voltage measurements can be manually recorded using

a digital voltmeter that floats at the potential of the measured component [80]. In this study, data is measured over a period on the order of 1 second, making manual temperature measurements impractical. The dangers of an electrode at a high potential to the heating element also apply to any sensors on the electrode. Attaching a thermocouple to the high potential electrode leads required isolation of the signal to protect the computer, which cannot float at the high potentials of the electrode.

Isolation amplifiers were used to safely monitor the temperature transducer signal by isolating the DAQ system from the high potential [81]. Other solutions considered included coil transformers and optical isolation techniques, but these are typically rated for voltages too low for this study, or have are prohibitively expensive, respectively. The AMC1100 isolation amplifier [82] was chosen due to its low cost, precision, and simplicity. Isolation amplifiers are rated with both working voltages and transient on-times and peak voltages. The AMC1100 itself is a small integrated circuit (IC), requiring further design to implement it into a usable device. The isolation amplifier was mounted on a circuit board within an enclosure to facilitate connections. The enclosure with the AMC1100 installed is shown in Figure 44. The device utilizes a plastic project enclosure, with holes drilled on either end to accept a high-potential voltage input. The signal data passes through the IC in the middle (shown on a PCB with required resistors), and then is routed to a low-potential output.

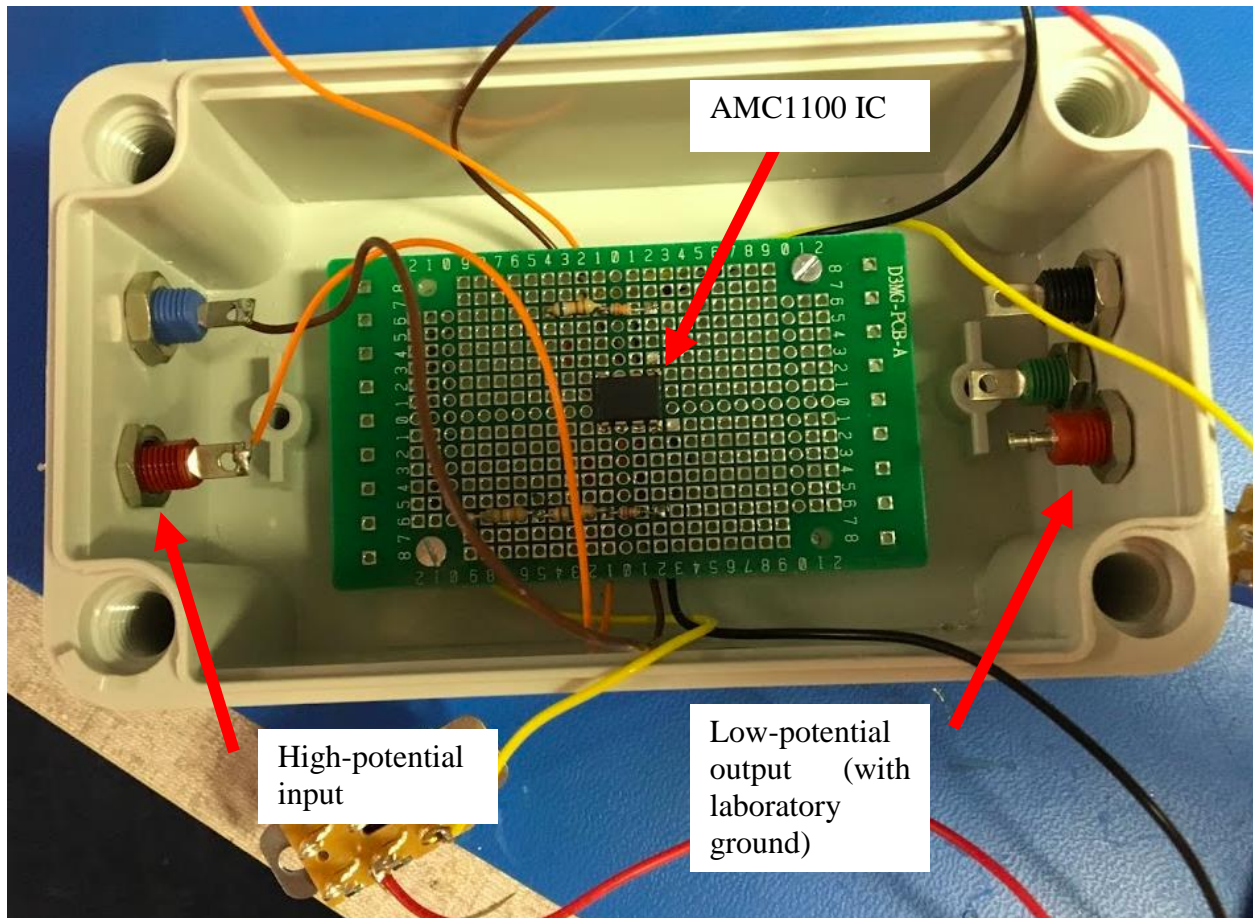


Figure 44: AMC1100 Isolation Device construction, showing the high potential input, Isolation amplifier, and low potential output.

While its working voltage is specified at 1200V, the AMC1100 has a maximum isolation voltage rating of 4250V. For this study, the duration of high potentials (i.e. considered anything above 1000 V) never exceeded the 60s transient on-time that the maximum isolation voltage specifies. The  $\pm 250\text{mV}$  input voltage range allows for data acquisition from a thermocouple amplifier calibrated to  $1^\circ\text{C}/\text{mV}$ , with an acceptable error. Of particular concern was powering the isolation amplifier, which requires a power source on both halves of the chip (high-potential side, and low-potential side). On the isolated, low-potential end, it would be possible to power the device with an external power supply, but using a lab power supply on the high-potential end would require additional isolation, as the power supply would itself have to float at a high potential. The

AMC1100 requires between 4.5 and 5.5 volts on the high-side, and 2.7 and 5.5 volts on the low-side. Based on the relatively low voltage requirements of the chip, the isolation amplifier (both high and low sides) can be powered from 9V batteries with voltage reduced by a splitter, as shown on diagrams in (Appendix A, also shown: voltage divider calculations). Using batteries eliminated the need for additional isolation of laboratory power supplies.

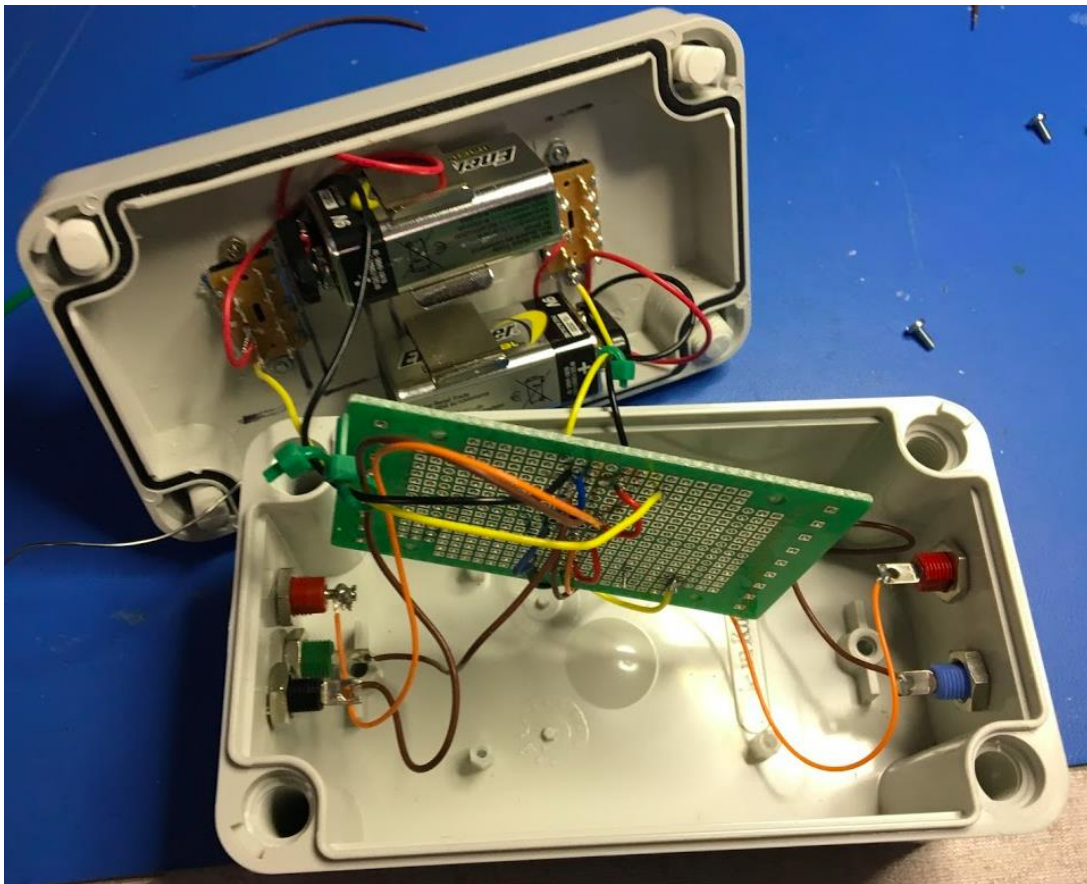


Figure 45: AMC1100 Isolation Device construction, including two separate batteries (for high- and low- potential chip sides).

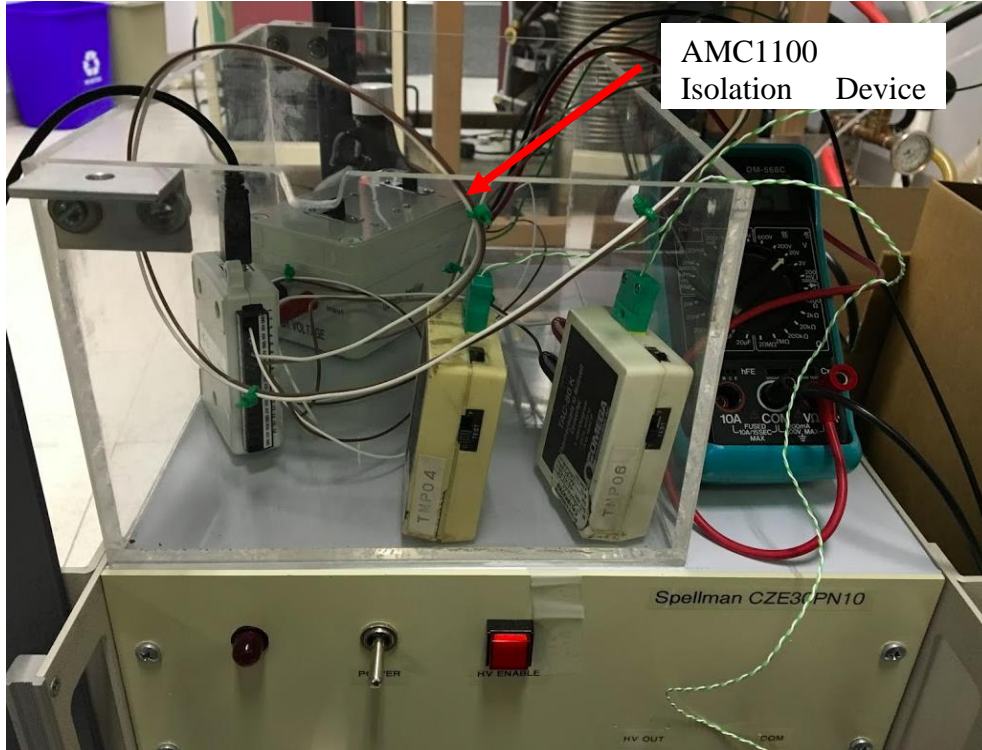


Figure 46: AMC1100 Isolation Device (box) shown in a protective Plexiglas container, alongside other components shown in Fig. 44 expected to float at high potential.

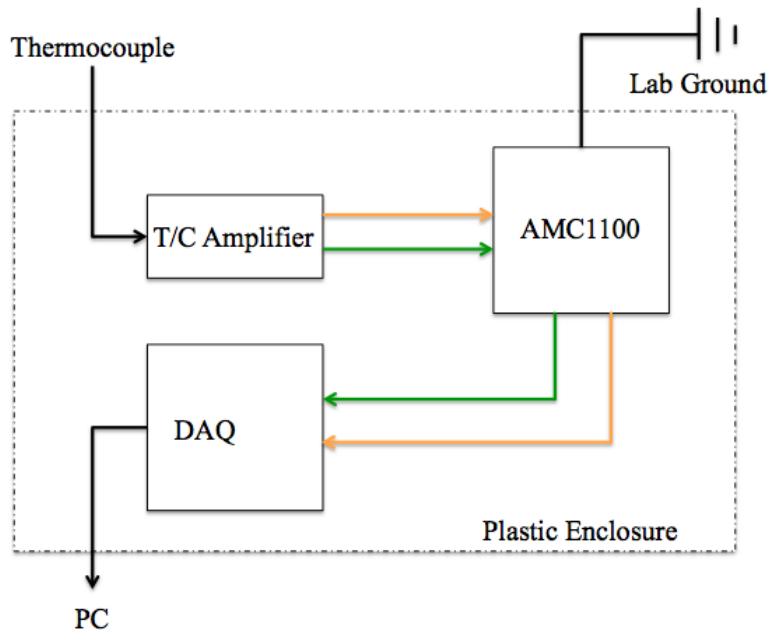


Figure 47: Data isolation system diagram.



The data isolation system was set up according to the diagram in Figure 38. Connected to the “common” node inside the AMC1100 device is a connection to the laboratory ground, to protect the downstream components in the event of an electrical short or device failure. The physical arrangement of the entire data isolation system is shown in Figure 46. The device, alongside other components on the high-potential side, is kept in an insulated (Plexiglass) enclosure for safety.

Lastly, the AMC1100 Isolation device was designed to prevent potential corona discharge on sharp elements in the box, such as wire ends or chip leads. To achieve this, Performix Liquid Electrical Tape was spread over these sharp points. This can be seen below in Figure 48.

The thermocouple amplifiers are Omega TAC-80K devices calibrated to a resolution of  $1^{\circ}\text{C}/\text{mV}$  (and verified through calibration with boiling water and ice). The amplifiers are required to condition or amplify the (microvolt) raw signal from a Type-K thermocouple, to a level that meets the input specifications of the DAQ. Under ideal circumstances, these thermocouple amplifiers would be installed “behind” the isolation amplifier (i.e. they would not be subject to high potential), in order to be protected from high voltages. However, the output noise of the AMC1100 is rated at  $3.1 \text{ mV}_{\text{rms}}$ . For the temperature range of interest ( $20\text{-}80^{\circ}\text{C}$ ), a Type K thermocouple has an output of  $0.2\text{-}4\text{mV}$ . With a specified amplifier gain of 8, the expected output for these temperatures from the AMC1100 would range from  $1.6\text{-}32\text{mV}$ , with each degree difference

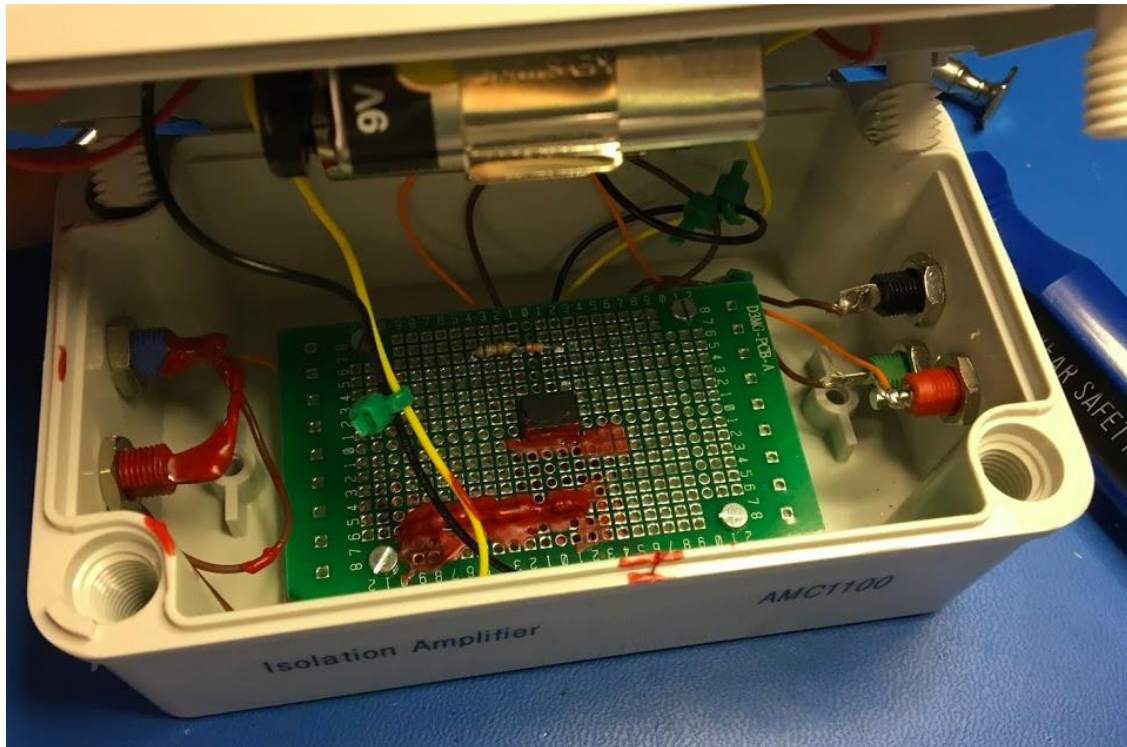


Figure 48: Liquid Electrical Tape spread over possible corona discharge prone locations (wire ends, sharp points, etc.). Not shown is the underside of the PCB, which is also protected with liquid electrical tape.

corresponding to approximately  $500 \mu\text{V}$ , below the noise threshold of the AMC1100, leading to inaccurate temperature measurements. Amplifying the signal before isolation means that each degree difference is on the order of  $8\text{mV}$ , higher than the noise threshold. When coupled with the isolation amplifier, the output must be calibrated to ensure accuracy. The calibration curve is shown in Figure 49, and incorporated into the LabVIEW VI, by modifying voltage input according to the curve. The fluid inlet temperature amplifier was factory calibrated to  $1\text{mV}/^\circ\text{C}$ , but the inclusion of the isolation amplifier in addition to the thermocouple amplifier connected to the copper electrode introduces the possibility of additional uncertainty or offset to the factory calibration. Utilizing boiling water and an ice bath, the new calibration curve for the entire system was determined by collecting temperature data from an ice bath three times, and comparing each voltage measurement to a known quality (from a handheld Fluke thermometer using the same

thermocouple). Next, the procedure is repeated using boiling water. Each of the three runs for each are averaged with each other, and compared to the “known quantity” voltage found from the Fluke.

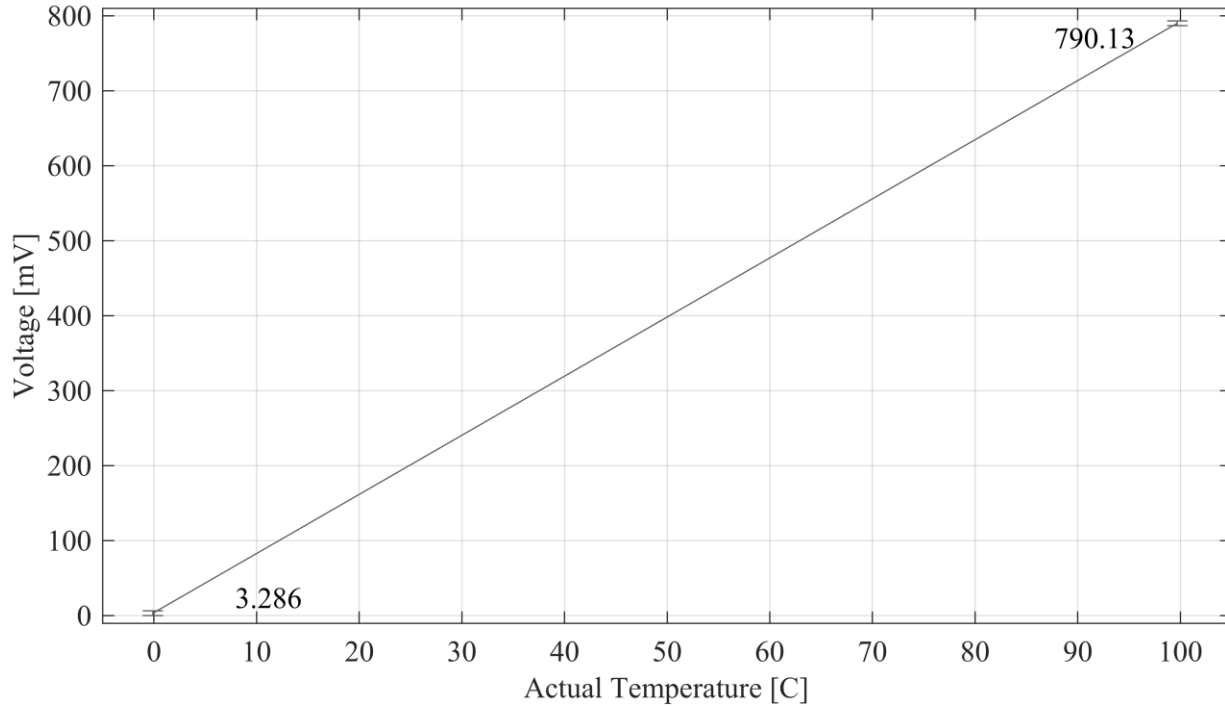


Figure 49: Thermocouple amplifier calibration curve.

Additionally, the two averages each had a standard deviation of 6.5mV, which is less than 1C when accounting for the gain. The error bars are too small to observe on the above graph. Interpretation of results requires the quick and accurate acquisition of test conditions such as temperature.

Thermocouple placement must accurately capture the temperature of the heated copper surface without affecting the boiling in the channel or the velocity profile of the cross flow. While capturing the exact temperature of the surface would be ideal, it is difficult to accomplish without influencing the boiling in the channel. Placing a thermocouple outside of the channel itself is

necessary for data acquisition. A thermocouple placed on the edge of the copper surface would be



Figure 50: Channel Mounting Apparatus.

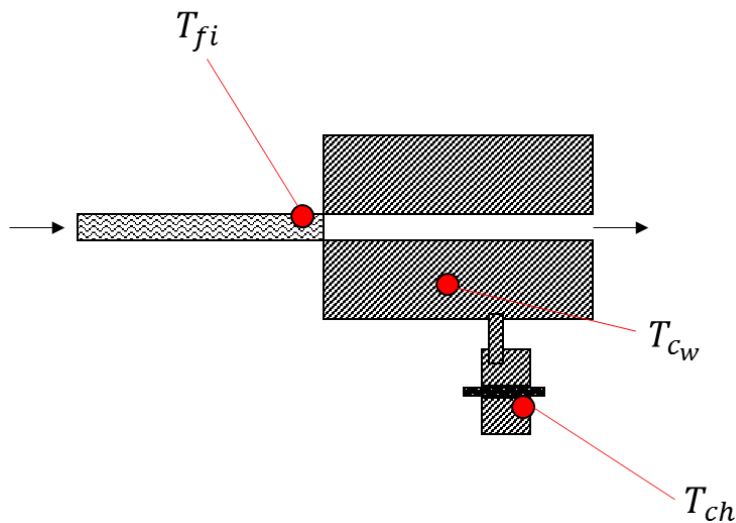


Figure 51: Thermocouple Placement.

affected by convection and ambient temperature. The bottom copper electrode is assumed to be isothermal, so that a thermocouple placed in a hole in the inside will be enough to characterize the relative temperature at the boiling wall. Thermocouple placement is shown in Figure 51.

#### 4.2.8. Imaging System

An imaging system was required in order to capture bubble behavior with sufficient spatial and temporal resolution to allow for quantitative analysis. Being able to resolve the evolution of the nucleating bubbles required use of a camera with a relatively high frame-rate. A typical, standard camera (e.g. Panasonic Lumix GF3) has a frame rate ranging from 30-60fps, corresponding to 33-17ms per each frame of video. With time between bubble detachment from a single site on the order of 100ms, a standard camera would be inadequate to capture detachment events or bubble deformation. A high-speed camera was therefore required. The camera used was an Edgertronic SC1, a portable, professional grade high-speed camera. The Edgertronic features a frame rate of up to 17,791 fps, dependent on the resolution of the camera and background lighting conditions. Typically, a resolution of approximately 900x400 pixels corresponds to a frame rate of 1500fps. With an expected bubble detachment on the order of 100ms, this frame rate provided adequate temporal resolution to visualize bubble detachment and growth, as well as a spatial resolution high enough for post-processing [83]. The Edgertronic uses a standard Nikon F-mount lens, so an F-mount to C-mount adapter was utilized to pair the camera with a Meiji UNIMAC Macrozoom with a magnification range of 0.7 to 4.5. The working distance of the lens is 94mm, and the depth of field ranges from 0.82 to 0.12mm. Integral to the visualization of bubble detachment is the lighting during the experiment. In order to maintain a fast shutter speed (corresponding to a high video frame rate) adequate illumination is necessary to achieve a satisfactory balance between shutter speed, ISO, and aperture. Together, these three settings are referred to as the “exposure triangle”, due to their dependence on one another. An increase in the shutter speed of the camera means less exposure time on the sensor, requiring a wider aperture for more light. The microscope lens used governs the aperture size, so any increases in shutter speed must come with an accompanying

increase in ISO, or an external light source. Increasing ISO can introduce more noise into the system, so increasing external lighting is the best way to achieve a fast shutter speed. Three light sources were used: A ring light (Stocker Yale Model 20), an overhead light in the fume hood used for the tests, and a standard fluorescent desk light. Additionally, the camera was positioned at an angle approximately 15 degrees raised above the parallel to the ground. This is done to reflect more light back into the camera from the bottom of the copper electrode, and to more easily bring bubbles of interest into focus, due to the lenses' narrow depth of field.

Images from the high-speed camera were used to collect quantitative and qualitative data.

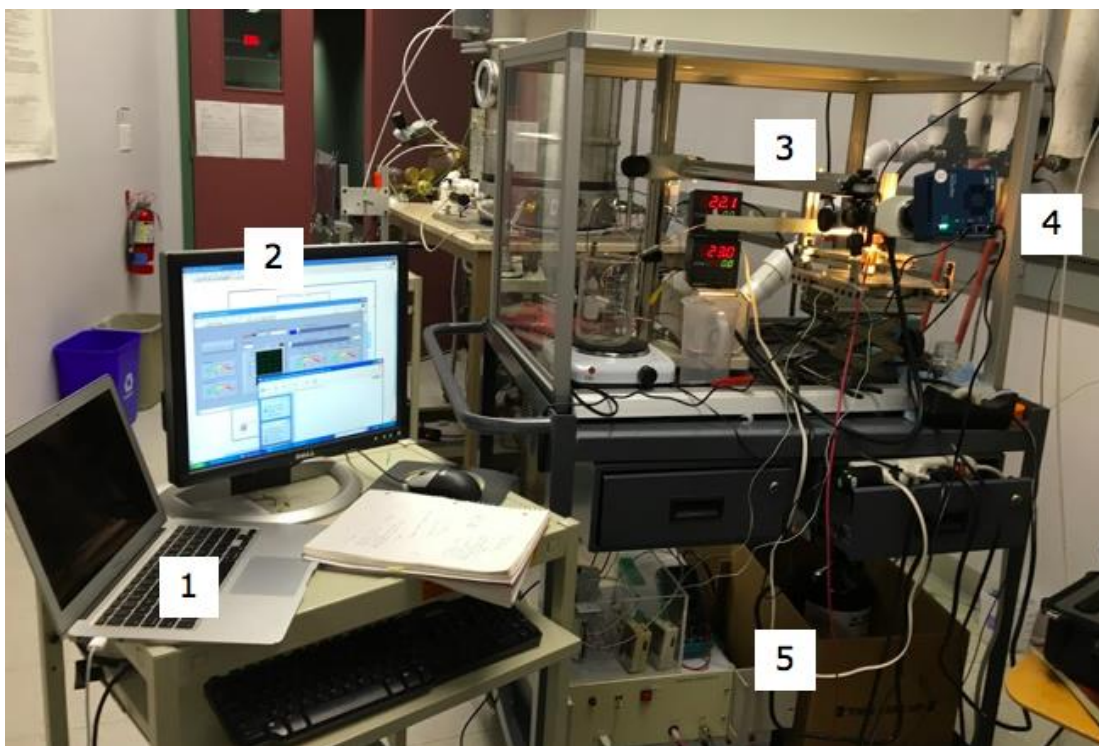


Figure 52: Final Lab Setup (1: Image capture computer 2: data collection computer 3: fume hood and test setup 4: high-speed camera 5: high voltage power supply).

Quantitative data was extracted from image analysis of the video files. MATLAB's Image Processing toolbox was used to post-process the resulting videos. MATLAB allows for custom scripting in order to calculate estimated bubble volume, radius, detachment frequency, and shape.

The final laboratory setup is shown in Figure 52. Item 1 is the image collection computer, connected to the high-speed camera via a direct Ethernet connection. Item 2 is the data collection computer, connected to the DAQ and thermocouples, and the controlling computer for the power supply. Item 3 is the channel support structure. Item 4 is the high speed camera, and item 5 is the power supply, thermocouple amplifier, and isolation amplifier. All items are contained under a fume hood, in an air conditioned laboratory.

### 4.3. Methodology

As described in Section 1.3, the objectives of this work were to investigate the possible enhancement of nucleate boiling subject to EHD effects. Of particular importance is the effect of electric fields on nucleation site density (i.e. the number of active nucleation sites on the electrode), size and position in the channel of bubbles that have separated, nucleating bubble shape and evolution prior to separation, bubble departure frequency and size at departure. The possibility of influencing, if not controlling, bubbles may lead to the delay of the onset of critical heat flux in a minichannel. Misale [22] defines the onset of the critical heat flux as the point at which increases in a controlled heat flux leads to noticeable rises in a surface temperature.

The tests presented followed a similar overall procedure. To investigate the effect that a non-uniform electric field has on the detachment of bubbles, it was necessary to first achieve steady state boiling in the channel, with a modest cross flow applied. With a uniform temperature along the copper channel bottom, a steady stream of bubbles is expected to flow out of the channel and out of the apparatus. In any particular test, bubble detachment is observed for a period of a few seconds. When the electric field is applied, bubble detachment is observed again for a few seconds. Within the scope of this study, the variables changed between studies were electric potential, polarity, and the time in which a potential was applied. Once the thermocouple and power supply

data signals have been calibrated as discussed in Section 4.2.6, the methodology for a specific test is as follows:

1. Physical Setup of Experimental Apparatus

First, the channel with the desired height to be used was identified and installed into the test apparatus. The potting compound incorporated metal standoffs (isolated from the high potential) that facilitated attachment to the test stand (Figure 53). With the channel in place, the inlet copper connection of the unheated entry length was connected to the outlet of the fluid pre-heater assembly, via Swagelok connections (which were pre-torqued prior to installation), shown in Figure 54. These connections (compression fittings) ensure no fluid leaking occurs.

2. Setting of Desired Control Test Conditions (per case)

With the physical setup complete, the test conditions need to be set. The controller temperature for the bottom electrode heating element is set, as well as the controller temperature for the fluid pre-heater prior to the unheated entry length. Unlike pumped-fluid systems, the syringe pump requires some fluid priming in order to obtain uniform flow in the visualization portion of the channel. Priming is complete when fluid flows through the outlet steadily, and no vapor or air bubbles are observed in the channel. Once the flow rate is set, the channel is monitored to ensure that there are no air bubbles in the channel (due to the channel being void of any fluid between runs) before any heating is applied or tests started.



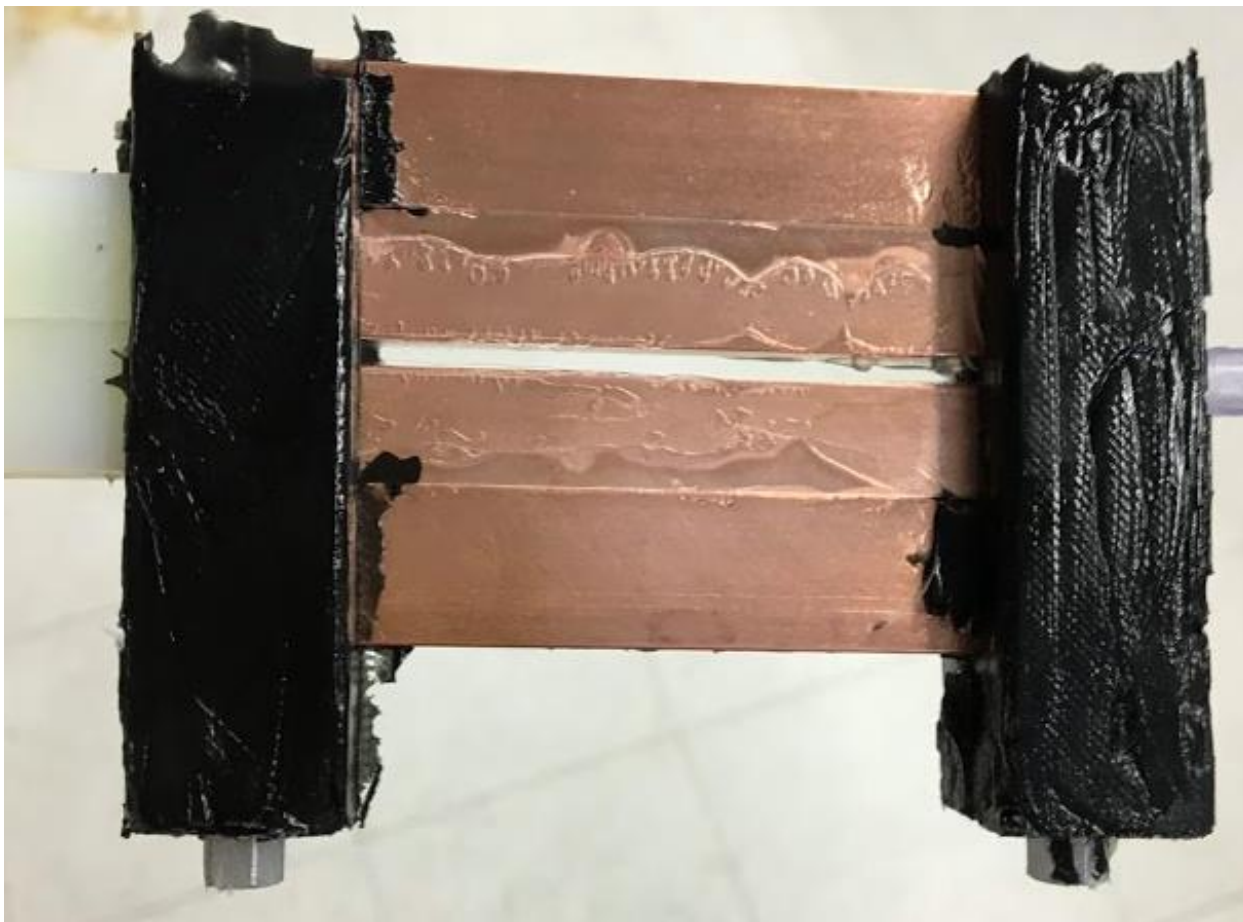


Figure 53: Channel section of apparatus showing metal support standoffs embedded in potting compound (protruding from bottom of each post).

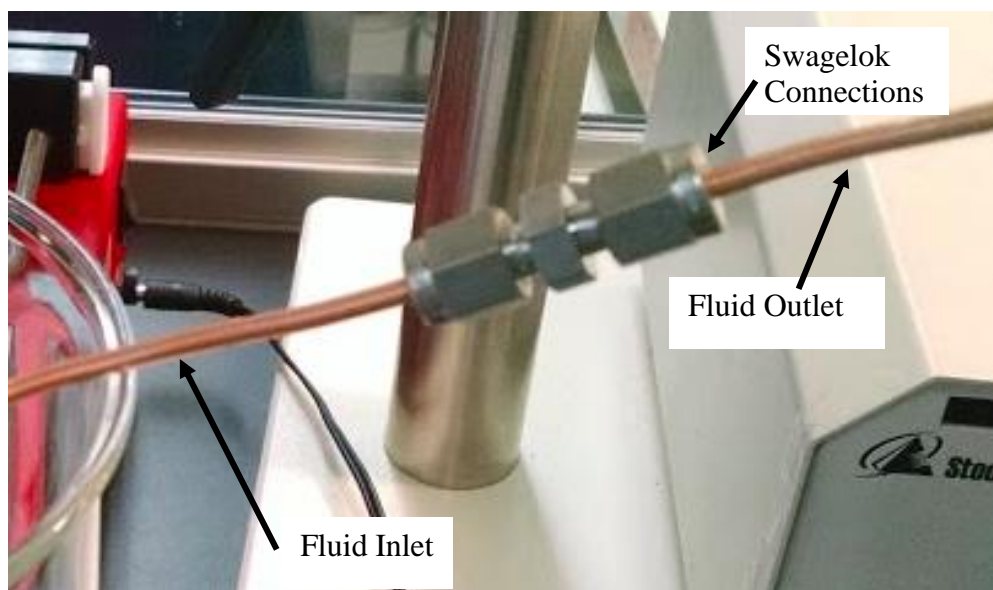


Figure 54: Fluid Connections between syringe pump and fluid preheater.

### 3. Initial camera focusing

The high-speed camera requires careful setup to ensure clear imaging of bubbles in the channel. While ideal camera placement would be such that the lens is completely perpendicular to the channel walls, this is unworkable in practice. Any lens that has a relatively large zoom (i.e. longer focal length, such as those like the microscope lens used here), must also have an aperture fast (large) enough to receive sufficient light for an acceptable image. This results in a narrow depth of field for the image, which is large enough to bring the entire diameter of a nucleation site area into focus (greater than 1mm), but not large enough to encompass the entire thickness of the channel (4.76 mm). Functionally, only the extreme edges of the channel were still blurred. While this was acceptable for visualization, it made bringing the camera into focus difficult. Due to the small depth of field of the camera and microscope lens combination, it would be impossible to focus on any single region of interest on the bottom electrode without knowing where bubbles nucleate first, especially given the effect of refraction. Figure 55 illustrates the refractive issue when imaging through a fluid medium [84]. With the channel evacuated of fluid, the camera would have its field of view distorted by the glass pane (as shown by the solid arrow inside the channel). While focusing the camera to account for this would be possible, the addition of fluid would distort field of view in a different manner (shown by the dotted arrow), requiring further focus adjustment. Additionally, with the microscope lens characterized by a very narrow depth of field, it can be more difficult to achieve satisfactory focus even with the bubble locations known. This can be beneficial as the blurring of the foreground and background (relative to bubbles) makes subsequent image analysis easier.

### 4. Channel Priming and Camera Refocusing

Depending on the conditions in the channel, obtaining focus on a particular region of interest may be difficult. The test procedure is designed to account for these differences. During experiments, the camera is typically focused with an empty channel to ensure that the visualization area is correct. Next, the channel is primed with fluid by turning the syringe pump on and waiting for the channel to fill, as well as waiting for all bubbles to clear from the channel. With fluid flowing through the channel during this priming phase, the camera is then again re-focused to ensure that the center is within focus (where a majority of bubbles are expected to form). During this time, the copper electrode is reaching a steady state temperature with heat applied. Boiling will begin to occur once the wall temperature reaches the saturation temperature.

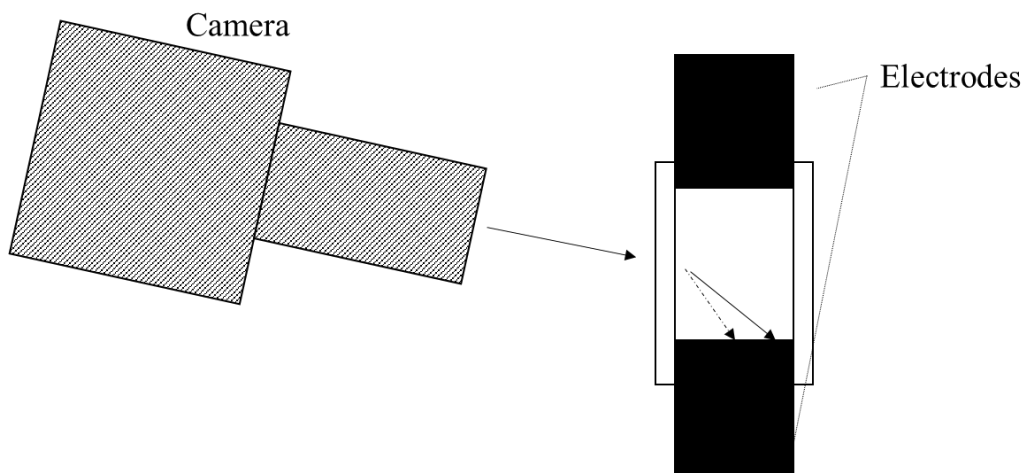


Figure 55: Effect of refraction through fluid on focusing point in channel.

## 5. Data Capture Setup

Once a steady state has been reached with respect to the electrode temperature, data capture system is initiated. The LabVIEW interface allow for customization of the data export filenames, to facilitate association of the numerous files with the corresponding high speed videos in post-processing. The nucleation site being visualized is recorded (based on the numbering scheme assigned to each site, described in Figure 33), as well as the channel height. Site numbers are

counted up sequentially from the channel inlet. Additionally, the “record time” (i.e. timestamp of the data collection initiation) is recorded in the LabVIEW data file. This study is based on achieving clear visuals of bubbles, and the primary motivation of utilizing a LabVIEW data capture system is to record what test conditions correspond with each high-speed video in as accurate a manner as possible. The “record time,” of which is part of the data file, is set to match the exact recording time of the high speed camera. This means that at every time step of the high-speed video, the corresponding fluid inlet temperature, wall temperature, and electric potential can be determined. The LabVIEW VI is shown in Figure 56.

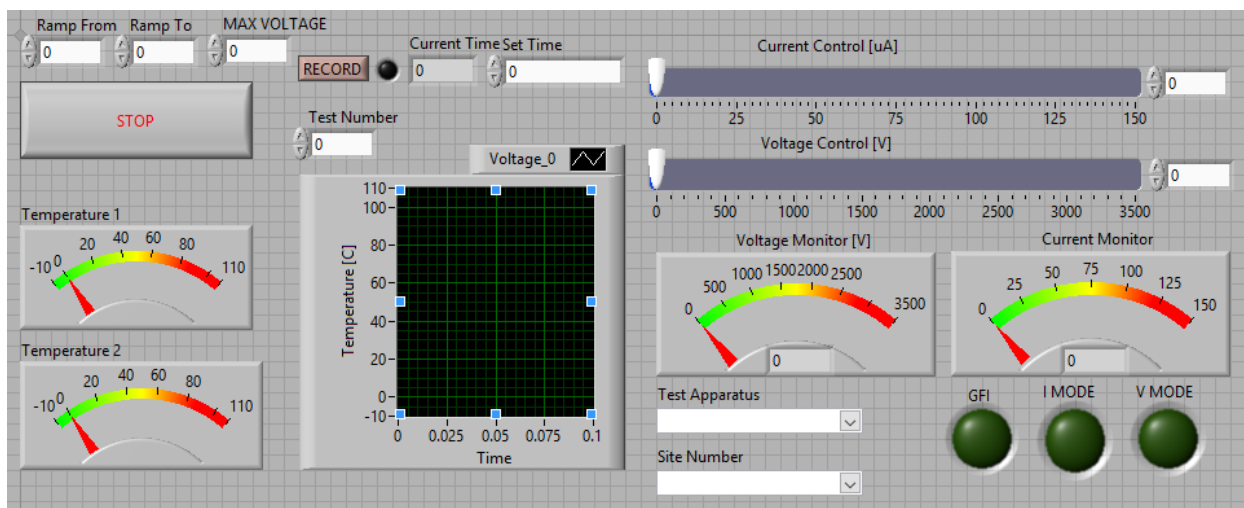


Figure 56: LabVIEW virtual instrument (VI).

On this virtual control panel, the display labeled “Temperature 1” and “Temperature 2” monitor the heated (channel bottom) electrode temperature and inlet fluid temperature (if applicable). The “Voltage\_0” display is a graphical representation of the last 100ms of temperature data from the thermocouples. At the onset of the study, voltages were controlled manually using the slider controls in the upper right portion of the VI. However as described earlier, it was determined that a more controllable method of raising the potential in the system was necessary to isolate some effects that were being seen in bubble behavior. To this end, the LabVIEW VI was modified in

order to allow for input of a maximum potential, a “start” and “end’-of-ramping time (seen in the upper left corner of Figure 56). Since the LabVIEW VI was already set up with a timer to record the current time during a test, a LabVIEW script was created to automatically control the input of the power supply sub-VI. Depending on the time of recording, the applied voltage can change. Before the time when the voltage ramping is to begin, the “ramp from” time ( $R_f$ ), the voltage applied is zero, to record the baseline bubble behavior with no potential applied to the channel. If the current time ( $t_c$ ) is greater than  $R_f$ , but less than the “ramp to” time ( $R_t$ ), the applied voltage will be a linear function of current time  $t_c$ . If the current time is greater than both  $R_t$  and  $R_f$ , the applied voltage will be that of the specified maximum,  $V_o$ . This logic can be seen in Figure 57.

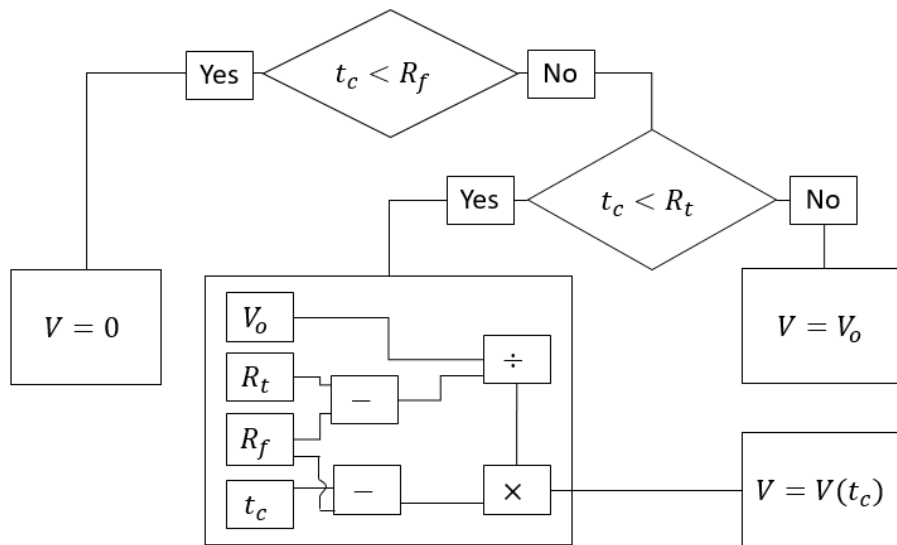


Figure 57: LabVIEW timer logic used to control voltage ramping.

The control to initiate recording of the data is located above the graphical temperature display on the VI. The “Test Number” control is used to assign a unique number to each file and ensures that output files are distinct and do not over-write old outputs. The “Set Time” control governs how long the program should capture data for, while the “Current time” display serves as feedback to the user about how long the process has been running (displaying current time  $t_c$ ). Upon the

selection of the “record” button, the VI automatically records temperature, potential, and current data, and saves to a comma delimited file. Current data may be used to examine the isolation characteristics of the fluid, as well as any changes that occur with the application of an electric field. The filename contains information identifying the current date (automatic), which test

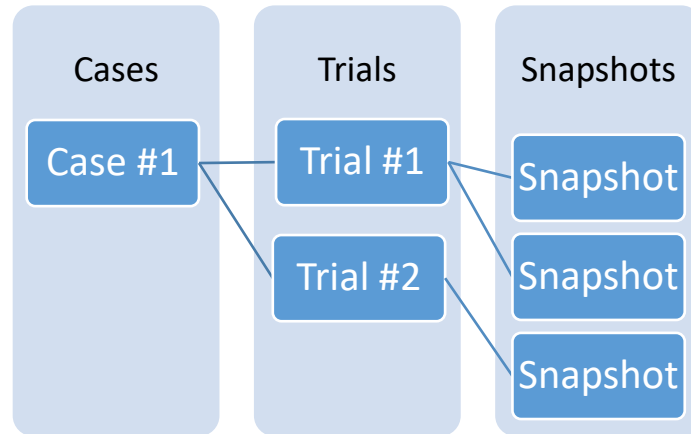


Figure 58: Testing hierarchy used to identify specific tests.

apparatus is used (if applicable), the artificial nucleation site as visualized by the high-speed camera, and the test number. On the right side of the VI are the controls for the power supply, which is controlled by a sub-VI, created as part of an earlier project. The complete block diagram of the VI is provided in Appendix 8.1.3. Once a test is over, if a new test is to be performed with the channel already heated and the pump primed, then steps 3-5 are repeated using the new test conditions.

#### 4.3.1. Image Analysis

After tests are completed, video files and data files are examined for qualitative data. Qualitative data is useful for developing generalizations on bubble behavior in the channel, and can help support certain conclusions. However, quantitative data is necessary to support certain findings, such as the effect of EHD on nucleation site density, bubble size, and bubble departure frequency. The primary vehicle for data collection was high-speed video, which is difficult to analyze without specific tools. MATLAB (with the Image Processing Toolbox) is utilized to

perform image analysis on the resulting video files. In this section, the nomenclature used for identifying and labeling specific tests is laid out. The notational hierarchy is shown Figure 58.

The series of tests performed are broken down into Cases, Trials, and Snapshots. At the most basic level, a snapshot is a moment in time of a given trial. A trial consisted of multiple attempts within the conditions of a given Case. Different sets of trials, corresponding to different sets of controlled parameters is are referred to as Cases. In this study, within a given Case, the enabled potential voltage (i.e. the “on” potential), the polarity, and the rate at which a potential is enabled are purposefully varied. The Cases comprise a specific set of polarities and applied potentials. The conditions measured (fluid inlet temperature, heater set point, and channel geometry) remain the same between all Cases. Within every trial, the EHD state (“on” or “off”) will be specified. A

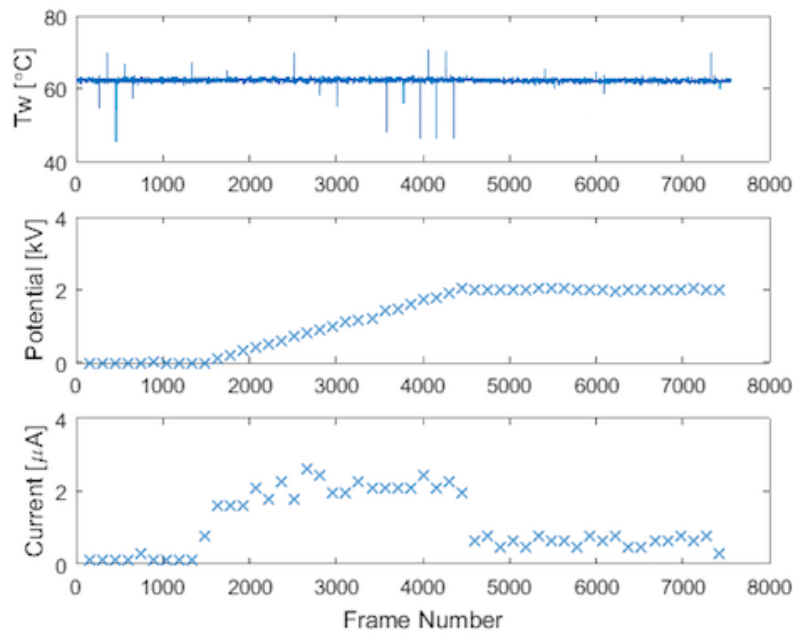


Figure 59: Data collected during a typical trial. Wall temperature of the bottom electrode (top), channel bias potential (middle), current (lower).

numbering scheme is identified to easily identify the trial being studied. From the onset of the test, trials were numbered sequentially (starting from Trial#1), regardless of their test conditions. After

an initial period of debugging trials, a series of cases were identified (starting from Case#1), serving as groupings of trials that share the same test conditions.

Because of the inherent variation in the behavior of any single bubble, a statistical approach was used in conjunction with the image analysis. The relative size of the channel leads to many bubbles in the field of view, many of which can be blocked by large vapor slugs. With a statistical approach, bubble characteristics can be characterized with statistical distributions which better allow for uncertainty analysis. Additionally, the limitations of the imaging equipment mean that only a portion of the channel can be captured during a trial, further necessitating statistical analysis.

Within the Edgetronic software, the video capture resolution can be defined. In this study, 992 x 400 pixels gave the best balance between clarity, maximum allowable frame rate, and saved image size. Given a scale of 100 pixels per mm, this corresponds to a capture area of 9.92 x 4 mm. This comprises the visible area on which image analysis is conducted. The visible area is defined as the width of the entire visible channel, right of the artificial nucleation site, as deep into the channel as visualization allowed. This area is calculated to be a rectangular patch, with an area of 47.2 mm<sup>2</sup> on the bottom electrode.

Several methods are developed to process data for critical areas. Bubble nucleation site density, departure frequency, and size are all important characteristics to be studied. The approach taken is one of mainly manual identification of bubbles or site of interest, with automation used to speed up data analysis. To prepare a video file for post-processing, it is first loaded into MATLAB. A MATLAB script can break up a video file into individual frames, and save each as a .jpg file. Due to the extremely large sizes of these file collections (thousands of photos and hundreds of megabytes), future MATLAB scripts should extract specific portions of these files into temporary directories for speed



The script to assist in calculating nucleation site density is shown in Appendix 8.3.1. To calculate nucleation site density, a range of frames in which to analyze video is determined. Typically, this corresponds to the frames in which EHD is on or off, excluding any transition period, as determined by the saved data files from LabVIEW. An example of this is shown in Figure 59. Frames F#0 to F#1500 would serve as the range where EHD is off, while frames from F#1500 to F#4300 are discarded as they are during a transition period.

Frames from F#5000 to F#6500 are included so that there are an approximately equal number of frames with and without EHD. With each range specified, a temporal resolution is also specified to keep user input to a minimum. This discretizes the range of frames into a certain number of discrete points in which bubbles will be counted. With frames ready to be analyzed, the script walks the user through the process. Each snapshot (as determined by the temporal resolution setting) is inspected and the number of currently visible nucleating bubbles are counted. The values presented are a count of nucleation sites, where a density can be inferred by using the visualization area (defined earlier in this section as  $47.2 \text{ mm}^2$ ).

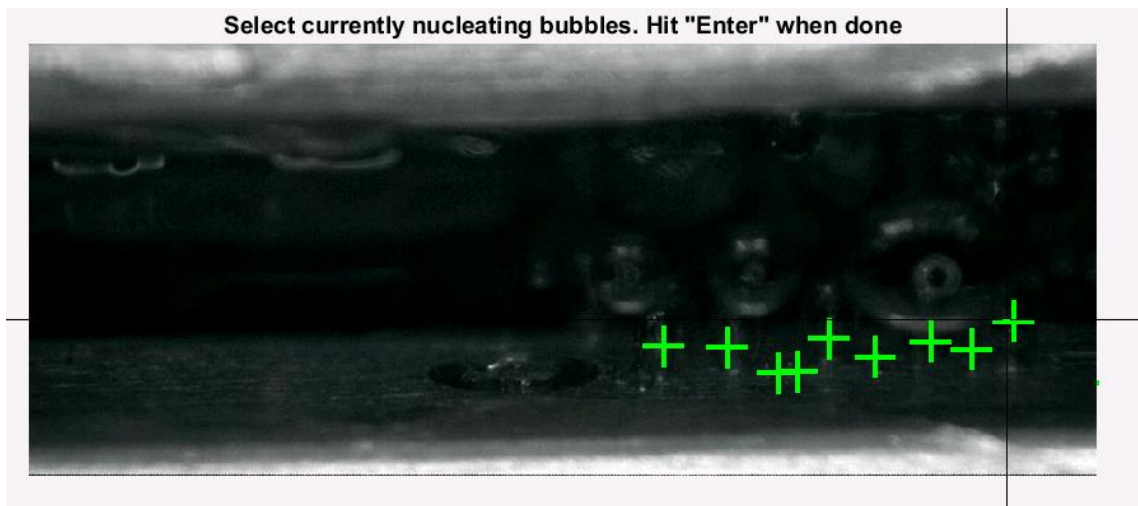


Figure 60: Selecting nucleating bubbles within a custom MATLAB GUI. Green marks denote selected bubbles.

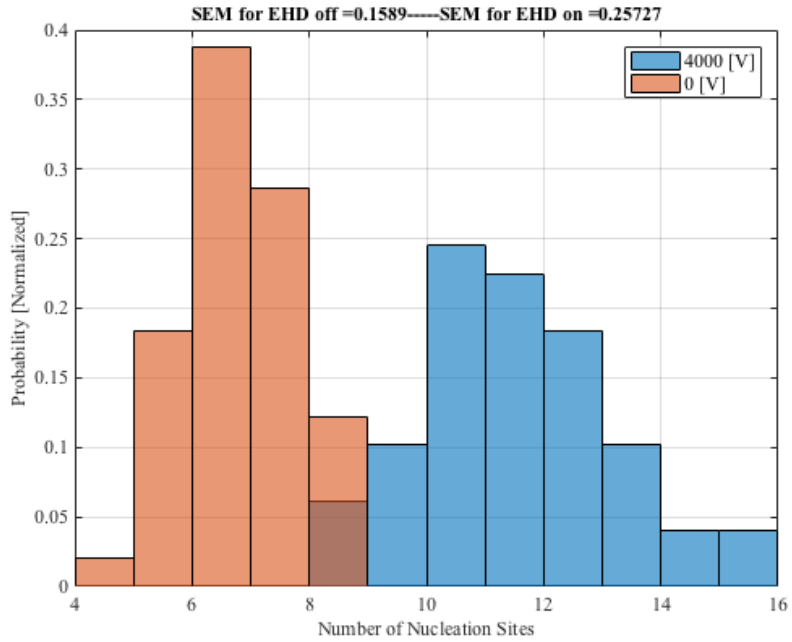


Figure 61: Example of statistical nucleation site density.

A nucleating bubble is defined as a bubble which is still attached to the bottom electrode, regardless of size, and growing. Bubbles are selected by clicking, and a counter is also placed to ensure that bubbles aren't counted twice. This interface is shown in Figure 60. Once all bubbles are selected in a given snapshot, the script automatically loads the next snapshot, and the process

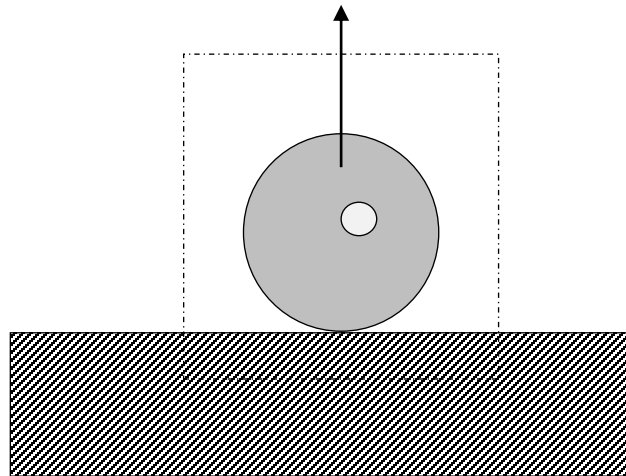


Figure 62: Diagram of nucleating bubble, detaching upward as to pass through the control volume (dotted line) boundary.

is repeated. With all snapshots analyzed for nucleating bubbles, the results are presented statistically, with a clear example (with distinct variation between peaks) shown in Figure 61. The statistical approach is further expanded upon in Section 4.3.3.

The next subjects for image analysis were the positions of free floating bubbles in the channel. These bubbles are counted in a similar manner as above, except that now their x and y coordinates in the channel were also recorded when selected. Free-floating bubbles are selected if they are not touching an electrode and are visible, regardless of size. The script (listed in Appendix 8.3.2) uses a similar method as described above, but each bubble that is selected has the coordinates of the marker stored and plotted. Bubbles are selected as close to the centroid of the visible bubble outline as possible.

Another object for image analysis was the determination bubble shapes and sizes. Based on modeling results and the literature, it was anticipated that the application of EHD would consistently alter the shapes of nucleating bubbles, elongating them in the direction of the electric field.

The final investigation for which image analysis was utilized was in measurement of the nucleating bubble departure frequency. The method used to determine departure frequency follows from a study by Euh [87] in which bubble departure frequencies could be determined through image analysis of image intensities. A control volume is defined around a nucleation site, through which bubbles will pass through as they nucleate. Given the nature of the experiment (with a front facing light source), bubbles will always have a characteristic bright spot at their center. As this bright spot passes through one side of a control volume, an automatic MATLAB script (listed in Appendix C) is used to plot the image intensity of that control volume boundary over time. The bright spot would correspond to a spike in image intensity, representing the passing of a bubble.

Depending on how the control volumes are positioned, this spike will correspond to the detachment and evacuation of a bubble, representing a nucleation event. Figure 62 illustrates this.

#### 4.3.2. Uncertainty Analysis

The measurement of spatial coordinates (for bubble sizes and position) and times (for departure frequencies) derived from image data are subject to error and uncertainty. When measuring length or coordinates, uncertainty can be introduced as a result of several factors. The uncertainties arise from several sources. Based on work by Gerardi [88], two primary sources are specific to image analysis problems. First, there is uncertainty due to the resolution of the camera. Also, there exists some uncertainty due to the coordinates chosen to represent bubble positions or shapes. These uncertainties form the basis of the uncertainty analysis for measuring lengths.

When the standard deviation, or standard error of mean (SEM) are presented, they are calculated in MATLAB using the following equations. The standard deviation is found from [85]

$$S = \sqrt{\frac{1}{N-1} \sum_{i=1}^N |A - \mu|^2} \quad (38)$$

Where  $S$  is the standard deviation,  $A$  is the vector to be observed made up of  $N$  elements, and  $\mu$  is the mean. For the SEM, the standard deviation is divided by square root of the number of elements [86].

$$\text{SEM} = \frac{S}{\sqrt{N}} \quad (39)$$

In this study, the measured quantities are either position (selected coordinates) or number of observed bubbles. For measuring selected coordinates, the user uses a cursor to select positions based on visualization. Specifically, the edges of the bubbles are blurred due to the resolution of

each image. When selecting these bubble edges manually, this means there is a range of pixels for which the bubble edge appears to exist. This results in an uncertain area of approximately 5 pixels, or  $50\mu\text{m}$ . This represents the uncertainty in coordinates presented. Due to the repeated measurements, this error does not compound, so final position averages presented could vary by up to  $50\mu\text{m}$ . This applies to all coordinate measurements. Time between bubble departures varies by the temporal resolution of the video, which can be found by dividing the number of frames per second. This corresponds to an uncertainty of  $670\mu\text{s}$ .

When counting nucleation sites for the purpose of measuring nucleation site density, the largest source of uncertainty stems from the ability to consistently identify the active sites to be included in the analysis. In addition, because the site density is the ratio of site number and the sampled area, uncertainty in either the number of counted sites or the area being sampled can contribute to the overall uncertainty. A statistical analysis is chosen in (as described in Section 4.3.3) to account for the population sampling. Additionally, if results were analyzed again by re-counting the number of bubbles within a trial, it was found that there was a maximum variation of only 1 to 2 bubbles. The methodology required counting bubbles both with EHD on and off under the same visual conditions, so the impact of over- or under-counting is minimized.

#### 4.3.3. Statistical Analysis

Because of the stochastic nature of boiling and bubble formation, the behavior of any individual bubble does not necessarily reflect the effect of EHD when applied to a heated channel where hundreds or thousands of bubbles could be forming and detaching every second. For this reason, a statistical approach is required in which the effect of EHD on populations, suitably sampled, can be used to make inferences.

From Reid [30], a statistic is used to enhance the quality of data, and assist in its interpretation. Means, maxima, or likelihoods can all be found using a statistical approach. In this study, a series of null ( $H_0$ ) and alternative ( $H_A$ ) hypotheses will be presented for a number of statements. For the purposes of this study, each result sub-section (4.4.X) claim a specific alternative hypothesis, where the “null”, or inverse of those statements are the “status quo” null hypotheses (i.e. the inverse of each result is the expected behavior of bubbles in the channel in the absence of EHD). Statistical data will serve to reject or accept the null hypotheses as claimed and derive a meaningful result.

When performing analysis, a series of tools can be used to determine a difference in the means. This is accomplished with the  $p$  –value of a test, or the probability of observing a statistic in relation to the significance level. Should a  $p$  –value be significantly smaller than the significance level, the null hypothesis will be rejected. There are simple ways to estimate  $p$  –values and reject the null hypothesis, and if those fail, more rigorous methods are used.

When means are plotted, error bars are included to represent the uncertainty. While overlapping standard deviations may suggest a difference in results, the best way of verifying a significant difference in means is with an overlap in confidence intervals, or with the standard error of mean [89]. Should error bars (defined by the standard error of mean value) overlap, it guarantees that  $p > 0.05$ . Should a comparison of error bars not yield this simple criteria, another approach can be used.

To test the null hypothesis of more similar means, a Student’s t-test [91][30] will be utilized.

$$t = \frac{\mu_1 - \mu_2}{\sqrt{\frac{s_x^2}{n} - \frac{s_y^2}{m}}} \quad (40)$$

Where  $t$  is the test statistic used to test the null hypothesis,  $\mu_1, \mu_2$  are the sample means,  $s_x, s_y$  are sample standard deviations, and  $n, m$  are sample sizes. In this test, a significance level  $\alpha$  is defined. [92] The significance level represents the probability of an observation falling into the rejection region of  $H_0$ . In using the two sample t-test, a default value of 0.05 is assumed for  $\alpha$ . The two sample t-test is means of determining if the differences between two means are from random variable distribution or not [93]. If variances are not found to be equal between means, considerations must be made in regards to the t-test. The MATLAB implementation allows for the test to take place with unequal variances.

Interpretation of the t-test results require an analysis of the confidence intervals. Confidence intervals specify the 95% confidence range that a difference of means ( $\mu_1 - \mu_2$ ) between two trials will lie in. This range is specified in this study by “ $c_i$  lower” and “ $c_i$  higher”. Should that range include a zero value (representing no difference in the means), it can be assumed that there is no statistical difference between a set of two means within the given confidence interval [93]. The confidence interval can be provided alongside the statistical analysis as a way of verifying the magnitude of the difference of the means, as opposed to a simple check.

Most hypotheses presented relate to the state of the electric field in the channel. Typically, the two sets of data that will be compared are between an electric field in the channel (at varying strengths), and the case of no external electric field. Should the two sample t-test find that the null hypothesis is rejected for a particular case, the alternative hypothesis presented in the result heading is accepted as a statistically significant finding.

#### 4.4. Results

As described earlier, the objectives of the experimental study were to characterize the effect of electric fields on nucleation site density, size and position in the channel of bubbles that have separated, nucleating bubble shape prior to separation, bubble departure frequency and size at departure. In most of the tests, the heated surface functioned as the positive electrode, however the polarity of the electrodes could be changed in order to study the effects of external field polarity on the nucleate boiling.

Initial trials were carried out to determine a baseline for behavior, and to help guide subsequent tests, as well as to allow for general debugging of the apparatus. Trials were run with multiple cases sorted into two categories: potential bias, and ramping speed. A table of these trials is presented in Table 2. Boxes in the table corresponding to a given “enabled” potential, bias, and enabling speed are identified as sequential Cases. Trials belonging to a given case are denoted as sequential numbers within each box. In this study, results will be discussed using the Trial identifier, where this table can be used to refer back to which case they belong to. More detailed information, such as potential ramping time, wall temperature, and current (during the entire length of a trial) can be found in Appendix 8.1.4.



Table 2: Unique test numbers (corresponding to a “Trial”) utilized in statistical analysis.

Bias Voltage [V]	Heater HV, Ramped Trial#	Heater GND, Ramped Trial#	Heater HV, Abrupt Trial#	Heater GND Abrupt Trial#
1000	57	66		
	60	69	N/A	N/A
	63	72	Case#7	Case#10
	Case#1	Case#4		
2000	58	67		
	61	70	N/A	
	64	73	Case#8	Case#11N/A
	Case#2	Case#5		
4000	59	68		
	62	71		
	65	74	N/A	
	77	76	Case#9	Case#12
	Case#3	Case#6		

Throughout this section, a “baseline” configuration and set of test conditions, listed in Table 3, serves as a reference set of conditions with which to compare results. More detailed test conditions for any trials used for analysis are given in Appendix 8.1.2.

Table 3: Reference conditions.

Flow Rates	4 ml/min
Channel Height	3mm
Polarity	Bottom/HV
Fluid Pre-heat	Yes
Applied Heat Flux	~45 W (subject to small convective or radiation losses)
Fluid Entry Temperature	24°C

Qualitative data uses a notation of “F#XXXX” to denote a specific high-speed camera video frame when referring to snapshots of each trial. The area of visualization for all data collected was chosen to be the area surrounding the 3<sup>rd</sup> artificial nucleation site, located approximately 36 mm downstream of the inlet to the heated channel, which has a total length of 75 mm. This site was easier to image clearly compared with sites closer to either end of the channel. Closer to the channel outlet, large vapor slugs made visualization of bubbles impossible on the bottom channel. Closer to the channel inlet, the nucleation density was less (as fluid entering the channel is not yet at saturation temperature), which made visualization more difficult.

4.4.1. What is the Effect of EHD on Nucleation Site Density?

The EHD effect serves to increase the relative density of nucleation sites from the bottom electrode (relative to the baseline configuration). EHD, as it was previously referred to in this study, is terminology used to quantify the effect that an electric field has on a fluid. For visualization, Test#35 was chosen as the representative case, due to good visual characteristics and

a good representation of many effects explored in these results. As Test#35 was a part of the initial debug tests it is not used in statistical analysis, and not included Table 2. However, for reference, its test conditions are noted in Figure 63.

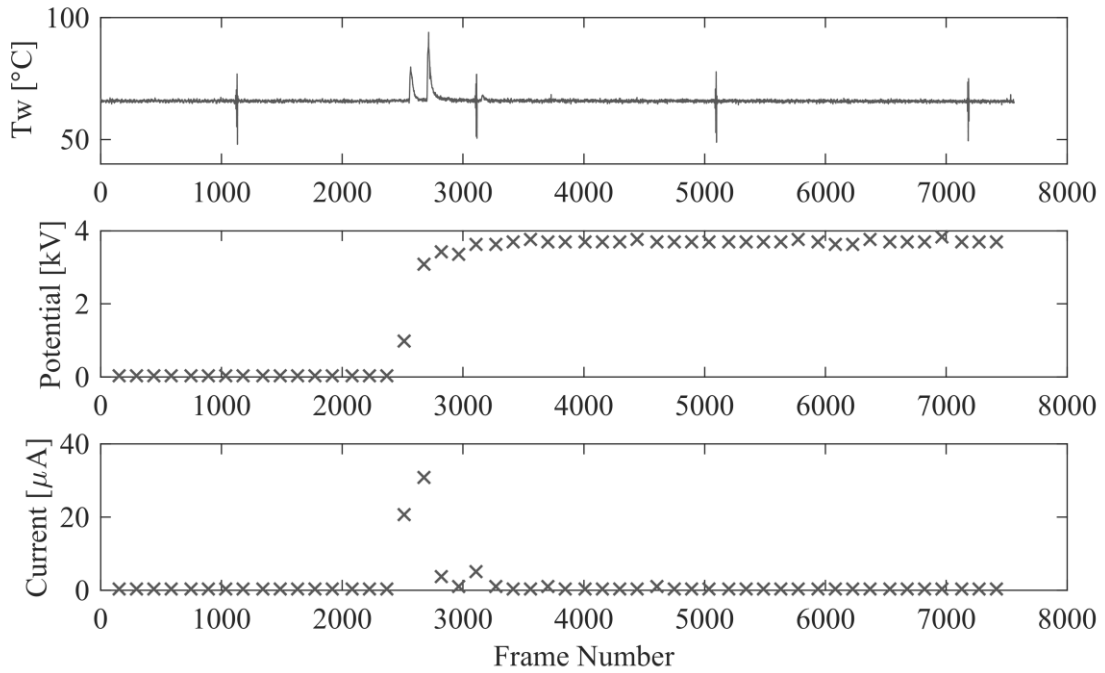


Figure 63: Trial#35 Test Conditions.

In Test#35, the density of nucleating bubbles can be seen in Figure 64, prior to the activation of an external electric field. Figure 64 shows a snapshot of nucleate boiling under no external electric field, for the baseline set of conditions, early in the trial.

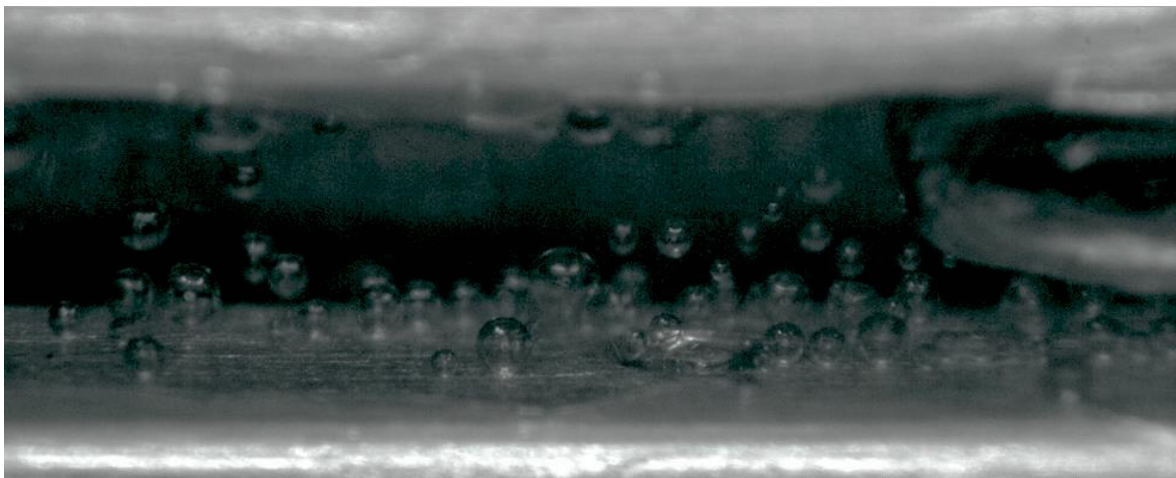


Figure 64: Trial#35,  $t=3.4\text{ms}$ , no EHD.

Later, at 100ms into the test and with EHD, the number of nucleation sites is seen to increase, and the boiling is observed to be more chaotic. This behavior can be seen in the snapshot shown in Figure 65.

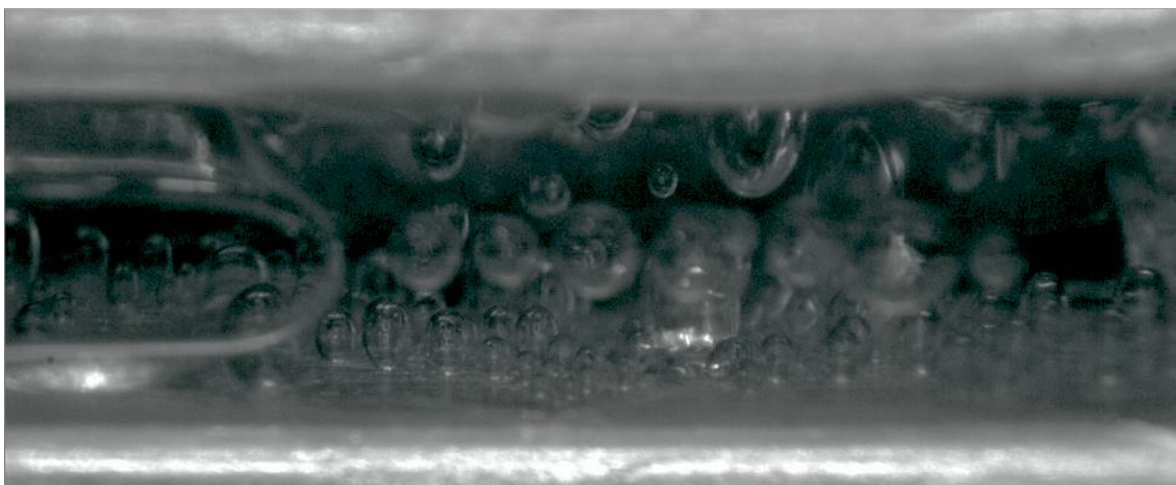


Figure 65: Trial#35,  $t=100\text{ms}$ , EHD.

Figure 66, Figure 67, and Figure 68 show the distribution of observed detachment events over a constant area, with and without an EHD effects. These histograms were obtained by evaluation of three different trials during which the EHD was switched on partway through (to maintain test condition continuity). Each result is derived from a sampling and analysis of 98 (for 1KV or 2KV trials) or 34 (for 4kV) snapshots within a single trial. For the first three trials, the

MATLAB script (Appendix C) analyzes between F#5001 and F#6501 (with EHD on), and F#0001 and F#1501 (with EHD off). Spacing is set to 30 frames, meaning that a sample of nucleation site density is taken every 30 frames. Notably, the wall temperature may vary between trials in a given case, due to the inability for the controller to maintain a heater temperature set point. The changes of a few degrees between Trial runs may lead to a difference in nucleation sites. While this effect is not noticed during the time a trial is run (5 seconds was not long enough to see this sweeping change), it is noticeable between trial ones. To account for this, another trial was also analyzed, with a wall temperature closer to that of Trial#62. Trial#69 was run in order to analyze how a difference in wall temperature in conjunction with an applied electric field of low magnitude can influence nucleate boiling density. Due to a large vapor slug, frames 5700 to 7200 were analyzed. Functionally, this makes no difference, as it was observed that nucleation site density appeared the same during this range.

While the heating system was adequate to maintain constant temperature during the running of a test, it was susceptible to long-term variations between trials (the time between trials was often as long as 5-10 minutes). Since trials may have different wall temperatures (due to these fluctuations), it is important to note the comparisons between means during a given trial, with and without EHD effects. Table 4 shows a summary of each test with number of samples, mean values, standard errors of mean, and standard deviations.

Table 4: Nucleation site density statistics for three different trials.

	0kV		1kV		2kV		3kV	
<b>Number of Samples</b>	49	Trial#61	49	Trial#60	49	Trial#61	19	Trial#62
	49	Trial#60						
	14	Trial#62						
<b>Mean</b>	8.9798	Trial#61	6.4082	Trial#60	10.8776	Trial#61	23.8947	Trial#62
	6.1020	Trial#60						
	15.7143	Trial#62						
<b>SEM</b>	0.1556	Trial#61	0.1842	Trial#60	0.2771	Trial#61	0.8089	Trial#62
	0.1577	Trial#60						
	0.4118	Trial#62						
<b>STDEV</b>	1.0895	Trial#61	1.2897	Trial#60	1.9433	Trial#61	3.5260	Trial#62
	1.1039	Test#60						
	1.5407	Test#62						

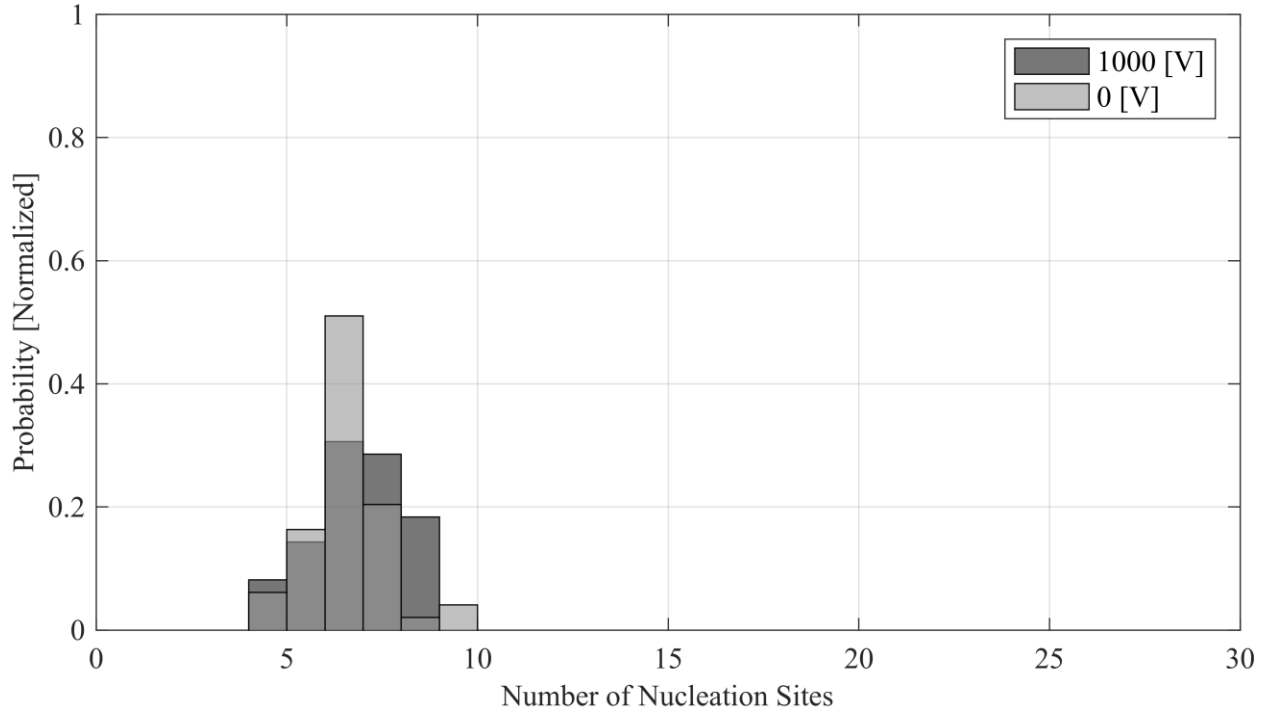


Figure 66: Comparison of nucleation site density between 1000V and 0V (Trial#60).

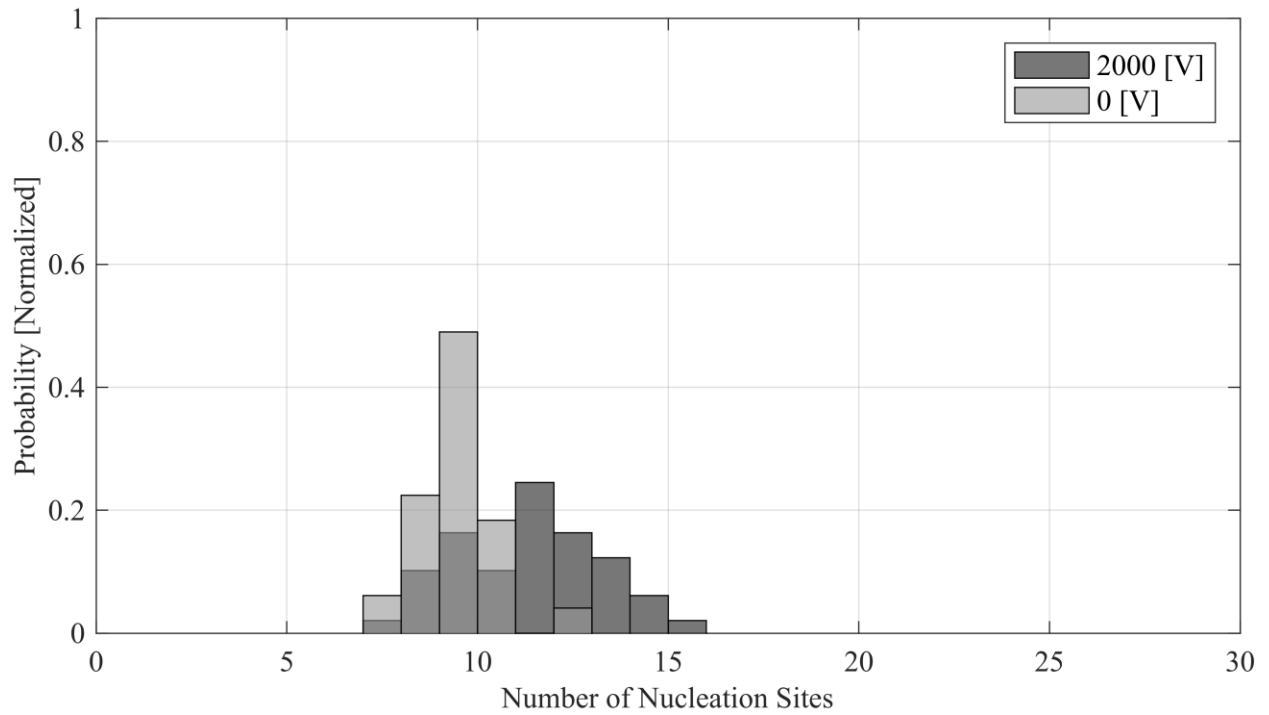


Figure 67: Comparison of nucleation site density between 2000V and 0V (Trial#61).

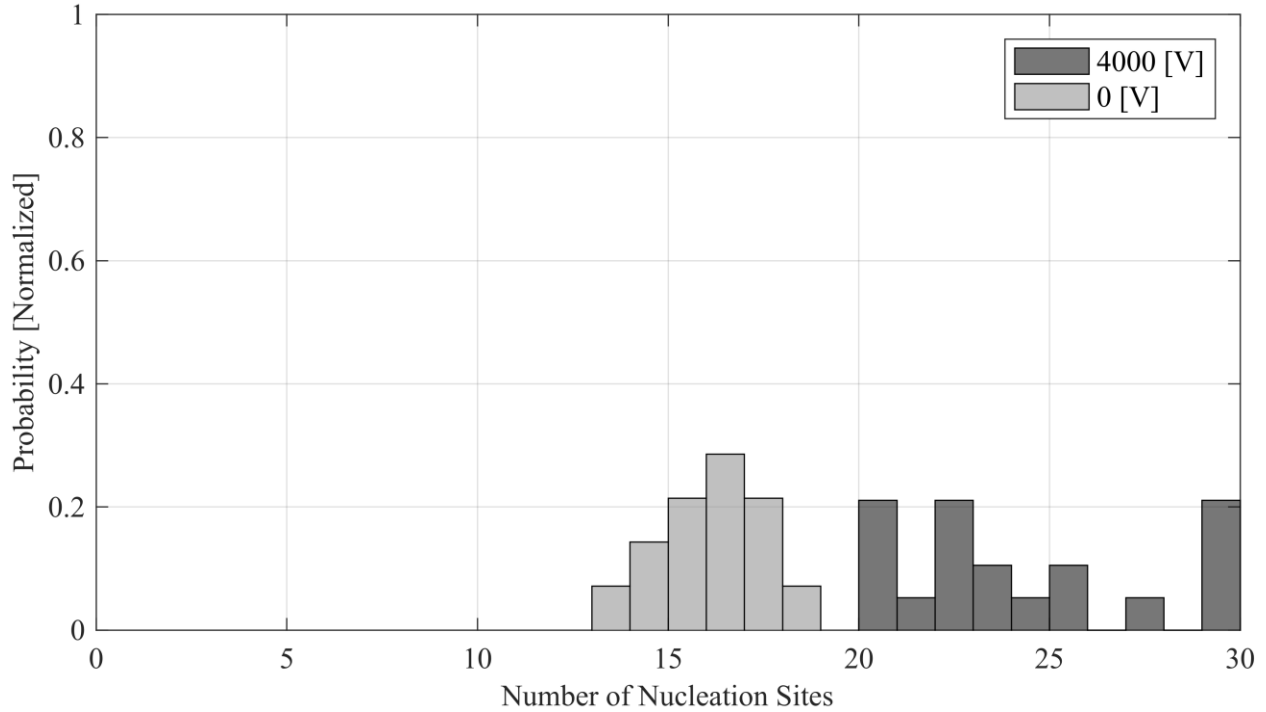


Figure 68: Comparison of Nucleation site density between 4000V and 0V (Trial#62).

Here, the number of nucleation sites in the visualization area is shown to increase with the application of EHD. Bubbles are chosen if they meet the following criteria: a) are not observed to be on the extreme front or back of the channel (in case they are leaking in from the sides) b) are attached to the bottom electrode and c) are entirely within the visual area (partial bubbles will not be counted). For the “No EHD” case, there were approximately 7 nucleation sites depending on the wall temperature.

Table 5: Statistical results for EHD enhanced nucleation density increase (1000V vs. 0V) for Trial#60.

Condition	n	Mean $\mu$ [mm]	Variance	$c_i$ lower	$\mu_1 - \mu_2$	$c_i$ higher	Difference in Means
1: EHD on	49	6.4082	1.6633	-0.1753	0.3061	0.7875	No
2: EHD off	49	6.1020	1.2185				



Table 6: Statistical results for EHD enhanced nucleation density increase (2000V vs. 0V) for Trial#61.

Condition	n	Mean $\mu$ [mm]	Variance	$c_i$ lower	$\mu_1 - \mu_2$	$c_i$ higher	Difference in Means
1: EHD on	49	10.8776	3.7764	1.2662	1.8980	2.5297	Yes
2: EHD off	49	8.9796	1.1871				

Table 7: Statistical results for EHD enhanced nucleation density increase (4000V vs. 0V) for Trial#62.

Condition	n	Mean $\mu$ [mm]	Variance	$c_i$ lower	$\mu_1 - \mu_2$	$c_i$ higher	Difference in Means
1: EHD on	19	23.8947	12.4327	6.1216	8.1805	10.2393	Yes
2: EHD off	14	15.7143	2.3736				

To further explore the role of channel temperature, another trial was analyzed (Trial#69) and results are presented in Figure 69 and Table 8. This trial had a much higher wall temperature than Trial#60, which also featured a ramping up to 1000V.

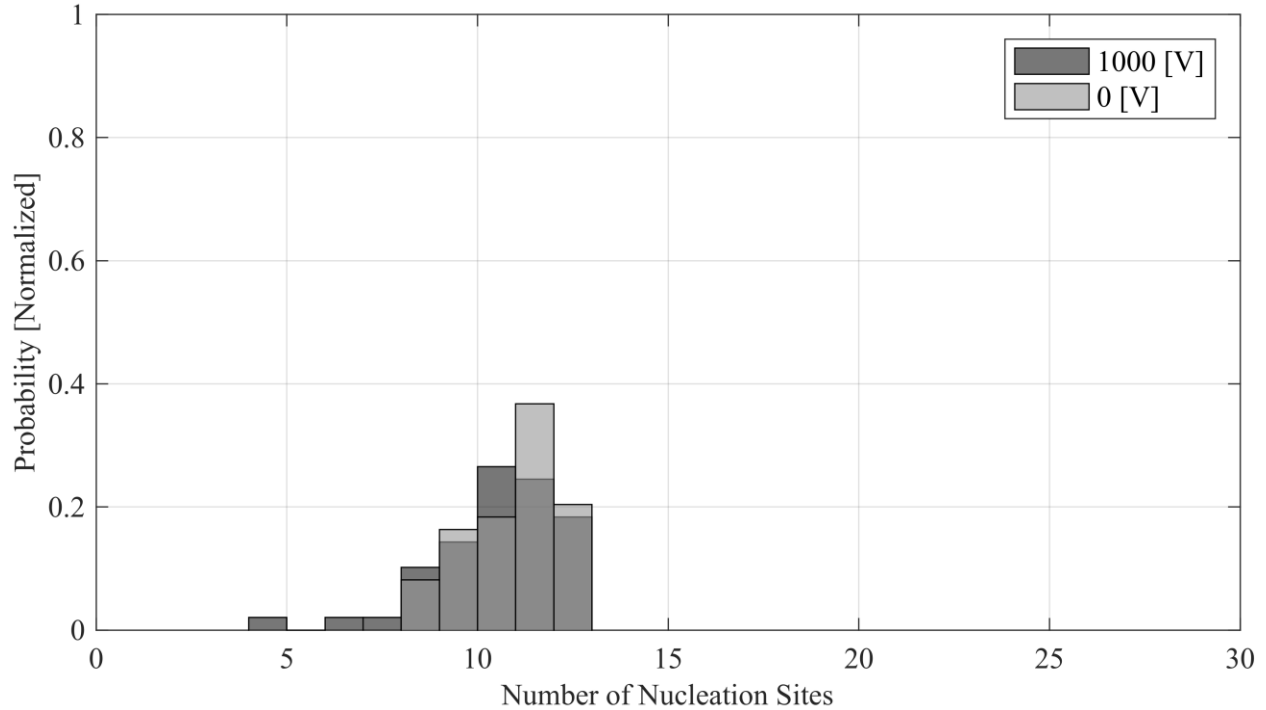


Figure 69: Comparison of nucleation site density between 1000V and 0V (Trial#60).

The statistical data for Trial#69 is presented below.

Table 8: Statistical results for EHD enhanced nucleation density increase (4000V vs. 0V) for Trial#69.

Condition	n	Mean $\mu$ [mm]	Variance	$c_i$ lower	$\mu_1 - \mu_2$	$c_i$ higher	Difference in Means
1: EHD on	49	10.0612	3.1420	-1.0507	-0.4286	0.1936	No
2: EHD off	49	10.4898	1.6718				

#### 4.4.2. How can EHD Influence the Position in the Channel of Bubbles that Have Separated?

During testing, it was observed that bubbles “center” in the channel, depending on their size before the application of an EFF. Centering, in this context, is defined as the behavior in which

bubbles appear to rest at equilibrium between both channels, nor do they float to the top of the channel as they would under typical circumstances.

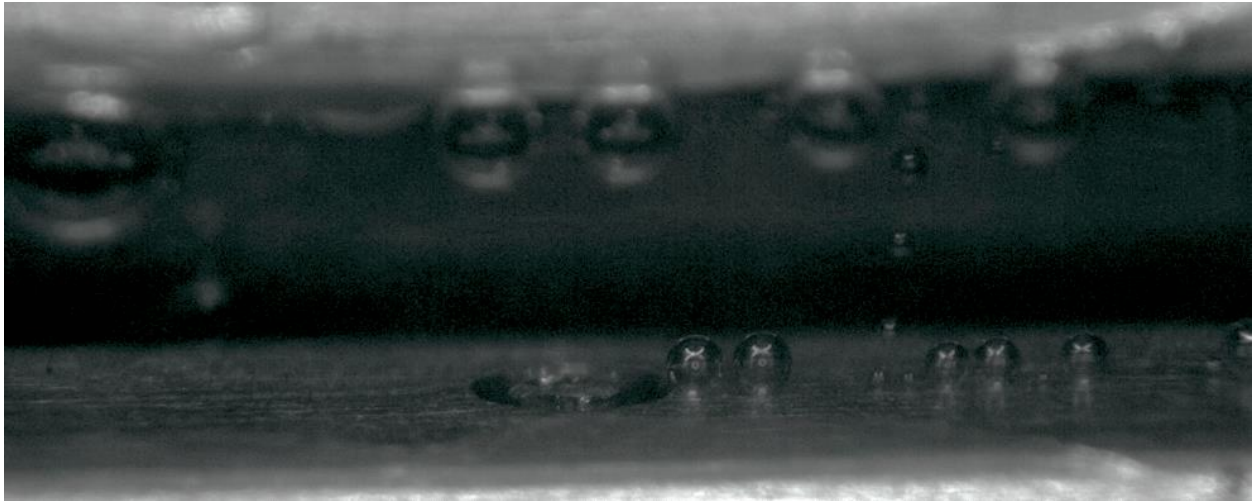


Figure 70: Trial#59, F#1753, EHD off.

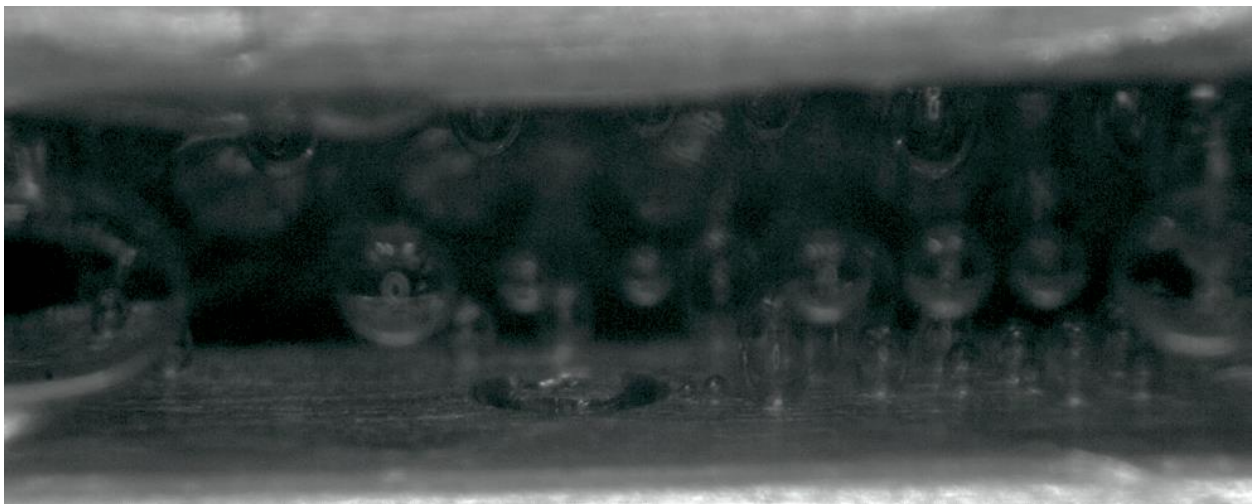


Figure 71: Trial#59, F#4716, EHD Enabled (4kV).

Upstream, nucleating bubbles were seen to coalesce and form larger bubbles that would float towards the top of the channel, due to buoyancy. However, the application of EHD serves to change the behavior of some of these bubbles as they float downstream. Figure 71 shows the same test with the application of EHD, where larger, detached bubbles tend towards the center of the

channel and steady there (steadily). Figure 70 shows the same trial, without EHD. Note that all larger, detached are either resting at the top of channel, or traveling there.

This behavior showcases an interesting uniformity in the detached bubble behavior. During the transition to a high-voltage potential, the bubbles gradually drift downward from the top of the channel wall, overcoming buoyant forces but remaining approximately midway between the two electrodes. Additionally, horizontal bubble spacing remains uniform, until coalescence occurs between two neighboring bubbles.

In certain cases, bubbles detach from the bottom electrode, being to rise, and then abruptly begin to drift back down towards the bottom electrode, to reach a final equilibrium position approximately midway between the two channels. This behavior is captured in Figure 72. Starting at F#4194, a bubble is shown nucleating. At F#4208, the bubble is shown detaching and rising towards the upper electrode. In F#4223, the bubble is shown in transit. F#4230 shows the bubble reaching an apex, with an elongated shape. After this, the bubble begins to descend toward the bottom electrode. Frame F#4240 shows the bubble in descent, where it eventually coalesces with another bubble. For clarity, the bubble in question is outlined by a red line.

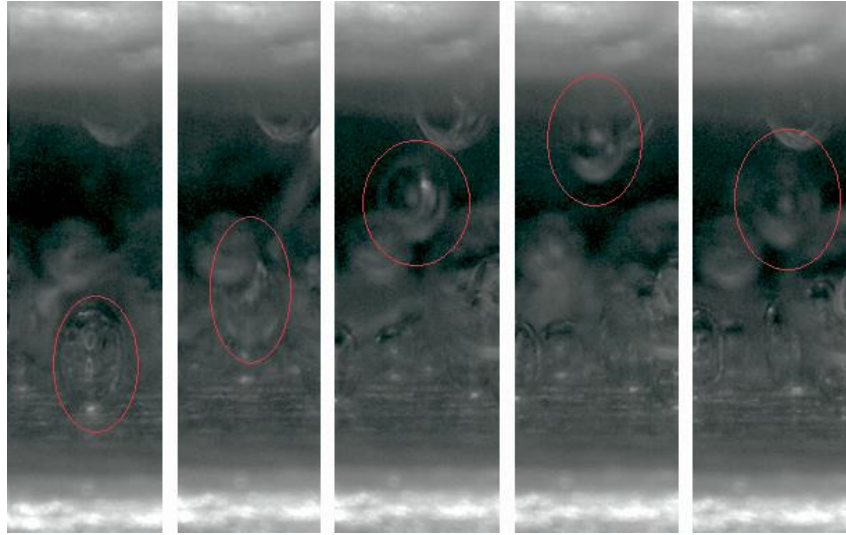


Figure 72: Trial#35, F#4194-4240.

In Trial# 57, 58 and 59, the same behavior is also observed to occur in varying degrees with the strength of the applied electric field. The image in Figure 73 compares the large vapor packets between three cases, 1kV, 2kV and 4kV of potential, at a specific snapshot in time.

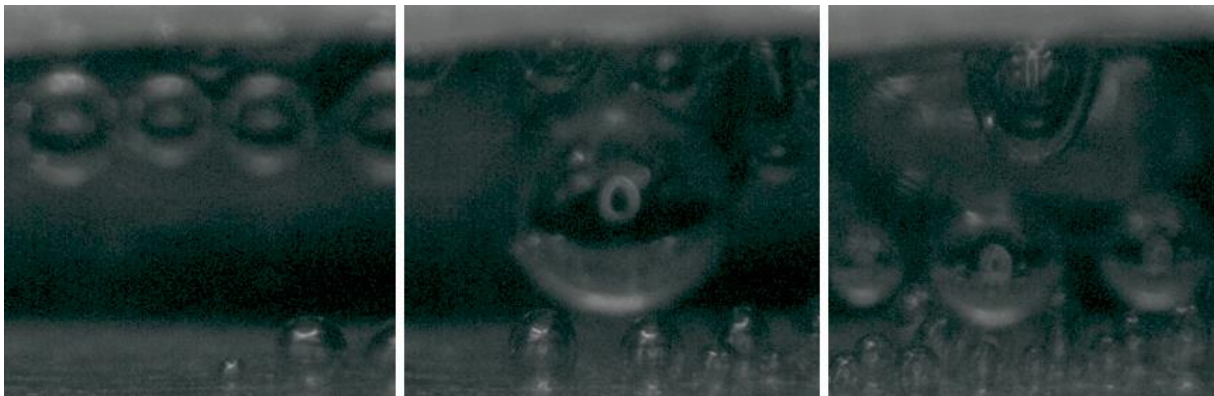


Figure 73: Comparison of large vapor packets between three potentials (from left to right: 1 kV, 2 kV, 4 kV) (from left to right, Trial#57, Trial#58, Trial#59).

On the left of Figure 73, the 1kV snapshot (F#5381, Trial#57) exhibits large bubbles organized in a line, remaining within 0.4 mm of the top surface of the channel. Detaching bubbles are observed to have their upward motion retard as they approach the upper electrode, slowing down as they get closer. In the second case, bubbles are observed to occupy a space lower down,

approximately 1.2 mm from the top of the channel (F#5137, Trial#58). In the case of 4 kV of applied potential, bubbles exit in the middle of the channel (F#5169, Trial#59), and are still observed to drift downward from the upper surface. Interestingly, nucleating bubbles from the bottom surface (in some cases) detach to coalesce with bubbles on the upper electrode.

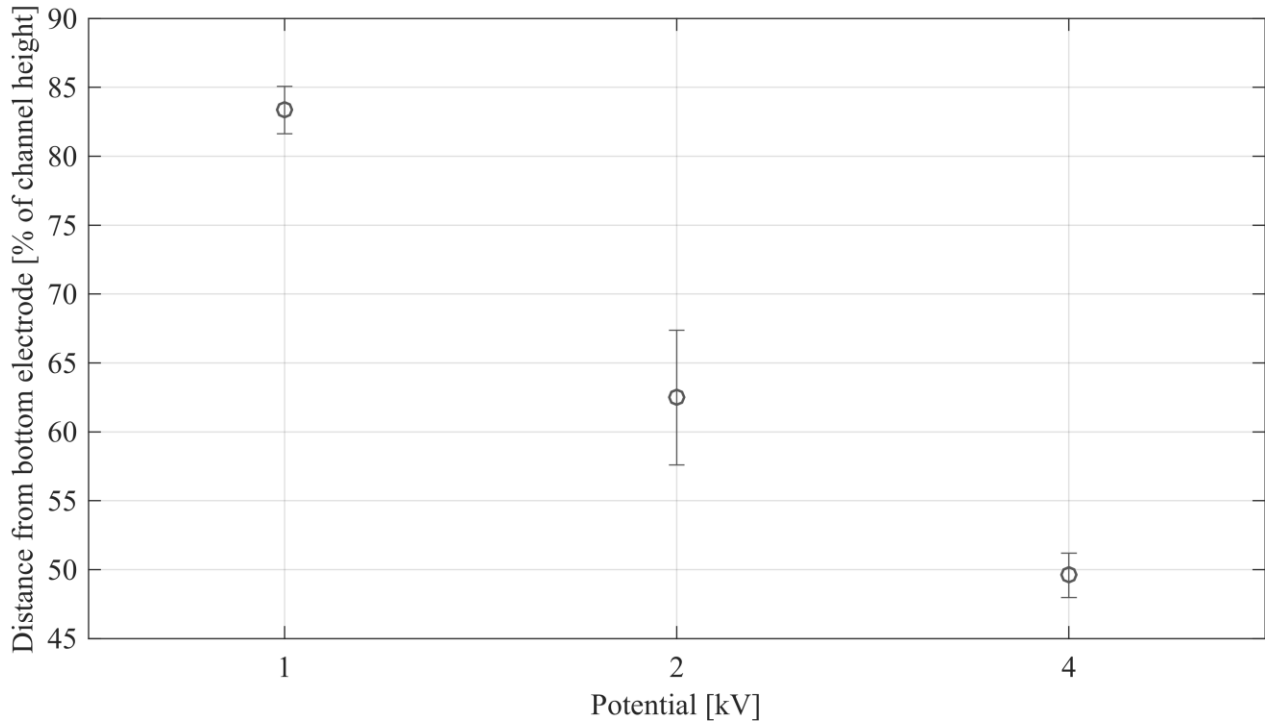


Figure 74: Bubble height in channel as a function of potential. N (number of snapshots) =24 for 1kV, 26 for 2kV, and 20 for 4kV. Error bars represent the standard deviation of the set of measurements

Figure 74 shows bubble heights in the channel as a function of the applied potential. The results are shown statistically, due to the chaotic conditions in which bubbles grow. Each bar above represents uncertainty in a representative series of bubbles from each trial (shown as 1 standard deviation of the average position). This is distinct from the uncertainty in an individual measurement, which is discussed in Section 4.3.2. Within a case, a trial is identified with a given potential. This trial is broken up into several snapshots, where bubbles are counted and their

coordinates recorded. At least 20 snapshots are counted (exact amounts listed in figure caption), with as many bubbles as are visible counted to compile the statistical data.

#### 4.4.3. Does the Polarity of the Electrodes Affect the Behavior of Nucleating Bubbles?

To isolate the root cause of the centering behavior of large vapor bubbles in the channel, the polarity of the electrodes was varied between cases. This was accomplished by moving the high voltage clip to the upper electrode, and clipping the grounded wire to the bottom post.

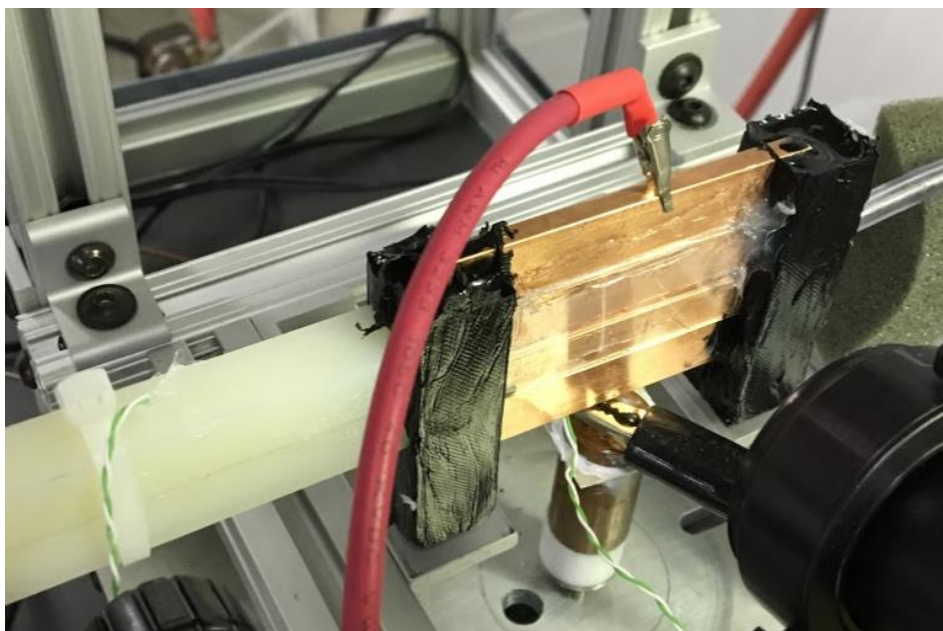


Figure 75: Reversed polarity setup. The red wire is the high potential, black is ground.

To observe the effects of reversed polarity, the magnitude of the potential was raised in the middle of a trial (in both a controlled, and abrupt manner). An example of the acquired data during a trial can be seen in Figure 76.

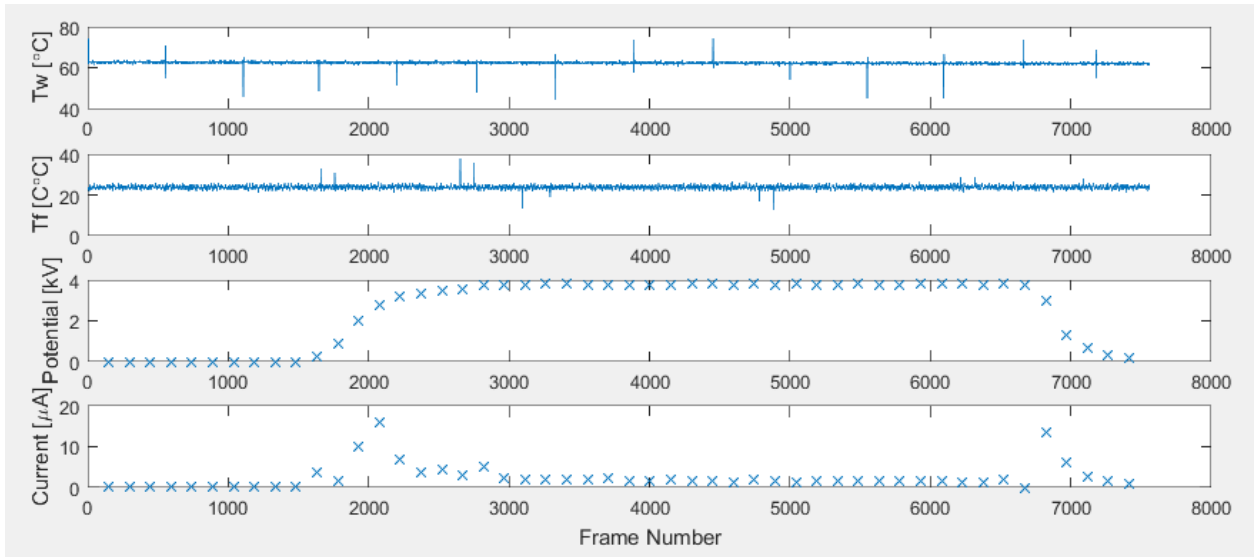


Figure 76: Ttrial#37, example of data acquired during a trial.

At F#2242 (in Figure 76), the effects of the electric field are first noticed on the bubbles (in the video) despite there being a potential starting at F#1631. Interestingly, the point at which the effects of the electric field are observed in the bubble behavior is the same point that the current in the channel peaks (F#2100), and begins its decline back to an equilibrium of approximately  $4\mu\text{A}$ . The periods between F#2242 and F#2503 in the video, show bubbles exhibiting a slow detachment from the upper electrode, and begin to center in the channel. However, at F#2503, the bubbles then begin a very sharp descent to the bottom electrode, at the moment when the potential surpasses 3.4kV. During the next 100 frames, the bubbles descend and detach to the bottom electrode, and begin a much more chaotic and violent boiling (shown in Figure 77). During this time, the channel is filled with a significantly more vapor, and the current in the channel settles on a much lower equilibrium value of  $1\mu\text{A}$ .



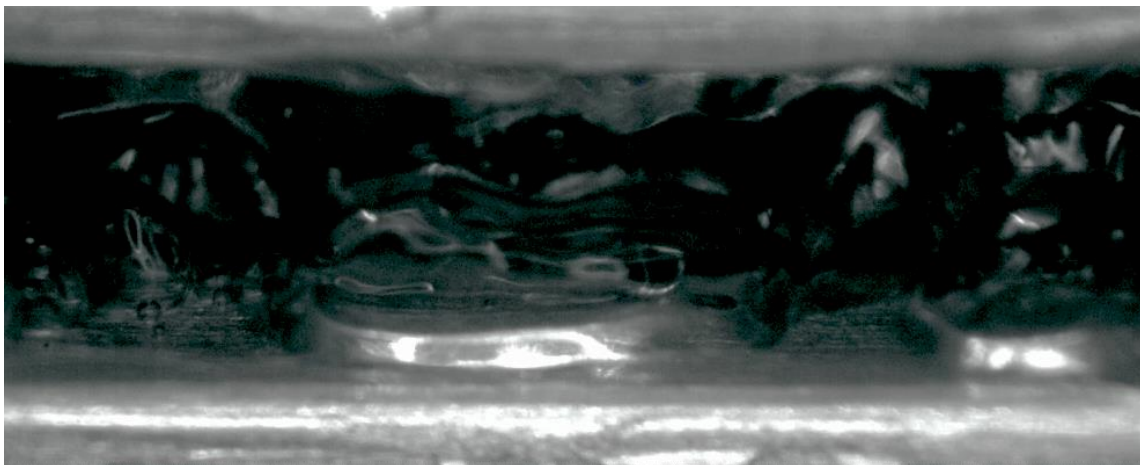


Figure 77: Trial#37 Chaotic Boiling during a rapid potential increase with reversed polarity.

The increase in the electric field under these reversed polarity conditions did not increase the nucleation site density at as high of a rate as the previously discussed case corresponding to the baseline conditions. In Test#37, the increase in electric field affects the large vapor packets but does not appear to increase the nucleation site density. Instead, the chaotic nature of the boiling made any statistical analysis difficult, as very few bubbles were available to perform statistical analysis on.

More trials were run to delve more into the possible effects of polarity reversal, with differing test conditions. Since the bubbles were observed to drift down toward the higher voltage electrode at lesser potentials, a 5 second (real-time) trial was carried out at a much lower potential, approximately 1kV. As expected, the bubbles detach from the upper (now positively biased) electrode, and maintain a “floating” position of 5  $\mu\text{m}$ , from the top of the bubble to the upper electrode, but do not center themselves in the channel, nor do they descend as much as when the potential is at a higher magnitude. This behavior is seen in Figure 78.

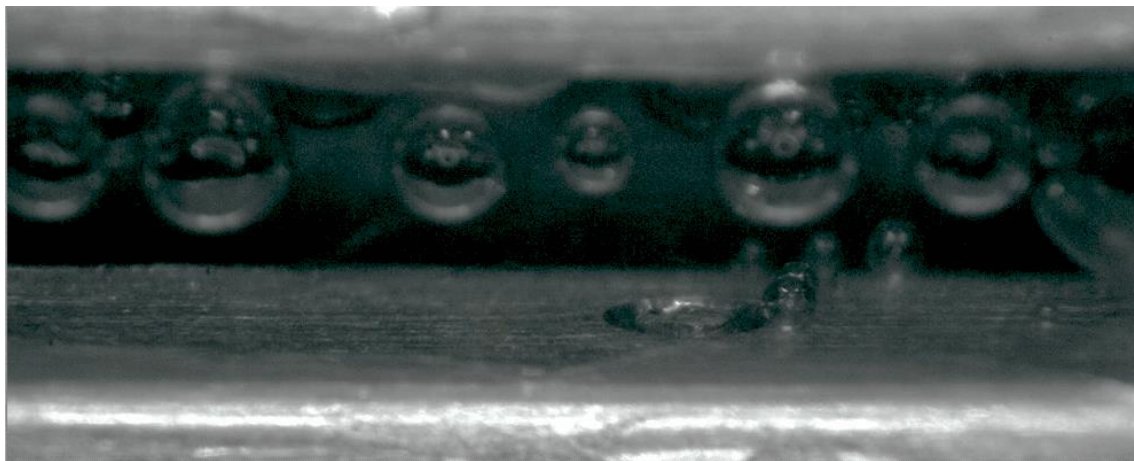


Figure 78: Trial#38, low potential bubble "hovering" between two electrodes.

This behavior, however, is not as clear in the event of a slow, controlled “ramping” of the high potential over a period of 2 seconds. When slowly raised, the reversed polarity case seems to exhibit little change from the standard polarity case. In both, bubbles detach from the upper electrode and settle into a position between the two electrodes. At lower voltages, bubble shapes remain relatively constant, and they appear to settle into a position slightly higher than equidistant between the two electrodes (possibly due to EHD forces not being able to entirely overcome buoyancy forces). At higher potentials, the shape of the bubbles are more chaotic, and while they appear to be more centered in the channel, it is harder to characterize their dynamics in the presence of such turmoil.

#### 4.4.4. How can EHD Influence Nucleating Bubble Shape and Evolution Prior to Separation?

As anticipated, the shapes of the bubbles are significantly affected by the application of an external electric field. Figure 79 (Test #35) shows an example of this. On the left, a nucleating bubble without any EHD grows in a circular shape, due to pressure forces on the inside. With the application of EHD, the bubble elongates as it grows.

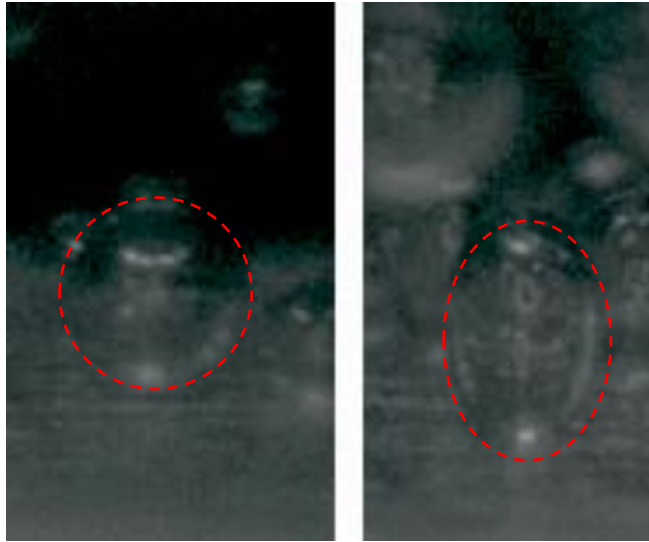


Figure 79: Comparison of bubble shapes without (left) and with (right) EHD (4kV). Bubble outlines are shown in red for clarity (Trial#35).

Figure 80 and Figure 81 show the bubble height and width as a function of an applied potential. Any uncertainty in these measurements is due to the uncertainty in where bubble edges are, discussed in Section 4.3.2. The two lighter color shades denote EHD and no EHD, where the darkest color in the graph denotes where the data overlaps. The data is acquired following the methods described in Section 4.3.1, where at several snapshots, bubbles have their upper, lower, left and right bounds marked, with the location data of each mark saved and assigned to each bubble. This data is post-processed by counting the number of bubbles with dimensions falling in a given bin (each bin is 0.01mm wide) and plotted on a histogram.

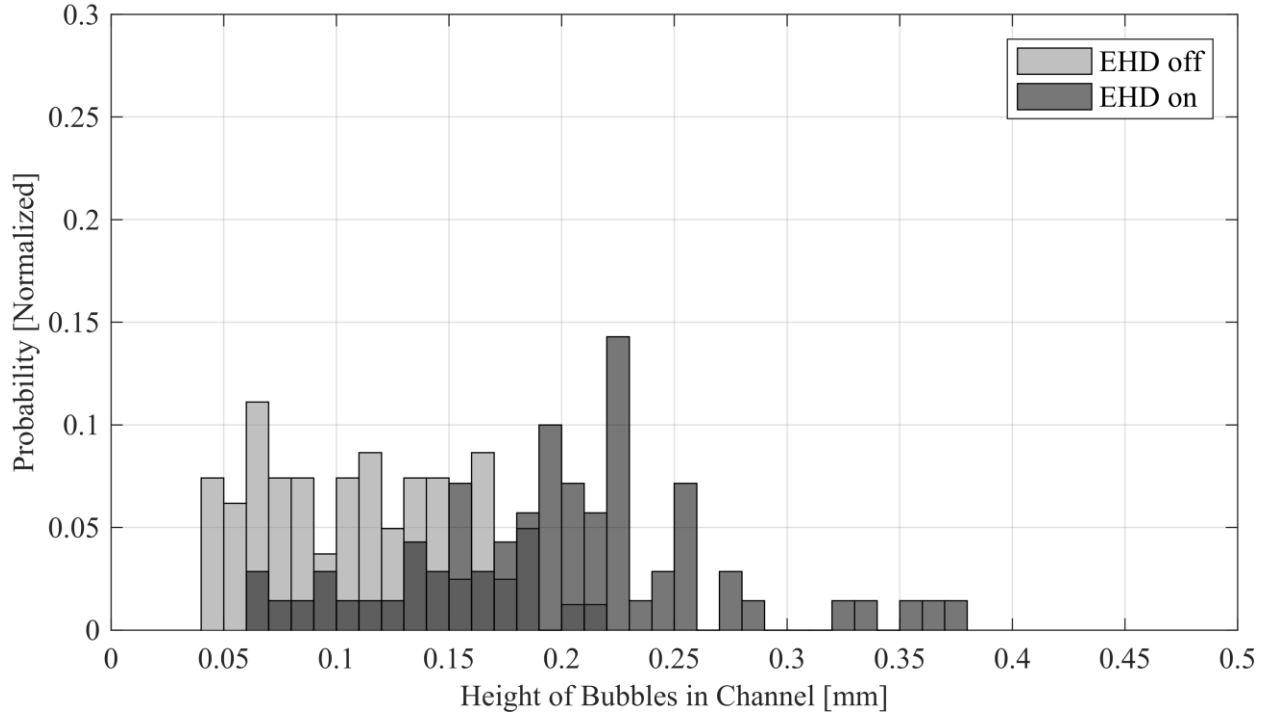


Figure 80: Distribution of bubble heights while nucleating, comparing EHD (4kV) and no EHD, for Trial#59.

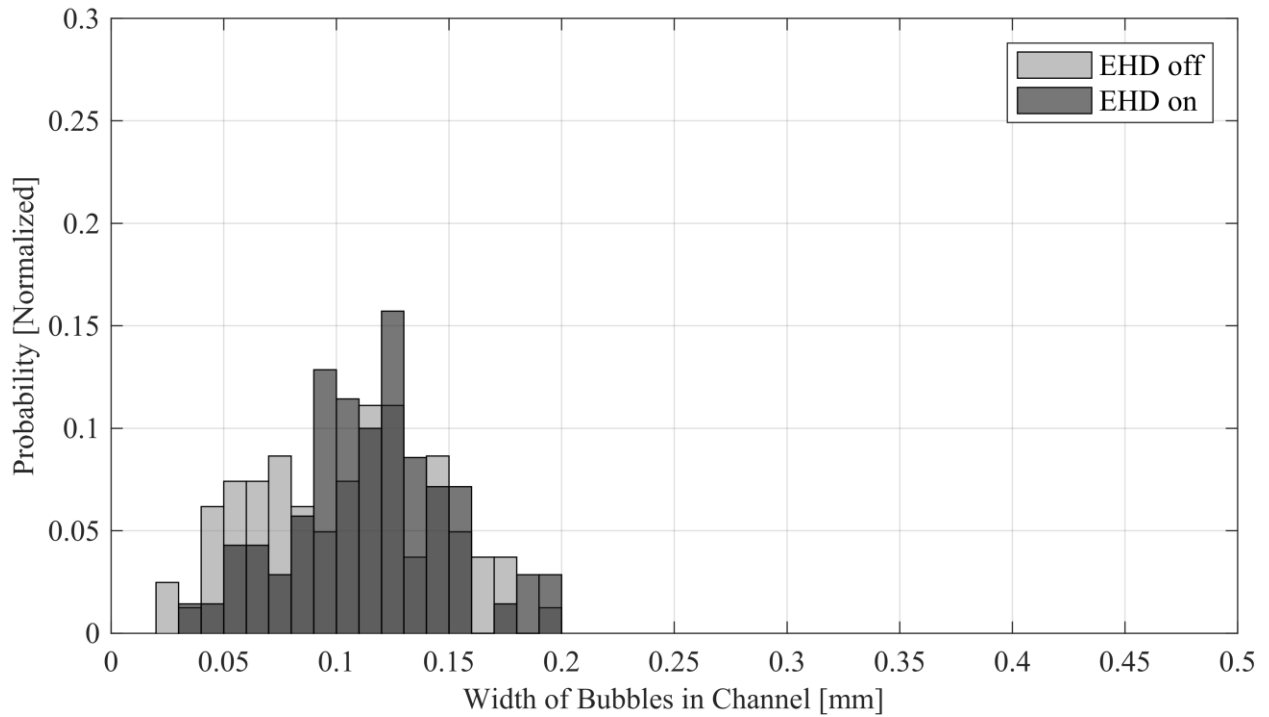


Figure 81: Distribution of Bubble widths while nucleating, comparing EHD (4kV) and no EHD, for Trial#59.

Table 9: Statistical Analysis for Bubble Height Comparison (Trial#59).

Condition	n	Mean $\mu$ [mm]	Variance	$c_i$ lower	$\mu_1 - \mu_2$	$c_i$ higher	Difference in Means
1: EHD on	70	0.1982	0.0045				
2: EHD off	81	0.1096	0.0020	0.0699	0.0886	0.1073	Yes

Table 10: Statistical Analysis for Bubble Width Comparison (Trial#59).

Condition	n	Mean $\mu$ [mm]	Variance	$c_i$ lower	$\mu_1 - \mu_2$	$c_i$ higher	Difference in Means
1: EHD on	70	0.1132	0.0012				
2: EHD off	81	0.1026	0.0016	-0.0016	0.0106	0.0228	No

#### 4.4.5. Does the Bubble Departure Frequency Increase Under EHD Forces?

Upon examining some nucleation sites (with favorable visualization characteristics, as well as with sites that exist in the same location between EHD and no EHD cases) it is noted that the application of an electric field significantly increases the departure frequency. Before the high potential is applied, bubbles can be observed departing from the surface once they reach a particular height at a relatively constant frequency. Once the high voltage is applied, bubbles immediately begin departing the surface at a much higher frequency. Due to the chaotic nature of boiling in the channel, this phenomenon is hard to characterize. However, one representative site was chosen in a trial with good visualization characteristics that allow for image analysis to take place. While the software approach for measuring image intensity worked as expected, the performance of that system in chaotic conditions (with many other bubbles) was limited. Section 4.3.1 explains this process in further detail.

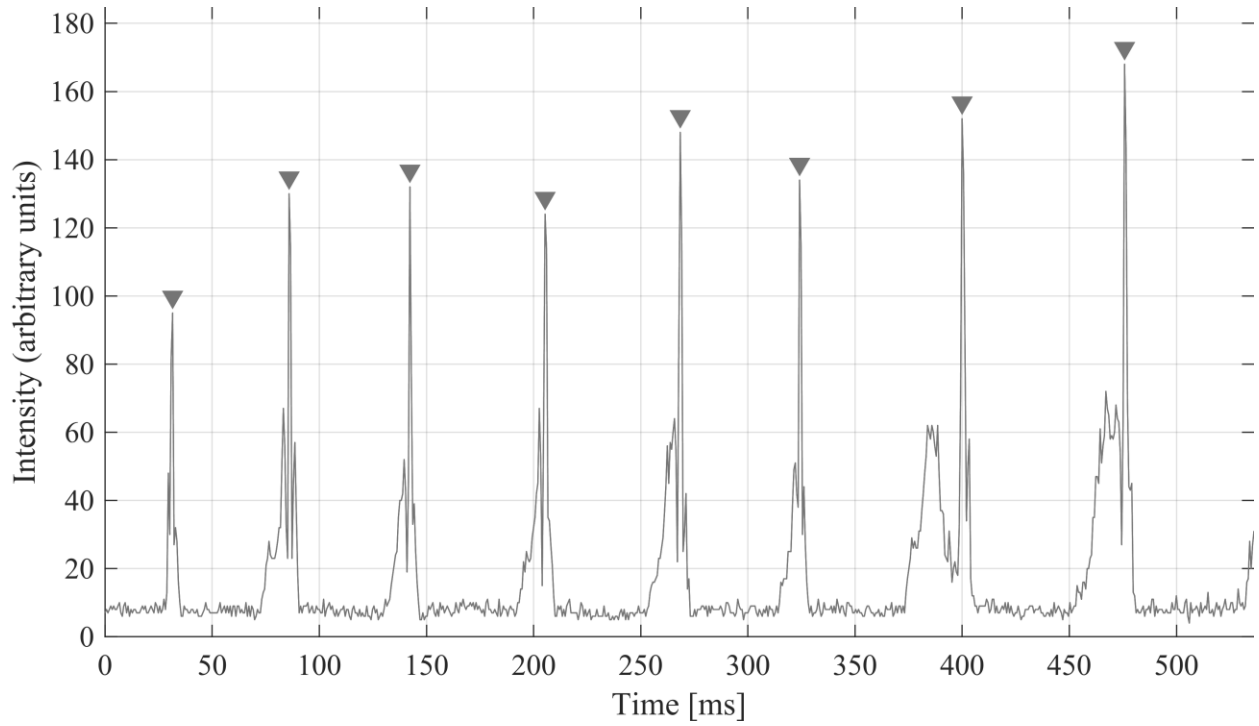


Figure 82: Image intensity (corresponding to the passage of a bubble) of a bubble from a single site vs. real-time elapsed during Trial#59, EHD off.

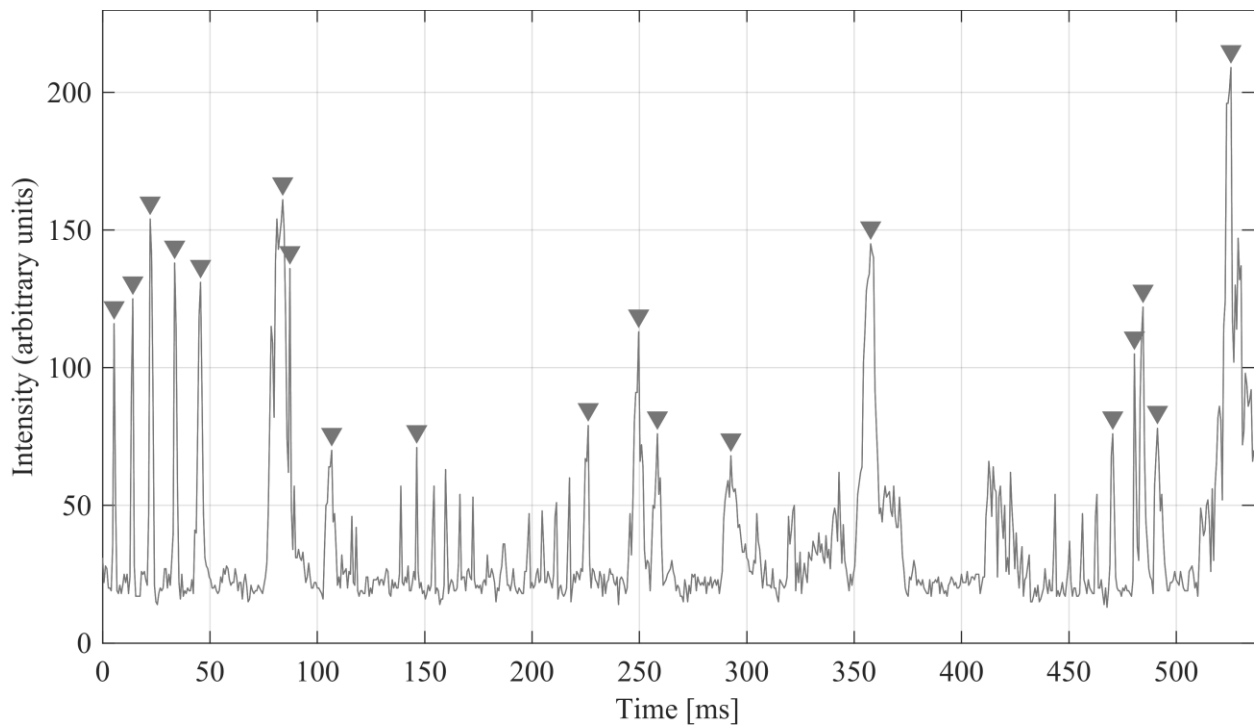


Figure 83: Image intensity (corresponding to the passage of a bubble) of a bubble from a single site vs. real-time elapsed during Trial#59, EHD on.

The frequency data for EHD is much harder to obtain due to the chaotic nature of boiling in the channel, and the crowded field of view. Additionally, due to the additional bubbles being generated at higher potential, less time was available for a clear view of nucleating bubbles from one site. However, the increase in departure frequency can be observed in spite of the difficulty in obtaining a large set of data. Additionally, the intensity used to calculate peaks varied due to the changing optical characteristics of the channel as a result of the chaotic bubble motion. In the case where EHD was applied, intensity values for peaks decreased to 50 (out of a possible 255, where 255 corresponds to a pure white pixel), which was also verified by observing the video. For these cases, bubbles departing the control volume were the metric used to define nucleation. Due to the coalescence of bubbles horizontally with EHD, it was difficult to use the upper bound of the control volume to define detachment. Instead, a bubble passing through the right face of the control volume served as a detachment metric.

The above figures provide image intensities over time, comparing EHD to a no-potential case. Within each trial, the number of departures over a given  $\Delta t$  (chosen to be 25 ms) were counted, from which a frequency for that given site was calculated. The frequency is calculated by dividing the number of departure events  $N$  by the time span,  $\Delta t$ . This is shown in Equation 41.

$$f = \frac{\Delta t}{N} \quad (41)$$

A histogram of these is presented (to within one significant figure) in Figure 84, with the statistical data presented in Table 11

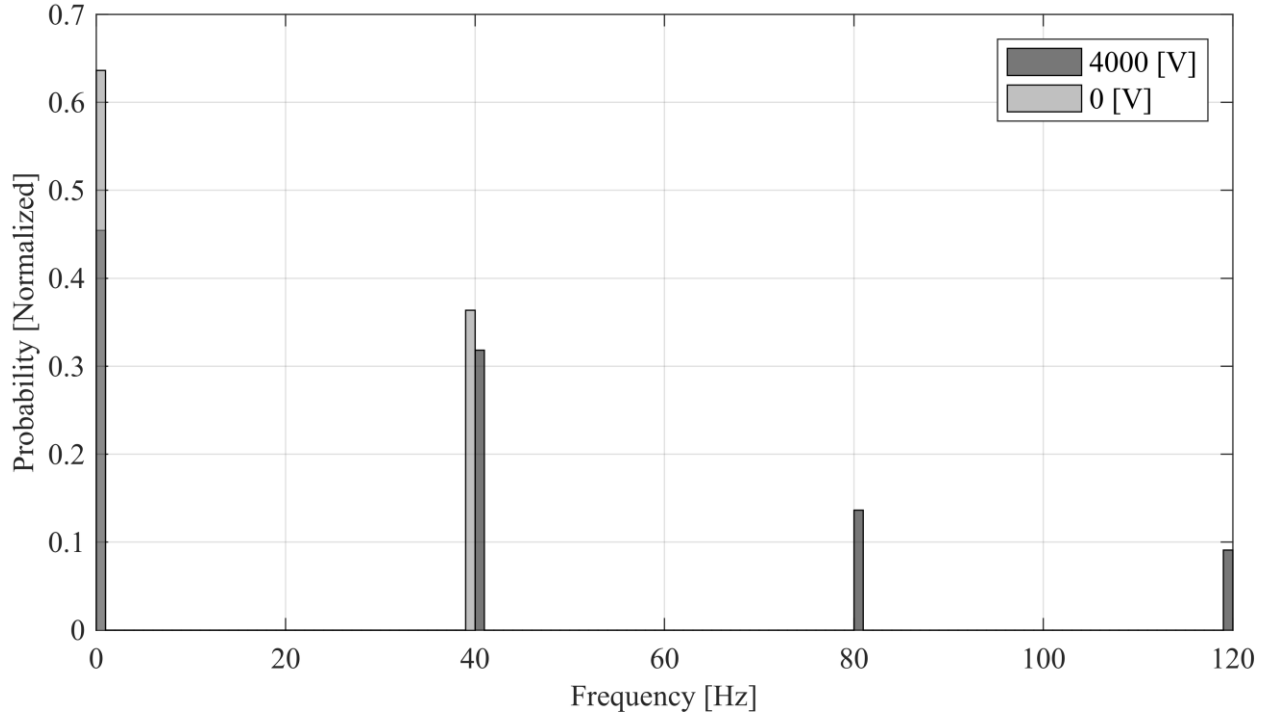


Figure 84: Histogram of detachment frequency during Trial#59, comparing 4kV and 0kV

Table 11: Statistical data for bubble departure frequency, Trial#59. Uncertainty of  $3\mu\text{Hz}$  due to time error

Condition	n	Mean $\mu$ [Hz]	Variance	$c_i$ lower	$\mu_1 - \mu_2$	$c_i$ higher	Difference in Means
1: EHD on	22	34.5	1568	0.97	20	39.0	Yes
2: EHD off	22	14.5	387				

## 4.5. Discussions

### 4.5.1. Results Discussions

The results in Section 4.4 related to bubble deformation, are consistent with results observed in other studies reviewed in Chapter 2. These results shown in Section 4.4, serve to explore the effects of EHD enhanced nucleate boiling in a minichannel, with a cross flow. As outlined in Section 4.1, the experimental component of this study was designed to explore the growth and detachment of nucleating bubbles in the presence of an externally applied electric field.



Some of the most significant challenges encountered in applying EHD to enhance nucleate boiling in a minichannel are discussed below.

- What is the effect of EHD on the nucleation site density?

First, the application of an electric field led to EHD forces in nucleating bubbles, increasing the nucleation site density of the heated electrode. While the inability for the controller to maintain the temperature set point makes it difficult to determine the magnitude in which EHD can increase nucleation sites, the numerical data supported the hypothesis that nucleation site density increases do occur, and at a more statistically significant rate with higher potentials. An increase in nucleation site density serves to increase the heat flux away from a surface, given a higher incidence of departing vapor from a surface. Kweon [94][95] notes that bubbles are attracted towards weaker electric fields, serving to force them away from the wall in which they are nucleating. Depending on the design of the channel, this effect could be exploited to a greater extent to increase the heat flux removed over a smaller surface area. In this study, it was found that the nucleation site density increase did not occur for potentials below 2 kV.

- How can EHD influence the position in the channel of bubbles that have separated?

Initially unpredicted by the modeling efforts in Chapter 3, detached bubbles in the channel exhibited a neutrally buoyant behavior during the application of an electric field to induce an EHD force. This behavior can be exploited in a real-world device, in order to control nucleate boiling effects in a minichannel under EHD. As mentioned earlier (Chapter 2), detached bubbles in a minichannel may attach to other heated surfaces, rapidly expanding and leading to thermal runaway effects. In these small channels, it can be assumed that any other surfaces may be heated, due to close proximity of other heated surfaces. By controlling the position of bubbles in a channel,

this effect can be mitigated. If detached bubbles in a channel can be kept away from other heated surfaces while EHD serves to increase nucleation site density (and therefore heat flux), greater performance could be obtained. As potential was increased, bubble positions drifted towards the center of the channel.

- Does the polarity of the electrodes affect the behavior of nucleating bubbles?

The polarity of the electric field was originally anticipated to change the behavior of EHD influenced bubbles, but testing showed this was dependent on the rate at which the reversed bias was applied. Abrupt increases in the potential, during initial tests, showed that reversed polarity led to chaotic nucleate boiling in the channel. Once potential increases were changed in a more controlled manner, this effect was not observed. In Section 4.5.2, a possible explanation is presented as to why this may occur, but it would be useful to note that in a real-world device, the manner in which an electric field is applied (i.e. speed in which it is activated) is operationally important.

- How can EHD influence nucleating bubble shape and evolution prior to separation?

As predicted by the modeling results in Chapter 3, the bubble shape was influenced by EHD effects in a minichannel, similar to the influence seen in pool boiling situations reported in the literature (Chapter 2). Consistent with these other findings, the extent to which this occurs is dependent on the magnitude of the electric field. Interestingly, for the flat surface, the bubble heights increase with the application of an electric field, but the widths of the bubbles remain the same, suggesting that the volume of bubbles in the channel is higher with EHD than without. While the bubble volumes may increase under EHD forces, nucleation departure frequencies were seen to increase as well, which serves to increase heat flux from the surface.

- Does the bubble departure frequency increase under EHD forces?

The departure frequency was also shown to be influenced by the application of EHD. Figure 84 shows this statistically, but the image intensity plots in Figure 82 and Figure 83 give a more comprehensive overview of the exact behaviors. Without EHD, the departures are uniformly spaced in time, with few departure frequency values observed. With EHD, the bubble detachment is more chaotic, occurring very quickly in some parts of the trial, and more slowly in others. However, the statistical analysis shows that overall, there is a difference in the average departure frequencies over the entire trial, to within 95% confidence.

#### 4.5.2. Secondary Effects

While not explicitly related to the enhancement of nucleate boiling in minichannels, other effects were observed. In many cases, the current was observed to change considerably while the system came to equilibrium after the potential was raised. Very early attempts at these trials led to current leakage problems, in which the potential was limited by the current capability of the power supply. The Spellman unit is capable of 15kV at 150uA, and initially, the system was only able to sustain around 1kV. During these trials, it was impossible to sustain any meaningful EHD effects, due to the low limit of the maximum voltage. By slowly raising the voltage, as opposed to an abrupt transition, it was found that these arcing events did not occur. Later, during the more controlled transition tests, it was observed that the current during the transition period seems to be related to the transition time, as well as the rate of transition. In the trials where the potential was raised over a 2 second period, the average value of the current during that time was constant at 1-3uA, depending on the maximum voltage. During the trial where the current was raised over a 1 second period, the value of the current was observed to be 5uA. When the voltage was ramped at a constant rate, the value of the current during that time remained relatively constant. For trials in

which the potential was raised logarithmically (Figure 8) with time, the current was observed to peak as high as 20uA for a 4kV maximum potential, a peak value never observed in cases where the voltage was increased at a lower rate.

While one of the initial efforts of this study was to explore the nucleation and detachment of bubbles from an artificial nucleation site, those results were inconclusive. While early trials run in quiescent fluid resulted in bubbles forming and nucleating from these artificial sites, the tests including cross flow did not yield this behavior. Bubbles did not grow at all from these artificial sites, instead growing on the flatter, smoother surface on the copper. On the occasions that bubbles were observed to grow, detach, and bound to the orifice of the inside of the artificial site, they appeared to grow and detach at larger diameters than the bubbles that were growing on the flat surface. This may be due to the behavior discussed at the beginning of Chapter 3, in which a bubble can bind to the outer orifice and continue growing. The fabrication approach used to form the artificial nucleation sites was limited to sites on the order of 700 $\mu$ m in diameter. This is smaller than the bubble widths at separation as measured in Section 4.4.4. Different nucleation site sizes could be explored either making sites bigger, or much smaller than the average width of detachment, to study if bubbles would more readily form on artificial sites.

As mentioned in Section 4.2.3, the artificial nucleation site did not function as planned. In passing, it was observed that bubbles may attach to the site as they pass through the channel and grow, but this was not repeatable. In addition, bubbles appeared to form and grow in the “trough” around the site itself. While the fabrication methods presented here are useful for future work looking to create artificial sites in copper, more work would need to be done to ensure that bubbles would nucleate and grow in the site in a reliable manner.

The application of an electric field affects the nucleate boiling in a minichannel significantly. When constrained by the presence of an upper electrode wall, vapor packets downstream of nucleation sites tend to drift towards the centerline of the channel. Work done by Kandlikar [34] found that one fundamental problem with nucleate boiling in minichannels is the presence of other heated walls.

The effect of centering detached bubbles in the channel, seen in Result 4.4.2 were not expected initially, based on the modeling efforts. It was determined that there may be several more forces acting on the bubble than were originally anticipated: It had been expected that the MST-derived forces would deform the bubble, which was observed for both baseline and reversed, controlled ramped polarity cases. Additional effects were observed however, such as the effect on detached bubbles. A possible explanation for this is presented in Section 4.5.3. More interestingly was the effect seen when the polarity was reversed. With the bottom electrode at a high potential and an abrupt voltage transient, bubble motion is observed that is likely not fully a result of only MST-derived forces.

The polarity of an EHD-enhanced minichannel boiling system must be carefully selected depending on the conditions in which a real-world device operates. Kweon [94] notes that the two most important properties that effect EHD forces are conductivity and permittivity. Additionally, that study notes the important of the charge relaxation time in EHD forces. When electric fields are applied to boiling Freon-113 for example, the charge relaxation time is on the order of 10 seconds whereas the time a single bubble inception and detachment is on the order of 10ms, so EHD forces are dominant on bubble behavior. With HFE-7100, the charge relaxation time is calculated to be on the order of 2ms, so likely there are more than just dielectrophoretic forces at work.

This was also echoed in work by Wang. [96] Wang found that if the charge relaxation time  $\tau_e$  is much, much larger than the characteristic time of the system (e.g. bubble detachment period)  $\tau_c$ , the liquid can be treated as an insulator and the electric field is distributed equally between the vapor and liquid phases. Conversely, if the charge relaxation time is much less than the bubble detachment time, the liquid is considered “conducting” in that the electric field is excluded from the liquid medium, and the voltage drop occurs at the liquid vapor interface (where free charges exist). In the case of this study, (Trial#59) bubble detachments are on the order of 100 frames, or approximately 16ms. Due to the timescales of this study, the free charges on the interface will have some effect on the detaching bubbles. Yagoobi [10] discusses the forces on a nucleating bubble. In that study, the bubble grows from a heated, grounded electrode in a non-uniform field. As Yagoobi noted, the dielectrophoretic forces reshape the bubble as it grows. Additionally, he notes that the bubble may be moved around the surface of the heater due to a non-uniform electric field distribution around the bubble (which happens due to the bubble deforming the field). Yagoobi notes that once the bubble departs from the heated surface, the Coulomb force attracts the bubble towards the energized electrode (for a length of time defined by the relaxation parameter).

This study echoes many results from the Siedel thesis [33], in that bubbles elongated under EHD. Siedel also notes that the electric field had no clear impact on the volume of any detaching bubbles in that test setup. However, that study focused on much higher potentials than were considered in this work, and without a bias applied to the heated surface.

Finally, the presence of EHD gives rise to an increased density of nucleation sites. While quantifying exactly how this increase in the density of nucleation sites can influence the wall temperature, the presence of more nucleation sites could lead to a lower wall temperature at the surface based on the principles discussed in at the start of Chapter 3. In small or constrained

systems, this could be the difference between an overheating chip, and a chip functioning well within its parameters.

In a microgravity situation, results would differ considerably. Without the buoyant force afforded by a gravitational field, bubbles would be unable to detach from the surface, as they would not overcome surface tension forces. However, the simplified calculations in this chapter (using the approximate relations derived by Pohl [19]) suggest DEP forces will have a magnitude on the order of the buoyant forces. These forces act towards the outer edge of the electrode. In practice, in microgravity, bubbles growing more towards the center of the channel (in regions of a more uniform electric field) would not be expected to overcome their surface tension forces and detach. Snyder utilized divergent electrodes to overcome this, successfully enabling nucleate boiling in microgravity conditions. Future work could re-create the experimental setup in this study with divergent electrodes, gaining both the advantage from the DEP force (driving bubbles towards a particular equilibrium position), effects due to narrow electrodes, and the divergent forces from the non-parallel nature of the electrode, which could serve to repel the bubble from the region where the electrodes are closer together.

Of note is the choice of incorporating an electrode design with two parallel plates. A straight rectangular channel was chosen to try and isolate the effects of the small-scale nucleation sites on bubble detachment, and not to manipulate individual bubbles as seen in skewed electrode EHD enhancement devices [18]. The motivation of such a geometry was to evaluate the benefits of these nucleation sites in a more conventional, rectangular channel, separate from the EHD forces that arise from divergent electrodes. A cross flow is relied on (as it would be in a pumped fluid heat transfer device) to remove bubbles away from the boiling surface, as opposed to relying on EHD

effects in a divergent electrode device. Future work could incorporate the effects seen in this study with those of a divergent electrode to manipulate bubbles without a cross flow.

While the heat flux leading to bubble growth is applied by the electric heater through the channel bottom, the fact that a non-zero leakage current was measured introduces the possibility that ohmic heating, due to current passing through the fluid, could have contributed to fluid heating and hence bubble growth. In order to assess the likelihood of this, a simple calculation was performed in which the maximum leakage current measured (maximum current of  $I_{max} = 35 \cdot 10^{-6}$  A, was observed in Trial #35, listed in Appendix 8.1.4) was assumed to have been conducted completely through the fluid. For this calculation, the fluid column in the channel is treated as a “slab” of length 76.2 mm (the channel length), width 4.76 mm (the channel width) and height 3 mm (the channel height). The fluid represents a circuit element with resistance given by

$$R = \rho \frac{h}{wL} \quad (42)$$

where  $\rho$  is the resistivity of the fluid (i.e. reciprocal of the conductivity). The ohmic dissipation (Joule heating) is then given by

$$Q_{Joule} = I_{max}^2 R \quad (43)$$

For the HFE-7100 fluid used, the conductivity is 0.93 S/m, corresponding to a resistivity of 1.08  $\Omega$  m.  $R$  is found to be 8.93  $\Omega$ . For the maximum leakage current observed, this corresponds to a Joule heating of  $1.09 \cdot 10^{-8}$  W, which is 9 orders of magnitude less than the applied electric heater power of 45.4 W. For this reason, it is unlikely that Joule heating played a significant role in heating of the fluid and bubble growth.

#### 4.5.3. Experimental Explanation via Further Modeling Work

The phenomena outlined in result 4.4.2 were not anticipated by the modeling work undertaken in Chapter 3. The model developed there was more concerned with single nucleating



bubbles and the effect of EHD at the base, so additional phenomena noted that concerned other bubbles in the channel must be explained more thoroughly. At the onset of the experimental work the electric field in the channel was assumed to be uniform in the direction of the flow. Figure 85 details an isometric view of the channel. One of the underlying assumptions of the computational model was that the phenomena is assumed to occur primarily in two dimensions ( $r$  and  $\Theta$ ). For the experimental work, the initial assumption was that the EHD forces would act only in the Y-Z direction, due to features only in the Y-Z plane. However, from a mathematical standpoint, detached bubbles were not predicted to center in the channel in a purely two-dimensional system as they were observed to do experimentally. In order to fully explain any EHD effects seen, the channel must be viewed and analyzed in all directions, especially in the Y-X plane (as opposed to the initial 2-D assumption).

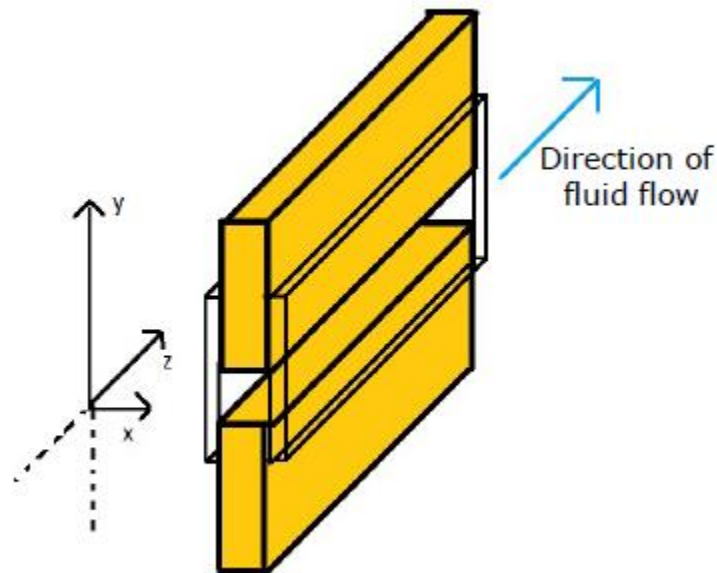


Figure 85: Isometric Channel View.

While the field may be uniform in the Y-Z plane as originally theorized, it appears from our observations of detached vapor packet behavior that there are significant non-uniformities in the Y-X plane. In order to explain this fully, a 2-D, steady model was developed in COMSOL to study the effect of narrow aspect ratio of this geometry on the electric field in the channel.

As opposed to the more detailed approach for finding EHD forces on bubbles outlined in Chapter 3, a more basic approach was taken as outlined by Pohl [19]. Equation 44 is derived by Pohl as

$$\mathbf{F}_e = 2\pi a^3 \epsilon_1 \epsilon_0 \left( \frac{\epsilon_2 - \epsilon_1}{\epsilon_2 + 2\epsilon_1} \right) \nabla |\mathbf{E}|^2 \quad (44)$$

where  $a$  represents the radius of a dielectric sphere, and  $\epsilon_1, \epsilon_2$  represent the relative permittivities of two media (1 and 2, respectively),  $\epsilon_0$  represents vacuum permittivity, and  $\mathbf{E}$  is an external, electric field. This solves for  $\mathbf{F}_e$ , the net force on a sphere. This equation is incorporated into COMSOL in a similar manner as described in Section 3, although is applied in post-processing and utilizes calculated values for the electric field. This simplified force equation, as derived by Pohl [19] can model the force felt by a discrete bubble. However, the derivation states that this relies on the assumption of a continuous, spherical body. In a more realistic scenario, bubbles would deform based on the application of an electric field [25]. Should these bubbles deform, it would change the nature of the electric field surrounding the bubble, further impacting the force felt by the bubble. If the effects of EHD are to be more accurately modeled on a nucleating bubble, a more rigorous approach must be taken to calculate the force. A model must be developed that can address the deformation of the bubble, similar to the one utilized in Chapter 3, to get a better understanding of how the bubble would deform in a channel of this nature.

The geometry in this model is provided in Figure 86. All material properties are defined for each domain, approximating their real-life material counterparts. Quartz glass is assumed for the channel viewing glass, copper assumed for the electrodes, HFE-7100 for the interior domain, and air assumed for the outside domain. The only material properties used in the model are relative permittivities, given in COMSOL standard material properties [35] or from the material properties of HFE-7100 [24]. Due to the relatively simple model used for EHD forces, only relative permittivities are needed in the domain required to calculate forces.

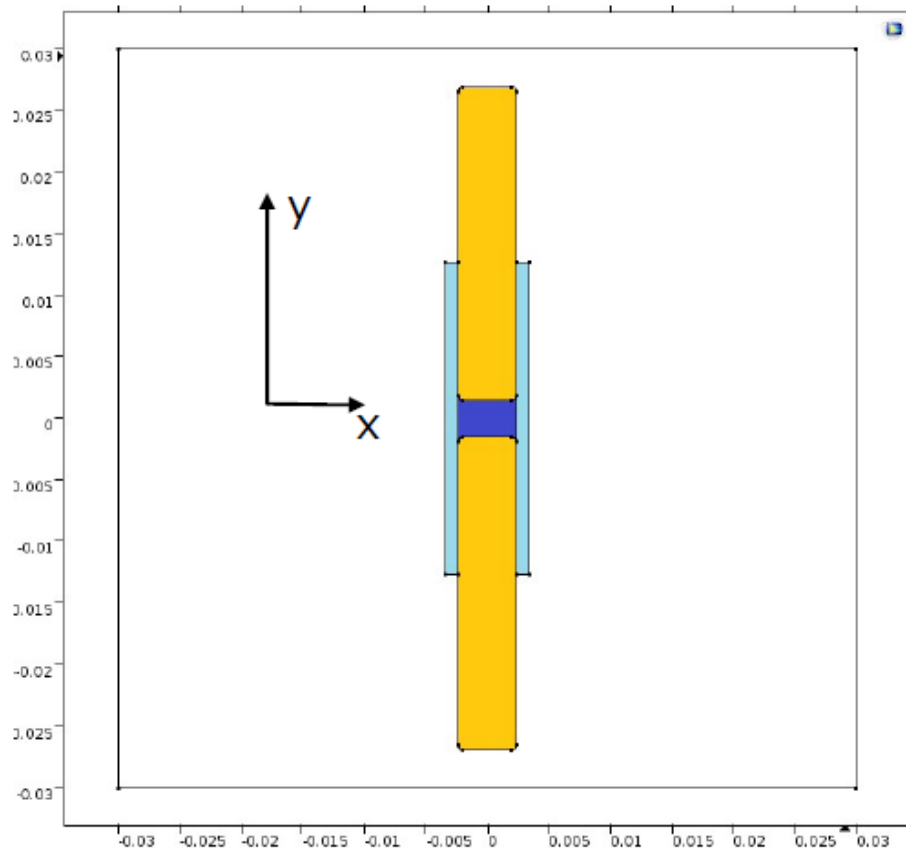


Figure 86: COMSOL model used to investigate electric field non-uniformity in the X-Y plane (dimensions in meters). Copper seen in yellow, quartz glass seen in light blue, and dark blue represents the fluid domain.

The basis for this model was from earlier work undertaken by the author, studying the effects on geometry on non-uniform fields. A small sample of this work is shown here, using Eq. 30 as a

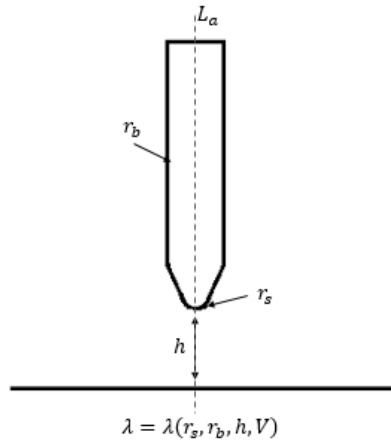


Figure 87: Example needle geometry.

basis for determining what the magnitude of the force would be on a small particle some distance away from a needle (Figure 87). That work applied Eq. 30 along the centerline of the positively charged needle, extending from the ground plane below to the tip of the needle. Exact values for

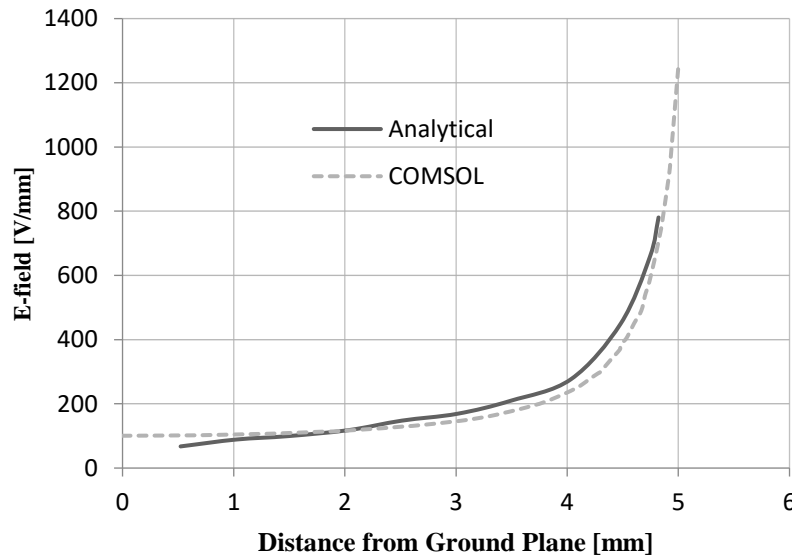


Figure 88: Example of a calculation of electric field strength from a ground plane to the tip of a needle (located 5mm higher), comparing a COMSOL solution vs. an analytical solution.

parameters varied, but a general form of the electric field is shown in Figure 88. These results

suggest that the rate of change of the electric field increases rapidly approaching a relatively sharp geometric feature. Work by Svitek [98] provides the analytic solution for this case, validating the simple needle model shown here. Based on results like these, it was determined that sharp points or features in a material can lead to highly non-uniform electric fields, increasing the magnitude of the force on a sphere due to the dependence on the electric field gradient seen in Eq. 30.

Based on that work, and the model described above, this further study in COMSOL aimed to prove the effect that some local non-uniformities might have on bubble behavior in a channel similar to that used in the Section 4. Early in this computational work, a mesh was auto-generated by COMSOL and refined until no changes were seen in the solution.

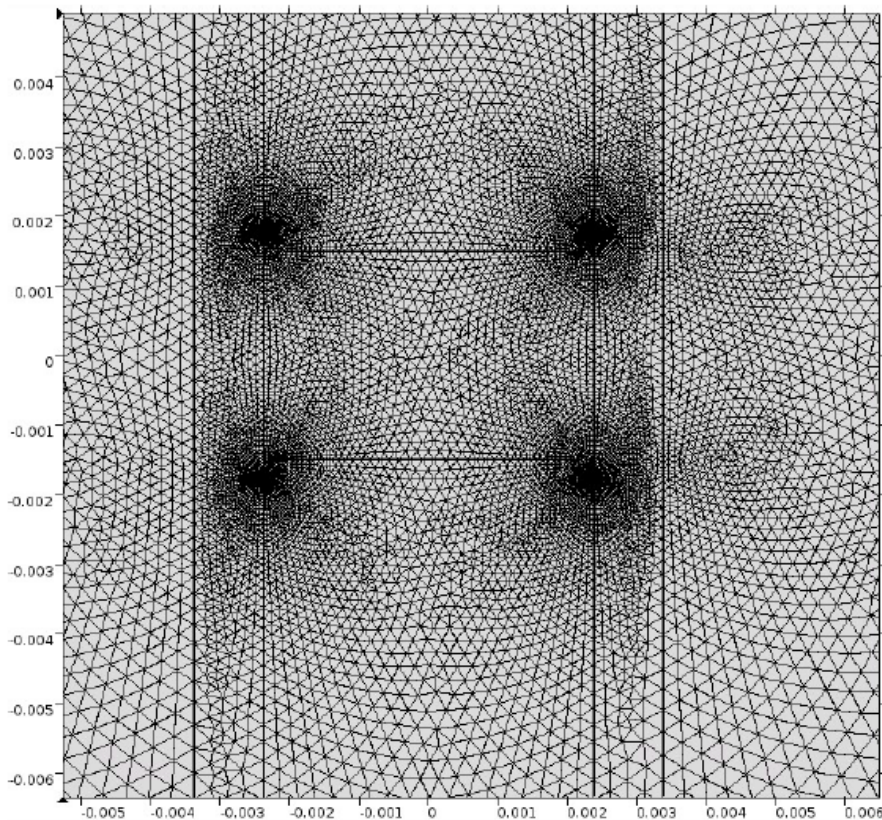


Figure 89: Visualization of mesh resolution in the domain, showing increased density in the regions of interest.

The mesh in Figure 89 is based on the model shown in Figure 86, with a domain large enough outside the area of interest to preclude any influence. The areas of increased mesh density represent the areas of interest in the model, the sharp geometric features.

A steady-state study is performed with these mesh parameters to study how an electric field behaves under those conditions. A surface plot is presented showing a “force” (based on Eq. 30) at any given point in a field that would be felt upon a hypothetical sphere. For simplicity, these spheres represent dielectric bubbles.

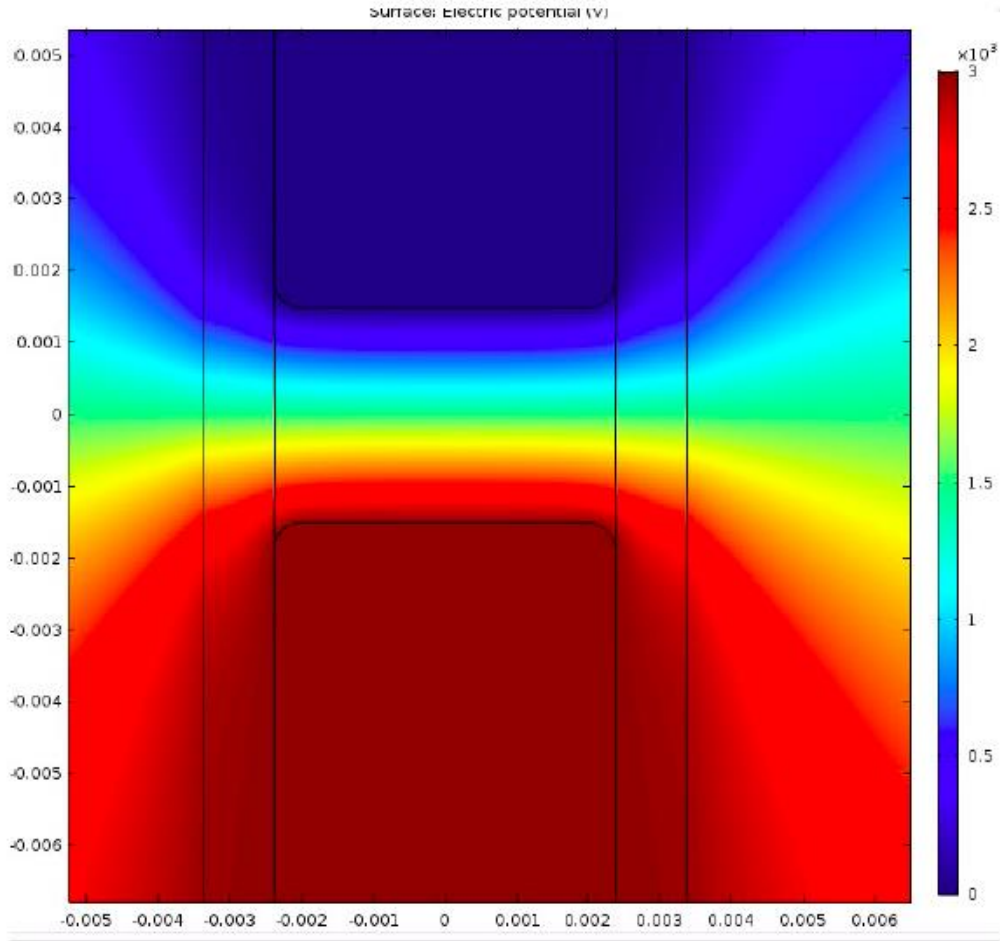


Figure 90: Potential in the channel, scale in Volts.

Figure 90 shows the electric potential in the channel, assuming the top electrode is at 3kV and the bottom is ground, with a zero-charge boundary condition applied to the edges of the domain. In this visualization, the edges of the domain are not shown in order to better visualize the behavior of the electric field near the geometric features (fillets at the edge of the electrodes). X and Y coordinates given in meters, as shown on the sides of the domain. While the change in potential inside the channel is relatively linear (away from the glass), this changes at the corners of the channel, with the natural copper electrode filleting and the transition to the air and glass domain leading to a rapid change in the electric field (i.e. a large gradient). Using the Pohl approximation as given in [19] and Eq. 30, a map of the force on a given particle can be provided in the domain. This is shown in Figure 91.

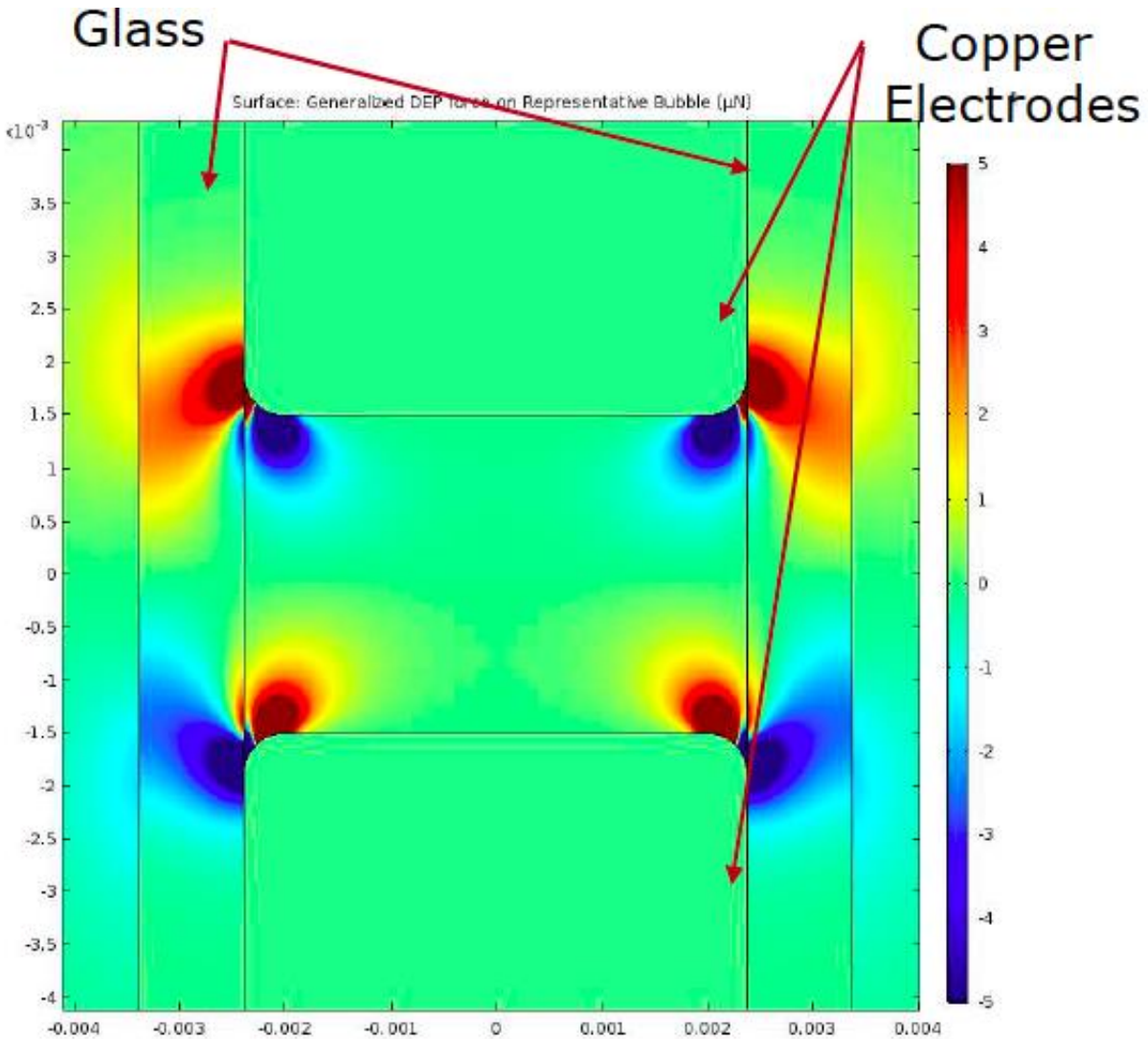


Figure 91: Force felt on a particle under EHD (3kV). Electrodes and glass sides are labeled, with the fluid domain comprising the rest of the solution domain.

Assuming  $700\mu\text{m}$  diameter particles, a relative buoyant force of  $3\mu\text{N}$  would be felt by a large vapor packet (i.e. sphere) on the side of the channel. From the figure above, a force of this magnitude would be felt by a bubble at a reasonable distance away from the channel wall, approximately one millimeter. These forces act to push a bubble away from either electrode, leading to the “centering” behavior of detached bubbles observed in Section 4.4.2. With a reduced applied voltage, the magnitude of the force felt by the bubble is much less, resulting in a bubble



that may not come to equilibrium in the center of the channel, but rather more towards the top electrode. This behavior was also observed experimentally.

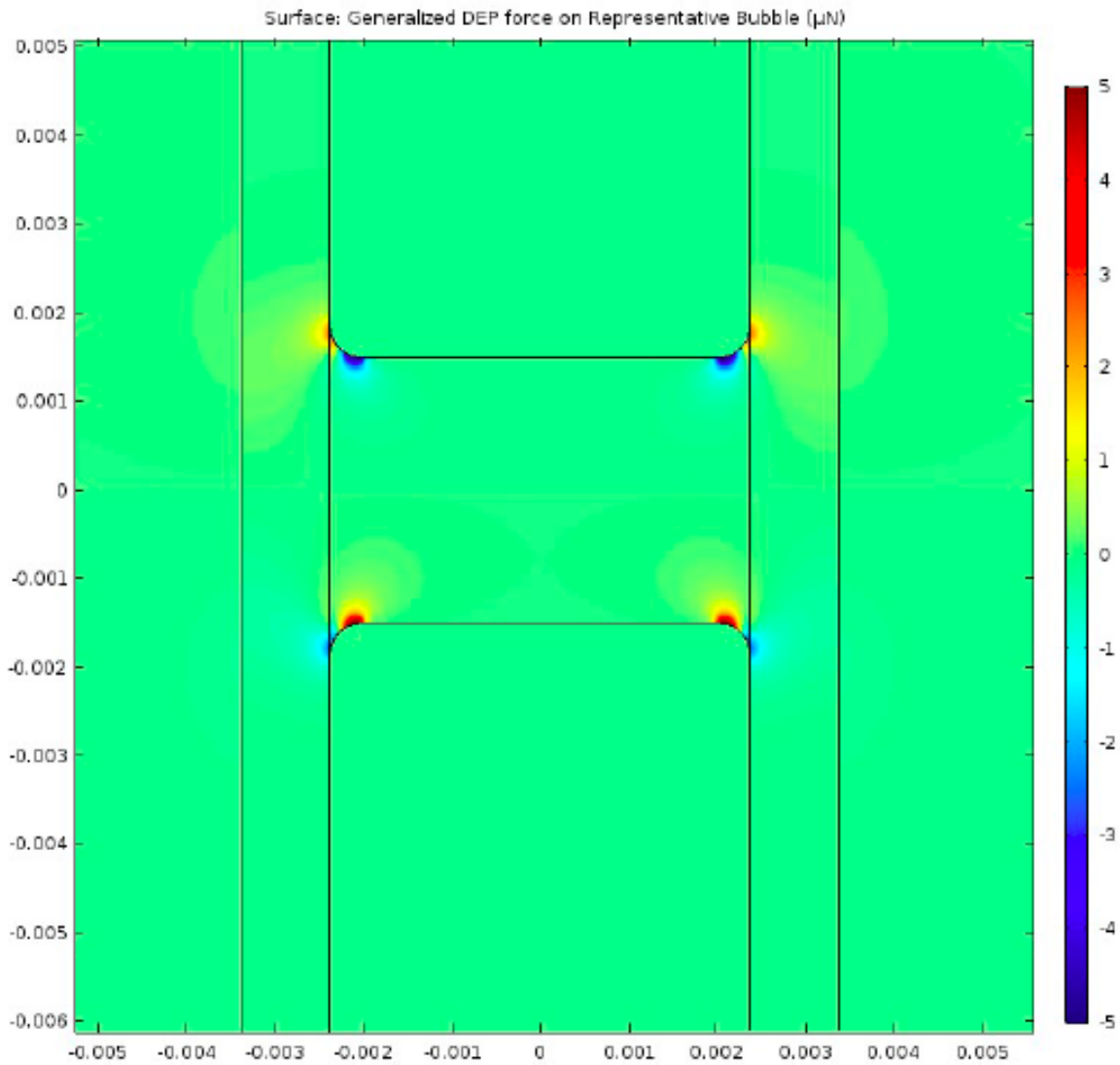


Figure 92: Force on a particle (1kV).

## 5. Conclusions & Future Work

While the study was unable to experimentally verify the efficacy of artificial nucleation sites, the information collected about bubble behavior in minichannels under the influence of an artificial electric field will be very important for future studies implementing these devices in real world applications. Several of the phenomena observed and characterized could be exploited to enhance nucleate boiling. Additionally, the objectives of determining how EHD can influence nucleating bubble growth and behavior, as well as the behavior of detached bubbles in an EHD-enhanced minichannel heat transfer device were met.

Overall, this study shows how EHD effects can be used to influence nucleate boiling in minichannels. EHD can influence bulk boiling behavior, which can be implemented in many devices. However, the unique challenges associated with the implementation of EHD boiling enhancement in minichannels requires an understanding of how individual bubbles behave while boiling, and not just overall heat flux from a heated surface to a fluid. In this study, Chapter 3 serves to describe one approach to modeling EHD effects on bubble growth and detachment computationally, paving the way for future work to develop more accurate and complex models. Chapter 4 of this study guides future work by identifying important EHD related boiling phenomena, and some of the problems associated with building such devices. Together, these results can be used to continue studies on EHD enhanced nucleate boiling in minichannels.

While it is difficult to quantify exactly how bubble detachment could improve heat flux directly (due to more accurate temperature measurements at the wall, or a more consistent input heat flux), the results of this study address some of the shortcomings of nucleate boiling in minichannels explored in Chapter 2. The effect of the field on already detached bubbles could lead to greatly improved boiling characteristics. By manipulating these already detached bubbles, the chance for

them to attach to another heated surface and continue to expand is greatly diminished. Additionally, this study serves as justification that EHD enhancement effects seen in pool boiling situations could also work under a constant cross flow, and in a constrained channel.

The final results of this study suggest an ability for EHD to control boiling in minichannels, although more work should be done to characterize exactly how this would occur. In Chapter 3, the artificial nucleation site was found to influence bubble detachment. While this exact approach could not predict exact heat transfer rates, bubble growth rates, or detachment frequencies (in an absolute sense), the results are useful when comparing how EHD can impact bubble detachment parameters, and also would be useful in driving the design of nucleation sites.

Some aspects of the experimental work (as they relate to the modeling work) were inconclusive, due to the difficulty in growing and detaching bubbles from artificial nucleation sites in particular. However, the results were positive in comparing bubble shapes under the influence of EHD, as the modeling predicted that bubbles would elongate. Additionally, results pertaining to detached bubble behavior in a minichannel under EHD were very interesting, and could be reliably applied to future devices that aim to control nucleate boiling.

An additional positive result comes from some of the lessons learned in developing this model and experimental approach, as challenges faced in this study would be faced by any future attempt at developing an EHD-enhanced minichannel heat transfer device. The challenges faced in the modeling include combining three separate physics (electrostatics, fluid flow, and heat transfer). The model presented in this study could be used as a solid foundation for which to build a more realistic, accurate boiling model. The lessons learned in the experimental portion are more numerous, and are outlined below.

### 5.1. Lessons Learned

Many of the techniques employed here in the construction of an EHD enhanced nucleate boiling device can be used to aid in the design of future experimental hardware. While sanding the copper surface seemed straightforward, care had to be taken to ensure that the surface was as smooth as possible. Figure 93 gives an example of the copper electrode surface pre-sanding and post-sanding at the finest grit available.

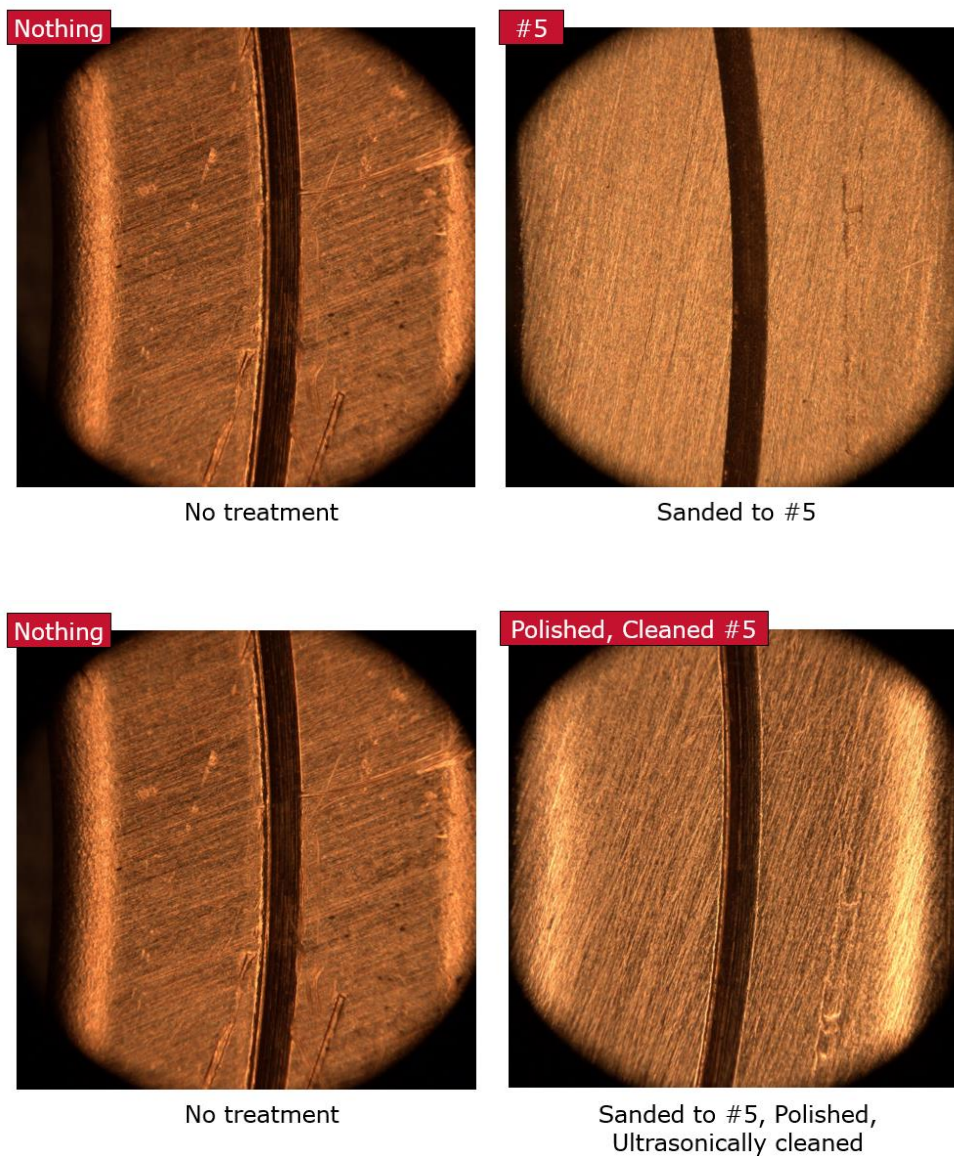


Figure 93: Comparison of finished copper.

Counter-intuitively, the original procedure to sand, polish, and clean the copper led to a rougher surface finished. It is expected that the polishing compound used damaged the copper surface more than the final surface roughness after sanding.

Another important lesson learned from the experimental work was how to account for the difficulty in biasing the heated electrode. As outlined in Section 4.2.6, one of the biggest challenges in biasing the heated electrode is that the cabling used to power the heater grounds the electrode, and the high potential could damage any data-collection equipment connected to the electrode. The approach used in this study, an isolation amplifier, has several advantages over other approaches. Other approaches include using indirect means of heating the biased electrode, which could include a laser or other radiative heat source. In addition to being expensive, using these methods would not solve the practical problem of having biased electrodes near sensitive equipment. In general, the isolation amplifier worked exactly as intended. Should the applied potentials exceed its maximum limits, however, equipment was observed to be damaged.

In addition to experimental set-up lessons learned, the results suggested that future design of an EHD-enhanced nucleate boiling device should be careful in how the geometry is designed. Initially, bubbles were expected to only be influenced by the artificial sites, and the elongation they undergo in a uniform field. However, the behavior noted in Section 4.4.2 shows that the narrow width of the channel (relative to the length) gave rise to a non-uniform force, causing bubbles to “hover” in the middle of the channel. This was originally not expected, as the electric force was only considered in the Y-Z plane (Figure 85). In future designs, these effects would have to be considered, and channels should not only be modeled in two dimensions. While a two-dimensional model was useful in characterizing bubble behavior, it would not be able to capture the nature of a real-world device.

## 5.2. Future Work

Initially, based on the modeling work, it was anticipated that bubbles would be able to form on the artificial nucleation site and detach while under the influence of EHD. This particular test setup was unable to verify this conclusion from the modeling work, although it is able to characterize bubble elongation and influence on detached bubbles on the scale of the entire channel, which would be useful in the implementation of a real-world device. Future work can expand upon this, and use the techniques developed here to continue and validate the modeling work. Additionally, the experimental techniques used here are conducive to rapid geometric variation (channel heights, etc.), which could be used to further explore the parameter space. The results show that there is a significant effect on boiling in a minichannel with EHD with a cross flow, and more work should be done to further expand upon this.

## 6. Works Cited

- [1] "U.S. Energy Information Administration - EIA - Independent Statistics and Analysis." *History of Energy Consumption in the United States, 1775–2009*. U.S. Energy Information Administration, 9 Feb. 2011. Web. 08 Jan. 2016.
- [2] Bergman, Theodore L., Frank P. Incropera, and Adrienne S. Lavine. *Fundamentals of heat and mass transfer*. John Wiley & Sons, 2011.
- [3] "Five Strategies for Cutting Data Center Energy Costs Through Enhanced Cooling Efficiency" Emerson Network Power. 2007. [http://www.emersonnetworkpower.com/documentation/en-us/brands/liebert/documents/white%20papers/data-center-energy-efficiency\\_151-47.pdf](http://www.emersonnetworkpower.com/documentation/en-us/brands/liebert/documents/white%20papers/data-center-energy-efficiency_151-47.pdf)
- [4] Moore, Gordon E. "Cramming more components onto integrated circuits, *Electronics*, 38: 8 (1965)." URL: <ftp://download.intel.com/research/silicon/moorespaper.pdf> 16 (2005).
- [5] Azar, Kaveh. "The History of Power Dissipation." *The History of Power Dissipation*. Electronics Cooling, 20 Jan. 2000. Web. 08 Jan. 2016.
- [6] Wirth, Eric. *Thermal management in embedded systems*. Diss. University of Virginia, 2004.
- [7] Lakshminarayanan, V., and N. Sriraam. "The effect of temperature on the reliability of electronic components." *Electronics, Computing and Communication Technologies (IEEE CONECCT), 2014 IEEE International Conference on*. IEEE, 2014.
- [8] Kakac, Sadk, et al., eds. *Microscale Heat Transfer-Fundamentals and Applications: Proceedings of the NATO Advanced Study Institute on Microscale Heat Transfer-Fundamentals and Applications in Biological and Microelectromechanical Systems, Cesme-Izmir, Turkey, 18-30 July, 2004*. Vol. 193. Springer Science & Business Media, 2006.
- [9] Kandlikar, Satish G. *Handbook of phase change: boiling and condensation*. CRC Press, 1999.
- [10] Seyed-Yagoobi, J., and J. E. Bryan. "Enhancement of heat transfer and mass transport in single-phase and two-phase flows with electrohydrodynamics." *Advances in Heat Transfer* 33 (1999): 95-186.
- [11] Snyder, Trevor J., Jacob N. Chung, and John B. Schneider. "Dielectrophoresis with application to boiling heat transfer in microgravity. II. Experimental investigation." *Journal of Applied Physics* 89, no. 7 (2001): 4084-4090.
- [12] Jones, Thomas B. "On the relationship of dielectrophoresis and electrowetting." *Langmuir* 18.11 (2002): 4437-4443.
- [13] Kandlikar, Satish G. "Nucleation characteristics and stability considerations during flow boiling in microchannels." *Experimental Thermal and Fluid Science* 30.5 (2006): 441-447.
- [14] Eastman, R. E. "Dynamics of bubble departure." In *AIAA, 19th Thermophysics Conference*, vol. 1. 1984.
- [15] Castellanos, Antonio, ed. *Electrohydrodynamics*. Vol. 380. Springer, 2014.
- [16] Wall, Staffan, et al. "The History of Electrokinetic Phenomena." *Current Opinion in Colloid & Interface Science* 15.3 (2010): 119-24. Web.
- [17] Jones, T. B. *Application of Electrohydrodynamic Phenomena to Space Processing*. Tech. no. 75N22345. N.p.: United States, 1975.

- [18] Snyder, T. J., and J. N. Chung. "Terrestrial and microgravity boiling heat transfer in a dielectrophoretic force field." *International journal of heat and mass transfer* 43, no. 9 (2000): 1547-1562.
- [19] Pohl, Herbert A. *Dielectrophoresis: the behavior of neutral matter in nonuniform electric fields*. Vol. 80. Cambridge: Cambridge university press, 1978.
- [20] Pohl, Herbert A. "The motion and precipitation of suspensoids in divergent electric fields." *Journal of Applied Physics* 22.7 (1951): 869-871.
- [21] Zuber, Novak. *Hydrodynamic aspects of boiling heat transfer (thesis)*. No. AECU-4439. California. Univ., Los Angeles; and Ramo-Wooldridge Corp., Los Angeles, 1959.
- [22] Misale, M., G. Guglielmini, and A. Priarone. "HFE-7100 pool boiling heat transfer and critical heat flux in inclined narrow spaces." *international journal of refrigeration* 32.2 (2009): 235-245.
- [23] El-Genk, Mohamed S., and Huseyin Bostanci. "Saturation boiling of HFE-7100 from a copper surface, simulating a microelectronic chip." *International Journal of Heat and Mass Transfer* 46.10 (2003): 1841-1854.
- [24] *Fluorochemicals in Heat Transfer Applications*. MG Chemicals, n.d. Web. <<http://www.mgchemicals.com/downloads/3m/3m-FAQ.pdf>>.
- [25] Patel, Viral K. "Terrestrial and Micro-Gravity Studies in Electrohydrodynamic Conduction-Driven Heat Transport Systems." Thesis. Worcester Polytechnic Institute, 2015.
- [26] Bejan, Adrian and Kraus, Allan D. *Heat Transfer Handbook, Volume 1*. John Wiley & Sons, 2003.
- [27] Helberg, Chris. *Fundamental Study of Utilizing Electrostatic Forces to Create Two-phase Pumping*. ProQuest, 2005.
- [28] Brutin, David, F. Topin, and L. Tadrist. "Experimental study of unsteady convective boiling in heated minichannels." *International Journal of Heat and Mass Transfer* 46.16 (2003): 2957-2965.
- [29] Sunder, Shyam, and Gaurav Tomar. "Numerical simulations of bubble formation from submerged needles under non-uniform direct current electric field." *Physics of Fluids* (1994-present) 25.10 (2013): 102104.
- [30] Reid, Howard M. *Introduction to statistics: fundamental concepts and procedures of data analysis*. Sage Publications, 2013. <http://www.mathworks.com/help/stats/ttest2.html>
- [31] Cattide, A., P. Di Marco, and W. Grassi. "Evaluation of the electrical forces acting on a detaching bubble." XXV UIT National Conference, Trieste. 2007.
- [32] Sugrue, R., J. Buongiorno, and T. McKrell. "An experimental study of bubble departure diameter in subcooled flow boiling including the effects of orientation angle, subcooling, mass flux, heat flux, and pressure." *Nuclear Engineering and Design* 279 (2014): 182-188.
- [33] Siedel, Samuel. *Bubble dynamics and boiling heat transfer : a study in the absence and in the presence of electric fields*. Other. INSA de Lyon, 2012. English.
- [34] Kandlikar, Satish G. "Fundamental issues related to flow boiling in minichannels and microchannels." *Experimental Thermal and Fluid Science* 26.2 (2002): 389-407.
- [35] "COMSOL Main Page." *COMSOL Multiphysics® Modeling Software*. N.p., n.d. Web. 21 Sept. 2016. <<http://www.comsol.com/>>



- [36] Cheung, Sherman CP, G. H. Yeoh, and J. Y. Tu. "On the modelling of population balance in isothermal vertical bubbly flows—average bubble number density approach." *Chemical Engineering and Processing: Process Intensification* 46.8 (2007): 742-756.
- [37] Chung, T. J. *Computational fluid dynamics*. Cambridge university press, 2010.
- [38] Anderson, Daniel M., Geoffrey B. McFadden, and Adam A. Wheeler. "Diffuse-interface methods in fluid mechanics." *Annual review of fluid mechanics* 30.1 (1998): 139-165.
- [39] Osher, Stanley, and James A. Sethian. "Fronts propagating with curvature-dependent speed: algorithms based on Hamilton-Jacobi formulations." *Journal of computational physics* 79.1 (1988): 12-49.
- [40] Schlegel, Fabrice. "Which Multiphase Flow Interface Should I Use?" COMSOL Blog Which Multiphase Flow Interface Should I Use Comments. COMSOL, 26 Jan. 2015. Web. 27 Jan. 2016. <<http://www.comsol.com/blogs/which-multiphase-flow-interface-should-i-use/>>.
- [41] Melcher, James R. *Continuum Electromechanics*. Vol. 2. Cambridge: MIT press, 1981.
- [42] Jackson, John David. *Classical electrodynamics*. Wiley, 1999.
- [43] Stratton, Julius Adams. *Electromagnetic theory*. John Wiley & Sons, 2007.  
Zu, Y. Q., and Y. Y. Yan. "A numerical investigation of electrohydrodynamic (EHD) effects on bubble deformation under pseudo-nucleate boiling conditions." *International Journal of Heat and Fluid Flow* 30, no. 4 (2009): 761-767.
- [44] Di Marco, Paolo, Ryo Kurimoto, Giacomo Saccone, Kosuke Hayashi, and Akio Tomiyama. "Bubble shape under the action of electric forces." *Experimental Thermal and Fluid Science* 49 (2013): 160-168.
- [45] Di Marco, Paolo. "The use of electric force as a replacement of buoyancy in two-phase flow." *Microgravity Science and Technology* 24.3 (2012): 215-228.
- [46] Smolianski, Anton, Heikki Haario, and Pasi Luukka. "Vortex shedding behind a rising bubble and two-bubble coalescence: A numerical approach." *Applied mathematical modelling* 29.7 (2005): 615-632.
- [47] COMSOL (2015). *CFD Module User's Guide* (COMSOL version 5.2). Included with COMSOL software package, Retrieved 10/1/16.
- [48] Cahn, John W., and John E. Hilliard. "Free energy of a nonuniform system. I. Interfacial free energy." *The Journal of chemical physics* 28.2 (1958): 258-267.
- [49] Yue, Pengtao, et al. "A diffuse-interface method for simulating two-phase flows of complex fluids." *Journal of Fluid Mechanics* 515 (2004): 293-317.
- [50] Jamet, Didier. "Diffuse interface models in fluid mechanics." GdR CNRS documentation, see [pmc.polytechnique.fr/mp/GDR/docu/Jamet.pdf](http://pmc.polytechnique.fr/mp/GDR/docu/Jamet.pdf) (2010).
- [51] Phan-Thien, Nhan. *Understanding viscoelasticity: basics of rheology*. Springer Science & Business Media, 2013
- [52] Hartmann, William M. *Signals, sound, and sensation*. Springer Science & Business Media, 1997.
- [53] Son, Gihun, and Vijay K. Dhir. "A level set method for analysis of film boiling on an immersed solid surface." *Numerical Heat Transfer, Part B: Fundamentals* 52.2 (2007): 153-177.
- [54] "Application Gallery." *Boiling Water*. COMSOL, n.d. Web. May 2014. <<http://www.comsol.com/showroom/documentation/model/3972/>>.

- [55] Dupuy, Pablo M., et al. "Using Cahn–Hilliard mobility to simulate coalescence dynamics." *Computers & Mathematics with Applications* 59.7 (2010): 2246-2259
- [56] Son, G., V. K. Dhir, and N. Ramanujapu. "Dynamics and heat transfer associated with a single bubble during nucleate boiling on a horizontal surface." *Journal of Heat Transfer* 121, no. 3 (1999): 623-631.
- [57] Cooper, M. G., and Lloyd, A. J. P., 1969, "The Microlayer in Nucleate Pool Boiling," *Int. J. Heat Mass Transfer*, Vol. 12, pp. 895-913.
- [58] Hänsch, Susann, and Simon Walker. "The hydrodynamics of microlayer formation beneath vapour bubbles." *International Journal of Heat and Mass Transfer* 102 (2016): 1282-1292.
- [59] Zhang, Lei, and Masahiro Shoji. "Nucleation site interaction in pool boiling on the artificial surface." *International Journal of Heat and Mass Transfer* 46.3 (2003): 513-522.
- [60] Kunkelmann, C., Stephan, Peter. "Numerical Simulation of the transient heat transfer during nucleate boiling of refrigerant HFE-7100". *International Journal of Refrigeration*. 2010
- [61] Di Marco, Paolo. "The use of electric force as a replacement of buoyancy in two-phase flow." *Microgravity Science and Technology* 24, no. 3 (2012): 215-228.
- [62] Fuhr, Guenter, Thomas Schnelle, and Bernd Wagner. "Travelling wave-driven microfabricated electrohydrodynamic pumps for liquids." *Journal of Micromechanics and Microengineering* 4, no. 4 (1994): 217.
- [63] Liu, J. W., D. J. Lee, and A. Su. "Boiling of methanol and HFE-7100 on heated surface covered with a layer of mesh." *International journal of heat and mass transfer* 44.1 (2001): 241-246.
- [64] Bonjour, Jocelyn, Marc Clausse, and Monique Lallemand. "Experimental study of the coalescence phenomenon during nucleate pool boiling." *Experimental Thermal and Fluid Science* 20.3 (2000): 180-187.
- [65] Gerlach, D., et al. "Quasi-static bubble formation on submerged orifices." *International Journal of Heat and Mass Transfer* 48.2 (2005): 425-438.
- [66] "RSB Home Page." *U.S National Library of Medicine*. U.S. National Library of Medicine, n.d. Web. 25 Oct. 2016. <<https://imagej.nih.gov/>>.
- [67] *700 Grade Industrial Sealant*. Dow Corning, n.d. Web. <<http://www.dowcorning.com/applications/search/products/details.aspx?prod=02026350&type=MATL>>
- [68] "High Temperature Epoxy Encapsulating & Potting Compound 832HT Technical Data Sheet." MG Chemicals, n.d. Web. <<http://www.mgchemicals.com/downloads/tds/tds-832ht-2parts.pdf>>
- [69] *ABSplus*. Statasys, n.d. Web. 06 Nov. 2016. <<http://www.stratasys.com/materials/fdm/absplus>>.
- [70] *Aluminum Nitride Properties*. Accuratus, 2013. Web. <<http://accuratus.com/alumni.html>>.
- [71] Cubaud, Thomas, Umberto Ulmanella, and Chih-Ming Ho. "Two-phase flow in microchannels with surface modifications." *Fluid Dynamics Research* 38.11 (2006): 772-786.
- [72] "NE-300." *SyringePump.com*. N.p., n.d. Web. 06 Nov. 2016. <<http://www.syringepump.com/NE-300.php>>.

- [73] Yu, Zhiqun, Kevin Hallinani, Wilbur Bhagat, and Reza Kashani. "Electrohydrodynamically augmented micro heat pipes." *Journal of thermophysics and heat transfer* 16, no. 2 (2002): 180-186.
- [74] Moghanlou, Farhad Sadegh, et al. "Experimental study on electrohydrodynamically induced heat transfer enhancement in a minichannel." *Experimental Thermal and Fluid Science* 59 (2014): 24-31.
- [75] Helberg, C., and J. E. Bryan. "Dielectrophoretic control of bubble transport in mesochannels—experimental study." *Journal of fluids engineering* 129, no. 9 (2007): 1131-1139.
- [76] *DIN Temperature/Process Controllers with Fuzzy Logic*. Omega, 27 Apr. 2016. Web. 06 Nov. 2016. <[http://www.omega.com/pptst/CN4000\\_Series.html](http://www.omega.com/pptst/CN4000_Series.html)>
- [77] Pak, Bockchoon, Young I. Cho, and Stephen US Choi. "Separation and reattachment of non-Newtonian fluid flows in a sudden expansion pipe." *Journal of Non-Newtonian Fluid Mechanics* 37.2 (1990): 175-199.
- [78] Schetz, Joseph A., and Allen E. Fuhs. *Fundamentals of fluid mechanics*. John Wiley & Sons, 1999.
- [79] "Thermal Grease 10-8109." *10-8109*. Newark, n.d. Web. 06 Nov. 2016. <<http://www.newark.com/gc-electronics/10-8109/thermal-grease-tube-1fl-oz/dp/00Z581>>.
- [80] *Learn the Importance of Isolation In Four Easy Lessons*. Dataq, n.d. Web. 06 Nov. 2016. <<https://www.dataq.com/data-acquisition/general-education-tutorials/learn-importance-of-isolation-in-four-easy-lessons.html>>
- [81] *Isolation Amplifier Techniques*. Analog Devices, n.d. Web. <<http://www.analog.com/media/en/training-seminars/tutorials/MT-071.pdf>>.
- [82] Texas Instruments, "AMC1100 Fully-Differential Isolation Amplifier" *Texas Instruments, Dallas, TX, 2014*
- [83] "Our Cameras.". Edgertronic, n.d. Web. 31 July 2016.
- [84] Stille, Darlene R. *Manipulating Light: Reflection, Refraction, and Absorption*. Capstone, 2005.
- [85] *Standard Deviation*. MathWorks, n.d. Web. 06 Nov. 2016. <<http://www.mathworks.com/help/matlab/ref/std.html>>.
- [86] Everitt, B. S. "The Cambridge Dictionary of Statistics 2002." *Cambridge, Cambridge*.
- [87] Euh, Dongjin, et al. "Characteristics of bubble departure frequency in a low-pressure subcooled boiling flow." *Journal of nuclear science and technology* 47.7 (2010): 608-617.
- [88] Gerardi, Craig et al. "Study of Bubble Growth in Water Pool Boiling Through Synchronized, Infrared Thermometry and Highspeed Video." *International Journal of Heat and Mass Transfer* 53.19-20 (2010): 4185–4192. Web.
- [89] Payton et al. *Overlapping confidence intervals or standard error intervals: what do they mean in terms of statistical significance?*. *J Insect Sci* (2003) vol. 3 pp. 34/
- [90] Sullivan, Lisa. "Introduction." *Confidence Intervals*. BU, n.d. Web. 06 Nov. 2016. <[http://sphweb.bumc.bu.edu/otlt/MPH-Modules/BS/BS704\\_Confidence\\_Intervals/BS704\\_Confidence\\_Intervals\\_print.html](http://sphweb.bumc.bu.edu/otlt/MPH-Modules/BS/BS704_Confidence_Intervals/BS704_Confidence_Intervals_print.html)>.

- [91] Grigelionis, Bronius. *Student's T-Distribution and Related Stochastic Processes*. Berlin: Springer, 2013.
- [92] Upton, Graham, and Ian Cook. *Introducing statistics*. Oxford University Press, 2001.
- [93] Boslaugh, Sarah. *Statistics in a nutshell*. " O'Reilly Media, Inc.", 2012.
- [94] "Two-Sample T-test." MathWorks, n.d. Web. 06 Nov. 2016. <<https://www.mathworks.com/help/stats/ttest2.html>>. Kweon, Y. C., and M. H. Kim. "Experimental study on nucleate boiling enhancement and bubble dynamic behavior in saturated pool boiling using a nonuniform dc electric field." *International Journal of Multiphase Flow* 26, no. 8 (2000): 1351-1368.
- [95] Kweon, Y. C., et al. "Study on the deformation and departure of a bubble attached to a wall in dc/ac electric fields." *International Journal of Multiphase Flow* 24.1 (1998): 145-162.
- [96] Wang, Ping. "Thermal Bubble Behaviour in Liquid Nitrogen Under Electric Fields". University of Southampton PhD Thesis, October 2008.
- [97] Jones, Thomas B., M. Gunji, M. Washizu, and M. J. Feldman. "Dielectrophoretic liquid actuation and nanodroplet formation." *Journal of applied Physics* 89, no. 2 (2001): 1441-1448.
- [98] Svitek, J. "Three-dimensional point-plane electric field analysis using integral equations." AFRICON'92 Proceedings., 3rd AFRICON Conference. IEEE, 1992.
- [99] Nave, R. *Voltage Divider*. Georgia State University, n.d. Web. <<http://hyperphysics.phy-astr.gsu.edu/hbase/electric/voldiv>>.

## 7. Bibliography

### Buoyancy-Driven Bubble Pumps

1. "U.S. Energy Information Administration - EIA - Independent Statistics and Analysis." *History of Energy Consumption in the United States, 1775–2009*. U.S. Energy Information Administration, 9 Feb. 2011. Web. 08 Jan. 2016.
2. Benhmidene, A., B. Chaouachi, and S. Gabsi. "A review of bubble pump technologies." *Journal of Applied Sciences(Faisalabad)* 10, no. 16 (2010): 1806-1813.
3. Shelestynsky, Stephen J., C. Y. Ching, and J-S. Chang. "Electrohydrodynamic pumping of vapour refrigerant bubbles in a two-phase natural circulation heat transport loop." In *Electrical Insulation and Dielectric Phenomena, 2003. Annual Report. Conference on*, pp. 702-705. IEEE, 2003.
4. Tas, N. R., J. W. Berenschot, R. G. R. Sanders, T. S. J. Lammerink, M. Elwenspoek, and A. van den Berg. "Bubble pump for integrated nanofluidics." In *Nanotechnology, 2001. IEEE-NANO 2001. Proceedings of the 2001 1st IEEE Conference on*, pp. 454-458. IEEE, 2001.
5. Tsai, Jr-Hung, and Liwei Lin. "Active microfluidic mixer and gas bubble filter driven by thermal bubble micropump." *Sensors and Actuators A: Physical* 97 (2002): 665-671.
6. White, Susan Jennifer. "Bubble pump design and performance." PhD diss., Georgia Institute of Technology, 2001.
7. Yin, Zhizhong, and Andrea Prosperetti. "A microfluidic 'blinking bubble' pump." *Journal of Micromechanics and microengineering* 15, no. 3 (2005): 643.
8. Zahn, Markus. "Magnetic fluid and nanoparticle applications to nanotechnology." *Journal of Nanoparticle Research* 3, no. 1 (2001): 73-78.

### DEP-Driven Bubble Pump

9. Darabi, J., M. M. Ohadi, and D. DeVoe. "An electrohydrodynamic polarization micropump for electronic cooling." *Microelectromechanical Systems, Journal of* 10, no. 1 (2001): 98-106.
10. Fuhr, Guenter, Thomas Schnelle, and Bernd Wagner. "Travelling wave-driven microfabricated electrohydrodynamic pumps for liquids." *Journal of Micromechanics and Microengineering* 4, no. 4 (1994): 217.
11. García-Sánchez, Pablo, Antonio Ramos, N. G. Green, and Hywel Morgan. "Experiments on AC electrokinetic pumping of liquids using arrays of microelectrodes." *Dielectrics and Electrical Insulation, IEEE Transactions on* 13, no. 3 (2006): 670-677.
12. Gencoglu, Aytug, David Olney, Alexandra LaLonde, Karuna S. Koppula, and Blanca H. Lapizco-Encinas. "Dynamic microparticle manipulation with an electroosmotic flow gradient in low-frequency alternating current dielectrophoresis." *Electrophoresis* 35, no. 2-3 (2014): 362-373.

13. Helberg, C., and J. E. Bryan. "Dielectrophoretic control of bubble transport in mesochannels—experimental study." *Journal of fluids engineering* 129, no. 9 (2007): 1131-1139.
14. Helberg, Chris. *Fundamental Study of Utilizing Electrostatic Forces to Create Two-phase Pumping*. ProQuest, 2005.
15. Helberg, Christopher M., Jenny E. Jackson, and James E. Bryan. "Control of Liquid-Bubble Interface to Create a Two-Phase, Dielectrophoretic Mesopump." In *ASME 2005 International Mechanical Engineering Congress and Exposition*, pp. 369-374. American Society of Mechanical Engineers, 2005.
16. Jones, Thomas B., M. Gunji, M. Washizu, and M. J. Feldman. "Dielectrophoretic liquid actuation and nanodroplet formation." *Journal of applied Physics* 89, no. 2 (2001): 1441-1448.
17. Lackowski, M., A. Krupa, and D. Butrymowicz. "Dielectrophoresis flow control in microchannels." *Journal of Electrostatics* 71, no. 5 (2013): 921-925.
18. Lei, U., C. W. Huang, James Chen, C. Y. Yang, Y. J. Lo, Andrew Wo, C. F. Chen, and T. W. Fung. "A travelling wave dielectrophoretic pump for blood delivery." *Lab on a Chip* 9, no. 10 (2009): 1349-1356.
19. Li, Shunbo, Ming Li, Kristelle Bougot-Robin, Wenbin Cao, Irene Yeung Yeung Chau, Weihua Li, and Weijia Wen. "High-throughput particle manipulation by hydrodynamic, electrokinetic, and dielectrophoretic effects in an integrated microfluidic chip." *Biomicrofluidics* 7, no. 2 (2013): 024106.
20. Liu, Dong, and Suresh V. Garimella. "Microfluidic pumping based on dielectrophoresis for thermal management of microelectronics." In *Thermal and Thermomechanical Phenomena in Electronic Systems, 2008. IThERM 2008. 11th Intersociety Conference on*, pp. 545-554. IEEE, 2008.
21. Liu, Weiyu, Yukun Ren, Jinyou Shao, Hongyuan Jiang, and Yucheng Ding. "A theoretical and numerical investigation of travelling wave induction microfluidic pumping in a temperature gradient." *Journal of Physics D: Applied Physics* 47, no. 7 (2014): 075501.
22. Marczak, Marcin, and Heinrich Diesinger. "Traveling wave dielectrophoresis micropump based on the dispersion of a capacitive electrode layer." *Journal of Applied Physics* 105, no. 12 (2009): 124511.
23. Ramos, A., H. Morgan, N. G. Green, A. Gonzalez, and A. Castellanos. "Pumping of liquids with traveling-wave electroosmosis." *Journal of Applied Physics* 97, no. 8 (2005): 084906.
24. Studer, Vincent, Anne Pépin, Yong Chen, and Armand Ajdari. "An integrated AC electrokinetic pump in a microfluidic loop for fast and tunable flow control." *Analyst* 129, no. 10 (2004): 944-949.
25. Suh, Junwoo, Debra Cytrynowicz, Frank M. Gerner, and H. Thurman Henderson. "A MEMS bubble pump for an electronic cooling device." *Journal of Micromechanics and Microengineering* 20, no. 12 (2010): 125025.
26. Tseng, Yi-Li, Ching-Wen Huang, U. Lei, Chii-Wann Lin, and Fu-Shan Jaw. "High efficient driving circuit for traveling wave dielectrophoretic pump." *Measurement* 44, no. 10 (2011): 1980-1985.

27. Yu, Zhiqun, Kevin Hallinani, Wilbur Bhagat, and Reza Kashani. "Electrohydrodynamically augmented micro heat pipes." *Journal of thermophysics and heat transfer* 16, no. 2 (2002): 180-186.

#### Bubble Tracking

28. Cheng, Da-chuan, and Hans Burkhardt. "Bubble tracking in image sequences." *International Journal of Thermal Sciences* 42, no. 7 (2003): 647-655.
29. Sacan, Ahmet, Hakan Ferhatosmanoglu, and Huseyin Coskun. "CellTrack: an open-source software for cell tracking and motility analysis." *Bioinformatics* 24, no. 14 (2008): 1647-1649.

#### DEP Electrode Geometry

30. Andersson, Helene, and Albert van den Berg. "Microtechnologies and nanotechnologies for single-cell analysis." *Current opinion in biotechnology* 15, no. 1 (2004): 44-49.
31. Hughes, Michael Pycraft. "AC electrokinetics: applications for nanotechnology." *Nanotechnology* 11, no. 2 (2000): 124.
32. Jones, T. B. "Liquid dielectrophoresis on the microscale." *Journal of Electrostatics* 51 (2001): 290-299.
33. Jones, Thomas B., M. Gunji, M. Washizu, and M. J. Feldman. "Dielectrophoretic liquid actuation and nanodroplet formation." *Journal of applied Physics* 89, no. 2 (2001): 1441-1448.
34. Lin, J. T. Y., and J. T. W. Yeow. "Enhancing dielectrophoresis effect through novel electrode geometry." *Biomedical Microdevices* 9, no. 6 (2007): 823-831.
35. Sano, Michael B., Roberto C. Gallo-Villanueva, Blanca H. Lapizco-Encinas, and Rafael V. Davalos. "Simultaneous electrokinetic flow and dielectrophoretic trapping using perpendicular static and dynamic electric fields." *Microfluidics and nanofluidics* 15, no. 5 (2013): 599-609.
36. Wakizaka, Yoshikazu, Masaru Hakoda, and Naohiro Shiragami. "Effect of electrode geometry on dielectrophoretic separation of cells." *Biochemical Engineering Journal* 20, no. 1 (2004): 13-19.
37. Svitek, J. "Three-dimensional point-plane electric field analysis using integral equations." AFRICON'92 Proceedings., 3rd AFRICON Conference. IEEE, 1992.

#### Dynamics of Bubble Formation and Separation without DEP

38. Afzal, M. U., and I. S. Kang. "A Numerical Study on Bubble Detachment from Solid Wall and Formation of Jet inside Detached Bubble."
39. Bonjour, Jocelyn, Marc Clause, and Monique Lallemand. "Experimental study of the coalescence phenomenon during nucleate pool boiling." *Experimental Thermal and Fluid Science* 20.3 (2000): 180-187.
40. Eastman, R. E. "Dynamics of bubble departure." In *AIAA, 19th Thermophysics Conference*, vol. 1. 1984.

41. Fuchs, Thomas, Jürgen Kern, and Peter Stephan. "A transient nucleate boiling model including microscale effects and wall heat transfer." *Journal of Heat Transfer* 128, no. 12 (2006): 1257-1265.
42. Fujikawa, Shigeo, Takeru Yano, and Masao Watanabe. *Vapor-liquid interfaces, bubbles and droplets: Fundamentals and applications*. Springer Science & Business Media, 2011.
43. Nahra, Henry K., and Y. Kamotani. "Prediction of bubble diameter at detachment from a wall orifice in liquid cross-flow under reduced and normal gravity conditions." *Chemical Engineering Science* 58, no. 1 (2003): 55-69.
44. Nigmatulin, T. R. "Surface of a Taylor bubble in vertical cylindrical flows." In *Doklady Physics*, vol. 46, no. 11, pp. 803-805. MAIK Nauka/Interperiodica, 2001.
45. Robinson, A. J., and R. L. Judd. "The dynamics of spherical bubble growth." *International journal of heat and mass transfer* 47, no. 23 (2004): 5101-5113.
46. Siedel, Samuel. *Bubble dynamics and boiling heat transfer : a study in the absence and in the presence of electric fields*. Other. INSA de Lyon, 2012. English.
47. Son, G., V. K. Dhir, and N. Ramanujapu. "Dynamics and heat transfer associated with a single bubble during nucleate boiling on a horizontal surface." *Journal of Heat Transfer* 121, no. 3 (1999): 623-631.
48. Sugrue, R., J. Buongiorno, and T. McKrell. "An experimental study of bubble departure diameter in subcooled flow boiling including the effects of orientation angle, subcooling, mass flux, heat flux, and pressure." *Nuclear Engineering and Design* 279 (2014): 182-188.
49. Trivedi, Gautam, and James E. Funk. *Dynamics and Stability of Electrolytic Bubbles: Bubble Departure Diameters*. No. THEMIS-17. KENTUCKY UNIV LEXINGTON BOILING AND PHASE-CHANGE LAB, 1970.
50. Zuber, Novak. *Hydrodynamic aspects of boiling heat transfer (thesis)*. No. AECU-4439. California. Univ., Los Angeles; and Ramo-Wooldridge Corp., Los Angeles, 1959.
51. Smolianski, Anton, Heikki Haario, and Pasi Luukka. "Vortex shedding behind a rising bubble and two-bubble coalescence: A numerical approach." *Applied mathematical modelling* 29.7 (2005): 615-632.

#### Dynamics of Bubble Formation and Separation with DEP

52. Allen, P. H. G., and T. G. Karayiannis. "Electrohydrodynamic enhancement of heat transfer and fluid flow." *Heat Recovery Systems and CHP* 15, no. 5 (1995): 389-423.
53. Cattide, A., P. Di Marco, and W. Grassi. "Evaluation of the electrical forces acting on a detaching bubble." XXV UIT National Conference, Trieste. 2007.
54. Di Bari, Sergio, and Anthony J. Robinson. "Adiabatic bubble growth in uniform DC electric fields." *Experimental Thermal and Fluid Science* 44 (2013): 114-123.
55. Di Marco, Paolo, Ryo Kurimoto, Giacomo Saccone, Kosuke Hayashi, and Akio Tomiyama. "Bubble shape under the action of electric forces." *Experimental Thermal and Fluid Science* 49 (2013): 160-168.
56. Di Marco, Paolo. "The use of electric force as a replacement of buoyancy in two-phase flow." *Microgravity Science and Technology* 24.3 (2012): 215-228.
57. Diao, Y. H., L. Guo, Y. Liu, Y. H. Zhao, and S. Wang. "Electric field effect on the bubble behavior and enhanced heat-transfer characteristic of a surface with rectangular microgrooves." *International Journal of Heat and Mass Transfer* 78 (2014): 371-379.



58. Dong, W., R. Y. Li, H. L. Yu, and Y. Y. Yan. "An investigation of behaviours of a single bubble in a uniform electric field." *Experimental Thermal and Fluid Science* 30, no. 6 (2006): 579-586.
59. Gao, Ming, Ping Cheng, and Xiaojun Quan. "An experimental investigation on effects of an electric field on bubble growth on a small heater in pool boiling." *International Journal of Heat and Mass Transfer* 67 (2013): 984-991.
60. Hristov, Y., D. Zhao, D. B. R. Kenning, K. Sefiane, and T. G. Karayiannis. "A study of nucleate boiling and critical heat flux with EHD enhancement." *Heat and mass transfer* 45, no. 7 (2009): 999-1017.
61. Kweon, Y. C., and M. H. Kim. "Experimental study on nucleate boiling enhancement and bubble dynamic behavior in saturated pool boiling using a nonuniform dc electric field." *International Journal of Multiphase Flow* 26, no. 8 (2000): 1351-1368.
62. Kweon, Y. C., et al. "Study on the deformation and departure of a bubble attached to a wall in dc/ac electric fields." *International Journal of Multiphase Flow* 24.1 (1998): 145-162.
63. Liu, Z., C. Herman, and D. Mewes. "Visualization of bubble detachment and coalescence under the influence of a nonuniform electric field." *Experimental thermal and fluid science* 31, no. 2 (2006): 151-163.
64. Pearson, Matthew R., and Jamal Seyed-Yagoobi. "Numerical study of dielectric fluid bubble behavior within diverging external electric fields." *Journal of Heat Transfer* 130, no. 3 (2008): 032901.
65. Seyed-Yagoobi, J., J. T. Hardesty, P. Raghupathi, and J. E. Bryan. "Experimental study of electrohydrodynamically augmented pool boiling heat transfer on smooth and enhanced tubes." *Journal of electrostatics* 40 (1997): 597-602.
66. Siedel, Samuel, Serge Cioulachtjian, A. J. Robinson, and Jocelyn Bonjour. "Electric field effects during nucleate boiling from an artificial nucleation site." *Experimental Thermal and Fluid Science* 35, no. 5 (2011): 762-771.
67. Siedel, Samuel, Serge Cioulachtjian, Anthony Robinson, and Jocelyn Bonjour. "Bubble Distortion due to EHD Stress." *International Journal of Plasma Environmental Science and Technology* 7, no. 1 (2013): 37-43.
68. Sunder, Shyam, and Gaurav Tomar. "Numerical simulations of bubble formation from submerged needles under non-uniform direct current electric field." *Physics of Fluids (1994-present)* 25.10 (2013): 102104.
69. Wang, Ping. "Thermal Bubble Behaviour in Liquid Nitrogen Under Electric Fields". University of Southampton PhD Thesis, October 2008.
70. Wang, Xujing, Xiao-Bo Wang, and Peter RC Gascoyne. "General expressions for dielectrophoretic force and electrorotational torque derived using the Maxwell stress tensor method." *Journal of electrostatics* 39, no. 4 (1997): 277-295.

#### DEP Enhanced Nucleate Boiling

71. Seyed-Yagoobi, J., C. A. Geppert, and L. M. Geppert. "Electrohydrodynamically enhanced heat transfer in pool boiling." *Journal of heat transfer* 118, no. 1 (1996): 233-237.

72. Behnke, E., T. Benjamin, S. J. Brice, D. Broemmelsiek, J. I. Collar, P. S. Cooper, M. Crisler et al. "Direct measurement of the bubble-nucleation energy threshold in a CF 3 I bubble chamber." *Physical Review D* 88, no. 2 (2013): 021101.
73. Di Marco, P., W. Grassi, G. Memoli, T. Takamasa, A. Tomiyama, and S. Hosokawa. "Influence of electric field on single gas-bubble growth and detachment in microgravity." *International Journal of Multiphase Flow* 29, no. 4 (2003): 559-578.
74. Di Marco, Paolo. "The use of electric force as a replacement of buoyancy in two-phase flow." *Microgravity Science and Technology* 24, no. 3 (2012): 215-228.
75. Forster, Christopher J., and Marc K. Smith. "The Transient Modeling of Bubble Pinch-Off Using an ALE Moving Mesh." (2010).
76. Iacona, Estelle, Cila Herman, Shinan Chang, and Zan Liu. "Electric field effect on bubble detachment in reduced gravity environment." *Experimental thermal and fluid science* 31, no. 2 (2006): 121-126.
77. Kurgan, Eugeniusz. "Stress Calculation in Two-Dimensional DC Dielectrophoresis." *PRZEGLAD ELEKTROTECHNICZNY* 87, no. 12 B (2011): 107-110.
78. Pachosa, D. M., and J. N. Chung. "Dielectrophoresis-driven nucleate boiling in a simulated microgravity environment." *Journal of heat transfer* 115, no. 2 (1993): 495-498.
79. Pearson, Matthew R., and Jamal Seyed-Yagoobi. "EHD Conduction-Driven Enhancement of Critical Heat Flux in Pool Boiling." *Industry Applications, IEEE Transactions on* 49, no. 4 (2013): 1808-1816.
80. Pearson, Matthew R., and Jamal Seyed-Yagoobi. "Numerical study of dielectric fluid bubble behavior within diverging external electric fields." *Journal of Heat Transfer* 130, no. 3 (2008): 032901.
81. Rosales, Carlos, and Kian Meng Lim. "Numerical comparison between Maxwell stress method and equivalent multipole approach for calculation of the dielectrophoretic force in single-cell traps." *Electrophoresis* 26, no. 11 (2005): 2057-2065.
82. Schweizer, Nils, Paolo Di Marco, and Peter Stephan. "Investigation of wall temperature and heat flux distribution during nucleate boiling in the presence of an electric field and in variable gravity." *Experimental Thermal and Fluid Science* 44 (2013): 419-430.
83. Sefiane, Khellil, Y. Hristov, D. B. R. Kenning, Tassos G. Karayiannis, and D. Zhao. "MODELLING OF THE GROWTH AND DETACHMENT OF A VAPOUR BUBBLE AND THE EFFECT OF AN ELECTRIC FIELD IN THE NUCLEATE BOILING REGIME." In *International Heat Transfer Conference 13*. Begel House Inc., 2006.
84. Seyed-Yagoobi, J., and J. E. Bryan. "Enhancement of heat transfer and mass transport in single-phase and two-phase flows with electrohydrodynamics." *Advances in Heat Transfer* 33 (1999): 95-186.
85. Snyder, T. J., and J. N. Chung. "Terrestrial and microgravity boiling heat transfer in a dielectrophoretic force field." *International journal of heat and mass transfer* 43, no. 9 (2000): 1547-1562.
86. Snyder, Trevor J., Jacob N. Chung, and John B. Schneider. "Dielectrophoresis with application to boiling heat transfer in microgravity. II. Experimental investigation." *Journal of Applied Physics* 89, no. 7 (2001): 4084-4090.

87. Snyder, Trevor J., John B. Schneider, and Jacob N. Chung. "Dielectrophoresis with application to boiling heat transfer in microgravity. I. Numerical analysis." *Journal of Applied Physics* 89, no. 7 (2001): 4076-4083.
88. Stratton, Julius Adams. *Electromagnetic theory*. John Wiley & Sons, 2007.
89. Zu, Y. Q., and Y. Y. Yan. "A numerical investigation of electrohydrodynamic (EHD) effects on bubble deformation under pseudo-nucleate boiling conditions." *International Journal of Heat and Fluid Flow* 30, no. 4 (2009): 761-767.

#### Electrohydrodynamics/DEP

90. Castellanos, Antonio, ed. *Electrohydrodynamics*. Vol. 380. Springer, 2014.
91. Castellanos, Antonio, et al. "Electrohydrodynamics and dielectrophoresis in microsystems: scaling laws." *Journal of Physics D: Applied Physics* 36.20 (2003): 2584.
92. Melcher, James R. *Continuum electromechanics*. Vol. 2. Cambridge: MIT press, 1981.
93. Pohl, Herbert A. *Dielectrophoresis: the behavior of neutral matter in nonuniform electric fields*. Vol. 80. Cambridge: Cambridge university press, 1978.
94. Pohl, Herbert A. "The motion and precipitation of suspensoids in divergent electric fields." *Journal of Applied Physics* 22.7 (1951): 869-871.
95. Wall, Staffan, et al. "The History of Electrokinetic Phenomena." *Current Opinion in Colloid & Interface Science* 15.3 (2010): 119-24. Web.
96. Whittaker, Edmund. "History of the Theories of Aether and Electricity." *Soil Science* 77.5 (1954): 417.

#### HFE-7100 Nucleate Boiling

97. El-Genk, Mohamed S., and Huseyin Bostanci. "Saturation boiling of HFE-7100 from a copper surface, simulating a microelectronic chip." *International Journal of Heat and Mass Transfer* 46.10 (2003): 1841-1854.
98. Gaertner, R. F. "Photographic study of nucleate pool boiling on a horizontal surface." *Journal of Heat Transfer* 87.1 (1965): 17-27.
99. Kunkelmann, C., Stephan, Peter. "Numerical Simulation of the transient heat transfer during nucleate boiling of refrigerant HFE-7100". *International Journal of Refrigeration*. 2010
100. Liu, J. W., D. J. Lee, and A. Su. "Boiling of methanol and HFE-7100 on heated surface covered with a layer of mesh." *International journal of heat and mass transfer* 44.1 (2001): 241-246.
101. Misale, M., G. Guglielmini, and A. Priarone. "HFE-7100 pool boiling heat transfer and critical heat flux in inclined narrow spaces." *international journal of refrigeration* 32.2 (2009): 235-245.

#### DEP In Microgravity

102. Jones, T. B. *Application of Electrohydrodynamic Phenomena to Space Processing*. Tech. no. 75N22345. N.p.: United States, 1975.

103. Jones, Thomas B. "On the relationship of dielectrophoresis and electrowetting." *Langmuir* 18.11 (2002): 4437-4443.

### Introductory Concepts

104. Bergman, Theodore L., Frank P. Incropera, and Adrienne S. Lavine. *Fundamentals of heat and mass transfer*. John Wiley & Sons, 2011.
105. "Five Strategies for Cutting Data Center Energy Costs Through Enhanced Cooling Efficiency" Emerson Network Power. 2007. [http://www.emersonnetworkpower.com/documentation/en-us/brands/liebert/documents/white%20papers/data-center-energy-efficiency\\_151-47.pdf](http://www.emersonnetworkpower.com/documentation/en-us/brands/liebert/documents/white%20papers/data-center-energy-efficiency_151-47.pdf)
106. Bejan, Adrian and Kraus, Allan D. *Heat Transfer Handbook, Volume 1*. John Wiley & Sons, 2003.
107. Azar, Kaveh. "The History of Power Dissipation." *The History of Power Dissipation*. Electronics Cooling, 20 Jan. 2000. Web. 08 Jan. 2016.
108. Kakac, Sadk, et al., eds. *Microscale Heat Transfer-Fundamentals and Applications: Proceedings of the NATO Advanced Study Institute on Microscale Heat Transfer-Fundamentals and Applications in Biological and Microelectromechanical Systems, Cesme-Izmir, Turkey, 18-30 July, 2004*. Vol. 193. Springer Science & Business Media, 2006.
109. Lakshminarayanan, V., and N. Sriraam. "The effect of temperature on the reliability of electronic components." *Electronics, Computing and Communication Technologies (IEEE CONECCT), 2014 IEEE International Conference on*. IEEE, 2014.
110. Moore, Gordon E. "Cramming more components onto integrated circuits, *Electronics*, 38: 8 (1965)." URL: <ftp://download.intel.com/research/silicon/moorespaper.pdf> 16 (2005).
111. Wirth, Eric. *Thermal management in embedded systems*. Diss. University of Virginia, 2004.

### Two Phase Modeling and Flow

112. "COMSOL Main Page." *COMSOL Multiphysics® Modeling Software*. N.p., n.d. Web. 21 Sept. 2016. <<http://www.comsol.com/>>
113. COMSOL (2015). *CFD Module User's Guide* (COMSOL version 5.2). Included with COMSOL software package, Retrieved 10/1/16.
114. Cheung, Sherman CP, G. H. Yeoh, and J. Y. Tu. "On the modelling of population balance in isothermal vertical bubbly flows—average bubble number density approach." *Chemical Engineering and Processing: Process Intensification* 46.8 (2007): 742-756.
115. Jackson, John David. *Classical electrodynamics*. Wiley, 1999.
116. Jamet, Didier. "Diffuse interface models in fluid mechanics." GdR CNRS documentation, see [pmc.polytechnique.fr/mp/GDR/docu/Jamet.pdf](http://pmc.polytechnique.fr/mp/GDR/docu/Jamet.pdf) (2010).
117. Schlegel, Fabrice. "Which Multiphase Flow Interface Should I Use?" COMSOL Blog Which Multiphase Flow Interface Should I Use Comments. COMSOL, 26 Jan. 2015.

Web. 27 Jan. 2016. <<http://www.comsol.com/blogs/which-multiphase-flow-interface-should-i-use/>>.

118. Son, Gihun, and Vijay K. Dhir. "A level set method for analysis of film boiling on an immersed solid surface." *Numerical Heat Transfer, Part B: Fundamentals* 52.2 (2007): 153-177.
119. Osher, Stanley, and James A. Sethian. "Fronts propagating with curvature-dependent speed: algorithms based on Hamilton-Jacobi formulations." *Journal of computational physics* 79.1 (1988): 12-49.
120. Yue, Pengtao, et al. "A diffuse-interface method for simulating two-phase flows of complex fluids." *Journal of Fluid Mechanics* 515 (2004): 293-317.
121. Kandlikar, Satish G. *Handbook of phase change: boiling and condensation*. CRC Press, 1999.
122. Hartmann, William M. *Signals, sound, and sensation*. Springer Science & Business Media, 1997.
123. Phan-Thien, Nhan. *Understanding viscoelasticity: basics of rheology*. Springer Science & Business Media, 2013.
124. Dunec, John. *Heat Transfer Simulations* [webinar] 9 August 2012. <http://video.webcasts.com/events/pmny001/viewer/index.jsp?eventid=43397>

#### Minichannels

125. Sturgis, J. Christopher, and Issam Mudawar. "Critical heat flux in a long, rectangular channel subjected to one-sided heating—I. Flow visualization." *International journal of heat and mass transfer* 42.10 (1999): 1835-1847.1
126. Galloway, J. E., and I. Mudawar. "CHF mechanism in flow boiling from a short heated wall—I. Examination of near-wall conditions with the aid of photomicrography and high-speed video imaging." *International Journal of Heat and Mass Transfer* 36.10 (1993): 2511-2526.
127. Kandlikar, Satish G. "Fundamental issues related to flow boiling in minichannels and microchannels." *Experimental Thermal and Fluid Science* 26.2 (2002): 389-407.
128. Kandlikar, Satish G. "Nucleation characteristics and stability considerations during flow boiling in microchannels." *Experimental Thermal and Fluid Science* 30.5 (2006): 441-447.
129. Kandlikar, Satish G., et al. "Stabilization of flow boiling in microchannels using pressure drop elements and fabricated nucleation sites." *Journal of Heat Transfer* 128.4 (2006): 389-396.
130. Cubaud, Thomas, Umberto Ulmanella, and Chih-Ming Ho. "Two-phase flow in microchannels with surface modifications." *Fluid Dynamics Research* 38.11 (2006): 772-786.
131. Moghanlou, Farhad Sadegh, et al. "Experimental study on electrohydrodynamically induced heat transfer enhancement in a minichannel." *Experimental Thermal and Fluid Science* 59 (2014): 24-31.

132. Brutin, David, F. Topin, and L. Tadrist. "Experimental study of unsteady convective boiling in heated minichannels." *International Journal of Heat and Mass Transfer* 46.16 (2003): 2957-2965.
133. Pak, Bockchoon, Young I. Cho, and Stephen US Choi. "Separation and reattachment of non-Newtonian fluid flows in a sudden expansion pipe." *Journal of Non-Newtonian Fluid Mechanics* 37.2 (1990): 175-199.
134. Schetz, Joseph A., and Allen E. Fuhs. *Fundamentals of fluid mechanics*. John Wiley & Sons, 1999.

#### Embedded Systems

135. Zurawski, Richard, ed. *Embedded Systems Handbook: Embedded Systems Design and Verification*. Vol. 6. CRC Press, 2009.
136. Zurawski, Richard, ed. *Embedded systems handbook*. CRC Press, 2005.
137. Kakaç, Sadik, et al., eds. *Microscale Heat Transfer-Fundamentals and Applications: Proceedings of the NATO Advanced Study Institute on Microscale Heat Transfer-Fundamentals and Applications in Biological and Microelectromechanical Systems, Cesme-Izmir, Turkey, 18-30 July, 2004*. Vol. 193. Springer Science & Business Media, 2006.

## 8. Appendices

### 8.1. Appendix A: System Design Background & Trial Details

#### 8.1.1. Isolation Amplifier Design Background

The following information was used to help guide the voltage divider resistor choices used in the isolation amplifier box. Resistors are chosen to satisfy the specified voltage inputs, but also to ensure maximum battery life.

Table 12: Isolation Amplifier Properties used in Calculation [82].

<b>Parameter</b>	<b>Test Conditions</b>	<b>Min</b>	<b>Typ</b>	<b>Max</b>	<b>Unit</b>
VDD1 high supply		4.5	5	5.5	V
VDD2 low supply		2.7	5	5.5	V
$I_{DD1}$ high current			5.4	8	mA
$I_{DD2}$ low current	$4.5 < VDD2 < 5.5$		4.4	7	mA
$P_{DD1}$ high power diss.			27	44	mW
$P_{DD1}$ low power diss.	$4.5 < VDD2 < 5.5$		22	38.5	mW

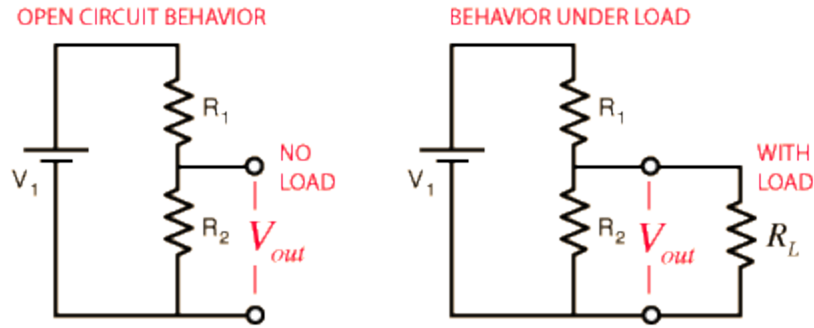


Figure 94: Voltage Divider Resistances ©C.R. Nave [99].

$$V_{out} = V_1 \left( \frac{IR_2}{I(R_1 + R_2)} \right) = \frac{V_1 R_2}{R_1 + R_2}$$

$$V_{out} = V_1 \left( \frac{IR_2}{I(R_1 + R_2)} \right) = V_1 \frac{(R_2 || R_L)}{(R_1 + R_2 || R_L)}$$

$$R_2 || R_L = \frac{R_2 R_L}{R_2 + R_L}$$

The specifications can be used to solve for the internal resistance  $R_L$  (which is not given). Using “typical” conditions, the power dissipation in the AMC1100 will be 27mW with a potential of 5V.

$$P = \frac{V^2}{R_L}$$

Solving for the internal resistance:

$$R_L = 925.9\Omega$$

Assuming this, and given that the voltage input into the divider will be 9V, we can solve for the two resistors in the voltage divider.

Arbitrarily setting  $R_1 = 550\Omega$  (this corresponds to the maximum amount so that the “open circuit” does not exceed 5.5 with a small safety factor)



$$V_{out} = V_1(R_2||R_L)/(R_1 + R_2||R_L)$$

$$5[V] = 9[V] (R_2||R_L)/(550\Omega + R_2||R_L)$$

$$687.5 = (R_2||R_L)$$

$$R_2||R_L = 687.5 = \frac{R_2R_L}{R_2 + R_L}$$

$$R_2 = 2670.12\Omega$$

$R_1$  and  $R_2$  are found. Given this, the potential for a theoretical “maximum case” can be calculated, given an input voltage of 9V and a chip loading corresponding to “maximum” conditions, which is 44mW and 5.5V (corresponding to a  $R_L = 687.5$ )

$$R_2||R_L = \frac{R_2R_L}{R_2 + R_L} = 546.72$$

$$V_{out} = V_1(R_2||R_L)/(R_1 + R_2||R_L)$$

$$V_{out} = 9[V] (R_2||R_L)/(550\Omega + R_2||R_L)$$

$$V_{out} = 4.488$$

Still well within specifications. With these resistors, the total power consumed by the entire device can be found. The total resistance “seen” by the battery is a series of  $R_1$  and  $(R_2||R_L)$ , which is 337.5 $\Omega$ .

$$P = \frac{V^2}{R}$$

$$P = 240[mW]$$

Solving for the current, we can use the energy stored in the battery to find total battery life.

$$P = I^2 R$$

$$I = 26.67[mA]$$

Given that the minimum AMC1100 input voltage is 4.5V, this corresponds to a  $V_1$  battery input of 8.1V. According to this plot, at a 100mA current (for a factor of safety), this means that the battery has an approximate life of 50mAh before dropping below that voltage. This would correspond to a battery life of around two hours continuous. Considering the device will only be powered on before high voltage events (lasting a few seconds at most), this should be acceptable. Realistically, the energizer has a total capacity of approximately 500mAh for a 40mA drain, which would mean that the capacity before dropping below 8.1V would be much less.

For the low side:

The specifications can be used to solve for the internal resistance  $R_L$  (which is not given). Using “typical” conditions, the power dissipation in the AMC1100 will be 22mW with a potential of 5V.

$$P = \frac{V^2}{R_L}$$

Solving for the internal resistance:

$$R_L = 1136.36\Omega$$

Assuming this, and given that the voltage input into the divider will be 9V, we can solve for the two resistors in the voltage divider.

Arbitrarily setting  $R_1 = 680\Omega$  (this corresponds to the maximum amount so that the “open circuit” does not exceed 5.5 with a small safety factor)

$$V_{out} = V_1(R_2 || R_L) / (R_1 + R_2 || R_L)$$

$$5[V] = 9[V] (R_2 || R_L) / (680\Omega + R_2 || R_L)$$

$$850 = (R_2 || R_L)$$

$$R_2 || R_L = 850 = \frac{R_2 R_L}{R_2 + R_L}$$

$$R_2 = 3373\Omega$$

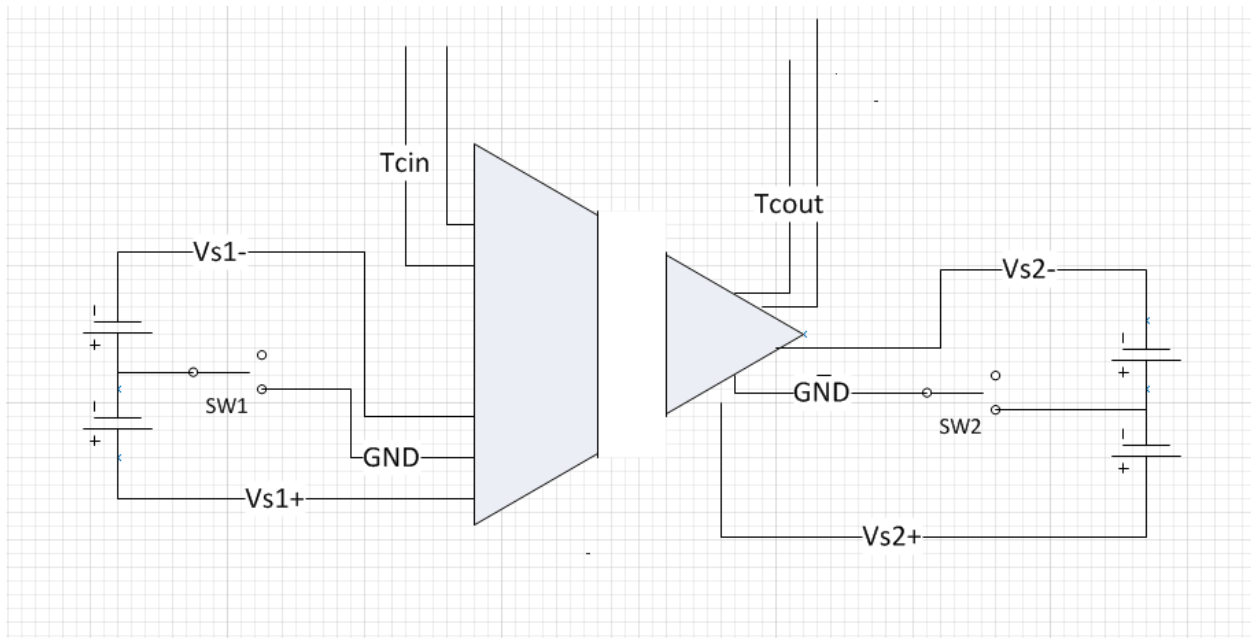


Figure 95: Schematic of Isolation Amplifier Circuit.

8.1.2. Table of Trials

<b>Trial Name</b>	<b>EHD</b>	<b>Polarity</b>	<b>Fluid Temperature In [°C]</b>	<b>Wall Temperature [°C]</b>
Test#1	Debug, no conditions recorded (white boxes)			
Test#2				
Test#3				
Test#4				
Test#5				
Test#6				
Test#7				
Test#8				
Test#9				
Test#10				
Test#11				
Test#12	Yes		46	
Test#13	No		46	
Test#14	No			
Test#15	Yes			
Test#16	No			

Test#17	Yes			
Test#18	Yes			
Test#19				
Test#20				
Test#21				
Test#22				
Test#23				
Test#24				
Test#25				
Test#26				
Test#27				
Test#28				
Test#29				
Test#30				
Test#31				
Test#32				
Test#33				
Test#34				
Test#35	Yes	Baseline	24.6	See Appendix 8.1.4
Test#36				
Test#37				
Test#38				

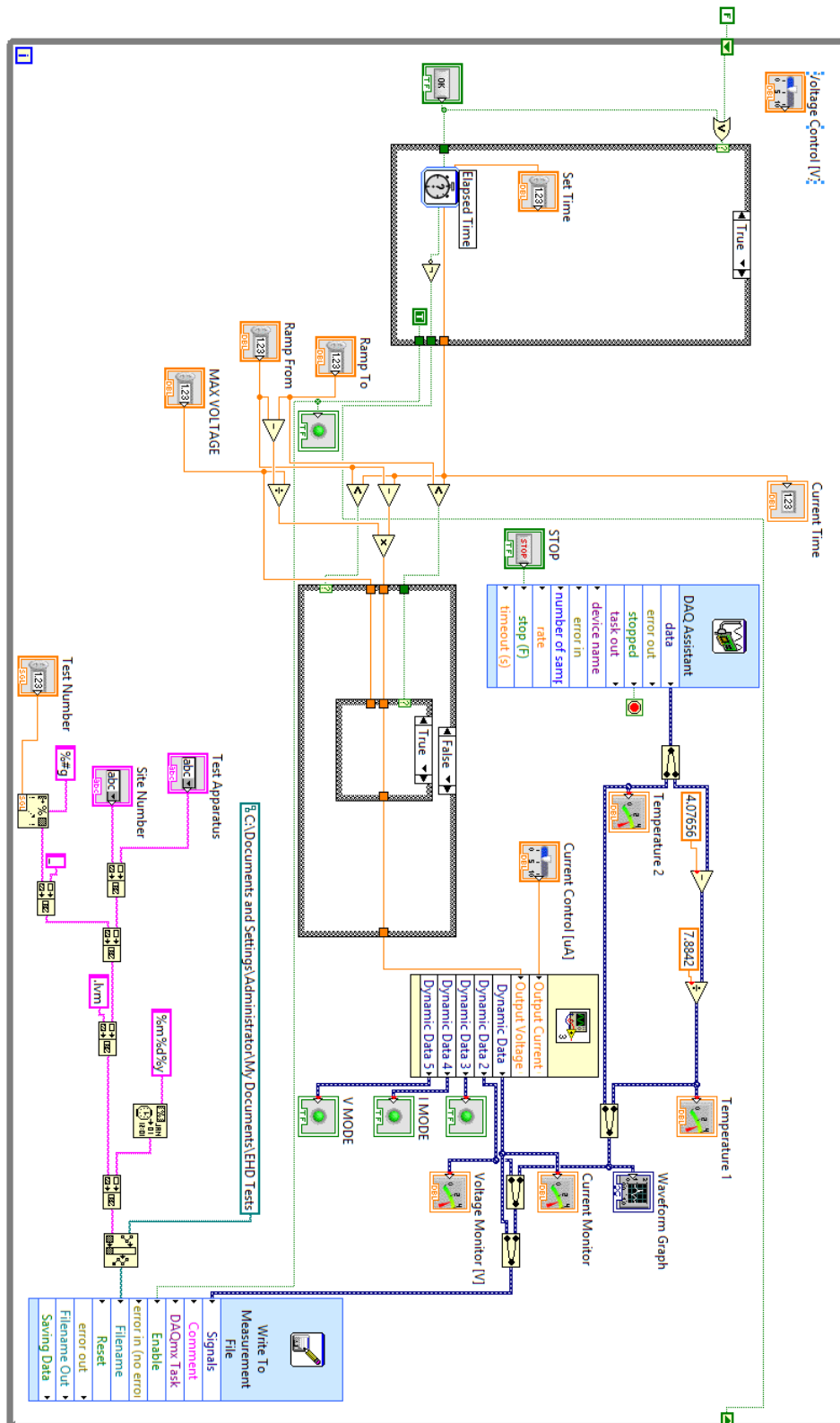
Test#39				
Test#40				
Test#41				
Test#42				
Test#43				
Test#44				
Test#45				
Test#46				
Test#47				
Test#48				
Test#49				
Test#50				
Test#51				
Test#52				
Test#53				
Test#54				
Test#55				
Test#56				
Test#57	1000V, 2s linear ramp	Baseline	24.6	See Appendix 8.1.4
Test#58	2000V, 2s linear ramp	Baseline	24.6	See Appendix 8.1.4

Test#59	4000V, 2s linear ramp	Baseline	24.6	See Appendix 8.1.4
Test#60	1000V, 2s linear ramp	Baseline	24.6	See Appendix 8.1.4
Test#61	2000V, 2s linear ramp	Baseline	24.6	See Appendix 8.1.4
Test#62	4000V, 2s linear ramp	Baseline	24.6	See Appendix 8.1.4
Test#63	1000V, 2s linear ramp	Baseline	24.6	See Appendix 8.1.4
Test#64	2000V, 2s linear ramp	Baseline	24.6	See Appendix 8.1.4
Test#65	4000V, 2s linear ramp	Baseline	24.6	See Appendix 8.1.4
Test#66	1000V, 2s linear ramp	Reversed	24.6	See Appendix 8.1.4
Test#67	2000V, 2s linear ramp	Reversed	24.6	See Appendix 8.1.4
Test#68	4000V, 2s linear ramp	Reversed	24.6	See Appendix 8.1.4
Test#69	1000V, 2s linear ramp	Reversed	24.6	See Appendix 8.1.4

Test#70	2000V, 2s linear ramp	Reversed	24.6	See Appendix 8.1.4
Test#71	4000V, 2s linear ramp	Reversed	24.6	See Appendix 8.1.4
Test#72	1000V, 2s linear ramp	Reversed	24.6	See Appendix 8.1.4
Test#73	2000V, 2s linear ramp	Reversed	24.6	See Appendix 8.1.4
Test#74	4000V, 2s linear ramp	Reversed	24.6	See Appendix 8.1.4
Test#75	400V, 3s linear ramp	Reversed	24.6	See Appendix 8.1.4



### 8.1.3. LabVIEW VI



#### 8.1.4. Selected Trial Test Conditions

Within this study, a subset of all trials conducted were used for statistical analysis, or for snapshots to be presented visually. The full test conditions for all trials used in this manner are provided here (Trial#35, Trial#57, Trial#58, Trial#59, Trial#60, Trial#61, Trial#62, Trial#63, Trial#69).

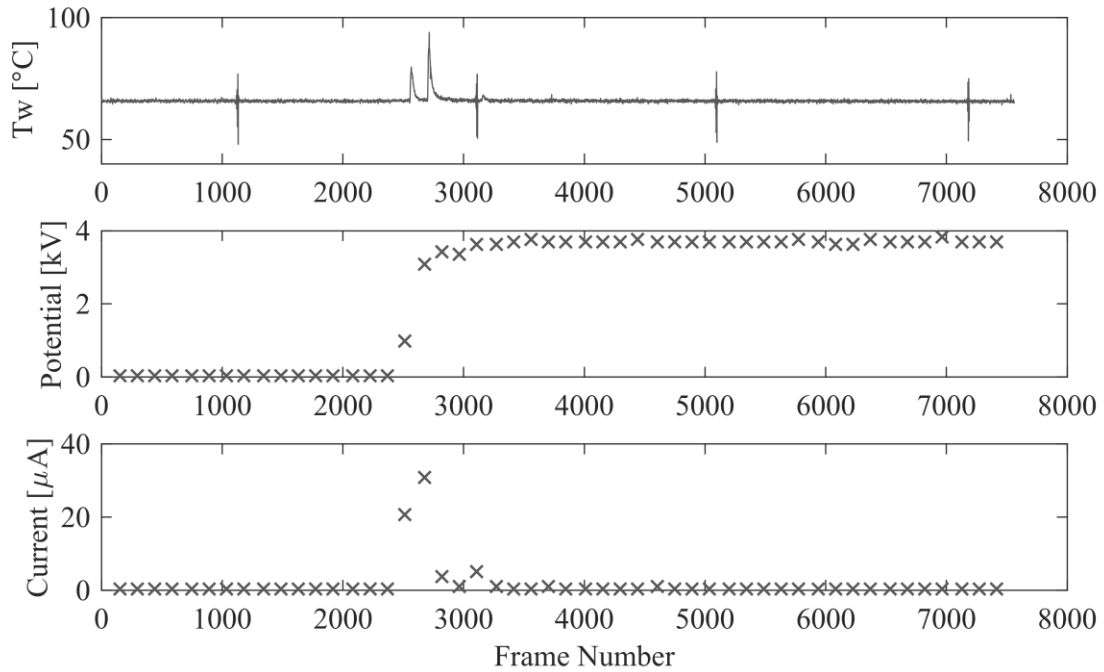


Figure 96: Test Conditions for Trial#35.

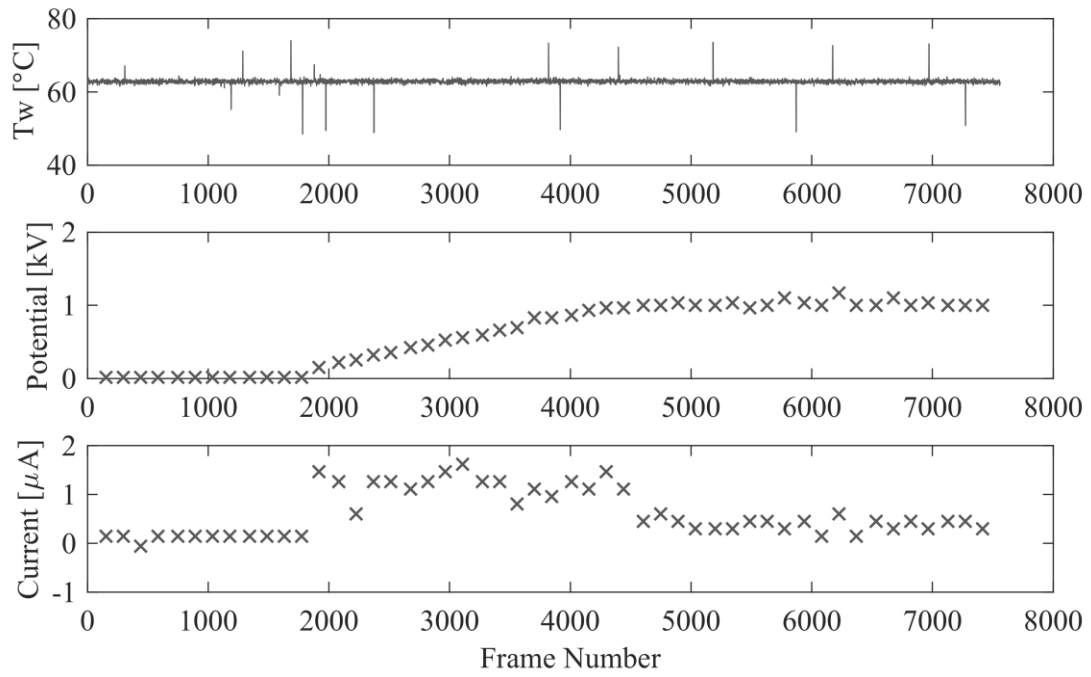


Figure 97: Test Conditions for Trial#57.

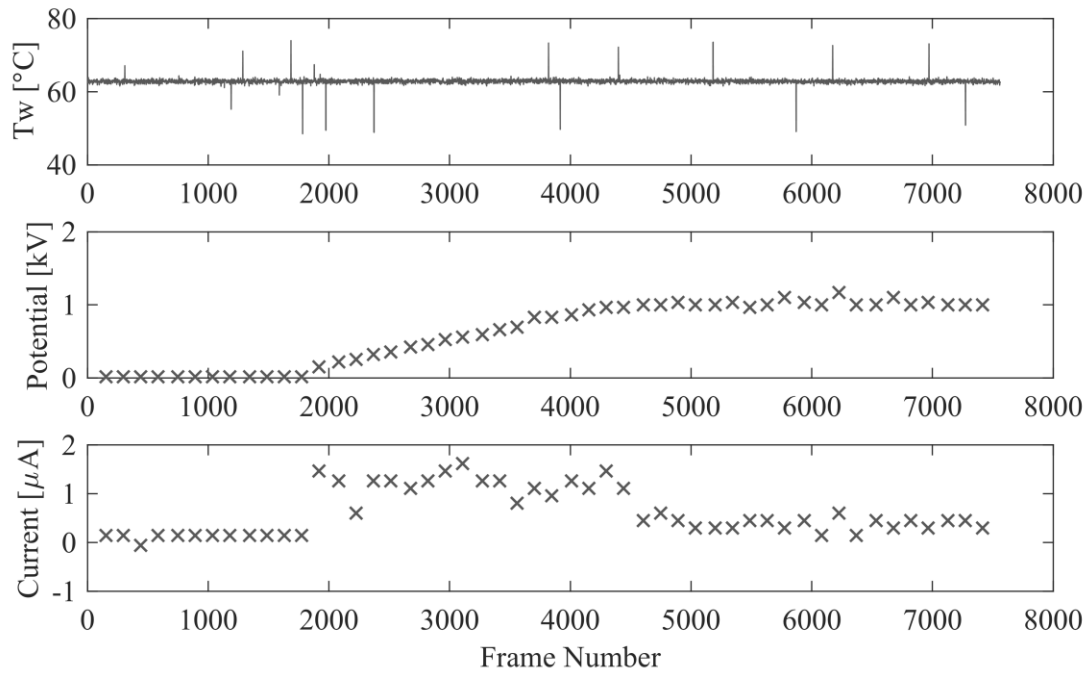


Figure 98: Test Conditions for Trial#58.

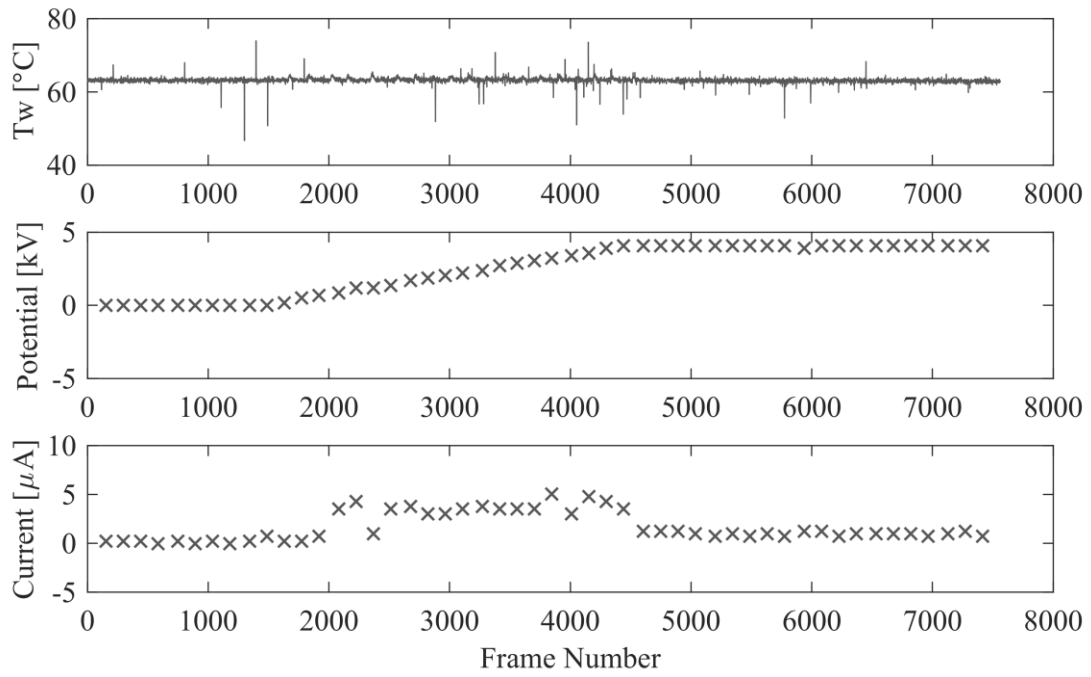


Figure 99: Test Conditions for Trial#59.

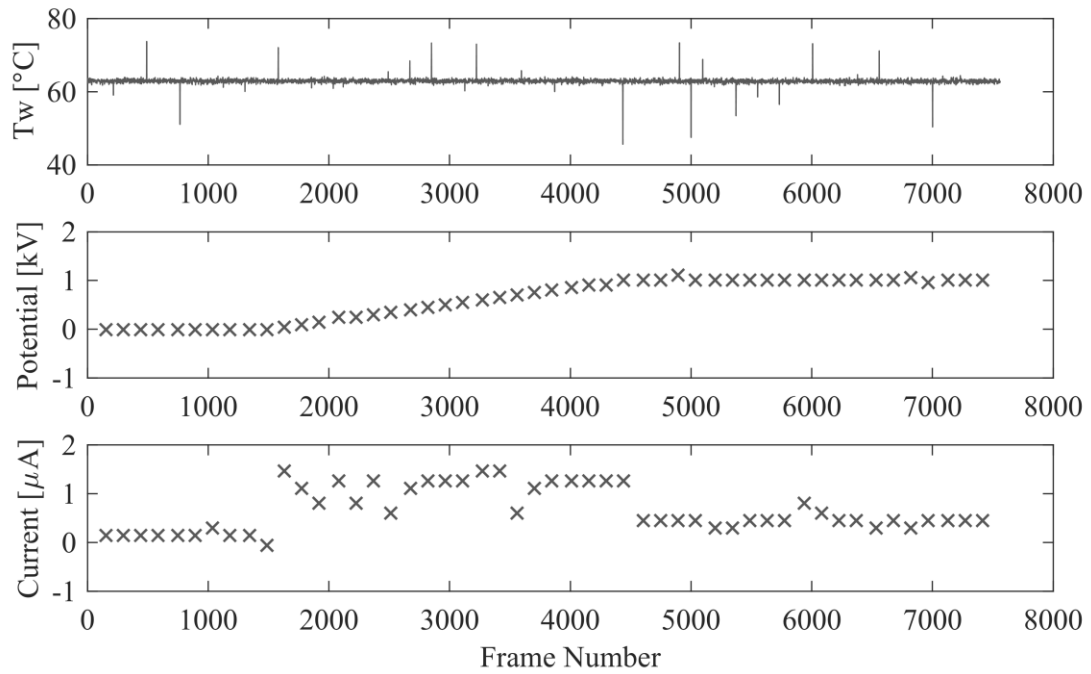


Figure 100: Test Conditions for Trial#60.

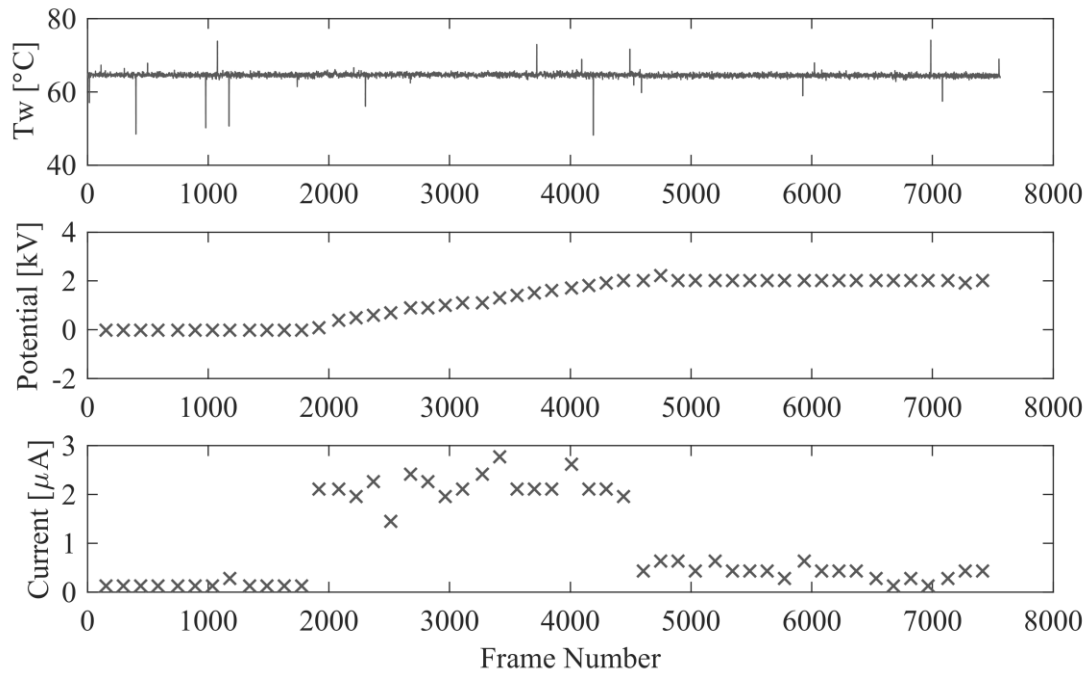


Figure 101: Test Conditions for Trial#61.

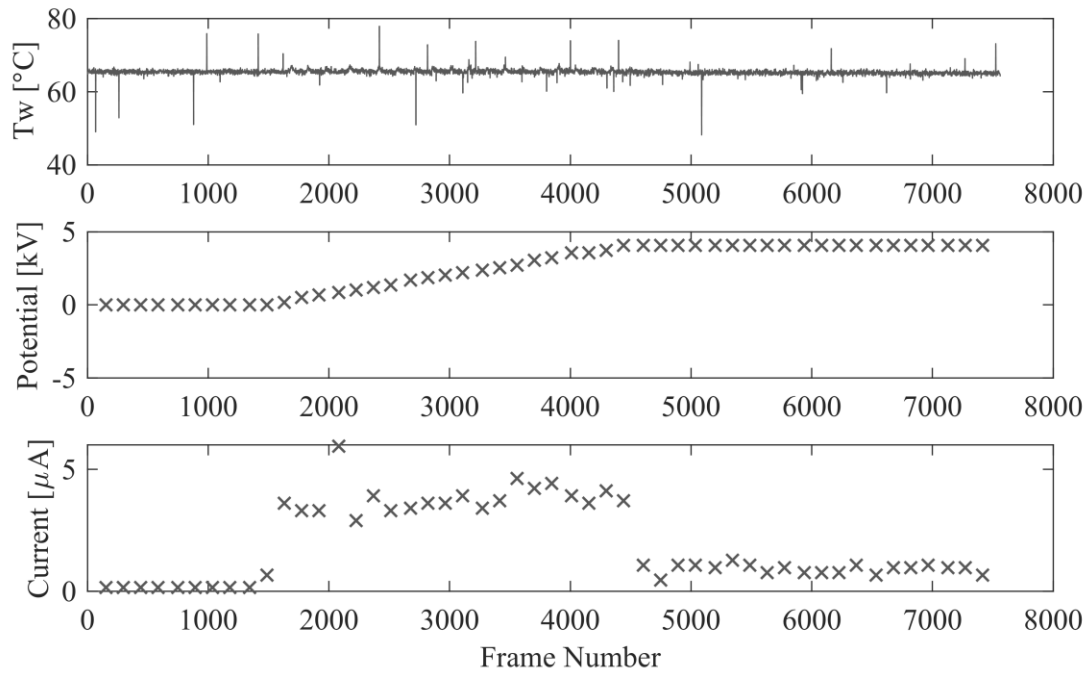


Figure 102: Test Conditions for Trial#62.

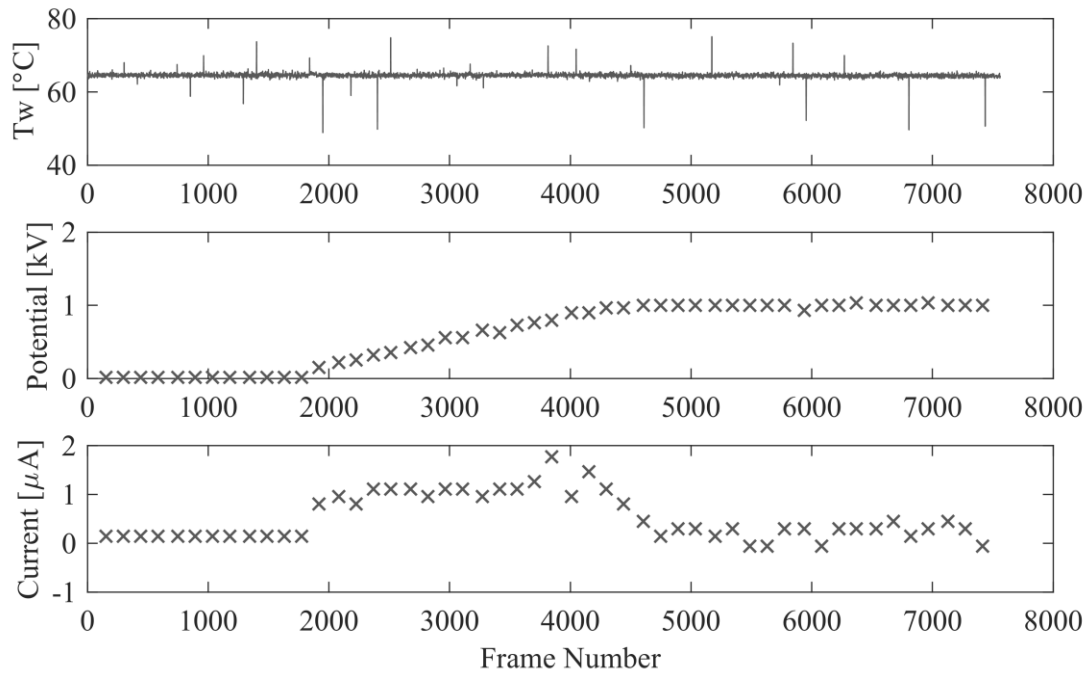


Figure 103: Test Conditions for Trial#63.

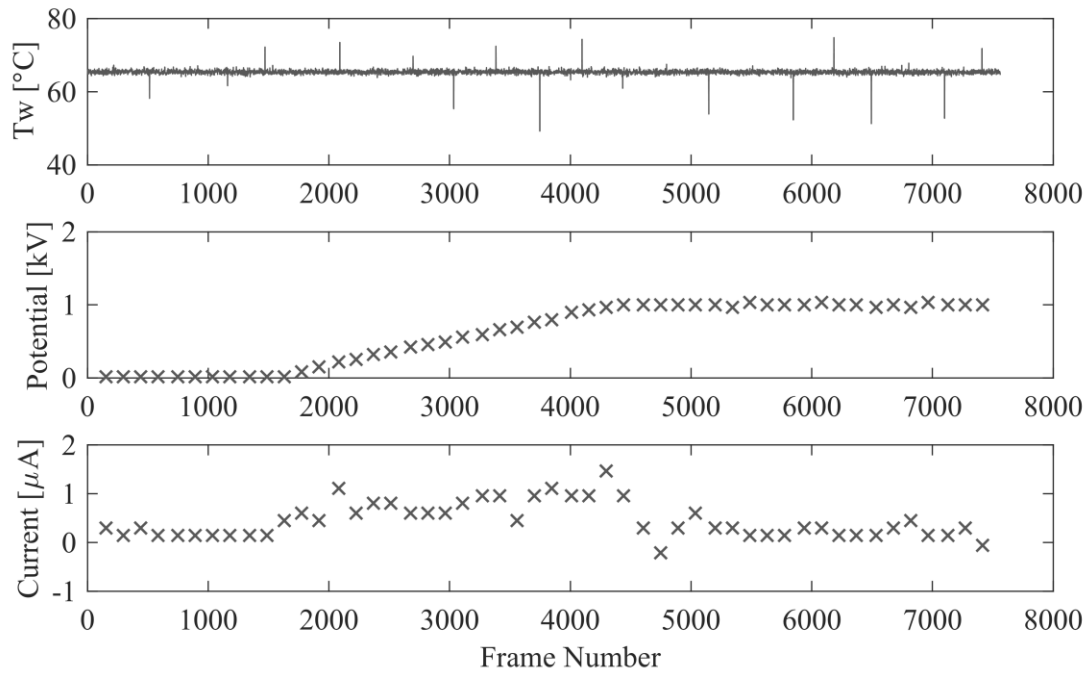


Figure 104: Test Conditions for Trial#69.

## 8.2. Appendix B: Debugging and Setup Validation

Initial tests were to verify the viability of the apparatus construction method, capturing images with a high speed camera, and ensuring that the heater can adequately bring the bottom electrode to a temperature enough to boil HFE-7100. The first tests of this system will be on a flat sheet of copper in order to ascertain how well the setup can capture bubble growth and departure in a small channel. Initial tests did not include the use of the fluid pump or unheated entry length, instead corresponding to pool boiling in a constrained channel, with a relief hole for vapor.

Further tests ensure that the system is able to maintain such a large potential across both surfaces without arcing. (show current vs. potential) Floating the bottom electrode at high potentials required careful consideration. First, the isolation equipment must be tested to ensure that any components downstream of it would not be damaged, and that the output sensor voltage remains consistent with the input signal voltage. While the AMC1100 was able to protect downstream components from transient overvoltages, there was no guarantee that floating the thermocouple at a high potential would yield the same measurement result. As a test for a constant voltage source, a AA battery was used with a voltage divider consisting of  $1.5\text{k}\Omega$  and  $150\Omega$  resistors. The resulting  $144\text{mV}$  supply voltage is passed through the isolation amplifier device, where an expected gain of 8 yields an output of  $1.129\text{V}$  (corresponding to a “calculated” input voltage of  $141.1\text{mV}$  corrected for gain) for an error of 2.0%. Next, the AA battery is floated at increasingly higher temperatures to ensure the output does not change, shown in Figure 105.

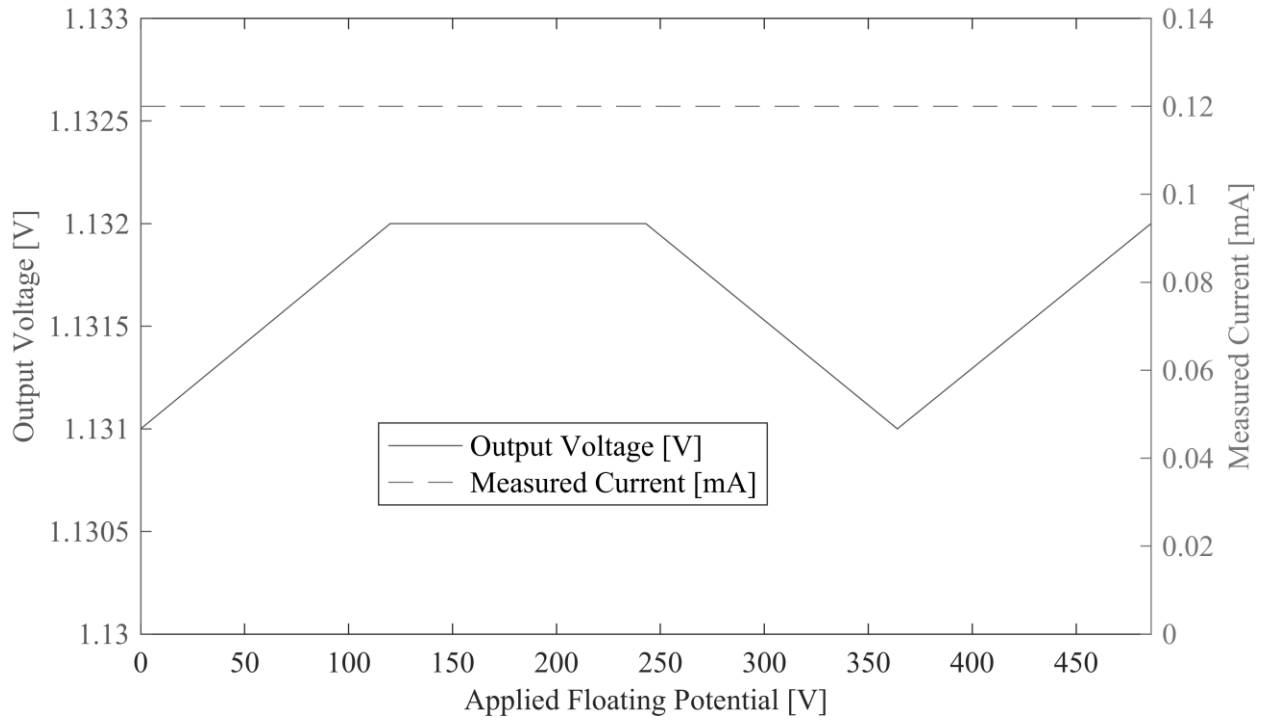


Figure 105: Verification of isolation amplifier effectiveness.

At its most severe swing, the output voltage changes by 0.001mV, a 0.09% difference when compared to the magnitude of measured output, which lends confidence to the accuracy of the isolation amplifier device both under the application of an external electric field, and when subjected to repeat tests.



## 8.3. Appendix C: MATLAB Scripts Used in Analysis

### 8.3.1. BubbleCounter.m

```
% Image Processing Automation
%This script allows for manual bubble counting within a video

clc
clear
close all
%% Add path of interest
%Points script to location where a given case's discretized frames are
%stored
path = '1466641636';
% %Add the path to the current folder
addpath(path)

%% State frames of interest
dialog = sprintf('Are the Selected frames with or without EHD?');
button = questdlg(dialog, 'Select Case', 'Without EHD', 'With
EHD', 'Cancel', 'Cancel');
if strcmpi(button, 'With EHD')
    EHD = 'EHDon';
else if strcmpi(button, 'Without EHD')
    EHD = 'EHDooff';
end
end

%Choose the frame range in which to perform analysis
%Typically, do one set pre-EHD, and one post-EHD
%Frames chosen should not include any ramping
FrameStart = 5001;
FrameEnd = 6501;
%Resolution in which to display and analyze images
spacing = 30;

FrameVector = FrameStart+spacing:spacing:FrameEnd

WidthVector = zeros(1,FrameEnd-FrameStart)

for j = 1:length(FrameVector)
    if j==1
        fstart = FrameStart;
    else
        fstart = FrameVector(j-1)
    end
    fend = FrameVector(j)
    numfiles = fend-fstart;

    % Only copy frame(fstart) to frame(fend) files to a temporary directory
    %Crease a temporary directory
    mkdir('temp')
    addpath('temp')
    %"Base" filename in which to construct image filenames
```

```

filename = 'frame';
filenum = fstart;

%% Copy range of files from directory to the temporary folder
%assign a string number
number = num2str(filenum);
%Append string number to filename
filename = strcat(path, '/', filename, number, '.jpg');
%Copy file to temporary directory
copyfile(filename, 'temp')

%% Manual image processing on each
cd('temp')
%Display each image (as dictated by the "spacing" variable, and count the
%number of markers representing nucleating bubbles. Each bubble can and may
%be counted twice, as taking a large number of samples will average out
%bubbles nucleating and departing

%Shorten filename (because temp directory is the root)
filename(1:11) = [];
imshow(filename)
hold on
counter = 0;

dialog = sprintf('Select currently nucleating bubbles. Hit "Enter" when
done');
title(dialog, 'FontSize', 14);
button = questdlg(dialog, 'Continue?', 'OK', 'Cancel', 'OK');
drawnow; % Refresh screen to get rid of dialog box remnants.
if strcmpi(button, 'Cancel')
    return;
end

while counter < 100 %automatically stops for too many bubbles
    % User clicks one point. If no point is selected, loop will end

    [bubblex, bubbley] = ginput(1);
    if isempty(bubblex)
        break;
    end

    % Put a cross over the point.
    plot(bubblex, bubbley, 'g+', 'MarkerSize', 24, 'LineWidth', 3);
    % Increment the count.
    counter = counter + 1

end

numbubbles(j) = counter

```

```

    cd ..

end

%% Post Processing
%Save data to a figure

clearvars -except EHD WidthVector j FrameStart FrameEnd spacing FrameVector
path numbubbles
%% Delete temporary directory
%Delete folder and all contents
rmdir('temp','s')
%Refresh MATLAB to ensure file can be created again
rehash()

exportfilename = strcat(path, '_',EHD, '.txt')
T = table(numbubbles)
writetable(T,exportfilename)

figure
histogram(numbubbles,10)
xlabel('Number of Nucleation Sites')
ylabel('Frequency')

```

### 8.3.2. BubbleCounter\_wPosition.m

```

%% Image Processing Automation
%This script allows for manual bubble counting within a video

clc
clear
close all
%% Add path of interest
%Points script to location where a given case's discretized frames are
%stored
path = '1466641070';
% %Add the path to the current folder
addpath(path)

%% State frames of interest
dialog = sprintf('Are the Selected frames with or without EHD?');
button = questdlg(dialog, 'Select Case', 'Without EHD', 'With
EHD', 'Cancel', 'Cancel');
if strcmpi(button, 'With EHD')
    EHD = 'EHDon';
else if strcmpi(button, 'Without EHD')
    EHD = 'EHDOff';
end

```

```

end
%Choose the frame range in which to perform analysis
%Typically, do one set pre-EHD, and one post-EHD
%Frames chosen should not include any ramping
FrameStart = 5001;
FrameEnd = 6501;
%Resolution in which to display and analyze images. Spacing allows for the
%above range to be broken up into smaller ranges
spacing = 100;

%Vecor containing specific frame counts
FrameVector = FrameStart+spacing:spacing:FrameEnd

%Loop through each smaller frame range, as defined by the spacing variable
for j = 1:length(FrameVector)
    %Determine the frame in which to start analysis
    if j==1
        fstart = FrameStart;
    else
        fstart = FrameVector(j-1)
    end
    fend = FrameVector(j)
    numfiles = fend-fstart;

    % Only copy frame(fstart) to frame(fend) files to a temporary directory
    %Crease a temporary directory
    mkdir('temp')
    addpath('temp')
    %"Base" filename in which to construct image filenames
    filebase = 'frame';
    filenum = fstart;

    %% Copy range of files from directory to the temporary folder
    %assign a string number
    number = num2str(filenum);
    %Append string number to filename
    filename = strcat(path, '/', filebase, number, '.jpg');
    %Copy file to temporary directory
    copyfile(filename, 'temp')

    %% Manual image processing on each
    cd('temp')
    %Display each image (as dictated by the "spacing" variable, and count the
    %number of markers representing nucleating bubbles. Each bubble can and may
    %be counted twice, as taking a large number of samples will average out
    %bubbles nucleating and departing

    %Shorten filename (because temp directory is the root)
    filename(1:11) = [];
    imshow(filename)
    hold on
    counter = 0;

```

```

%Dialog with instructions.
dialog = sprintf('Select "floating" bubbles. Hit "Enter" when done');
title(dialog, 'FontSize', 14);
button = questdlg(dialog, 'Continue?', 'OK', 'Cancel', 'OK');
drawnow; % Refresh screen to get rid of dialog box remnants.
if strcmpi(button, 'Cancel')
    return;
end

while counter < 100 %automatically stops for too many bubbles
    % User clicks one point. If no point is selected, loop will end
    [bubblex,bubbley] = ginput(1);
    if isempty(bubblex)
        break;
    end

    % Put a cross over the point.
    plot(bubblex, bubbley, 'g+', 'MarkerSize', 24, 'LineWidth', 3);
    % Increment the count.
    counter = counter + 1

    %% Plot bubble locations as a function of the current frame and the
    counter number

    posarray(counter,:,j) = [bubblex bubbley]
end

numbubbles(j) = counter

cd ..

end

%% Post Processing
%% Save data to a figure

clearvars -except posarray EHD WidthVector j FrameStart FrameEnd spacing
FrameVector path numbubbles
%% Delete temporary directory
%Delete folder and all contents
rmdir('temp','s')
%Refresh MATLAB to ensure file can be created again
rehash()

%% Plot the average height of each bubble (erase zero entries)
catarray = posarray(:, :, 1)
exportfilename1 = strcat(path, 'hoverposition_', EHD, '.txt')
for k = 2:length(posarray(1,1,:))
    catarray = cat(2, catarray, posarray(:, :, k))
end
T = table(catarray)
writetable(T, exportfilename1)

```

```

heights = posarray(:,2,:);
heights(heights==0) = []
numentries = length(heights)
height_stdev = std(heights)
averageheight = mean(heights)

data = [averageheight,height_stdev]
exportfilename = strcat(path,'heights_',EHD,'.txt')
T1 = table(data)
writetable(T1,exportfilename)

```

### 8.3.3. BubbleWidth.m

```

%% Width of bubbles at detachment
%This script will allow the user to identify bubbles just before
%detachment, and then plot the widths and heights of each bubble at that moment

clc
clear
close all
%% Add path of interest
%Points script to location where a given case's discretized frames are
%stored
path = '1466641636';
% %Add the path to the current folder
addpath(path)

%% State frames of interest
dialog = sprintf('Are the Selected frames with or without EHD?');
button = questdlg(dialog, 'Select Case', 'Without EHD', 'With
EHD', 'Cancel', 'Cancel');
if strcmpi(button, 'With EHD')
    EHD = 'EHDOn';
else if strcmpi(button, 'Without EHD')
    EHD = 'EHDoff';
    end
end

%Choose the frame range in which to perform analysis
%Typically, do one set pre-EHD, and one post-EHD
%Frames chosen should not include any ramping
FrameStart = 5001;
FrameEnd = 6501;
%Resolution in which to display and analyze images
spacing = 100;

FrameVector = FrameStart+spacing:spacing:FrameEnd

WidthVector = zeros(1,FrameEnd-FrameStart)

%initialize the number counter for each bubble
numbubble = 1

```

```

%% Select 4 points per bubble, going clockwise from the base
for j = 1:length(FrameVector) %j is the number of frames
    if j==1
        fstart = FrameStart;
    else
        fstart = FrameVector(j-1)
    end
    fend = FrameVector(j)
    numfiles = fend-fstart;

    % Only copy frame(fstart) to frame(fend) files to a temporary directory
    %Create a temporary directory
    mkdir('temp')
    addpath('temp')
    %"Base" filename in which to construct image filenames
    filebase = 'frame';
    filenum = fstart;

    %% Copy range of files from directory to the temporary folder
    %assign a string number
    number = num2str(filenum);
    %Append string number to filename
    filename = strcat(path, '/', filebase, number, '.jpg');
    %Copy file to temporary directory
    copyfile(filename, 'temp')

    %% Manual image processing on each
    cd('temp')
    %Display each image (as dictated by the "spacing" variable, and count the
    %number of markers representing nucleating bubbles. Each bubble can and may
    %be counted twice, as taking a large number of samples will average out
    %bubbles nucleating and departing

    %Shorten filename (because temp directory is the root)
    filename(1:11) = [];
    imshow(filename)
    hold on
    counter = 0;

    dialog = sprintf('Select currently nucleating bubbles. Hit "Enter" when
done');
    title(dialog, 'FontSize', 14);
    button = questdlg(dialog, 'Continue?', 'OK', 'Cancel', 'OK');
    drawnow; % Refresh screen to get rid of dialog box remnants.
    if strcmpi(button, 'Cancel')
        return;
    end

```

```

while counter < 100 %automatically stops for too many bubbles
    % User clicks one point.  If no point is selected, loop will end

    [bubblex,bubbley] = ginput(1);
    if isempty(bubblex)
        break;
    end

    % Put a cross over the point.
    plot(bubblex, bubbley, 'g+', 'MarkerSize', 24, 'LineWidth', 3);
    % Increment the count

    counter = counter + 1

    posarray(counter,:,j) = [bubblex bubbley]
    %if 4 locations have been counted, save as one bubble coordinates

    if mod(counter,4)==0
        bubblewidth= posarray(4,1,j) - posarray(2,1,j)
        bubbleheight = posarray(1,2,j) - posarray(3,2,j)
        bubblestats(numbubble,:) = [bubblewidth bubbleheight] ; %save the
height and width in each column, with each row representing a new bubble
        numbubble = numbubble + 1
        counter = 0 ; %reset counter
        clear posarray
    end

end

numbubbles(j) = counter

cd ..

end

%% Post Processing
%Save data to a figure

clearvars -except posarray bubblestats numbubble EHD WidthVector j FrameStart
FrameEnd spacing FrameVector path numbubbles
%% Delete temporary directory
%Delete folder and all contents
rmdir('temp','s')
%Refresh MATLAB to ensure file can be created again
rehash()

exportfilename = strcat(path, '_', 'bubbledimensions', EHD, '.txt')
T = table(bubblestats)
writetable(T,exportfilename)

```



```

figure
histogram(numbubbles,10)
xlabel('Number of Nucleation Sites')
ylabel('Frequency')

```

### 8.3.4. Frequency

```

%% Frequency
%This script automates the statistical analysis of bubble departure frequency

clc
clear
close all
%% Add path of interest
%Points script to location where a given case's discretized frames are
%stored
path = '1466641636';
%Add the path to the current folder
addpath(path)

%% State frames of interest
%Choose the frame range in which to perform analysis
FrameStart = 410;
FrameEnd = 810;
spacing = 400;

FrameVector = FrameStart+spacing:spacing:FrameEnd

WidthVector = zeros(1,FrameEnd-FrameStart)

for j = 1:length(FrameVector)
if j==1
fstart = FrameStart;
else
    fstart = FrameVector(j-1)
end
fend = FrameVector(j)
numfiles = fend-fstart;

% Only copy frame(fstart) to frame(fend) files to a temporary directory
%Crease a temporary directory
mkdir('temp')
addpath('temp')
%"Base" filename in which to construct image filenames
filebase = 'frame';
    filenum = fstart;
%Copy range of files from directory to the temporary folder

```

```

i=1
movcount = 1
for i=1:numfiles+1
    %assign a string number
    number = num2str(filenum);
    %Append string number to filename
    filename = strcat(path, '/', filebase, number, '.jpg');

    %Copy file to temporary directory
    copyfile(filename, 'temp')

    %% Crop images if desired (Set Control Volume)
    I = imread(filename);
    tempfilename = strcat('temp/', filebase, num2str(filenum), '.jpg');
    delete(tempfilename)
    if i == 1 %open crop tool
        [I2, rect] = imcrop(I);
        imwrite(I2, tempfilename);
    else
        I2 = imcrop(I, rect);
        K2 = rangefilt(I2);
        imwrite(K2, tempfilename);
        imshow(K2)

        M(movcount) = getframe;

        %Vectors to define intensity line
        imsize = size(K2);

        hi = imsize(1);
        wi = imsize(2);

        Intens = improfile(K2, [0 wi], [hi*.2 hi*.2]);
        maxIntens(movcount) = max(max(Intens));
        movcount = movcount + 1;
        clear Intens
    end
    %Count to next file number
    filenum = filenum + 1;
end

%% Compute Spacing

figure
framerate = 1492; %fps
times = linspace(0, length(maxIntens), length(maxIntens)) / framerate * 1000
plot(times, maxIntens)
hold on
findpeaks(maxIntens, times, 'MinPeakProminence', 40)
xlabel('Time [ms]')
ylabel('Intensity')
axis([0 max(times) 0 max(maxIntens)*1.1])

[pks locs] = findpeaks(maxIntens, 'MinPeakProminence', 40);

```

```

framereate = 1492; %fps
timespacing = diff(locs/1492); %seconds, distance between detachment events
meantime = (mean(timespacing)) * 1000
freq = 1/(mean(timespacing))
timeserror = std(timespacing) * 1000
freqerror = 1/std(timespacing)
%% Post-Processing
firstpoint = ans(1,:);
secondpoint = ans(2,:);

width = secondpoint - firstpoint

WidthVector(1,j*spacing-(spacing-1):j*spacing) = width

clearvars -except WidthVector j FrameStart FrameEnd spacing FrameVector path
%% Delete temporary directory
%Change directory up one level
cd ..

%Delete folder and all contents
rmdir('temp','s')
%Refresh MATLAB to ensure file can be created again
rehash()

end

Frames = FrameStart:1:FrameEnd-1

figure
plot(Frames,WidthVector)
xlabel('Frame Number')
ylabel('Width [px]')
axis([FrameStart FrameEnd 20 45])

```